Investigation of Magnetic Properties and Barkhausen Noise of Electrical Steel

PhD Thesis

Nkwachukwu Chukwuchekwa

A thesis submitted to the Cardiff University in candidature for the degree of Doctor of Philosophy

Wolfson Centre for Magnetics

Cardiff School of Engineering

Cardiff University

Wales, United Kingdom

December 2011

DECLARATION

This work has not previously been accepted in substance for any degree and is not concurrently submitted in candidature for any degree.

Signed …………………… (candidate) Date …………………………………...

STATEMENT 1

This thesis is being submitted in partial fulfillment of the requirements for the degree of PhD.

Signed ………………… . (candidate)   Date …………………………………...

STATEMENT 2

This thesis is the result of my own independent work/investigation, except where otherwise stated. Other sources are acknowledged by explicit references.

Signed ………………… (candidate)   Date …………………………………...

STATEMENT 3

I hereby give consent for my thesis, if accepted, to be available for photocopying and for inter-library loan, and for the title and summary to be made available to outside organisations.

Signed ………………… (candidate)   Date …………………………………...

Acknowledgements

I am very grateful to my primary supervisor, Professor Anthony J. Moses, for his guidance, stimulation and encouragement from the inception to the end of this research. His supervision, counsels and expertise improved this work significantly. He also supported and approved my attendance at four International conferences to present my research.

I wish to also thank my second supervisor, Dr Philip Anderson for his advice, comments and alternative views/suggestions. Constructive criticisms from Staff and students at the Wolfson Centre especially during monthly seminar presentations and weekly project meetings were of immense help. The visit to Wolfson Centre of Dr. E. N. C. Okafor, my senior colleague and the then Head of department of Electrical/Electronic Engineering (EEE), Federal University of Technology Owerri (FUTO) Nigeria was of great encouragement.

All the staff of the research office, finance office, IT services, mechanical workshop, and electrical/electronic workshop of the School of Engineering too numerous to mention are all appreciated.

The support and encouragement I received from my wife and best friend, Mrs. Joy Ulumma Chukwuchekwa is second to none. Her sacrifice and that of my children, Deborah, Ebenezer and Abigail during the period of my PhD are deeply appreciated. I say a big thank you to my mother, Mrs. Eunice Chukwuchekwa and my siblings for their moral and spiritual support especially during the difficult times.

As a believer in Jesus Christ, I am pleased to thank God for the success of this research. My Christian brethren, friends, relatives, well wishers, students and colleagues in EEE department, FUTO too numerous to mention are also appreciated. Finally, I am grateful to the UK Magnetics Society for financial support to travel and present my research at the 20th Soft Magnetic Materials (SMM 20) Conference in Kos Island, Greece.

Summary

Magnetic characteristics of grain oriented electrical steel (GOES) are usually measured at high flux densities suitable for its applications in power transformers. There are limited magnetic data at low flux densities which are relevant for the characterisation of GOES for applications in metering instrument transformers and low frequency magnetic shielding in MRI (magnetic resonance imaging) medical scanners. Magnetic properties of convention grain oriented (CGO) and high permeability grain oriented (HGO) electrical steels were measured and compared at high and low flux densities at power magnetising frequency. HGO was found to have better magnetic properties at both high and low magnetisation regimes. This is because of the higher grain size of HGO and higher grain-grain misorientation of CGO.

As well as its traditional use in non-destructive evaluation, Barkhausen Noise (BN) study is a useful tool for analysing physical and microstructural properties of electrical steel which control their bulk magnetic properties. Previous works deal with measurements carried out at high flux densities (0.2 T and above) but this work demonstrates that BN has different characteristics at low flux densities. The results show that the amplitude sum and the rms BN signals are higher for HGO than CGO steels at high flux densities. Below 0.2 T, the BN signal becomes higher for CGO steel. This is because of grain size/misorientation effects. Mechanically scribing of HGO samples on one surface transverse to the rolling direction was found to reduce the BN amplitude at high flux densities due to the decrease of domain width by scribing. The trend reverses again at low flux density.

Removal of the coating from the surface of CGO and HGO electrical steels was found to increase the BN due to the widening of the 180° domains as a result of the release of the tensile stress imparted to the materials during coating.
The BN characteristics of decoated samples with a 3 MPa tension applied were found to be similar to those observed before decoating demonstrating the close similarity between the effects of coating stress and externally applied stress on BN due to their similar roles in domain refinement. A strong correlation between average velocity of domain wall movement and changes in BN in conventional and high permeability steels was found which demonstrates that the dominant factor responsible for BN

emission is the mean free path of domain wall movement and hence the width of the predominant 180° domains in these materials.

 BN of commercially produced non-oriented electrical steel was found to be influenced by silicon contents and sample thickness. BN was found to increase with decreasing strip thickness and increase with increasing silicon contents owing to eddy current shielding effects. The rms values of the BN and the total sum of amplitudes were found to increase with the rate of change of flux density at all the peak flux densities measured. The findings show that the influence of sample thickness and silicon content is significant and must be taken into consideration when measuring and interpreting BN in non-oriented electrical steel.

Abbreviations

B	Magnetic Flux density
BN	Barkhausen noise
BOS	Basic oxygen system
CGO	Conventional grain oriented
CuMnS	Copper manganese sulphide
DAQ	Data acquisition
GOES	Grain oriented electrical steel
H	Magnetic field
HGO	High grain oriented
HTCA	High temperature coil anneal
KMO	Kerr magneto-optic
LabVIEW	Laboratory virtual instruments engineering workbench
M	Magnetisation
MFL	Magnetic flux leakage
MgO	Magnesium oxide
MnS	Magnesium sulphide
MPa	Mega Pascal
NGO	Non grain oriented
PXI	**P**eripheral component interconnect e**X**tension for **I**nstrumentation
RMS	Root mean square
SST	Single sheet tester
TCR	Temperature Coefficient of Resistance
TNP	Total number of peaks
TSA	Total sum of amplitudes
UKAS	United Kingdom accreditation service

Table of Contents

List of figures

List of tables

List of equations

$\vec{B} = \mu_0(\vec{H} + M) = \mu_0(1 + \chi)\vec{H} = \mu_0\mu_r\vec{H}$ (1.1)	3
$E_k = K_1(\alpha_1^2\alpha_2^2 + \alpha_2^2\alpha_3^2 + \alpha_3^2\alpha_1^2) + K_2((\alpha_1^2\alpha_2^2\alpha_3^2)$ (2.1)	12
$E_m = 1/2\,N_D\,M^2$ (2.2)	13
$E_\lambda = -\dfrac{3}{2}\lambda_{100}\sigma(\alpha_1^2\gamma_1^2 + \alpha_2^2\gamma_2^2 + \alpha_3^2\gamma_3^2) - 3\lambda_{111}\sigma(\alpha_1\alpha_2\gamma_1\gamma_2 + \alpha_2\alpha_3\gamma_2\gamma_3 + \alpha_3\alpha_1\gamma_3\gamma_1)$ (2.3)	13
$E_H = HM\cos\phi$ (2.4)	14
$\vec{B} = \mu\vec{H}$ (2.5)	16
$\vec{B} = \mu_0\vec{H}$ (2.6)	16
$\vec{B} = \mu_r\mu_0\vec{H}$ (2.7)	16
Total loss = Hysteresis Loss + Classical eddy current loss + Excess Eddy Current loss (2.8)	18
$W_{cl} = \dfrac{\sigma d^2\pi^2 B_m^2}{\beta}f$ (2.9)	18
$W_{exc} = CB_m^{1.5}f^{0.5}$ (2.10)	20
$Total\,sum\,of\,amplitudes = \sum\limits_{i=1}^{z=20}(\sum\limits_{k=1}^{m}(|a_k|))_i$ (4.1)	47
$rms\ \ \psi = \sqrt{\dfrac{1}{N}\sum\limits_{i=0}^{N-1}x_i}$ (4.2)	47
$Form\,factor = \dfrac{V_{rms}}{|V_{average}|} \overset{ideal}{=} \dfrac{\pi}{2.\sqrt{2}} = 1.11072$ (5.1)	54
$H(t) = \dfrac{N_1 i(t)}{l_m}$ (5.2)	57

$$v_{eff} = \dfrac{u^4(y)}{\displaystyle\sum_{i=1}^{N} \dfrac{v_i^4(y)}{v_i}}$$

Chapter 1　　General introduction

1.1　　Introduction

Electrical steel is categorised into a number of product types. These are comprised of grain oriented and non grain oriented electrical steels. Grain oriented electrical steel (GOES) is a soft magnetic material and usually has a silicon level of 3% and is so called because it contains a grain structure with a distinct preferred orientation. The magnetic properties such as relative permeability and power loss are optimised when the material is magnetised along this direction of preferred orientation. For this reason GOES is usually used in the construction of medium to large transformer cores. GOES is comprised of the conventional grain oriented (CGO) and high permeability grain oriented (HGO) steels.

Non grain oriented (NGO) electrical steels are also soft magnetic materials but contain a much finer grain structure and exhibit little or no preferred orientation and are most commonly used in applications such as rotating electrical machines and small transformers used in domestic appliances that require isotropic magnetic properties in the plane of the sheet. In these applications, the magnetic flux is oriented at various angles with respect to the rolling direction of the sheet in some parts of the magnetic circuits. They can be supplied with or without one of a range of coatings either in a fully processed state or semi-processed condition depending on the intended use of the steel. Fully processed material requires no further processing by the customer because it is supplied after final properties developing anneal. With semi-processed material, tempering during the extension pass is the last stage of processing that is undertaken by the supplier. The process involves giving the strip a final cold reduction which results in a material with an increased surface hardness. This surface stiffness helps the stamping of laminations especially where strip is supplied without a coating. The laminations then require a final property developing customer anneal to fully optimise their magnetic properties [1.1]. Strips are supplied without coating to allow for gas penetration if decarburisation is needed in the final customer anneal.

As these materials are extensively used, they are responsible for a large portion of the energy loss in electrical power systems because of the non-linearity of the B-H characteristic. For this reason, the study and the control of the magnetic and microstructural parameters of these steels becomes a very important economic issue [1.2] and this accounts for the reason why these materials are investigated in this study. Microstructural features such as grain size, number and distribution of pinning sites, grain boundaries and grain-grain misorientation are the main parameters that distinguish CGO from HGO in relation to their bulk magnetic properties.

Magnetic characteristics of electrical steel are usually measured at the high flux densities suitable for applications in power transformers, motors, generators, alternators and a variety of other electromagnetic applications. Magnetic measurements at very low inductions are useful for magnetic characterisation of electrical steel used as cores of metering instrument transformers and low frequency magnetic shielding such as for protection from high field MRI (magnetic resonance imaging) medical scanners. Magnetisation levels in these applications are generally believed to be in the low flux density region so material selection based on high flux density grading is seriously flawed.

Barkhausen Noise (BN) is a very important tool for non-destructive characterisation [1.3-1.5]. Although the BN was reported more than 90 years ago [1.6], its origin and characteristics remain not fully understood [1.2]. The BN mechanism can provide understanding of the microstructure of the material, without the use of laborious methods such as the Epstein frame typically used for characterisation of electrical steels. The Barkhausen effect arises from the discontinuous changes in magnetisation (M) under the action of a continuously changing magnetic field (H) when domain walls encounter pinning sites [1.7]. This noise phenomenon can be investigated statistically through the detection of the random voltage observed on a search coil placed on the surface or encircling the material during the magnetisation of the material. BN are related to the way domain walls interact with pinning sites, such as defects, precipitates and grain boundaries, as domains reorganise to align magnetic moments in the direction of the applied magnetic field. Within the body of a pinning site, magnetic dipoles are formed at the surrounding interface. This dipole arrangement is split forming a four-pole system if a domain wall bisects the pinning site thereby reducing the overall magnetostatic energy and pinning the domain wall as

a result [1.8, 1.9]. The number of Barkhausen emissions is determined by the number of pinning sites provided that the volume of the sites is sufficient to cause pinning. BN is therefore an important tool for evaluating the scale of interaction between pinning sites of varying sizes and magnetic domains [1.10].

1.2 Relationship Between Barkhausen Noise and Bulk Magnetic Properties

It is required that the magnetisation, M, be reproduced for each measurement in order to generate consistent BN. A general description of bulk magnetic behaviour in a material is:

$$\vec{B} = \mu_0(\vec{H} + M) = \mu_0(1 + \chi)\vec{H} = \mu_0\mu_r\,\vec{H} \qquad (1.1)$$

where B is the flux density, μ_0 is the permeability of free space having a value of 4π x 10^{-7} H/m, χ is the susceptibility, and μ_r is the relative permeability and is dimensionless. In ferromagnetic materials, $\chi \gg 1$ in regions where BN primarily occurs [1.11], so B $\approx \mu_0$M.

Therefore, the dominant contribution to flux density distribution in a ferromagnetic material is the sample magnetisation distribution, making B a suitable control parameter for Barkhausen noise measurements [1.12].

1.3 Aims of the Investigation

BN at low and high flux densities in electrical steel were studied in this work. It is believed that low magnetisation Barkhausen studies particularly at power magnetising frequencies have not been carried out on such materials previously. This gives a new approach to studying the effects of micro structure on magnetic properties of electrical steel. BN measurements at high and low flux densities were compared.

Magnetic properties such as the B-H loop, coercivity, relative permeability and specific power loss were also measured at both high and low flux densities.

In summary, the main aims of this work are as follows:

➢ To investigate the magnetic properties and BN of GOES.

➢ To investigate the effect of domain refinement on BN and magnetic properties of HGO.

➢ To study the effects of surface coating and externally applied stress on BN in GOES and their role in domain refinement.

➢ To study the effects of strip thickness and silicon content on BN of NGO electrical steel.

➢ To investigate the effects of strips thickness on BN of GOES.

1.4   Research Methodology

A laboratory based technique was developed to magnetise single strips at 50 Hz over a flux density range from 0.008 T to 1.5 T. The single strip rig is capable of incorporating a linear stressing mechanism to evaluate the effect of external stress in the strips. Equipment for generating B-H characteristics, magnetic properties and BN of electrical steel were assessed and procured. Accurate, repeatable and reproduceable measurements of magnetic properties and BN at low flux densities (0.008 T – 0.2 T) are extremely challenging so proper care was taken to avoid external influence on the measurements and the use of very low distortion generation and amplification stages (in onboard DAQ card) in the design together with improved systems for waveform control.

Static magnetic domain observation was carried out using magnetic domain viewer for coated samples and Kerr magneto optic (KMO) microscope for decoated samples to determine how magnetic properties and BN of the samples are affected by domain width and also under coated and decoated conditions. The results of the magnetic properties were evaluated in terms of the coercivity, relative permeability and power loss. BN was analysed using the root mean square (rms), total sum of amplitudes (TSA) and total number of peaks (TNP) of the induced voltage peaks.

1.5   Structure of the Thesis

Chapter one gives an introduction to the research, the objectives of the research and the research methodology. The basics of ferromagnetism is treated in chapter two. Also included in this chapter is the magnetic domain theory including closely related energy components and the effects of domains and domain walls motion during magnetisation. In chapter three, the development and production of electrical steel comprising CGO, HGO and NGO electrical steels are highlighted. The effects of applied stress in these materials are also discussed. The BN phenomenon and the various factors that affect it are discussed in chapter four. Past works of other researchers are also reviewed in this chapter including the parameters used to analyse BN in this work. The details of the development of the magnetisation and BN measurement systems used in this work are given in chapter 5. The tension stressing rig for the application of tensile stress and the KMO technique for magnetic domain observation are discussed. The uncertainty in the measurements as recommended by UKAS (United Kingdom Accreditation Service) M3003 is detailed in this chapter.

The experimental results and discussions on:

a) Measurement of magnetic properties and BN of GOES
b) Effect of domain refinement on BN and magnetic properties of HGO steel.
c) Effect of surface coating and external stress on BN of GOES.
d) Effect of strip thickness and silicon content on BN of NGO electrical steel and
e) Effect of strip thickness on BN of GOES

are presented in chapters 6 – 10 respectively.

The thesis is concluded in chapter 11 followed by suggestions for further work.

References to chapter 1

[1.1] J. P. Hall, Evaluation of residual stresses in electrical steel, PhD thesis, Cardiff University, 2001.

[1.2] A Moses, H. Patel, and P. I. Williams, AC Barkhausen noise in electrical steels: Influence of sensing technique on interpretation of measurements, Journal of Electrical Engineering, Vol. 57. No. 8/S, pp. 3-8, 2006.

[1.3] C. C. H. Lo, J. P. Jakubovics, and C. B. Scrub, Non-destructive evaluation of spheroidized steel using magnetoacoustic and Barkhausen emission, IEEE Transactions on Magnetics. Vol. 33, No. 5, pp. 4035-4037, 1997.

[1.4] H. Kikuchi, K. Ara, Y. Kamada, and S Kobayashi, Effect of microstructure changes on Barkhausen noise properties and hysteresis loop in cold rolled low carbon steel, IEEE Transactions on Magnetics, Vol. 45, No.6 , pp. 2744-2747, 2009.

[1.5] K. Hartmann, A. J. Moses and T. Meydan, A system for measurement of AC Barkhausen noise in electrical steels, Journal of Magnetism and Magnetic Materials, Vol. 254-255 , pp. 318-320, 2003.

[1.6] H. Barkhausen and B. Gerausche, Ummagnetisieren von Eisen, Physikal Zeitschr, 20, pp. 401-403, 1919.

[1.7] M. F. de Campos, M. A. Campos, F. J. G. Landgraf and L. R. Padovese, Anisotropy study of grain oriented steels with magnetic Barkhausen noise, Journal of Physics, Conference Series 303 , 012020, 2011.

[1.8] D.C Jiles, Introduction to Magnetism and magnetic materials, Chapman and Hall, New York, 1991.

[1.9] L. J. Dijkstra and C. Wert, Effect of Inclusions on Coercive Force of Iron, Physical Review, 79, pp. 979-985, 1950.

[1.10] S. Turner, A. Moses, J. Hall and K. Jenkins, The effect of precipitate size on magnetic domain behaviour in grain-oriented electrical steels, Journal of Applied Physics, 107, 09A307-09A309-3, 2010.

[1.11] T. Krause, J. M. Makar and D. L. Atherton, Investigation of the magnetic field and stress dependence of 180° domain wall motion in pipeline steel using magnetic Barkhausen noise, Journal of Magnetism and Magnetic Materials, Vol. 137, pp. 25–34, 1994.

[1.12] S. White, T. Krause, and L. Clapham, Control of flux in magnetic circuits for Barkhausen noise measurements, Measurement Science Technology, Vol.18, pp. 3501–3510, 2007.

Chapter 2   Ferromagnetism and domain theory

2.1   Introduction

Study of electrical steel requires background knowledge of ferromagnetic materials and magnetic domains. The existence of ferromagnetic materials is due to the presence of magnetic domains which are spontaneously magnetised regions separated by domain walls in the material. In this chapter, the effect of domains and domain walls motion including the various related energy components during magnetisation are discussed. The total loss at power magnetisation frequency composed of hysteresis, eddy current and anomalous losses are also highlighted.

2.2   Magnetic moments

The magnetic moments of individual atoms lead to bulk magnetic behaviour. The two contributions to the atomic magnetic moment come from the momentum of electrons viz: spin and orbital motion. From Pauli Exclusion Principle, only one electron in an atom is allowed to have a particular combination of the four quantum numbers: n, l, m_l and m_s. The electron energy state is specified by the first three quantum numbers. The fourth, m_s, can only take values $\pm 1/2$. Up to two electrons may therefore be contained in each energy state. If only one electron is present, its spin moment contributes to the overall spin moment of the atom. A second electron having an antiparallel spin to the first will cause the two spins to cancel out, giving no net moment. Materials which have a larger number of unpaired spins have strong magnetic properties. In crystalline solids, the orbital moments are strongly coupled to the atomic lattice and therefore cannot change direction when a magnetic field is applied and as a result the magnetic moments in solids can be considered as being due to the spins only.

2.3   Ferromagnetic materials

Atoms in ferromagnetic materials possess permanent magnetic moments that are aligned to each other in parallel over extensive regions. Ferromagnetic materials

contain spontaneously magnetised magnetic domains where each individual domain's magnetisation is oriented differently with respect to the magnetisation of its neighbour. This spontaneous domain magnetization exists due to unpaired electron spins from partially filled shells, spins aligned parallel to each other because of strong exchange interaction between neighbouring atoms. The arrangement of spins and the spontaneous domain magnetisation are dependent on temperature. The total magnetisation of a material is the vector sum of the domain magnetisations. When the total resultant magnetisation of all magnetic domains is zero, a ferromagnetic material is said to be demagnetised. When a high enough magnetic field is applied however, the resultant magnetisation changes from zero to saturation value. When the magnetic field is decreased and reverses in direction, the magnetisation may not retrace its original path relative to the magnitude of the field, thus exhibiting hysteresis [2.1]

In anti-ferromagnetic material, the exchange interaction between neighbouring atoms leads to anti-parallel alignment of the atomic magnetic moments. This causes the magnetisation to be cancelled out and the material appears to behave to some extent as paramagnetic. Paramagnetic materials possess a positive but small susceptibility to magnetic fields and so do not retain the magnetic properties when the external field is removed. Ferromagnetic materials also have a Curie point above which they exhibit paramagnetic behaviour [2.2]. Examples of ferromagnetic materials are iron, cobalt, nickel, several rare earth metals and their alloys. A strong ferromagnet such as electrical steel has a high relative permeability.

Other forms of magnetism exist such as diamagnetism and paramagnetism but the material permeabilities are very low [2.3, 2.4] and not relevant to this research.

2.4   Magnetic domains

In ferromagnetic materials, individual atomic magnetic moments tend to stay parallel to each another, keeping the exchange energy low, (the exchange energy is brought about when individual atomic magnetic moments attempt to align all other atomic magnetic moments within a material). Such an alignment can increase the magnetostatic energy by creating a large external magnetic field as shown in Fig. 2.1 (a). Magnetostatic energy is a self-energy owing to the interaction of the magnetic field created by the magnetization in some portion of the material on other portions of

the same material. Therefore within the material, many magnetic domains are created to lower the external magnetic field as in figures 2.1 (a) and (b). Within each domain, individual magnetic moments add up to a total domain magnetization [2.2]. Furthermore, the domain magnetizations of neighbouring magnetic domains are antiparallel. In this configuration, the exchange energy is increased, however the magnetostatic energy is lowered. Domain walls are formed between magnetic domains. It should be noted that some of these walls of different orientation occur in closure domains as illustrated in figure 2.1 (d). The latter are created when the material divides into magnetic domains to allow more of the magnetic flux to stay within the material, thereby minimizing magnetostatic energy [2.4].
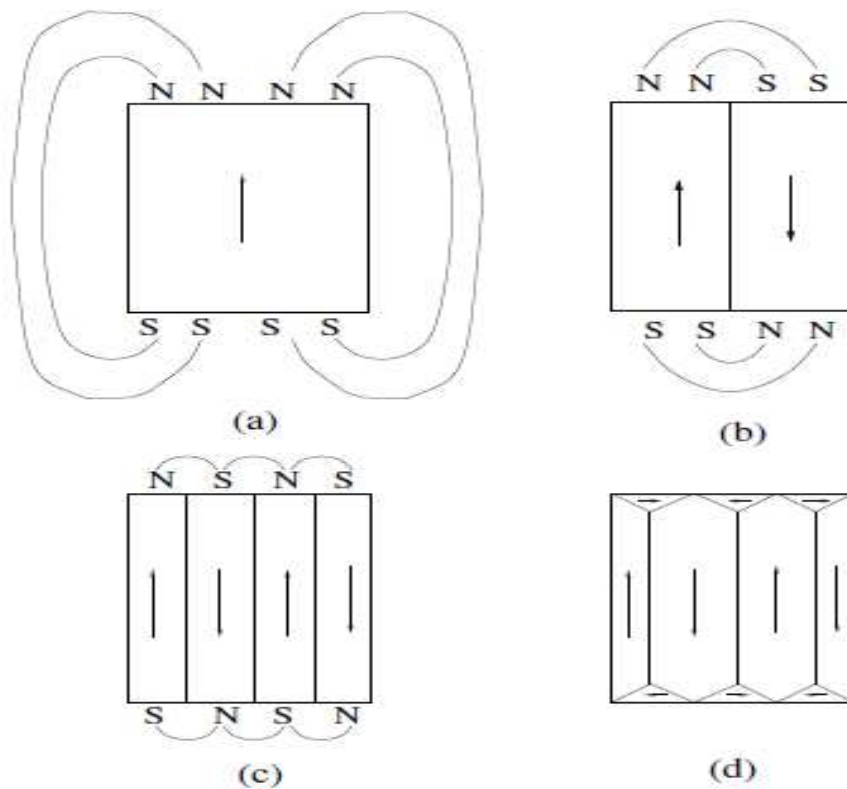
Fig. 2.1: Rearrangement of domains at the demagnetised state due to the energy minimization: a) saturated sample with high magnetostatic energy, E_m, b) dividing into two reduces E_m c) more division reduces E_m further d) free poles eliminated by closure domains [2.5].

2.5   Domain walls

Domains are separated by domain walls containing layers of atoms. As shown in figure 2.2, within a domain wall, the direction of magnetic moments changes from its direction in one domain to the direction in another domain leading to the creation of a transitional region. If the transition from one magnetization direction to another is abrupt, such as the case for a perfect antiparallel domain magnetization, the exchange energy will be too high to keep this domain configuration in equilibrium. A domain wall of a certain thickness that is comprised of atomic magnetic moments of slowly varying orientation as shown in figure 2.2 ensures a smoother transition opposite to domain magnetization direction thereby decreasing the exchange energy. The thickness of the transition layer is determined, being limited by the magnetocrystalline energy, which tends to keep atomic magnetic moments aligned along one of the easy directions of the crystal axes in order to maintain a minimum [2.4].
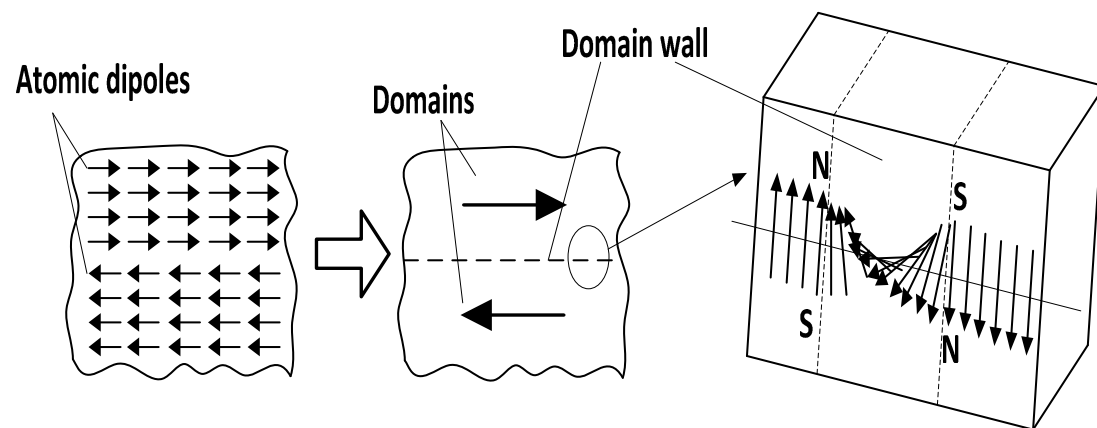
Fig. 2.2: Illustration of domains and domain wall containing atomic magnetic moments of gradually varying orientation, ensuring a smoother transition to opposite domain magnetization in a single crystal of iron [2.2].

Since domain magnetizations tend to align with one or more of the preferred crystallographic axes in iron alloys, domain walls separating domains of different orientations can be classified as 180° or 90° as in iron depending on the angles these crystallographic axes make in a specific lattice [2.4].

2.6   Magneto crystalline anisotropy energy

Anisotropy is the directional dependence of the properties of a material. Magnetocrystalline anisotropy is defined as the variation of magnetic properties of a material from one crystallographic direction to another. For a given magnetic field along the crystallographic directions, the measured magnetization varies. The concept of easy and hard directions of magnetization arises because of this. The magnetic field needed to reach saturation magnetization in the easy direction is less than the field needed to reach saturation in the hard direction. The easy and hard directions can be easily determined by measuring the magnetic properties of single crystals magnetised along different directions and vary from material to material. Iron and electrical steel alloys have easy direction along <100> and the hard directions along <111> with the intermediate being <110>.

The amount of magnetocrystalline anisotropy is normally represented in terms of energy density which varies with crystal structure because of different lattice symmetries. The grains in electrical steels which have a cubic crystal structure, magnetocrystalline anisotropy energy, E_k, is given by:

$$E_k = K_1 (\alpha_1^2 \alpha_2^2 + \alpha_2^2 \alpha_3^2 + \alpha_3^2 \alpha_1^2) + K_2 (\alpha_1^2 \alpha_2^2 \alpha_3^2) \qquad (2.1)$$

where α_1, α_2 and α_3 are the cosines of the angles between the saturation magnetization, M_S, and the x, y and z axis of the cubic crystal structure. K_1 and K_2 are the first and second order cubic anisotropy constants respectively which for 3% silicon iron at room temperature are 4.8 x 10^4 J/m^3 and 5 x 10^4 J/m^3 respectively [2.2]. A positive value of K shows a material having the direction of domain moments aligned with the [100] crystal direction while a negative value show an alignment with the [111] direction.

2.7   Magnetostatic energy

The magnetostatic energy indicates the total free pole energy of the domain structure. When considering a piece of ferromagnetic material containing only a single domain, free magnetic poles exist at the discontinuous ends of the sample. This would create a

field within the sample known as the demagnetising field. The demagnetising field has an energy E_m associated with it given by [2.6]:

$$E_m = 1/2 \, N_D \, M^2 \tag{2.2}$$

where N_D is its demagnetising factor of the material. Subdividing the material into two oppositely magnetised domains will reduce the demagnetising field and hence the magnetostatic energy. The subdivision would continue indefinitely with each subsequent division reducing the magnetostatic energy further if the magnetostatic energy were the only contributing factor.

2.8   Magnetoelastic energy

Application of stress causes reorientation of the atomic magnetic moments of the lattice. This reorientation takes place because the mechanical strain that is set up in the lattice moves the magnetic moments away from the easy axis of the lattice. The magnetic energy that is associated with these lattice strains is called magnetoelastic energy. Stress has similar effects on both magnetoelastic energy and magnetocrystalline anisotropy where there is the creation of easy axes of magnetisation. The magnitude of the magnetoelastic energy, E_λ, for a cubic crystal under uniform stress (σ) can be expressed as shown in equation 2.3:

$$E_\lambda = -\frac{3}{2}\lambda_{100}\sigma(\alpha_1^{\ 2}\gamma_1^{\ 2} + \alpha_2^{\ 2}\gamma_2^{\ 2} + \alpha_3^{\ 2}\gamma_3^{\ 2}) - 3\lambda_{111}\sigma(\alpha_1\alpha_2\gamma_1\gamma_2 + \alpha_2\alpha_3\gamma_2\gamma_3 + \alpha_3\alpha_1\gamma_3\gamma_1)$$

$$\tag{2.3}$$

where λ_{100} and λ_{111} are the magnetostriction constants with strains measured under magnetic field along the <100> and <111> directions respectively. γ_1, γ_2, and γ_3 are the direction cosines of the stress components with respect to the crystal axes [2.7].

2.9   The effect of an externally applied field

If a small magnetic field is applied to a magnetic material such as electrical steel, magnetisation occurs by the motion of 180° and 90° domain walls until the net force on all walls is zero. This takes place by the motion of domain walls through the

material such that domains in the direction of the applied field grow at the expense of all others. A second effect that may also occur during magnetisation is that the magnetic moments within a domain may be rotated out of the easy axes of magnetisation and into the direction of the applied field. A higher applied magnetic field than domain wall motion is needed in this effect since the domain magnetisation is being moved away from the easy axes and is associated with an increase in the stored magnetocrystalline anisotropy energy [2.8]. The energy due to an externally applied field can be described by equation 2.4 [2.1] as follows:

$$E_H = HM \cos \phi \qquad (2.4)$$

where H is the applied magnetic field, M is the magnetisation and ϕ is the angle between the easy lattice direction and the field.

2.10   Energy loss due to magnetisation

Magnetic materials are characterised uniquely by their B-H loops.
Work is done in changing the magnetisation of a magnetic material resulting in the dissipation of energy (mainly heat) from the material to its surroundings. As the material is taken through a magnetisation cycle the time lag between the instantaneous applied H and the corresponding B of the material results in a typical B-H loop as shown in figure 2.3.
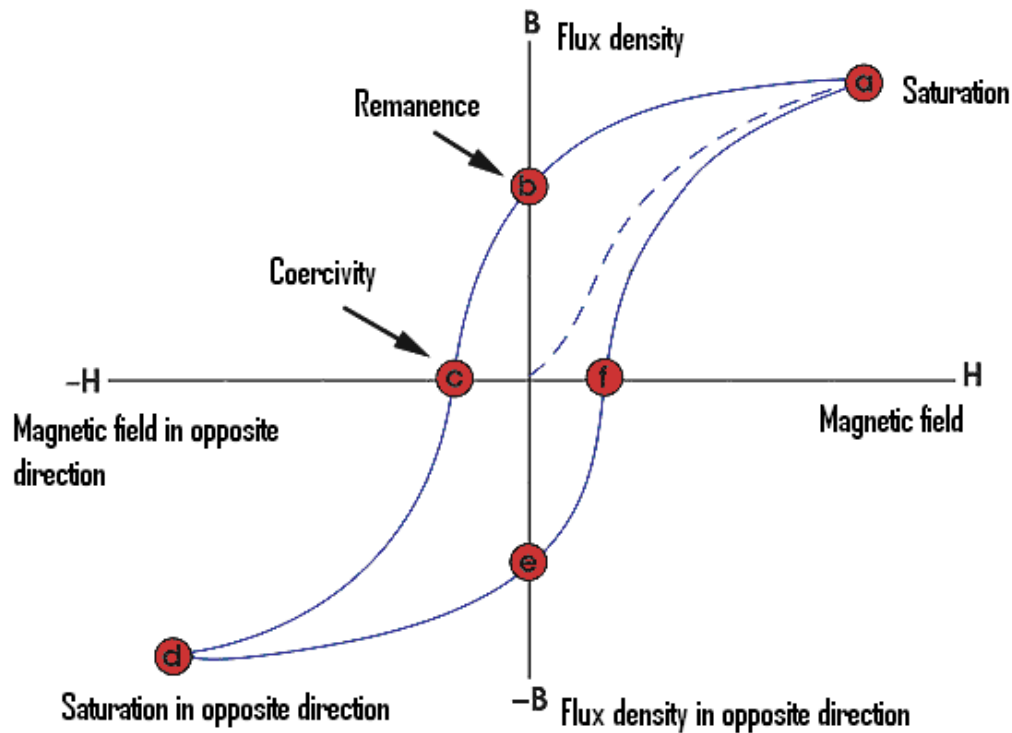
Fig. 2.3: Typical B-H loop of a ferromagnetic material [2.9].

The B-H loop is generated by measuring B of a ferromagnetic material while H is changed. A ferromagnetic material that has been completely demagnetized will follow the dashed line as H is increased from zero along a given direction. All of the magnetic domains are aligned at point "a" and an increase in H will produce very little increase in B. At this point, the material has almost reached magnetic saturation. The curve arrives at point "b" when H is reduced to zero where some magnetic flux remains in the material even though H is zero. This is known as the state of remanence often denoted as B_R which is caused by domain walls being pinned by impurities. The point "c" will be reached after H is reversed, which is known as the coercive point, H_C, where the flux has been reduced to zero. Point "d" will be reached where the material will again become magnetically saturated as H is increased in the opposite direction. Reducing H to zero brings the curve to point "e" which will have a level of remanence equal to that achieved in the other direction. Applying H again along the positive direction will return B to zero. From point "f", the curve will take a different path back to the saturation point where the loop will be completed [2.9]. The

area enclosed by the loop is directly proportional to the energy loss in the material per unit volume per magnetisation cycle which is often referred to as hysteresis loss.

A number of basic magnetic properties of a material can be determined from the hysteresis loop viz:

Remanence – This is the magnetic flux density that remains in a material when the magnetic field is zero. It is the value of B at point b in figure 2.3 and can be represented with the symbol B_R.

Coercivity – This is the amount of reverse magnetic field that is applied to a magnetic material to make the magnetic flux density to return to zero. It is the value of H at point c in figure 2.3. It is also known as the coercive field and is symbolised as H_C.

Permeability –The ease at which magnetic flux is established in a material defines the permeability of that material. Permeability (μ) is used to define the relationship between B and H as:

$$\vec{B} = \mu \vec{H} \qquad\qquad (2.5)$$

The relationship between B and H in free space is written as:

$$\vec{B} = \mu_0 \vec{H} \qquad\qquad (2.6)$$

B is expressed relative to free space in other mediums as:

$$\vec{B} = \mu_r \mu_0 \vec{H} \qquad\qquad (2.7)$$

When a small external magnetic field is applied, domains with moment oriented nearest to the direction of the field will grow at the expense of their neighbours as illustrated in figure 2.4 for a crystal of iron. The blue lines in the figure show domain wall positions in the absence of an applied field. The black vertical lines are the new wall position under the influence of applied field. The distance between the blue and the black lines in the figure is the domain wall displacement. This growth occurs by 180° domain wall movement in this particular case and this process is reversible when

the magnetic field is removed. At higher field amplitude the domain wall motion becomes irreversible and irreversible domain rotation also occur. When the field amplitude is further increased, saturation occurs and the sample will be converted into a single domain. This is the state of technical saturation magnetisation.

Fig.2.4: Schematic diagram showing domains with moments aligned most closely with the applied field will increase in volume at the expense of the other domains.

2.11   Hysteresis process and energy loss

The wider the B-H loop, the more energy is stored and dissipated in the material. Permanent magnets which are hard magnetic materials require wider B-H loops to store more energy while B-H loops of soft magnetic materials like electrical steel should be narrow to achieve low loss. The anhysteretic (i.e. without hysteresis) B-H characteristic is ideal for soft magnetic material. Under ac magnetisation, the B-H loop in figure 2.3 is wider due to additional magnetic fields from the eddy current (electric currents which are created when the material experiences changes in magnetic field) and excess losses (explained in section 2.13) and the energy loss per cycle is higher than under quasi-static (so slowly as appear to be static) condition.

These losses are frequency dependent and are referred to as dynamic losses [2.10]. The static hysteresis losses are frequency independent.

The loop area is equal to the total energy lost per cycle for sinusoidal magnetisation. This total loss can be broken into components which can be expressed as:

Total loss = Static hysteresis Loss + Classical eddy current loss + Excess (anomalous) loss   (2.8)

2.12   Classical eddy current loss

When an alternating magnetic field is applied to a magnetic material, its magnetization changes which in turn gives rise to a flux. This flux leads to eddy currents which results to a distribution of flux density through the material. The eddy currents will, in turn, create a counter field encircled by them. The originally applied field is opposed by the counter field leading to a shielding effect which is proportional to the rate of change of flux density [2.11]. Classical eddy current loss is as a result of circulating currents induced in a thin lamination. Fig. 2.5 is a simplified diagram showing the distribution of eddy currents (I_{eddy}) in an infinite sheet of homogeneous magnetic material when subjected to sinusoidal magnetisation at a frequency, f.

The classical eddy current loss, W_{cl}, in the material in figure 2.5 is given by [2.12]:

$$W_{cl} = \frac{\sigma d^2 \pi^2 B_m^2}{\beta} f$$ (2.9)

where σ is the electrical conductivity, B_m is the peak value of the flux density, β is a geometrical factor and d is the thickness of the lamination. Equation (2.9) is derived from Maxwell's equation assuming a perfectly homogenous body with a uniform flux distribution over the sheet. For a sheet β = 6 [2.13]. For a sinusoidal applied field of frequency, f, the value of β is valid when d is smaller than the depth of penetration [2.14], i.e.:

$$d < \sqrt{\frac{1}{\pi\mu_r\mu_0\sigma f}}$$

there will be eddy current shielding effect if the condition in the expression above is not satisfied and greater opposing field caused by the eddy currents will be exhibited by the inner regions of the material than the outside regions. The shielding effects occur when eddy currents flowing in the material produce magnetic fields which oppose the applied field thereby reducing the net magnetic flux and causing decrease in current flow as the depth increases. The shielding effect will increase with frequency since eddy current increases with frequency.
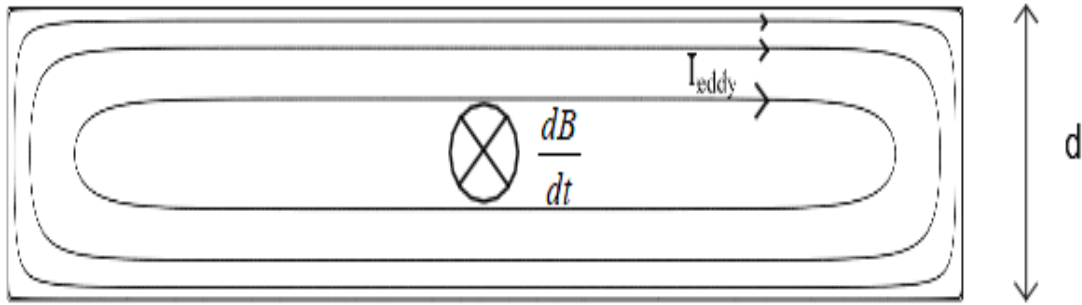
Fig.2.5. Schematic diagram of the distribution of eddy current in a lamination of width w and thickness d [2.11].

2.13   Anomalous loss

The discrepancy between the total measured loss and that due to the sum of the classical and static hysteresis loss account for the anomalous or excess losses and is known to be due to complex domain structures causing inhomogeneities in the magnetisation of the material. This leads to higher eddy current losses than those due to the classical loss. Both eddy current and anomalous losses are dependent on the rate of change of magnetization. The anomalous loss in modern grain-oriented electrical steel is responsible for about 50% of the total loss for the power frequency range [2.14], [2.15]. Hence, it is important for the causes of this loss to be defined. Early experiments [2.12], [2.15] attributed the excess loss to such causes as the formation of domain walls and domain wall angles, change of domain wall spacing with thickness of laminations, domain wall pinning and bowing, effects of grain size and nucleation of domains. Attempts have been made to connect excess losses with

Barkhausen noise [2.16], or to attribute them to continuous rearrangements of the domain configuration [2.17]. This loss has been found to occur in many magnetic materials but as with the curvature of loss per cycle against frequency characteristics shown in figure 2.6, the phenomenon has been found to be most prevalent in grain-oriented materials [2.15]. Figure 2.6 is a sketch showing the division of total power loss into its constituent parts as expressed in equation 2.8 and explained in sections 2.11, 2.12 and 2.13.

A statistical loss theory built on description of the magnetization that has some active correlation regions that are randomly distributed in the material was proposed [2.14], [2.15]. The microstructure of the material such as grain size, crystallographic textures and residual stresses are connected to the correlation regions. The excess losses per cycle for sinusoidal induction in grain oriented steel can be expressed as [2.15]:

$$W_{exc} = CB_m^{1.5} f^{0.5} \hspace{4cm} (2.10)$$

where C is a fitting parameter.
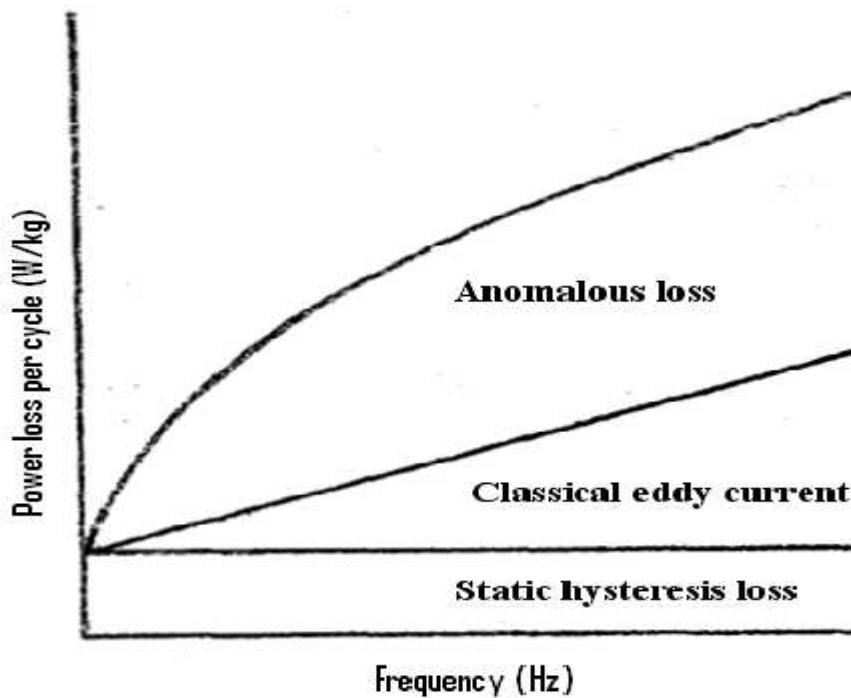
Fig. 2.6: Sketch showing division of total loss into constituent parts [2.15].

References to chapter 2

[2.1] R. M. Bozorth, Ferromagnetism, IEEE Press, New York, 1993.

[2.2] D.C Jiles, Introduction to Magnetism and Magnetic Materials, Chapman and Hall, New York, 1991.

[2.3] S. Chikazumi, Physics of Magnetism, Oxford University Press Inc, New York, 1997.

[2.4] B.D. Cullity, Introduction to Magnetic Materials, 2nd edition, Addison-Wesley, New York, 1972.

[2.5] V. Yardley, Magnetic detection of microstructural change in power plant steels, PhD thesis, University of Cambridge, April 2003.

[2.6] J. W. Shilling and G.L.Jr. House, Magnetic properties and domain structure in grain-oriented 3% Si-Fe, IEEE Transactions on Magnetics, Vol. 10, No. 2, pp.195-222,1974.

[2.7] R. Becker, W. Doring, Ferromagnetismus, Springer, Berlin, 1939.

[2.8] P. Anderson, A novel method of measurement and characterisation of magnetostriction in electrical steels, PhD thesis, Cardiff University, 2000.

[2.9]http://www.ndt.ed.org/EducationResources/CommunityCollege/Mag Particle/Physics/HysteresisLoop.htm. Accessed on 20th June 2011.

[2.10] S. E. Zirka, Y. I. Moroz, P. Marketos, and A. J. Moses, Evolution of the loss components in ferromagnetic laminations with induction level and frequency, Journal of Magnetism and Magnetic Materials, Vol. 320, No. 20, pp.1039–1043, 2008.

[2.11] D. Ribbenfjärd, Electromagnetic transformer modelling including the ferromagnetic core, Doctoral thesis in Electrical Systems Stockholm, Sweden 2010.

[2.12] G. Bertotti, Hysteresis in Magnetism, Academic Press, Inc., California, USA, 1998.

[2.13] D.C. Jiles, Modelling the effects of eddy current losses on frequency dependent hysteresis in electrically conducting media, IEEE Transactions on Magnetics, Vol. 30, No. 6, pp. 4326-4328, 1994.

[2.14] G. Bertotti, General properties of power losses in soft ferromagnetic materials, IEEE Transactions on Magnetics, Vol. 24, No. 1, pp.621-630, 1988.

[2.15] K.J. Overshott, The use of domain observation in understanding and improving the magnetic properties of transformer steels, IEEE Transactions on Magnetics, Vol. 12, No. 6, pp.840-845, 1976.

[2.16] P. Mazzetti, Block walls correlation and magnetic loss in ferromagnetics, IEEE Transactions on Magnetics, Vol.14, No. 5, pp.758-763, 1978.

[2.17] J. E. L. Bishop, Enhanced eddy current loss due to domain displacement, Journal of Magnetism and Magnetic Materials Vol. 49, Issue 3, pp. 241-249, 1985.

Chapter 3   Electrical   steel   production   and processing

3.1   Introduction

 Electrical steels may have originated from the work of Barret, Hadfield and Brown in the turn of the 20th century. They discovered [3.1] that alloying high purity steel with silicon greatly increased the resistivity of the steel thereby reducing eddy current losses. Alloying with silicon also improved the magnetic properties by reducing coercivity and increasing permeability. Another major breakthrough took place in 1934 [3.2] when a rolling process was developed which caused a large proportion of individual grains in the electrical steel to be aligned with a <001> direction along the rolling direction of the sheet. In 1940, Armco Steel Corporation developed this method which was subsequently adopted by other producers of electrical steel from 1953. This preferred orientation is known as the Goss texture and the sheet becomes a (110) plane.

Grain oriented electrical steel (GOES) has usually a silicon level of 3% by mass. It is produced in such a way that the best magnetic performance occurs when magnetised along the rolling direction, due to preferential secondary recrystallisation of [001] (110) grains. Secondary recrystallisation is a process by which grain size increases consisting in an exaggerated growth of only a few larger grains at the expense of the many smaller ones and occur in the presence of conditions which can inhibit normal grain growth [3.3]. Figure 3.1 shows the schematic diagram of the [001] (110) grain orientation in a crystal of silicon iron.

The resulting product had grain-grain misorientation in the angle of yaw of around 7° and is known as Conventional Grain Oriented (CGO) steel. Nippon Steel Company exploited this method in 1966 which lead to the development of high permeability grain oriented silicon steel known as 'Hi-B' [3.4] which has grain-grain misorientation of around 3° [3.5]. In this thesis high permeability grain oriented silicon steel is referred to as High grain oriented (HGO) steel. The grain size of HGO is on average higher, approximately 9.0 mm diameter compared to 4.0 mm in CGO.

Grain orientation determines the static magnetic domain configuration. The wall spacing is wide in grains oriented near (110) [001], and narrower in grains having [001] directions out of the sheet plane [3.6]. As a rule, the grain-grain misorientation in (110)[001] oriented silicon steel increases as the grain size decreases, larger grain boundary micro demagnetising fields would be expected in small grain materials[3.6] such as CGO compared to HGO.
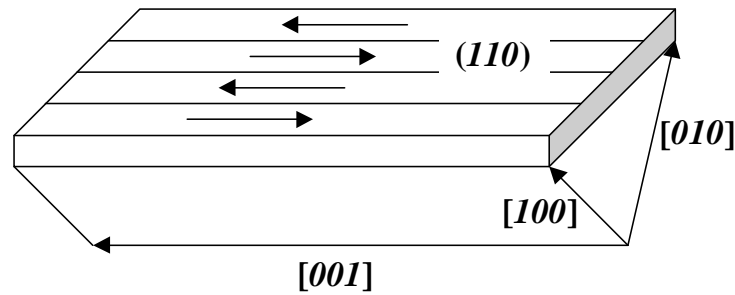
Fig. 3.1: (110) [001] grain orientation in a crystal of silicon-iron.

The magnetic properties of non grain-oriented (NGO) electrical steels are much more isotropic in nature. They are less expensive and are utilised in applications where the direction of magnetic flux changes in the plain of the sheet. They are mainly used for cores in motors, generators, alternators, ballasts, small transformers and a variety of other electromagnetic applications. They are also used in applications where efficiency is not paramount and also when there is lack of space to adequately orient components in order to make use of the anisotropic properties of GOES.

Precipitates greatly influence the magnetic properties of electrical steels either as an essential controlled requirement involved in the process of production or in the final product as an unwanted harmful residual. In the electrical steel matrix, they are second phase particles, usually metal sulphides, carbides or nitrides in the size range 10-400 nm [3.7]. Precipitates in the form of grain growth inhibitors play an important role in the manufacture of grain-oriented electrical steels because during secondary recrystallization they promote the development of Goss texture [3.8] but can have a detrimental effect on loss and permeability in the final product as they create non magnetic voids within the iron lattice that interferes with domain wall motion during the magnetisation process.

3.2 Manufacture of grain oriented electrical Steel

3.2.1 Conventional grain oriented electrical steel production route

The steel is produced using the basic oxygen steel (BOS) making process with elements like carbon, manganese, sulphur and silicon added during the vacuum degassing stage. Carbon is essential for maintaining the correct phases after hot band and intermediate anneal and also for the cultivation of the desired texture during cold reduction [3.9]. Manganese on the other hand with the combination of sulphur forms manganese sulphide (MnS) during the high temperature coil annealing (HTCA) process to inhibit primary grain growth. Silicon increases the resistivity of the steel thereby minimizing eddy currents in the steel laminations. A typical composition of the added elements could be 0.035% for Carbon, 0.06 % for manganese, 0.025 % for sulphur and 3.25 % for silicon.

The alloy is cast into ingots and then passed to a reheating stage where the temperature of the slab is maintained at about 1400°C. The high temperature at this stage is necessary for the MnS to form solution and well homogenised throughout the metal. The steel is then rapidly cooled after hot rolling and coiled at around 600°C to cause the MnS to precipitate in a finely dispersed form to ensure that the correct microstructure is developed for the eventual growth of the oriented grains in the finished product. The thickness after hot rolling is normally 1.9 mm.

As shown in figure 3.2, this hot rolled coil is conveyed to the electrical steel production line where it is side trimmed, then annealed, descaled and pickled. The steel is initially annealed continuously at around 950°C, descaled by removing the iron oxide scale physically using iron shot fired at the strip's surface by a wheel abrator and then pickled by cleaning in a hydrofluoric and sulphuric acid mixture which is followed by a hot dip in an alkaline oil solution all in a bid to refine the metallurgical structure of the hot rolled coil and make it suitable for cold rolling.

The next stage as shown in figure 3.2 is that of cold reduction. The coil is reduced to around twice the finished gauge. In order to produce steel of flat shape of appropriate intermediate gauge, the coil is reduced to an intermediate thickness of around 0.6 mm determined by the final gauge of the strip. High density of dislocations follows this

gauge reduction which causes the larger grains to break up and leads to energy storage in the strip necessary for the secondary recrystallisation of the well oriented grains. As shown in the blue arrow in figure 3.2, a return to the anneal and pickle line for an intermediate anneal follows this primary gauge reduction which leads to stress relief, recrystallisation and softening of the material ready for final rolling.

A final cold reduction brings the material to finished gauge of 0.23 to 0.50 mm and this introduces further energy into the strip necessary for the development of the Goss texture during the high temperature anneals.

The next stage is the decarburising anneal line as shown in figure 3.2. In this line, preheating is done in an open furnace to burn off a residue of the rolling oil on the surface of the strip. Decarburisation is achieved by annealing in an atmosphere of moist hydrogen and nitrogen at about 840°C to eradicate the relatively high levels of carbon in the steel which are no longer useful and are detrimental to the magnetic properties of the strip. This anneal also recrystallises the well oriented grains and also forms an oxide layer on the surface of the strip made of silica (SiO_2) bonded to the surface and Fayalite (Fe_2SiO_4) lying on top of this.

A magnesium oxide (MgO) coating is then put on the strip after being quickly cooled and one of the main reasons for this is to prevent sticking during the next stage of HTCA.

For the HTCA, the coils are stacked on end in an atmosphere of dry hydrogen at about 1200°C and may take as much as 4-5 days in all. This length of time is needed to ensure that the required temperature is reached by all of the coils for at least two hours. This produces secondary recrystallisation of well oriented grains. Also, the MgO on the steel surface reacts with the silica and Fayalite to form an electrically insulating glass film mostly made of Forsterite ($2MgO.SiO_2$) that prevents the build up of eddy currents between the laminations in a transformer. The HTCA also removes impurities such as sulphur, nitrogen and oxygen that are absorbed into the coating [3.10] so that these inclusions do not impede domain wall motion.

The strip is washed to remove unreacted magnesium oxide powder with a dip in a bath of sulphuric acid solution. This is followed by coating the strip with a phosphate

solution which is then cured at a temperature of approximately 800°C. The coating creates a tension at the surface of the steel, due to the effect of the difference in thermal expansion coefficient between the coating and the steel base during the application onto the steel surface thereby reducing the power loss and magnetostriction that occur during magnetisation of the fully processed steel [3.11], [3.12].

Strip distortions caused by the high temperature coil anneal process are removed by a thermal flattening process. The strip may also be laser scribed at this stage to improve magnetic properties.

Finally, the edges of the coil are trimmed before the coil is sent to be packaged or slit into several widths.
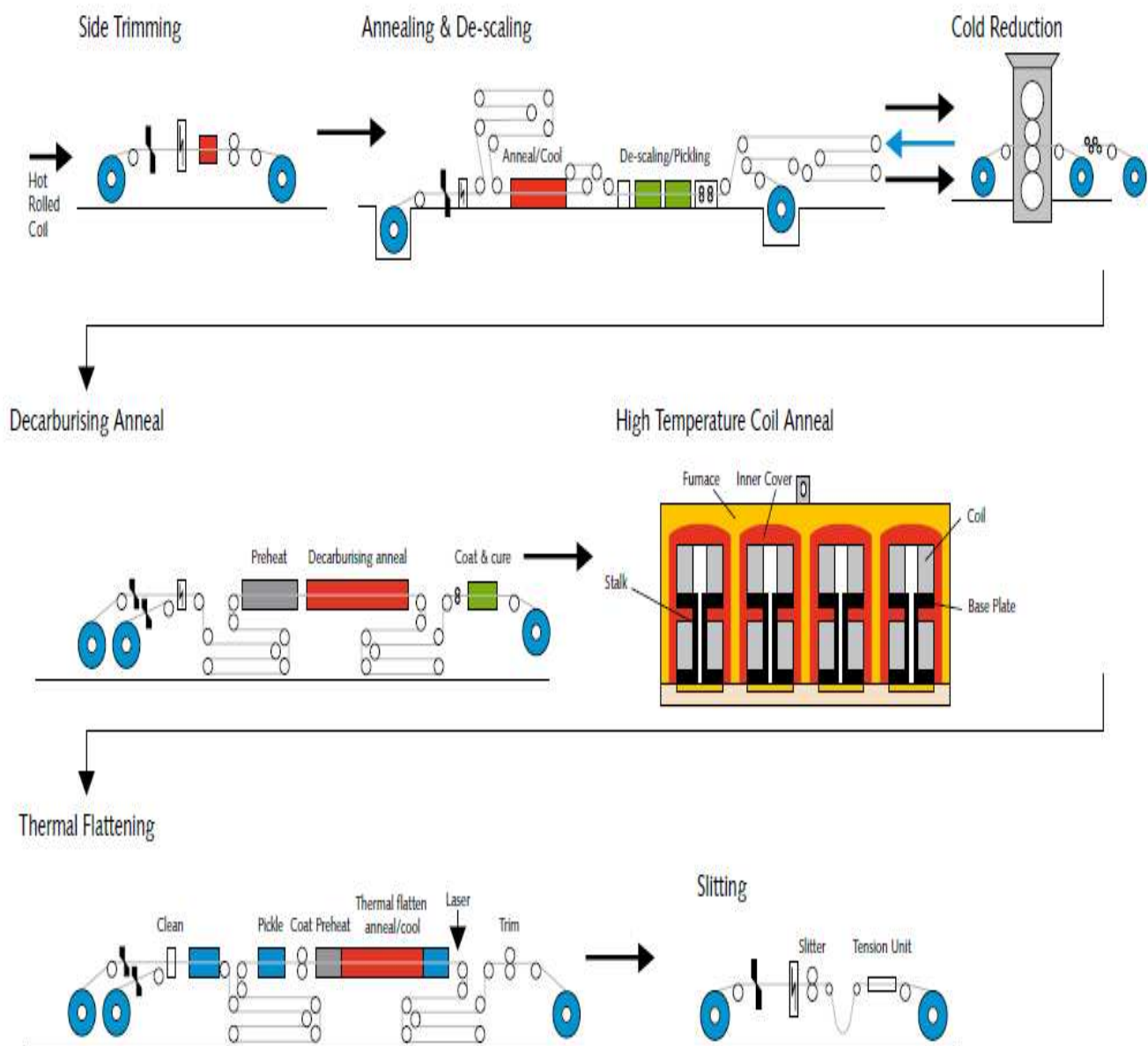
Fig.3.2: CGO Electrical Steel Production Process at Cogent Power Ltd, Newport, UK [3.13].

3.2.2 High permeability grain oriented electrical steel production route

The manufacturing route for HGO differs slightly from that of CGO. HGO utilises aluminium nitride in addition to MnS as a grain growth inhibitor [3.14] and the cold reduction is accomplished in one operation. This additional inhibitor is required

because the strain energy in the strip is greater than from a single stage cold reduction. The remaining processes are similar to that of the CGO described in section 3.2.1.

In comparison, HGO has lower core loss and higher permeability than CGO and as a result is used for high efficiency transformer applications. Core loss is a measure of the amount of electrical energy that is lost as heat when magnetic flux flows through the steel. The higher grain size and better grain orientation of HGO are the reasons for the superior magnetic properties of HGO over CGO. Figure 3.3 shows a typical grain structure of HGO having large grains.

Fig. 3.3: Grain structure of a typical HGO showing large grain size [3.15].

3.3 Non Grain Oriented Electrical Steel Production Route

Non grain oriented (NGO) electrical steel grades contain between 0.5 and 3.25% silicon plus up to 0.5% aluminium which are added to improve the resistivity and reduce the temperature of primary recrystallisation. NGO electrical steel grades generally have much smaller grain growth than the GOES grades.

Processing to the stage of hot rolled band is similar to that described for the CGO and HGO grade. The bands are usually cold rolled directly to final gauge after surface conditioning and sold to the end user in either fully-processed or semi processed state. The strip is annealed, decarburised and the grain structure needed for the magnetic properties developed after the final cold rolling.

Fully processed NGO electrical steels are generally used in applications in which quantities are too small to warrant stress relieving by the consumer or grain oriented

steel laminations are so large that it would be difficult to maintain good physical shape after an approximately 800°C stress relief anneal.

The NGO electrical steels have a random orientation i.e., the grain structure is isotropic. Fully processed electrical steels in comparison with semi-processed products are given full strand anneal in order to develop the maximum magnetic properties making them softer and harder to punch. Grades of steel having higher alloy content are harder and so are easier to punch. Compared with semi-processed products, improved punchability can be provided in fully processed NGO electrical steels by addition of organic coating acting as a lubricant when stamping and also gives some insulation to the base scale.

Semi processed electrical steel products have more level of carbon than fully processed material because after the final cold rolling they are generally given a lower-temperature decarburizing anneal. In order to obtain additional decarburization and optimise the magnetic properties, the end user will subsequently stress relief anneal the material in a wet decarburizing atmosphere. After the mill decarburization anneal, samples are cut into specimens and decarburized at about 800°C for at least one hour and tested to grade the coil.

Other advantages of coating NGO steel include:

> To provide electrical insulation between the laminations
> To provide oxidation resistance
> To give a uniform surface
> To improve hardness
> To improve temperature stability

The coatings used depend on the requirements of the final product.

The NGO steel production process can be summarised as follows:

> BOS making process followed by a continuous casting of slabs designed to give a clean, homogenous material with very low levels of impurities.

> Hot rolled down to approximately 2 mm.

➢ The hot rolled coil is cleaned and trimmed.

➢ Some grades then go through a strand anneal before cold rolling to an intermediate gauge.

➢ Strand anneal in a moist hydrogen atmosphere at approximately 800ºC which decarburises the steel and recrystallises the material.

➢ Cold rolling to final gauge (usually between 0.35 and 0.65 mm).

➢ Fully finished strip has a continuous anneal in order to develop the correct grain size.

Figure 3.4 shows the grain structure of typical NGO steel. The grain size is smaller than that of GOES.
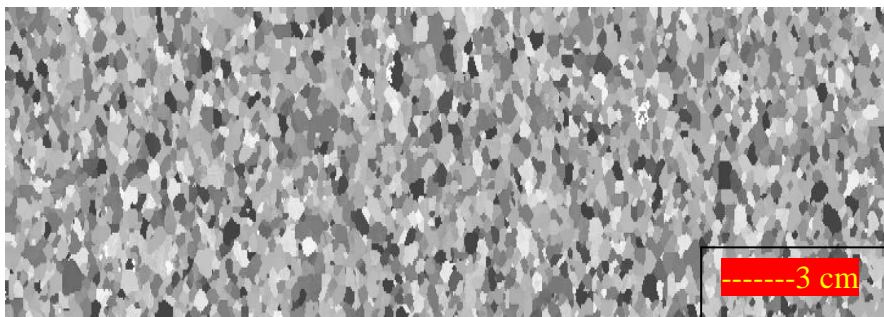
Fig. 3.4: Grain structure of a typical NGO steel showing small randomly oriented grains [3.16].

Electrical steels are used to manufacture efficient transformers and motors which results in significant reduction of the total energy needed throughout their lives span. This saving amount to more than the carbon dioxide emissions generated from the original production stage. The key challenge from the electrical steel industry is to work closely with its customers in optimising the design and use of electrical steel in their products. In order to continue these efforts and to identify all the opportunities to reduce the carbon emissions from steel's life cycle, it is necessary to take a full life cycle approach. This approach considers both the emissions associated with the

manufacture of electrical steel products and the reduction in energy consumption associated with the use of new generation electrical steels in lighter and stronger products. Further, the inherent recyclability of electrical steel must be given serious consideration in the search for sustainable materials for the future [3.17].

3.4   Stress effects of applied coatings on CGO and HGO electrical steel

The coating applied on GOES could be organic or inorganic and depends on the intended use of the steel, the heat treatment of the laminations, the operating temperature of the steel and whether the lamination will be immersed in oil. Primitive practice was to insulate the laminations with a varnish coating or layer of paper but with the disadvantage of limiting the maximum temperature and reducing the stacking factor of the core.

When the steel is coated with an insulating solution and baked at high temperature, the insulating coating imparts tension to the steel due to a difference in thermal expansion coefficient between the coating and the steel base. The coating film tension, which refines the magnetic domain size, reduces the core loss and the magnetostriction induced vibration of the core [3.14].

The primary purpose of the formation of two separate coatings on the surface of HGO and CGO electrical steel is the provision of electrical insulation between adjacent laminations. The effects of these coatings have been reported by many authors. It was reported in [3.18] and [3.19] when forsterite coatings was applied to electrical steel that the 180° domain structure was refined with the domains narrowing which is consistent with the behaviour of a tension applied in the rolling direction. The effects of applying various secondary coatings was investigated in [3.20] and reported that further refinement of the 180° domain structure occurred.

The authors of [3.21] carried out laboratory experiment to determine the role of phosphate coating by studying the effects both of removing the coating and of heat treatment under tension on the stress sensitivity of magnetostriction and power loss of silicon iron. The investigation showed that coating plays two main roles in determining the stress sensitivity of the steel; not only does it hold the steel in a state

of isotropic tension, caused by the different contractions but it can also hold the steel in a state of uniaxial tension along the rolling direction.

Nippon Steel conducted research to solve the shortcomings of a conventional insulating coating composed of magnesium phosphate alone and developed a new insulating coating of the colloidal silica-aluminium phosphate based acid system [3.22].

3.4.1 Longitudinal tensile stress

When a tension is applied parallel to the rolling direction in grain oriented electrical steel, little effect will be produced on a well oriented grain with mainly [001] domains. However, there will be refinement of domains with transverse supplementary structure leading to the disappearance of the supplementary structure. The resultant effect of the application of a tension in the <100> direction is the increase of the magnetoelastic energy of the transverse domains while at the same time decreasing that of the longitudinal domains [3.10]. This will make the longitudinal domains to become energetically more favourable and so will grow at the expense of the transverse supplementary domains. The magnetostatic energy will increase because of the removal of the supplementary structure by the applied stress. This is countered by reducing the demagnetising field by the narrowing of the [001] domains [3.1]. Fig.3.5a shows domain pattern of grain oriented steel without tension. Fig.3.5b shows the domain pattern under applied tension of 3 MPa in the rolling direction with the domains refined. The rolling direction is 180° to the direction of the bar domains in both figures. The images were obtained using the equipment and technique described in sections 5.5.2 and 8.2 respectively.

<div align="center">

(a)   (b)

</div>
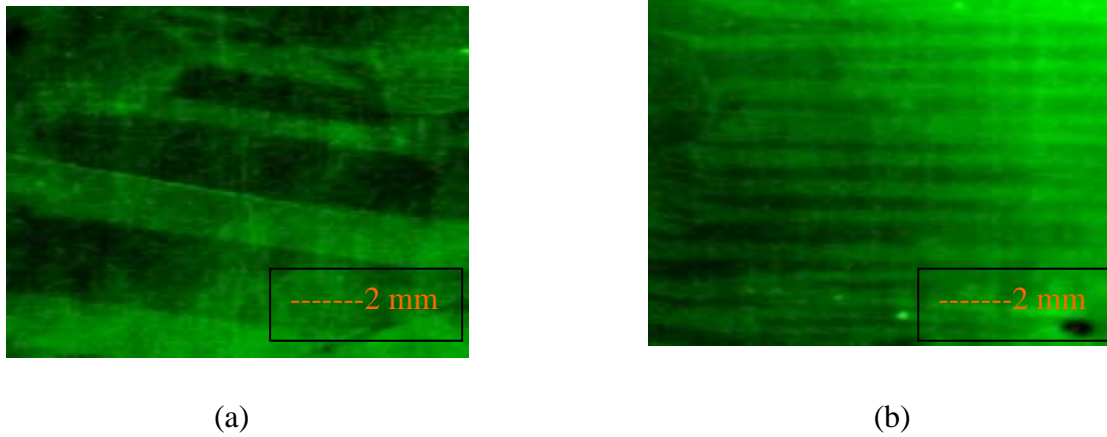
Fig .3.5: Domain structure of grain oriented steel (a) without tension (b) with tension.

3.4.2 Longitudinal compressive stress

When a compressive stress is applied along the rolling direction of grain oriented electrical steel, the magnetoelastic energy of the [001] domains increases. This leads to a rearrangement of the domain structure to give two patterns that are distinct viz: Stress Pattern I and Stress Pattern II, after a transition stage where the domain pattern seem to disappear completely [3.23]. Stress pattern I is the simplest of the structures and is the first to appear. The now energetically favourable [100] domains with small [001] flux closure domains constitutes the bulk of the domain. Increasing the compressive stress results in further increase of the magnetoelastic energy of the flux closure domains and consequently decreasing in size at the expense of the [100] domains. The decreasing size of the closure domains leads to a simultaneous narrowing of the bulk domains by the same mechanism as with applied tension.

In stress pattern II which is more complex, the main domains are still in the [100] direction and the domain wall lie in the <010> direction. The main domains no longer transverse the strip at 90° to the rolling direction. The surface closure structure has a zigzag pattern although still consisting of [001] domains. It was proposed in [3.19] that the transition between stress pattern I and stress pattern II occur due to the decreasing domain width with stress of the main [100] domains of stress pattern I and the corresponding increase in wall energy. It was also shown in [3.19], how the domain wall energy of stress pattern II decreases with increasing stress and therefore becomes more energetically favourable. This transition typically occurs at a compressive stress of 2 to 3 MPa in a well oriented grain [3.10]. Figure 3.6 shows the domain structure of unstressed domains, stress pattern I and II in grain oriented steel.
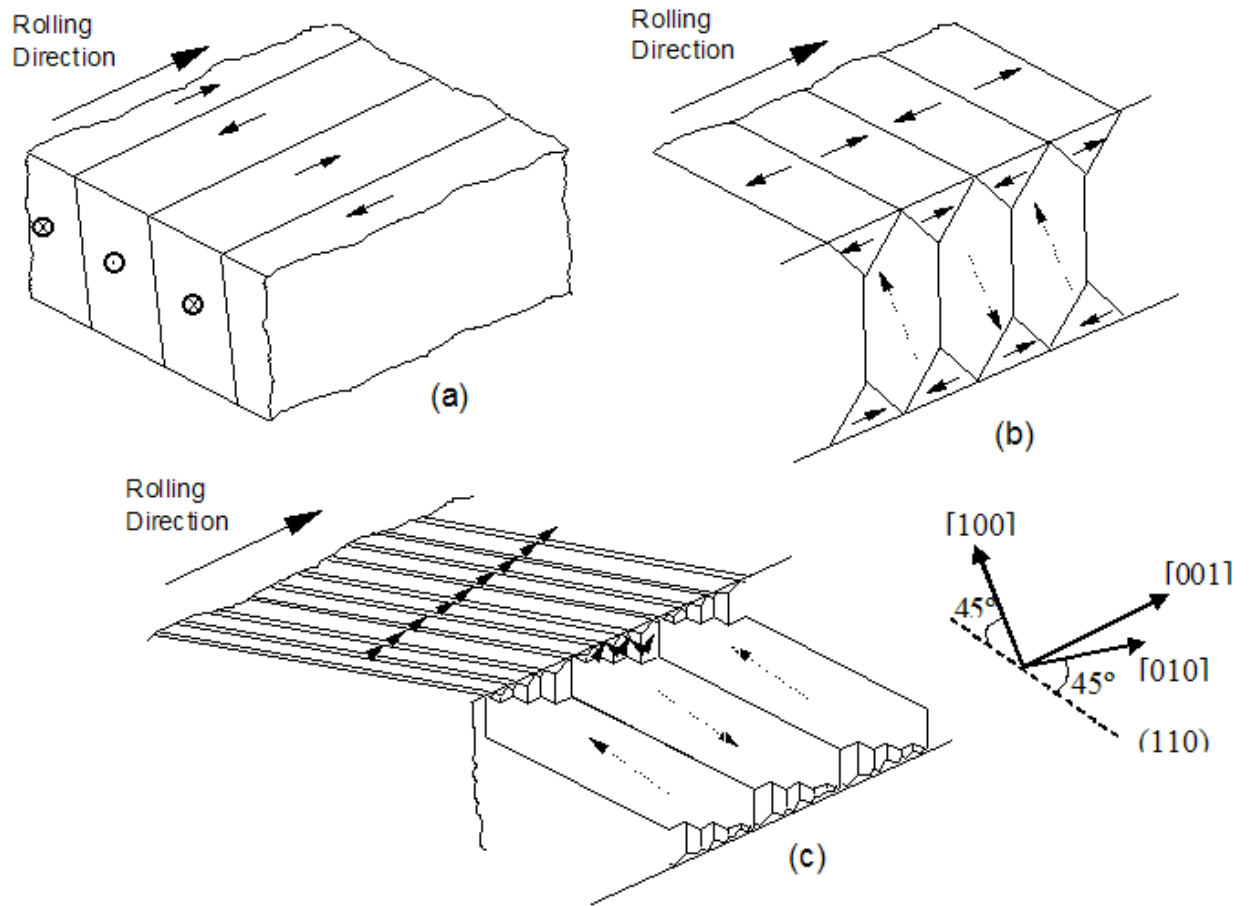
Fig.3.6: Domain structure of (a) unstressed domains; (b) Stress pattern I; (c) Stress pattern II in grain oriented steel [3.23].

References to chapter 3

[3.1] W. F. Barrett, W. Brown and R. A. Hadfield, Researches on different alloys of iron, Journal of Institute of Electrical Engineers, Vol. 31, pp. 674-722, 1902.

[3.2] N. P. Goss, New development in electrical strip steels characterized by fine grain structure approaching properties of a single crystal, Transactions of American Society on Metals, Vol. 23, pp. 515-531, 1935.

[3.3] C. Antonione, G. D. Gatta, G. Riontino and G. Venturello, Grain growth and secondary recrystallisation in iron, Journal of Material Science, Vol. 8, No. 1, pp. 1-10, 1973.

[3.4] S. Taguchi, A. Sakakura and H. Takashima, US Patent 3287183, 1966.

[3.5] M. F. Littmann, Structures and magnetic properties of grain oriented 3.2% silicon-iron, Journal of Applied Physics, Vol. 38, issue 3, pp. 1104-1108, 1967.

[3.6] J. W. Shilling and G.L.Jr. Houze, Magnetic properties and domain structure in grain-oriented 3% Si-Fe, IEEE Transactions on Magnetics, Vol. 10, No. 2, pp. 195-222, 1974.

[3.7] K. Jenkins and M. Lindenmo, Precipitates in electrical steel, Journal of Magnetism and Magnetic Material, Vol. 320, pp. 2423-2429, 2008.

[3.8] S. Turner, A. Moses, J. Hall, and K. Jenkins, The effect of precipitate size on magnetic domain behaviour in grain-oriented electrical steels, Journal of Applied Physics, Vol. 107, issue 3, pp. 307-309, 2010.

[3.9] A. Coombs, Solid and Laminated Soft Magnetic Materials, UK Magnetics Society Seminar Paper, 1997.

[3.10] P. Anderson, A novel method of measurement and characterisation of magnetostriction in electrical steels, PhD thesis, Cardiff University, 2000.

[3.11] S. Cho, S. Kim, J. Soh, and S. Han, Effect of tension coating on iron loss at frequencies below 1 KHz in thin-gauged 3% Si-Fe sheets, IEEE Transactions on Magnetics, Vol. 45, no. 10, pp. 4165-4168, 2009.

[3.12] A. J. Moses, H. V. Patel and P. I. Williams, Challenges in quantifying Barkhausen noise in electrical steel, Electromagnetic NDE(X), Vol. 28, pp. 178-185, 2007.

[3.13] http://www.orb.gb.com/downloads/cogent_brochure.pdf. Accessed on 28th June 2011.

[3.14] http://en.wikipedia.org/wiki/Electrical_steel. Accessed on 30th June 2011.

[3.15]. A. J. Moses, Electrical Steels: Past, Present and Future Developments, IEE Proceedings, Vol.137, Pt. A, No.5, pp. 233-245, 1990.

[3.16] D. S. Petrovic, Non-oriented electrical steel sheets, Materials and technology, Vol. 44, issue 6, pp. 317-325, 2010.

[3.17] http://www.worldsteel.org/publications/position-papers/Steel-s-contribution-to-a-low-carbon-future.html . Accessed 13th April 2012.

[3.18] O. Tanaka, H. Kobayashi and E. Minematsu, New insulating coating for grain oriented electrical steel, Journal of Material Engineering, Vol.13, pp. 161-168, 1991.

[3.19] S. D. Washko, T. H. Shen and W. G. Morris, The effect of forsterite coatings on the magnetic properties and domain structure of grain oriented 3% SiFe, Journal of Applied Physics, Vol. 53, No. 11, pp. 8296-8298,1982.

[3.20] W. G. Morris and J. W. Shilling, Effect of forsterite coatings on the domain structure of grain oriented 3% SiFe, IEEE Transactions on Magnetics, Vol.14, No.1, pp. 14-17, 1978.

[3.21] S. D. Washco and E. G. Choby, Evidence for the effectiveness of stress coatings in improving the magnetic properties of high permeability 3% SiFe, IEEE Transactions on Magnetics, Vol. 15, No. 6, pp. 1586-1591, 1979.

[3.22] A. J. Moses, S. M. Pegler and J. E, Thompson, Role of phosphate coating in determining the magnetic properties of Goss Oriented Silicon Iron, Proceedings of the IEE, vol. 119, No.8, pp. 1222-1228, 1972.

[3.23] L. A. Dijkstra and H. M. Martius, Domain pattern in silicon iron under stress', Review of Modern Physics, Vol. 25, 146-150, 1953.

.

Chapter 4   Barkhausen Noise

4.1   Introduction

The BN phenomenon is discussed in this chapter. Domains and domain wall processes and their contribution to BN are discussed. The effects of stress, grain size, precipitates, measurement depth, magnetising waveform and magnetising frequency on BN and previous works in these areas are also presented.

4.2   Origin of Barkhausen Noise

Barkhausen noise (BN) was discovered in 1917 and firstly published in 1919 [4.1]. It was found that the magnetisation change as a function of the applied magnetic field is not smooth but increases in random steps. The magnetic flux density, B, changes discontinuously when the magnetic field, H, is changed continuously. A given volume of a ferromagnetic material such as electrical steel will contain a number of sites which include dislocations, grain boundaries, precipitates, voids, etc and cause local variations in the magnetoelastic energy, and non-magnetic inclusions, which minimise both wall area and the magnetostatic energy of the inclusion. These lattice defects will pin the moving domain wall until the applied field is increased sufficiently to overcome it. When this condition is reached, sudden changes in magnetisation shown in the magnified B-H curve in figure 4.1 are produced by the abrupt movement of domain walls. This phenomenon can be macroscopically observed as a Barkhausen voltage pulse induced in a search coil placed around the specimen.
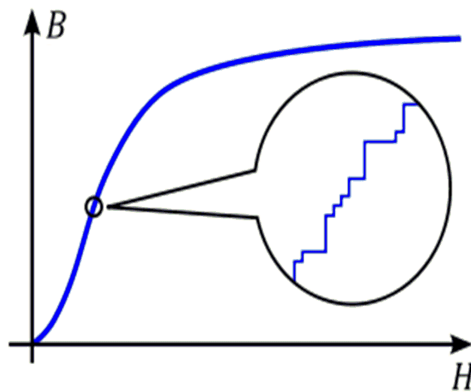
Fig. 4.1: Barkhausen jumps along the initial magnetisation curve.

A representation of this pinning effect, the most important cause of Barkhausen noise, is shown in figure 4.2 with increasing magnetic field:
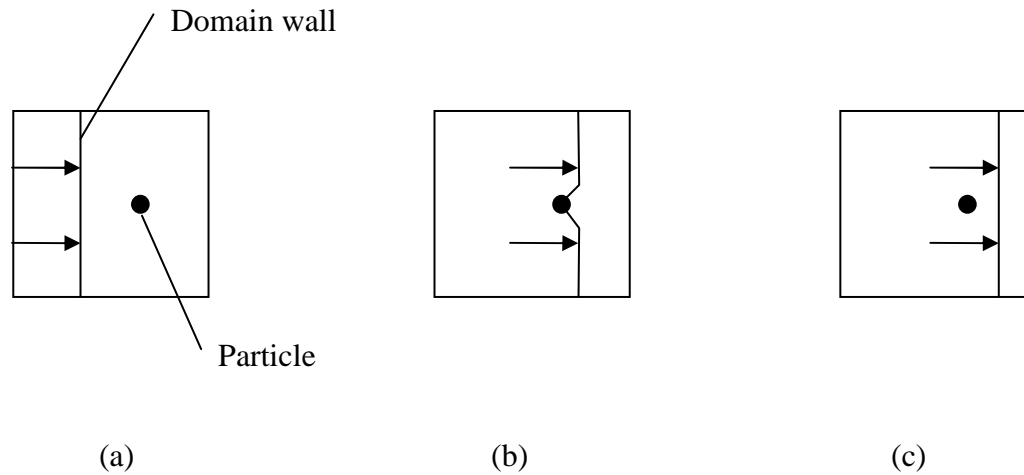
Fig . 4.2: (a) The domain wall will start moving towards the particle (pinning site) (b) The domain wall hits a pinning site and is pinned ('bows') (c) The domain wall releases the pinning site and generates a Barkhausen jump.

Domain wall motion contributes more to BN than domain rotation as can be explained by looking at the nature of the effects. When a domain wall moves, it travels a greater distance than a domain wall which 'bows' and is still fixed on the ends as in figure 4.2 (b) thus generating higher rate of change of magnetisation which results in more BN amplitude. When considering a B-H loop, most Barkhausen activities occur in the area around the coercive field where the rate of change of magnetisation is highest [4.2, 4.3]. The shape and amplitude of the BN depends on microstructure. This makes its examination an important method for investigating properties such as grain size, heat treatment, strain, and mechanical properties such as hardness of magnetic materials [4.4]. This noise phenomenon can be investigated statistically through the detection of the random voltage observed on a search coil during the magnetisation of the material [4.5]. There are two types of search coil techniques for BN measurement viz: surface and encircling. For surface BN measurement, a search coil (pick-up coil) is placed on the surface of the specimen while in the encircling type, the search coil is wrapped around the specimen. Surface BN measurement makes use of a surface transducer for detecting magnetic field transients and magnetisation discontinuities with the advantage of a rapid and continuous structure control [4.6]. It was highlighted that when a search coil has many turns to provide high output signals, its

resistance might become too high with the consequence of higher thermal noise because of the heating effect of the magnetising current.

Analysis of BN can give information on the compositional microstructure of a magnetic material or the interaction between domain walls and stress configurations. It is also a complementary non-destructive evaluation (NDE) technique to both eddy-current probe sensors [4.7] and magnetic flux leakage (MFL) [4.8]. Whereas eddy current probe sensors and MFL detect cracks, corrosion and impurities in steel structures, BN sensors are incorporated in the system to detect stress in the steel under evaluation.

4.3 Domain Processes and their role in Barkhausen noise

Application of a magnetic field to a magnetic material leads to two domain processes viz: domain wall motion and domain rotation as shown in figure 4.3.
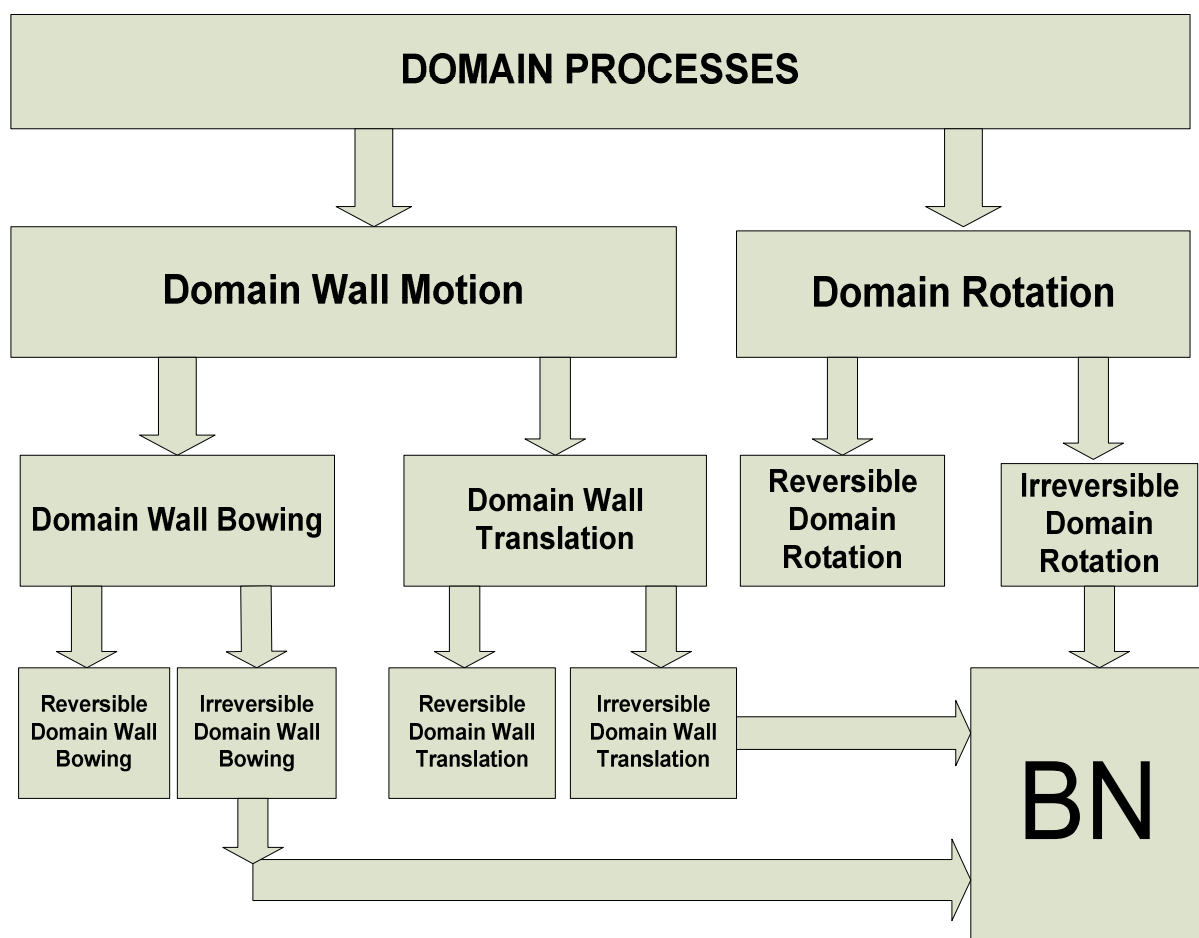
Fig. 4.3: Domain magnetisation processes and their role in BN.

Three reversible and three irreversible domain processes occur. A reversible process is one such that if the external magnetic field is reduced or removed the magnetisation in the material returns to its original value. Domain wall motion is classified into domain wall bowing and domain rotation. Domain wall bowing can be either reversible or irreversible under certain conditions. When a low magnetic field is applied, this process is reversible. The domain wall is likened to a rubber band which extends under the influence of the magnetic field and returns to its original position when the magnetic field is removed. When the domain wall is sufficiently deformed such that the extension continues without further increase of the magnetic field the effect becomes irreversible. A second even more important process which makes this effect irreversible is when the domain wall, while extending, encounters a further pinning site. This pinning site prevents the wall from returning to its original position when the field is removed. The pinning effect occurs when the magnetic field further increases and the domain wall breaks away from its pinning sites [4.4].

Domain wall translation is usually irreversible unless no pinning sites exist in the material. Hence when the field is removed, all walls can return to their original positions. Irreversible domain wall translation is the effect which contributes most to BN generation.

Domain rotation is a process where the atomic magnetic moments in a domain are turned from their original position towards the direction of a magnetic field applied to the sample. It is reversible in low fields when magnetic moments just slightly turn from their preferred low energy axis towards the direction of the magnetic field. For intermediate to high fields domain rotation becomes irreversible when the magnetic moments change their direction from their original preferred low energy axis to the one which is closest to the field direction. This occurs when the field energy overcomes the anisotropy energy [4.5]. All the irreversible domain processes lead to BN.

4.4   Barkhausen noise and 180° domain walls

It is believed that BN occur mainly because of 180° domain wall motion [4.5], [4.9] as the 90° domain walls have associated stress fields with them making magnetisations lie at right angles on either side of the wall, causing lattice spacing to be slightly larger in the direction of magnetisation. The resulting strain impedes 90°

domain wall motion, making it less significant than 180° domain walls that have a higher velocity [4.10]. In [4.11] and [4.12], the authors developed a method of determining the size distribution and number of Barkhausen jumps over all or any part of the magnetisation cycle. A slowly varying magnetic field was applied to a specimen hard-drawn iron and the Barkhausen jumps were amplified and detected as voltage pulses on an oscilloscope for visual inspection. Based on the above experimental investigation the authors concluded that Barkhausen jumps originate mostly from movement of 180º domain walls [4.13]. They observed that the number of countable Barkhausen discontinuities in a half-cycle was very large and to minimise overlap effects the rate of change of magnetic field must be vey small.

4.5   Barkhausen noise and stress effects

Due to its high sensitivity to stress, BN can be used in NDE of elastic and plastic deformations [4.14]. A stress will change the bulk magnetization of a ferromagnetic material even if no field is applied [4.5]. Magnetic domains undergo stress-induced volume changes just as they do under the influence of an external magnetic field. The magnetic field needed to move a domain wall across a pinning site and the wall energy gradient increases as the internal elastic stress increase [4.4]. The pinning sites themselves are also influenced by stress. In fact, elastic strain effects are more influential on BN than plastic strain effects [4.15]. To gain a better idea of how stress influences BN, its influence on magnetic domains should be considered.

An applied stress disturbs the balance of the energy terms described in chapter 2. If no external field is present, the magnetostatic energy is zero and the magnetocrystalline and magnetoelastic energy are dominant [4.16]. Both magnetocrystalline and magnetoelastic energy compete to determine the direction of the domain magnetization under stress. A new energy configuration is achieved when under applied uniaxial tensile stress domains lying closest to the stress direction grow at the expense of domains with perpendicular domain magnetization while the domains with magnetic moments perpendicular to the axis of applied stress become favourable energetically under compressive stress [4.17].

Generally under stress, the 180° domain wall population in the stress direction increases if the stress is tensile. Since BN is associated with wall pinning, a lower signal is obtained with compressive stress, and a higher for tensile stress [4.18].

The influence of applied stress on BN amplitude was first observed in [4.9]. It was shown that the most favourably oriented domains increased in size primarily by movement of 180° walls when the applied field was increased. A magnetising frequency of 0.09 Hz was used to magnetise the samples. In [4.19], Barkhausen discontinuities were generated by a triangular waveform with a maximum frequency of 4 Hz.

BN was generated by a 50 Hz applied magnetic field in [4.20]. It was found that an ac excitation field to generate Barkhausen jumps gives a cleaner and more reproducible Barkhausen signal. BN was also found to increase with frequency. This same trend was found at both high and low fields in this thesis.

Investigation of the BN envelope amplitude and its relation to surface stress in a surface modified steel specimen was conducted in [4.21]. The result showed that the Barkhausen signal envelope amplitude decreases with increasing compressive stress.

4.6   Barkhausen noise and depth variation in electrical steel

BN is sensitive to changes in the surface condition of electrical steel because the magnetic properties are closely linked to stress through magnetoelastic coupling and are reported to be within the frequency range of 20-200 kHz in steel in [4.22]. The frequency bandwidth of the detected signal can be selected to control the depth sensitivity to analyse material condition at different depths. Changes in material condition at different depths inside the material are evaluated by the selective attenuation of high frequency components of the BN signal as a result of eddy currents.

The authors in [4.21] found the frequency band at which BN was detected to be inversely proportional to skin depth using the standard skin depth expression given in section 2.12. These frequencies correspond to the mean of each of the five frequency bands over which measurements were taken. The values of the classical skin depth for a material with $\sigma = 1 \times 10^6$ $\Omega^{-1}.m^{-1}$ and $\mu_r = 200$ are given for different frequencies in Table 4.1.

Table 4.1: BN penetration depth (skin depth) at different detection frequency bandwidths.

BN detection frequency Bandwidths (kHz)	Calculated penetration depth (mm)
120-160	0.095
100-120	0.107
80-100	0.119
50-80	0.140
20-50	0.190

4.7   Effect of grain size on Barkhausen noise

Grain boundaries affect domain structures by the generation of closure domains (reverse spikes) at and by acting as obstacles to wall movement. The domain width in 3% Si-Fe increases with increasing grain size [4.10] as illustrated in figure 4.4 showing fine (smaller) and coarse grains in grain oriented electrical steel. This is because domains follow the easy direction in each grain although they are continuous over the grain boundaries, and since the boundary has no special angular relationship to the [001] directions of the two grains, the normal component of magnetisation across the boundary is generally discontinuous. If a grain is of larger size, domain walls can move further between pinning sites than in a grain with a smaller size. Since BN is mainly caused by domain wall motion, it is affected by grain size and boundaries of grains are likely sources for domain wall pinning [4.23].

The effect of grain size and carbon content on BN was investigated in decarburized steels [4.24]. Carbon content was seen to have a direct influence on the grain size, which becomes smaller when the carbon content is increased. It was observed that BN is affected by grain size and the number and distribution of inclusions. The rms value of the BN signal was found to increase with increasing grain diameter. The reason advanced was that increased grain size and therefore reduced carbon content allow domain walls to move further between pinning sites thereby generating larger changes in magnetisation which results in a larger BN signal.
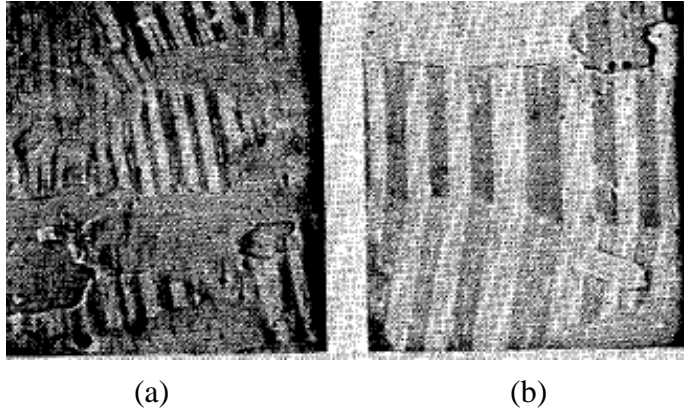
Fig. 4.4: Domain spacing in (a) fine and (b) coarse (110) [001] grain oriented silicon steel [4.10].

It was reported in [4.26] that a large number of grain boundaries result in more intense BN signals. Large number of grain boundaries is found in small grain samples. Small grain samples it argued have larger BN emissions because the grain boundaries act as pinning sites, and because their volume fraction is larger, more pinning sites need to be overcome when the walls move. It was stated in [4.18] that the 180° domain walls increases in number in the presence of applied tensile stress, and an expression was derived for the resulting change in magnetoelastic energy. From this expression, a threshold stress which depends on the grain size and increases with the number of existing domain walls was calculated that would be required to add another domain wall to the configuration. Hence, BN emission is linked to grain boundaries and grain size. Reference [4.25] advanced the idea that the interaction between the domain walls and dislocation angles leads to different BN profiles than the interaction between the walls and grain boundaries. This argument was used to explain secondary peaks observed in some of the BN signals. This is because the physical nature of the pinning site is assumed to dictate the restoring force acting on the wall. It was shown in [4.26] that rms BN is inversely proportional to the square root of the grain size in carbon steel consisting of ferrite grains. This implies that large number of Barkhausen pulses mean smaller grains, therefore more pinning sites in this material. The authors of [4.27] also reported a decrease in BN signal when the grain size in iron samples increased. However, segregation of phosphorus at grain boundaries and precipitates can act as additional pinning sites for domain walls thereby increasing the number of BN pulses even in specimens with large grains, as experimentally observed in

decarburized steel [4.28]. This shows that more or less precipitates can change the relationship between grain size and BN.

4.8   Evaluation of Barkhausen noise signals

BN are analysed statistically after filtering due to the stochastic nature of the signals. Figure 4.5 shows the shape of the BN signal obtained as voltage pulses from a search coil during one cycle of magnetisation. Since the voltages produced in the search coil are both positive and negative, the average is always nominally zero. So there is the necessity of choosing parameters that account for both positive and negative amplitudes of instantaneous BN events [4.29].
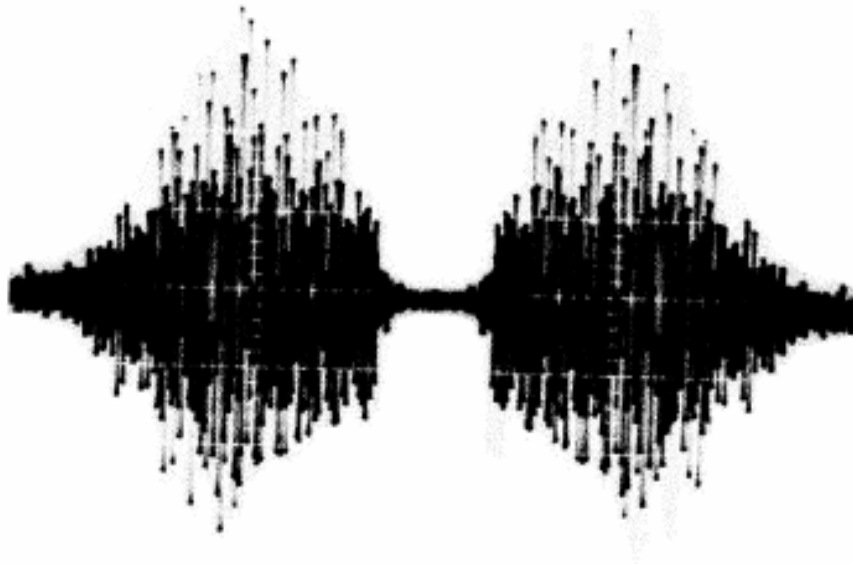
Fig. 4.5: Barkhausen noise emission pulse [4.30].

Three main parameters were utilised to analyse BN in this work using LabVIEW viz: total sum of amplitudes (TSA), root mean square (rms) and total number of peaks (TNP). These three parameters were selected because they are mostly used methods of analysing BN in order to allow comparison with the work of other investigators. The data points acquired during one cycle of magnetisation were stored within an array. The amplitude sum of the absolute values within the array added together in 20 successive cycles (to have good representation of the BN events) is given by:

$$Total\,sum\,of\,amplitudes \;=\; \sum_{i=1}^{z=20}\left(\sum_{k=1}^{m}\left(\left|a_k\right|\right)\right)_i \qquad\qquad (4.1)$$

where the variable 'a' represents the amplitude of the measured data point, index 'k' shows its position within the measured data point array 'm'. Variable 'z' indicates that the measurement has been taken 20 times successively. Index 'i' displays how often the measurement has been carried out. The TSA represents the sum of the individual voltage pulses in the BN cycle.

RMS value of the BN is the mean BN event amplitude in the BN cycle and is given by:

$$rms\;\;\psi \;=\; \sqrt{\frac{1}{m}\sum_{k=0}^{m-1} a_k} \qquad\qquad (4.2)$$

TNP is the sum of all detected BN events from the LabVIEW peak detection algorithm and is equivalent to integrating the probability of an event occurrence over the range of flux in the BN cycle. Using figure 4.5 as an example, the TNP would be the sum of the peaks of the voltage pulses in the BN cycle.

Other statistical parameters that are used in the analysis of BN include arithmetic mean, standard deviation, variance, median, mode, skewness, kurtosis and power spectrum [4.31].

4.9   Effects of precipitates on Barkhausen noise

BN are influenced by the way domain walls interact with pinning sites, such as precipitates, as domains reorganize so that magnetic moments can be aligned in the direction of the applied field. Within the body of a precipitate, magnetic dipoles are formed at the surrounding interface [4.4, 4.32]. If a domain wall then bisects the precipitate, the dipole arrangement is split thereby reducing the magnetostatic energy and pinning the wall as a result. The number of Barkhausen jumps is to some extent determined by the number of precipitates provided that their volume is sufficient to

cause pinning. This makes BN an important tool for evaluating the scale of interaction between precipitates of different sizes and magnetic domains.

The presence of copper-manganese sulphide (CuMnS) precipitates increased the rms BN in grain oriented steel but precipitates which are relatively small compared to the width of domain walls, approximately 150 nm, for 180° domain wall do not impede domain wall motion [4.33]. This is because the inclusions are completely engulfed by the wall, and thus the dipole surrounding the inclusion is maintained.

4.10   Effects of magnetising waveform on Barkhausen noise

The influence of sinusoidal, triangular and square wave form excitation on Barkhausen emissions were investigated in [4.34]. The frequency spectra of sinusoidal and triangular alternating field excitations showed similar behaviours but the spectrum under square wave excitation was different due to the existence of high frequency components during square wave switching. It was observed that changes in the field waveform led to different emission pulse shapes. When a square wave excitation was used the total sum of amplitude of the Barkhausen pulse was four times higher than in the case of a triangle excitation. Under sinusoidal excitation, the total sum of total sum of amplitude of the Barkhausen pulse was about 1.6 times higher than under triangle excitation. It was also found that the signal to noise ratio changed, square wave excitation had the highest signal to noise ratio and lowest for triangle excitation. Nevertheless, sinusoidal and triangle waveform excitation were rated to be more suitable than square wave excitation because the latter can lead to spurious signals (harmonics) because of the high frequency content at the voltage step.

4.11   Effects of magnetising frequency on Barkhausen noise

The influence of magnetising frequency and ac flux density on BN per cycle of pipeline steel magnetised up to 50 Hz, 1.5 T was detected by a surface mounted coil [4.35]. Increasing the flux density caused the Barkhausen noise to initially increase then decrease at high flux density. It was also shown that the BN increases with increasing magnetising frequency.

The research in [4.31] showed both an increase of Barkhausen noise with increasing flux density and increasing magnetising frequency for electrical steel. When the BN amplitude was plotted against magnetising frequency while the peak flux density was held constant, a linear relationship between BN amplitude and frequency was found. A benefit of a higher frequency of magnetisation is that the time needed to capture a cycle is reduced. For BN measurement at quasi-static dc, the period of the magnetising waveform will be a few seconds or more while at a frequency of 50 Hz, the capturing time is reduced to 20 ms if events in one cycle are captured.

References to chapter 4

[4.1] H. Barkhausen, Gerausche bien ummagnetisieren von eisen, Physikalishe Zeitschr, 20, pp. 401-403, 1919.

[4.2] H. V. Patel, S. Zurek, T. Meydan, D.C Jiles, and L. Li, A new adaptive automated feedback system for Barkhausen signal measurement, Sensors and Actuators, Vol. 129, pp. 112-117, 2006.

[4.3] D. C. Jiles, The effect of stress on magnetic Barkhausen activity in ferromagnetic steels, IEEE Transactions on Magnetics, Vol. 25, No.5 , pp. 3455-3457, 1989.

[4.4] D. C. Jiles, Introduction to Magnetism and magnetic materials, Chapman and Hall, New York, 1991.

[4.5] S. Chikazumi, Physics of Magnetism, Oxford University Press Inc, New York, 1997.

[4.6] S. Saynajakangas, A new surface transducer for generating and detecting magnetic field transients in ferromagnetics, IEEE Transactions on Magnetics, Vol. 10, No.1, pp. 44-50, 1974.

[4.7] S. Nath, B. Wincheski, J. P Fulton and M. Namkung, Study of the new eddy current non-destructive testing sensor on ferromagnetic materials, IEEE Transactions on Magnetics, Vol. 30, No.6, pp. 4644-4646, 1994.

[4.8] V. Babber, B. Shiari and L. Clapham, Mechanical damage detection with magnetic flux leakage tools: modelling the effect of localized residual stresses, IEEE Transactions on Magnetics, Vol. 40, No.1, pp. 43-49, 2004.

[4.9] C. G. Gardner, G. A. Matzkanin and D. L. Davidson, The influence of mechanical stress on magnetization processes and Barkhausen jumps in ferromagnetic materials, International Journal of Nondestructive Testing, Vol. 3, No. 2, pp. 131-169, 1971.

[4.10] J. W. Shilling and G.L.Jr. House, Magnetic properties and domain structure in grain-oriented 3% Si-Fe, IEEE Transactions on Magnetics, Vol. 10, No. 2, pp. 195-222, 1974.

[4.11] H. D. Bush and R. S. Tebble, The Barkhausen effect, Proceedings of the Physical Society London, Vol. 60, No. 4, pp. 370-381, 1948.

[4.12] R. Tebble, S. Skidmore and L. Corner, The Barkhausen effect, Proc. Phys. Soc. London, A63, pp. 739-761, 1950.

[4.13] E. Stoner, The analysis of magnetic curves, Reviews of Modern Physics, Vol.25, No.1, pp. 2-16, 1953.

[4.14] C. G. Stefanita, Surface magnetic Barkhausen noise response to plastic yield of steel, Ph.D. Thesis, Department of Physics, Queen's University, Kingston, Ontario, Canada, 1999.

[4.15] C. G. Stefanita, D.L. Atherton and L. Clapham, Plastic versus elastic deformation effects on magnetic Barkhausen noise in steel, Acta Materialia, 48, pp. 3545-3551, 2000.

[4.16] B. D. Cullity, Introduction to Magnetic Materials, 2nd edition, Addison-Wesley, New York, 1972.

[4.17] D. Utrata and M. Namkung, Uniaxial stress effects on the low-field magnetoacoustic interactions in low and medium carbon steels, Review of Progress in Quantitative Non destructive Evaluation, Vol. 2, pp. 1585-1592, 1987.

[4.18] T. W. Krause, L. Clapham, A. Pattantyus and D.L. Atherton, Investigation of the stress dependent magnetic easy axis in steel using magnetic Barkhausen noise , Journal of Applied Physics, Vol. 79, No.8, pp. 4242-4252, 1996.

[4.19] S. Titto, On the influence of microstructure on magnetisation transitions, Applied Physics Series No. 119, UDC 621.317.49:620.18, pp. 1-77, 1977.

[4.20] L. B. Sipahi, D. C. Jiles and D. Chandler; Comprehensive analysis of Barkhausen emission spectra using pulse height analysis, frequency spectrum, and pulse wave form analysis, Journal of Applied Physics, Vol. 73, No.10, pp. 5623-5625, 1993.

[4.21] D. C. Jiles, and L. Suominen, Effects of surface stress on computer simulation of Barkhausen effect emissions: model predictions and comparison with X-ray diffraction studies, IEEE Transactions on Magnetics, Vol. 30, No. 6, pp. 4924-4926, 1994.

[4.22] A. P. Parakka, J. Batey, and D. C. Jiles, Effect of surface mechanical changes on magnetic Barkhausen emissions, IEEE Transactions on Magnetics, Vol. 33, No 5, pp. 4026-4028, 1997.

[4.23] G. Bertotti, F. Fiorillo and A. Montorsi, The role of grain size in the magnetization process of soft magnetic materials, Journal of Applied Physics, Vol. 67, issue 9, pp. 5574-5576, 1990.

[4.24] R. Ranjan, D. C. Jiles and P. K. Rastogi, Magnetic Properties of Decarburized steels: An investigation of the effects of grain size and carbon content, IEEE Transactions on Magnetics, Vol. 23, No. 3, pp. 1869-1876, 1987.

[4.25] D. H. L. Ng, K. S. Cho, M. L. Wong, S. L. I. Chan, X-Y. Ma, and C. C. H. Lo, Study of microstructure, mechanical properties, and magnetization process in low carbon steel bars by Barkhausen emission, Material Science and Engineering A, Vol. 358, pp.186-198, 2003.

[4.26] H. Sakamoto, M. Okada, and M. Homma, Theoretical analysis of Barkhausen noise in carbon steels, IEEE Transactions on Magnetics, Vol. 23, No.5, pp. 2236-2238, 1987.

[4.27] C. Gatelier-Rothea, J. Chicois, R. Fougeres and P. Fleischmann, Characterization of pure iron (130 P.P.M.) and carbon-iron binary alloy by Barkhausen noise measurements: Study of the influence of stress and microstructure, Acta Materialia , Vol. 46, pp. 4873-4882, 1998.

[4.28] R. Ranjan, D.C. Jiles, O. Buck, R.B. Thompson, Grain size measurement using magnetic and acoustic Barkhausen noise, Journal of Applied Physics, Vol. 61, issue 8, pp. 3199-3202, 1987.

[4.29] V. E. Iordache, E. Hug, and N. Buiron, Magnetic behaviour versus tensile deformation mechanisms in a non-oriented Fe- (3 wt %) Si steel, Material Science and Engineering, A359, pp. 62-74, 2003.

[4.30] M. Willcox and T. Mysak, An introduction to Barkhausen noise and its applications, Insight NDT, pp. 1-19, 2004.

[4.31] K. Hartmann, Relationships between Barkhausen noise, power loss and Magnetostriction in Grain-oriented silicon iron, PhD thesis, Cardiff University, March 2003.

[4.32] L. J. Dijkstra and C. Wert, Effect of inclusion on the coercive force of iron, Physical Review, Vol. 79, pp. 979-985, 1950.

[4.33] S. Turner, A. Moses, J. Hall, and K. Jenkins, The effect of precipitate size on magnetic domain behaviour in grain-oriented electrical steels, Journal of Applied Physics, Vol. 107, issue 3, pp. 307-309, 2010.

[4.34] L. B Sipahi, D.C. Jiles, and D. Chandler, Comprehensive analysis of Barkhausen emission spectra using pulse height analysis, frequency spectrum, and pulse wave form analysis, Journal of Applied Physics Vol. 73, issue 10, pp. 5623-5625, 1993.

[4.35] A. Dhar and D. L. Atherton, Influence of magnetizing parameters on the magnetic Barkhausen noise, IEEE Transactions on Magnetics, Vol. 28, No.6, pp. 3363-3366, 1992.

Chapter 5   The magnetisation and Barkhausen noise measurement system

5.1   Introduction

The details of the magnetising and BN measurement system are presented in this chapter. The tensile stressing rig and the domain observation techniques used are illustrated. The specifications of the equipment used are also highlighted. The chapter concludes with the calculation of the uncertainty in the measurements.

5.2   The measurement system

The BN measuring system comprising of the magnetisation system and a signal detection unit shown in figure 5.1 [5.1] was used as a reference for the development of the measurement system used in this work. The feedback circuit shown in the figure ensured that the time variation of the flux density was sinusoidal with a form factor better than $1.11 \, {}^+_- \, 3$ % over the measurement range. Form factor is the ratio of the rms value to the average value and is calculated using equation 5.1 below:

$$Formfactor = \frac{V_{rms}}{\left|V_{average}\right|} \overset{ideal}{=} \frac{\pi}{2.\sqrt{2}} = 1.11072 \qquad (5.1)$$

Two 80 turns search coils connected in series opposition and would around a plastic carrier slid provided a differential signal feed to a National Instruments (NI) 4552 AD card with a resolution of 16 bit, sample rate of 204 kHz and 95 kHz bandwidth. The output signal at 50 Hz from each coil was of the order of 200 mV$_{rms}$ (at 1.4 T) and comprises a dominant Faraday emf component and the low level (in micro volts range) Barkhausen signal so by connecting in series opposition the Faraday emf cancels out and the voltage fed to a personal computer (PC) mainly comprised the Barkhausen noise component [5.2].

Digital signal processing was carried out with the NI software package LabVIEW. The 1 Ohm resistor in figure 5.1 was used so that the potential difference across it will give the current that will magnetise the sample.
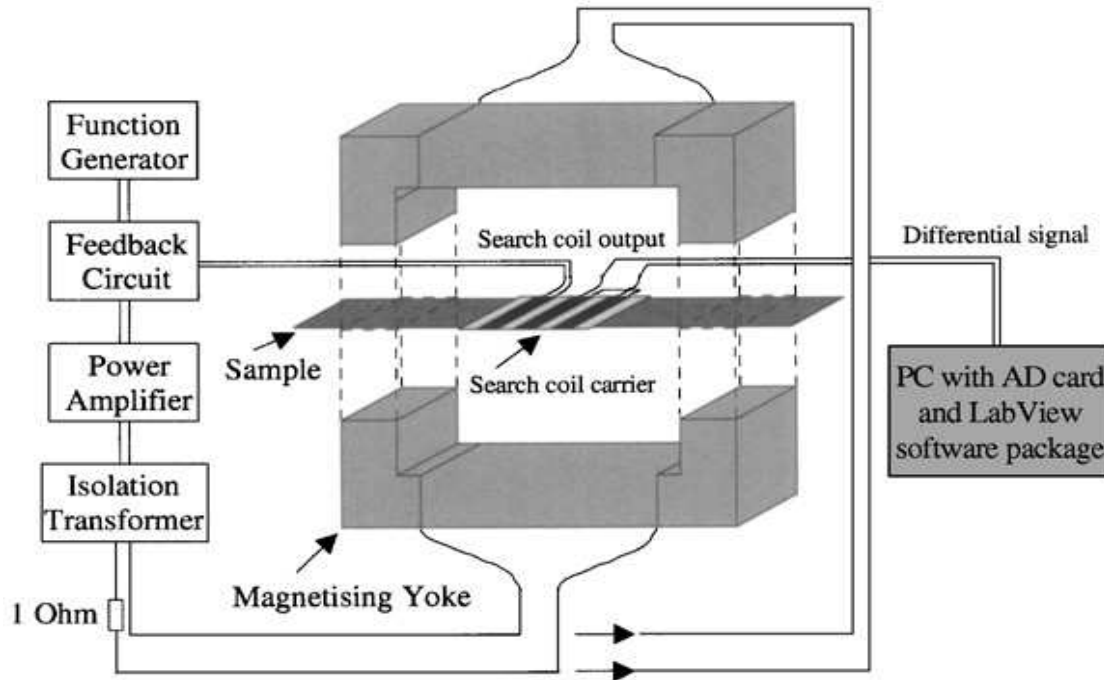
Fig. 5.1: BN measuring system [5.1].

In this study, a computer-controlled system capable of providing high accuracy and automatic measurements was developed for the magnetisation and measurement of BN of electrical steels at high and low flux densities. It does not require any discrete instrument since a program written in LabVIEW is used to calculate magnetic properties. Figure 5.2 shows a schematic diagram of the system. It comprises a PC in which LabVIEW version 8.5 from NI was installed, a NI 4461 data acquisition (DAQ) card [5.3], an impedance matching transformer, Krohn-Hite model MT- 56R, to match the 600 Ω minimum load impedance of the DAC card with the 5 to 20 Ω low impedance of the magnetising circuit, and a 4.7 Ω shunt resistor (R_{sh}) from Tyco Electronics BDS2A1004R7K having less than 40 nH inductance corresponding to reactance of 12.6 $\mu\Omega$, so adds virtually no error to amplitude and phase of the current measurement. The shunt resistor has 100 W power rating and low Temperature Coefficient of Resistance (TCR) (150ppm/°C). Low TCR was necessary to ensure

that changes in its temperature will not affect the overall accuracy of the system. The shunt was attached to a thermo electric heat sink device, model TDEX3132/100, in conjunction with silicon based thermal grease.

A double vertical yoke made of grain-oriented (GO) steel which is 290 mm long and 32 mm wide is used. A 500-turn secondary winding (search coil, N_2), about 80 mm in length, was wound around a plastic former, 270 mm x 40 mm, housing the sample, while a 100-turn primary winding (magnetising coil), covering the entire length of the plastic former was wound over the secondary winding. A standard Epstein strip (305 mm x 30 mm) to be tested is placed between the yokes.
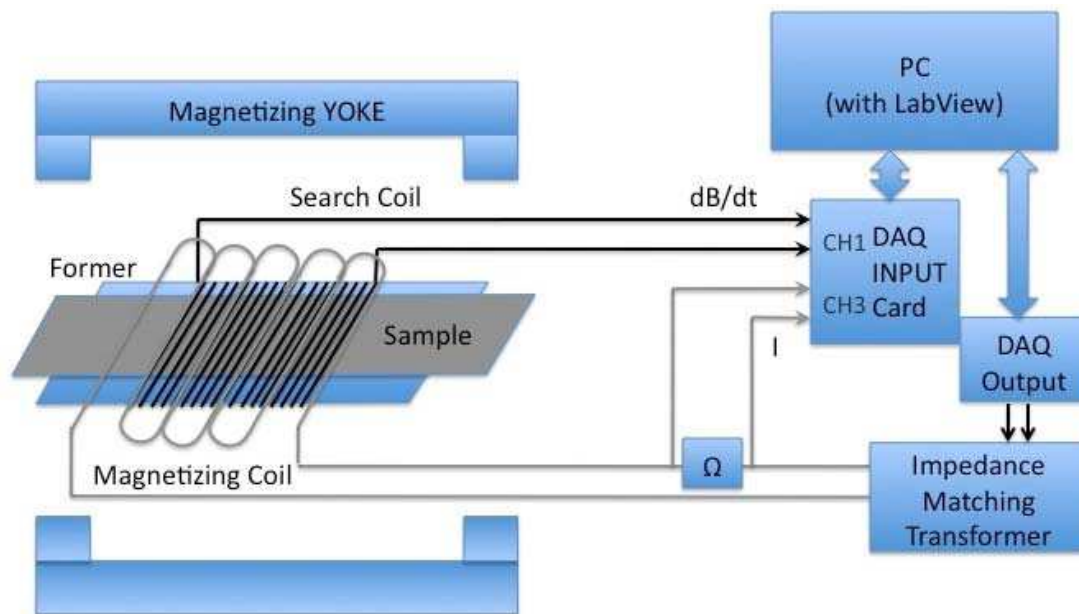
Fig 5.2: Block diagram of Barkhausen Noise measurement system.

The magnetising voltage was generated by the LabVIEW program through a voltage output from the DAQ card. The voltage drop across the shunt resistor, V_{sh}, and the secondary voltage, e, were acquired by the card for calculation of magnetic field strength and flux density respectively. The sampled waveforms of e and V_{sh} had 3000 points per cycle which is large enough to avoid quantization errors.

The instantaneous magnetic field strength, H (t) was calculated inside the LabVIEW program thus;

$$H(t) = \frac{N_1 i(t)}{l_m} \tag{5.2}$$

where $i(t) = \dfrac{V_{sh}}{R_{sh}}$, N_1 is the number of primary turns, l_m is the magnetic path length, which is the distance between the inner edges of the yoke which is 0.27 m in this system.

The instantaneous flux density B (t) was obtained by means of digital integration of the e signal as:

$$B(t) = -\frac{l\rho}{N_2 m} \int e\, dt \tag{5.3}$$

where l is the sample length, m is the mass of the sample, and ρ is the density of the sample.

The specific power loss, P, was determined by multiplying the total energy, W, by the magnetising frequency, f, over ρ. The amount of energy lost when magnetising a magnetic material is related to the B-H loop area. The total energy needed if a material is taken through a complete B-H loop is given by:

$$W = \int H.dB \qquad J/m^3 \tag{5.4}$$

Therefore the specific power loss is:

$$P = \frac{f}{\rho} . \int (H. \frac{dB}{dt}) dt \qquad W/kg \tag{5.5}$$

The AC relative permeability, μ_r, was derived from:

$$\mu_r = \frac{B_{peak}}{\mu_0 H_{peak}} \tag{5.6}$$

where H_{peak} is the peak value of magnetic field and B_{peak} is the peak flux density. B_{peak} and H_{peak} were determined numerically by using the maximum function in LabVIEW.

A feedback control system implemented in LabVIEW was used to control the flux density and to make the induced secondary voltage waveforms sinusoidal to have repeatable and comparable measurements. The form factor (FF) of the induced secondary voltage was maintained at $1.111 \, {}^{+}_{-} \, 0.3\%$ which satisfies the recommendation in [5.4] to ensure that the time variation of the flux density was sinusoidal over the measurement range. Figure 5.3 shows the procedure for each measurement. Firstly, a table of B_{peak} values and the measurement criteria which are the 0.3% error of B_{peak} and the 0.3% error of the ideal FF of the induced secondary voltage is read. This is followed by applying the first magnetising waveform to the single sheet tester. If the criteria are met, the flux density and the magnetic field waveforms are averaged to minimise random errors and improve repeatability [5.5], otherwise the magnetising waveform is adjusted by the feedback algorithm. After averaging, the criteria are re-checked then the measurement data for this point is saved. A spread sheet file is generated if all the values of B_{peak} are measured and the sample is demagnetised by reducing the magnetic field gradually to zero.

The system is also capable of low-field measurements because the 24 bit resolution of the NI data acquisition card makes it capable of sensing signals as small as 10^{-6} V. The system shown in figure 5.2 was used to measure power loss, permeability, coercivity, magnetic field and B-H loops.
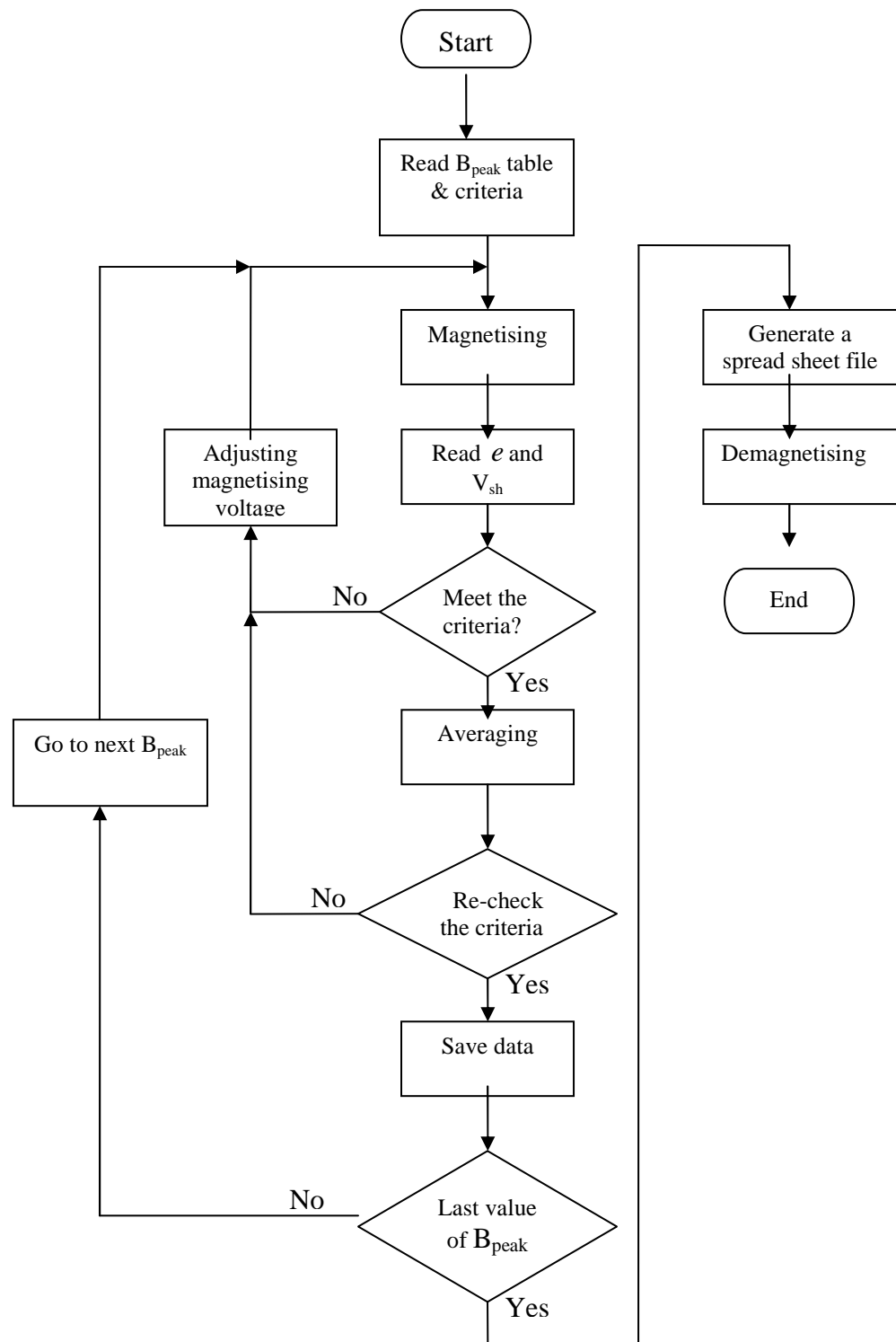
Fig. 5.3: Flowchart showing procedure of each measurement of the single strip tester [5.6].

5.3   Measurement and evaluation of Barkhausen noise signals

The secondary voltage was filtered to remove the dominant Faraday emf in order to obtain the BN signals. A digital band pass filter was used so that components in the range 25 kHz to 75 kHz were detected at a magnetizing frequency of 50 Hz. It was at this bandwidth that the Barkhausen emission which is maximum at the coercive points was detected. As observed previously in section 4.6 from the work of others, BN detection frequency lie any where in the range of 20 kHz – 200 kHz.

One search coil technique rather than a double coil arrangement is used to avoid losing some Barkhausen events in the subtraction process [5.7]. Using two search coils connected in series opposition has been mentioned in section 5.2. This is the differential search coil arrangement with the advantage of eliminating the dominant Faraday emf component which allows for the selection of the smallest input range and the best resolution of the data acquisition card. The disadvantage of the differential coil arrangement is that some Barkhausen jumps cancel each other [5.2, 5.7].

The major challenge in BN measurement is the reduction of background noise. It was also reported in [5.1] that one way to improve background noise measurements with a single search coil would be to use an acquisition system with a high resolution. The low noise NI4461 card with 24 bit resolution and a sampling rate of 204.8 KHz and 92 KHz bandwidth was chosen to take the measurements to minimize the influence of thermal noise. The card was placed in a PXI (**P**eripheral component interconnect e**X**tension for **I**nstrumentation) platform instead of in a computer system hence it operates in a predictable environment which means the measurements are more reliable and repeatable. In order to reduce environmental noise, the yokes, sample and search coil carrier were placed in a noise shielding chamber. Figure 5.4 shows the measurement system in the noise shielding chamber and the DAQ in a PXI interface. The computer monitor was remote from the measuring system to avoid interference with the measurements. Coaxial cables were used for all connection leads. The noise level of the measurement system is more than 100 times lower than the lowest BN signal to be measured as shown in figure 6.10.
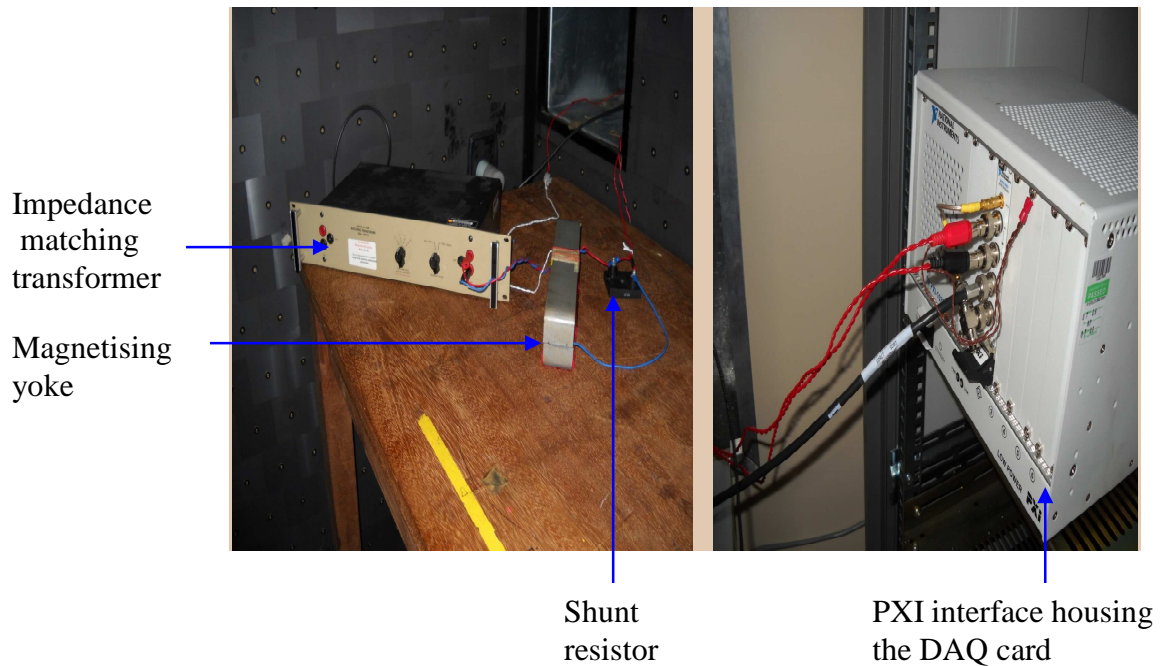
Fig. 5.4: Barkhausen Noise measurement system in the noise shielding chamber and the PXI platform housing the data acquisition card.

5.4   System for measurement of tensile stress in Epstein strips

The rig for applying tensile stress during BN measurement is shown in figure 5.5. The rig has jaws to clamp an Epstein strip at each end. Omega strain gauges with specifications shown below were used to measure the longitudinal strain: Resistance (120 Ω), Gauge factor (2.1±5%), Gauge length (7 mm), Gauge width (3 mm) and Package diameter (16 mm) [5.7]. The error range stated is used to calculate the measurement uncertainty.

The strain gauge was attached at the middle of the Epstein strip. The insulating coatings on each strip were removed by dipping into 36% hydrochloric acid and then cleaning with acetone. Two scratched lines were marked approximately at the centre of the samples by an empty ball-pointed pen with the aid of a metal ruler. The top side of the strain gauge was attached with transparent adhesive tape and then the gauge was positioned on the marked lines. Once the gauge was correctly positioned, half of the adhesive tape length was lifted. A drop of Omega 496 instant adhesive [5.8] was spread on the sample over the gauge area. After using the palm to press the gauge on the sample for about 2 minutes, the adhesive tape was carefully removed and the

strain gauge leads were connected to a Vishay 3800 strain indicator [5.9]. The bond was given 24 hours to firmly set. The circular head of the tensile stressing rig is moved in anticlockwise direction to create a tensile stress on the sample and the strain read from the strain indicator from which the stress was calculated from the stress-strain relationship:

$$\sigma = E\varepsilon \tag{5.7}$$

where σ is the stress, ε is the strain and E is the elastic modulus which for CGO and HGO in the rolling direction are 114.9 and 113.9 KN/mm^2 [5.10] respectively. Tensile stress was applied to the samples and a strain of 20 ppm (part per million) was read from the strain indicator which corresponds to a stress of approximately 2.3 MPa using equation 5.7. More tension was added to the material to increase the strain to 26 ppm from which a stress of approximately 3 MPa was calculated. These amount of stress fall within the range of beneficial stress that is imparted to grain oriented electrical steel during manufacture [5.11].
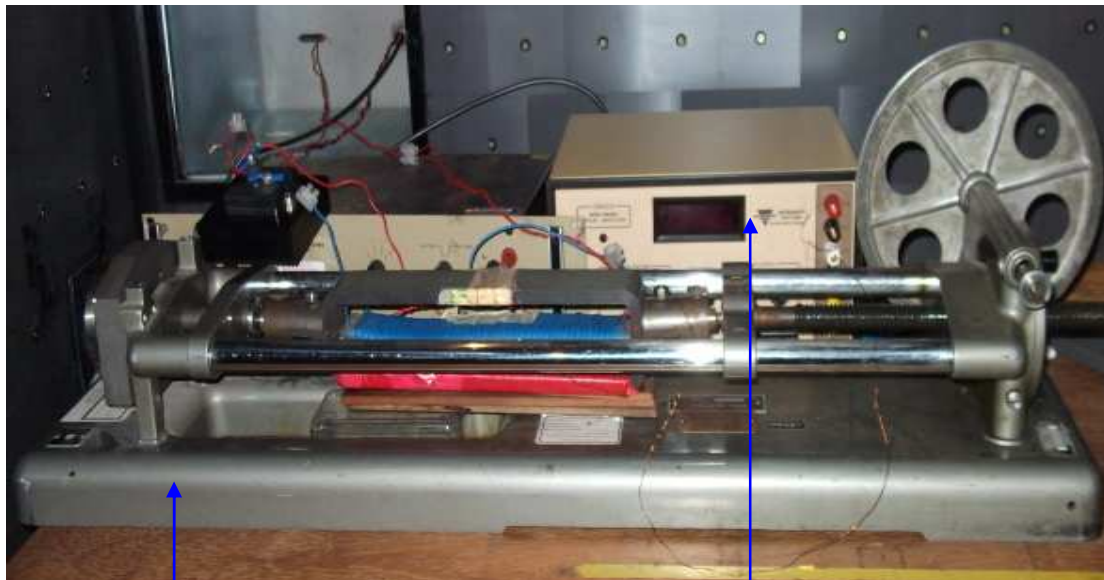
Tension stressing rig with
the BN measuring system

Strain indicator

Fig. 5.5: Barkhausen noise measurement system with tension stressing rig and strain indicator.

5.5   Methods used for domain observation

Magnetic domains are observed and studied so as to understand the properties of magnetic materials. Domains are regions of uniform magnetisation which are so arranged for energy minimization in the material. There are a number of different methods used to study the domain structure of magnetic materials. The magnetic domain viewer and the Kerr magneto-optic (KMO) effect [5.12] are the methods used in this work to observe the domains in the coated and decoated samples respectively. The KMO technique makes use of the longitudinal Kerr effect to form domain patterns [5.13].

5.5.1   The magnetic domain viewer

In this method, a magnetic pattern is formed in the magnetic domain viewer. The domain viewer uses colloidal magnetic particles to detect surface leakage fields. By applying a low vertical dc magnetic field using an enwrapping coil, the small ferromagnetic particles congregate on the domains that are in the direction of the magnetic field and avoid the others that are not in the field's direction. This makes for the observed domain contrast in the sample under observation. The domain patterns of coated CGO and HGO steels observed in this work using the domain viewer are shown in figures 8.1a and 8.2a respectively.

5.5.2   The Kerr magneto-optic technique

 The principle of operation of the KMO effect is that the light reflected from the surface of the specimen to be observed will interact with the magnetization at the specimen surface. This interaction will rotate the polarisation plane of the light and the difference between the incident and reflected beams can be utilized to study the magnetisation within different regions of the specimen.

The magnetic domain structure of the prepared samples was examined using a low-magnification longitudinal Kerr effect microscope. The schematic diagram of the components of a Kerr microscope is shown in figure 5.6. A high pressure mercury light that illuminates the sample is the light source which is reflected with changes in polarization, amplitude, and phase determined by the orientation of the magnetisation. This light is reflected back through the sample under observation through the

polarizing beam splitter and the analyzer before being focused on the camera after under going changes due to the orientation of the magnetization. The second polarizer (analyser) functions as a filter for the light which reflects off the sample without changes in polarization. The rotation angle of the polarization is very low and consequently the signal of the Kerr-affected light is very weak. This weak signal passes through the analyzer into the camera which is connected to a computer for image processing and enhancement [5.14]. Three types of Kerr effect microscopy are used viz: polar, transverse and longitudinal. The polar case have the magnetization normal to the reflecting surface while in the transverse case, the magnetization vector in the surface is normal to the plane of incidence. In the longitudinal case, the magnetization vector is in the plane of incidence and parallel to the surface. It is used widely in electrical steel due to comparably better contrast than other Kerr effects.

The KMO technique was preferred to other domain imaging techniques in this research because it is ideal for view relatively large domains with high image contrast. The CGO and HGO electrical steel used in this research have relatively large domains. The high image contrast obtainable often eliminates the need for image processing. The second reason for choosing KMO technique is that no optical elements other than the sample exist between the polariser and the analyser, there is no depolarisation of the light beam.
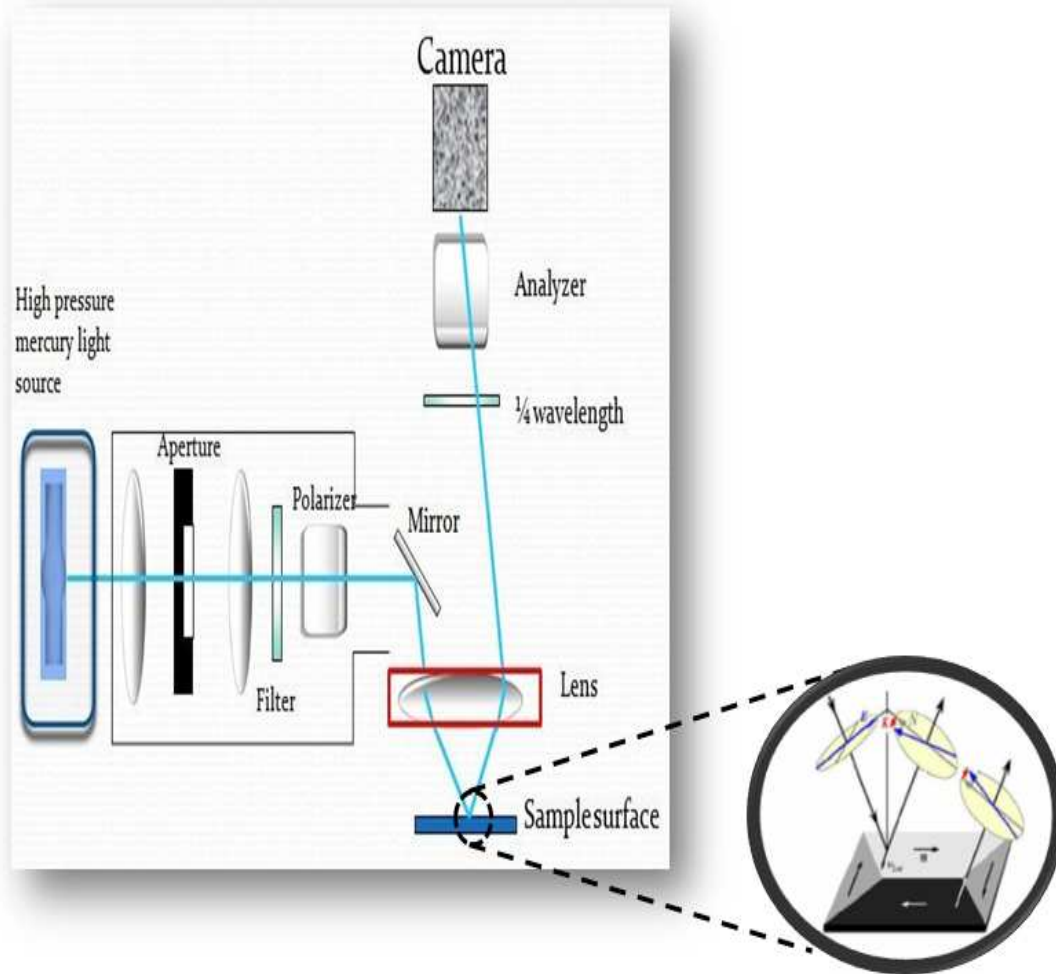
Fig. 5.6: Schematic representation of the main components of a Kerr microscope. Inset shows the longitudinal effect.

The model of the polarising microscope is Neoark BH-780-IP and the specifications are as shown below:

- Super high pressure mercury light source (100 W).
- Mitsutoyo M plan Apo, strain free, long working distance objective lens (50x, 20x, 10x & 5x) with better than 1 µm resolution.
- Polarisation optical unit incorporating polariser and analyser made from Calcite (Glan-Thompson) prisms.
- ¼ wavelength optical filter.
- Micro translation sample stage with X, Y, Z fine movement.

The specifications of the High Speed Intensified Digital CMOS Camera (model HCC-1000) are as follows:

- 1024 x 1024 pixels sensor format.
- 462 frames/sec. at full resolution.
- Up to 512 Mbytes internal memory.
- Progressive scan.

- 8-bit digital output with up to 30 frames/sec.
- Control via RS-232.
- C-mount compatible sensor size (2/3").
- Power supply: 12 V, 500 mA.

5.6 Uncertainty in measurement

Uncertainties in the measurements were estimated from the recommendations in UKAS (United Kingdom Accreditation Service) M3003 [5.15]. The standard uncertainty is divided into two viz: Type A and Type B. Type A uncertainty is evaluated by statistical analysis of a series of observations and is normally used to obtain a value for the repeatability or randomness of a measurement process. On the other hand, systematic components of uncertainty, which account for errors that remain constant while the measurements are made, are estimated from Type B evaluations. The combined uncertainties of the measurement has been tabulated and shown in Appendix A while Appendix B shows the type A uncertainties.

5.6.1 Mathematical expression for type A and type B uncertainties

The measurand, y, is the functional relationship of the input quantities, $x_1, x_2, ..., x_N$ as

$$y = f(x_1, x_2, ..., x_N)$$
(5.8)

The type A uncertainty of $y(u_A(y))$ is obtained from the standard deviation, (s_d), of the n times repeated measurements as

$$u_A(y) = \frac{s_d}{\sqrt{n}}$$
(5.9)

The standard deviation derivation is defined as

$$s_d = \sqrt{\frac{1}{n-1} \sum_{i=1}^{n} (q_i - \overline{q})^2}$$
(5.10)

where q_i is the measured value of y, $\overline{q}$ is the mean value of y and is expressed as

$$\bar{q} = \frac{1}{n}\sum_{i=1}^{n}q_i \qquad\qquad\qquad (5.11)$$

The type B uncertainty is contributed by the standard uncertainties $(u(x_1))$ of the measurement inputs x_1 and is mathematically expressed as

$$u_B^2(y) = c_1^2 u^2(x_1) + c_2^2 u^2(x_2) + \ldots + c_N^2 u^2(x_N) \qquad\qquad (5.12)$$

where c_i is called the sensitivity coefficient and is the partial derivative $\dfrac{\partial y}{\partial x_i}$.

In measurement of magnetic properties, c_i can be experimentally determined from $\dfrac{\Delta y}{\Delta x_i}$ by varying the value of x_i [5.15].

The combined standard uncertainty of y is derived from $u_A(y)$ and $u_B(y)$ as:

$$u(y) = \sqrt{u_A^2(y) + u_B^2(y)} \qquad\qquad\qquad (5.13)$$

which is finally multiplied by the coverage factor, K_{95}, to be the expanded uncertainty, $U(y)$. K_{95} provides a confidence level of 95% of the normal distribution [5.6].

Thus $U(y) = K_{95}u(y)$ $\qquad\qquad\qquad\qquad\qquad\qquad$ (5.14)

The measured value of $y(Y)$ is then reported as $y = Y \pm U(y)$.

The uncertainty sources obtained from equipment specification sheets were divided by 2 before used as the sources of uncertainties since these values were supposed to be expanded uncertainties with $K_{95} = 2$. If the specification sheet were not found, the uncertainty values have been estimated to be a half of their minimum scale divided by $\sqrt{3}$ as a coverage factor of the rectangular distribution.

The number of degrees of freedom (v_i) is infinity for all the uncertainty sources because it can be any value whereas v_i for Type A uncertainty is $n-1$.

The effective number of degrees of freedom

$$v_{eff} = \frac{u^4(y)}{\sum\limits_{i=1}^{n} \dfrac{v_i^4(y)}{v_i}}$$

v_{eff} is eventually used to determine K_{95} from the t-distribution table. v_{eff} is often infinity where $K_{95} = 2$ and n is the number of repeated measurements.

The values in the tables of appendix A have been estimated in the following way:

a) Accuracy of NI PXI-4461 DAQ card: the accuracy of the voltage measurement range of ± 3 V is $\pm$ 10.4mV [5.3]. Thus the relative accuracy is 10.4 mV/3 V x 100 = 0.347%

b) Frequency setting: this value (0.002 %) was taken from the base clock accuracy of the NI PXI-4461 DAQ card.

c) Sample mass measurement: the mass of the sample was measured using an Avery Berkel FB31 scale with a resolution of 0.01 g and accuracy of ± 0.0002 g. Each sample was weighed 5 times and the expanded uncertainty of all samples was within $\pm 0.01\%$.

d) Sample length measurement: the length of every sample was measured using a metal ruler with a resolution of 0.5 mm. Its uncertainty was assumed as a half of the resolution resulting in 0.082% of the nominal length of 305 mm. It was approximated to 0.1 %.

e) Control of Bpeak and form factor: the control algorithm written in LabVIEW was able to maintain the value of Bpeak and form factor of the secondary voltage within $\pm 0.3\%$.

f) Shunt resistor: Calculated by getting standard deviation of ten measurements and dividing the result by the number of measurements taken. The result (0.000434) is further divided by the resistance (4.7 Ω) then multiplied by 100. The value is 0.009 %.

g) Shunt temperature change was calculated by multiplying the temperature coefficient (1.50E-04) by the expected temperature variance ($\pm 30\%$). The result was truncated to 0.005.

h) Magnetic path length: A metal ruler with a resolution of 0.5 mm was used to measure the length between the inner edges of the flux closure yoke. The

nominal length is 270 mm, so the relative uncertainty was 0.25 mm/270 mm x 100 = 0.093 %, rounded to 0.1 %.

i) Density: The quoted value is 7650 kg/m^3. The uncertainty is presumably a half of the last digit of the quoted value which is ±0.0025. This yields a relative value of 0.033%.

j) Type A uncertainty was derived from the standard deviation of 3 times repeated measurements of each sample tested.

k) Accuracy of the strain amplifier: The gain of the strain amplifier of the Vishay system 3800 has a resolution of 0.05% [5.9].

l) Accuracy of the shunt calibration resistors: The shunt calibration resistors of the strain indicator of the Vishay system 3800 have the accuracy of ±0.05 Ω.

m) Width of the sample: the sample width was measured by means of a digital veneer calliper having an accuracy of 0.02 mm. It is 0.067 of the nominal value at the nominal value of 30 mm. It is approximated to 0.07%.

n) Thickness of the sample: A digital micrometer was used to measure the thickness and its accuracy was 0.0025 mm, which is 0.83% of the 0.30 mm thick sample.

o) Gauge factor: the uncertainty of the gain factor is ±1% [5.7].

p) Jaw gripping: The sample has the tendency of slipping slightly at the start of applying tensile stress. It was difficult to quantify this effect, so the uncertainty of ±2.5% was estimated [5.6].

References to chapter 5

[5.1] K. Hartmann, Relationships between Barkhausen noise, power loss and magnetostriction in grain-oriented silicon iron, PhD thesis, Cardiff University 2003.

[5.2] K. Hartmann, A.J. Moses and T. Meydan, A system for measurement of AC Barkhausen noise in electrical steels, Journal of Magnetism and Magnetic Materials Vol. 254–255, pp. 318–320, 2003.

[5.3] National Instruments, Dynamic signal acquisition user manual, August 2002.

[5.4] BS EN 10280:2001 + A1:2007, Magnetic Materials- Methods of measurement of the magnetic properties of electrical sheet and strip by means of a single sheet tester, British Standard, 2007.

[5.5] S. Zurek, P. Marketos, P. I. Anderson, and A. J Moses, Influence of digital resolution of measuring equipment on the accuracy of power loss measured in Epstein frame, Przeglad Elektrotechniczny (Electrical Reviews), Vol. R. 83, pp. 50-53, 2007.

[5.6] S. Somkun, Magnetostriction and magnetic anisotropy in non oriented electrical steel and stator core laminations, PhD thesis, Cardiff University, September 2010.

[5.7] (www.omega.com/techref/pdf/strain-gage-technicaldata.pdf). Strain gauge technical data manufacturer'smanual. Accessed on 15th July 2011.

[5.8] Omega, SG496 Rapid Cure Strain Gauge Adhesives User's Guides, 2008.

[5.9] Instruction manual of model 3800 wide range strain indicator.

[5.10] P. Klimcyzk, Novel technique for characterisation and control of magnetostriction in grain oriented silicon steel, PhD thesis, Cardiff University, 2012.

[5.11] B. Fukuda, K. Satoh, T. Ichida, Y. Itoh, and H. Shimanaka, Effect of surface coatings on domain structure in grain oriented 3% Si-Fe, IEEE Transactions on Magnetics, Vol.17, No.6, pp. 2878-2880, 1981.

[5.12] A. Hubert and R. Schäfer, Magnetic Domains. Berlin, Germany, Springer-Verlag, 1998.

[5.13] J. Kerr, On rotation of the plane of polarization by reflection from the pole of a magnet, Philosophical Magazine, Vol. 3, pp.321–343, 1877.

[5.14]http://www.ece.neu.edu/faculty/dimarzio/capstone/samples/Final%20Capsto
ne%20Report.pdf. Accessed on 20th July, 2011.

[5.15] UKAS M3003, The expression of uncertainty and confidence in
measurement, 1997.

Chapter 6   Investigation of magnetic properties and Barkhausen noise of grain oriented electrical steel

6.1   Introduction

The experimental results obtained on the strips of CGO and HGO steels using the measurement equipment described in section 5.2 are presented in this chapter. Measurements of coercivity, B-H loop, AC relative permeability and specific power loss are presented and discussed. Experimental measurements of BN of the test samples at high and low flux densities are also presented and discussed.

An average of 3 measurements made on every strip was used in analysing the result. Between repeatability measurements each sample was removed and then re-inserted into the test system. The percentage difference of the measured properties was quantified using equation 6.1. The actual difference could be positive or negative depending on the values of the measured parameters under consideration. The parameters quantified are the rms, TSA, coercivity, relative permeability and power loss. The actual difference is the result of subtracting the one value of a parameter from another value of the same parameter in the different samples under consideration. The subtrahend is the 'original value' in equation 6.1.

% Difference = Actual difference/Original value x 100 %   (6.1)

6.2 B-H loops, coercivity, relative permeability and specific power loss of CGO and HGO

This part of the investigation was carried out on samples of HGO and CGO steels, 305 mm x 30 mm x 0.27 mm from Cogent Power Limited United Kingdom. 40 strips comprising 20 CGO and 20 HGO were tested. The HGO and CGO strips had average grain sizes of 9 mm and 4 mm respectively. Each strip was singly magnetised under sinusoidal peak flux density from 8.0 mT to 1.5 T at a magnetising frequency of 50 Hz. The uncertainty of measurement for the peak flux density and peak magnetic field at low and high flux densities are shown in tables A1-A3.

Typical B-H loops of HGO and CGO strips measured at 50 Hz, 1.5 T are shown in figure 6.1. The B-H loops of all strips tested had similar characteristics, e.g., the coercive field of CGO samples was always higher than that of HGO sample at all flux densities as expected.

Figure 6.2 shows the variation of average coercive fields of the same CGO and HGO strips with peak flux density at 50 Hz. In the materials under investigation, the average domain width decreases by 22 % because the average domain width of the HGO is 0.63 mm and that of CGO is 0.49 mm as illustrated in section 8.2. Figure 6.3 shows the variation of the percentage difference of average coercivity of CGO and HGO at high and low flux densities. The highest percentage difference of 14 % occurred at 0.2 T. From 0.008 T to 0.2 T referred to as low flux densities in this work, the percentage difference maintained a steady rise except at 0.04 T where the value decreased. The percentage difference at 0.3 T is 12 % and thereafter every other two measured peak flux density had approximately the same percentage difference viz: 11 % at 0.4 T and 0.6 T, 13 % at 0.8 T and 1.0 T, 11 % at 1.2 T and 1.3 T, and 10 % at 1.4 T and 1.5 T. The above figures did not tally with the earlier stated decrease of 22 % in average domain width of CGO because such other factors as number and distribution of pinning sites, precipitates, grain boundaries etc also influence coercivity and in fact other magnetic properties such as relative permeability and power loss.
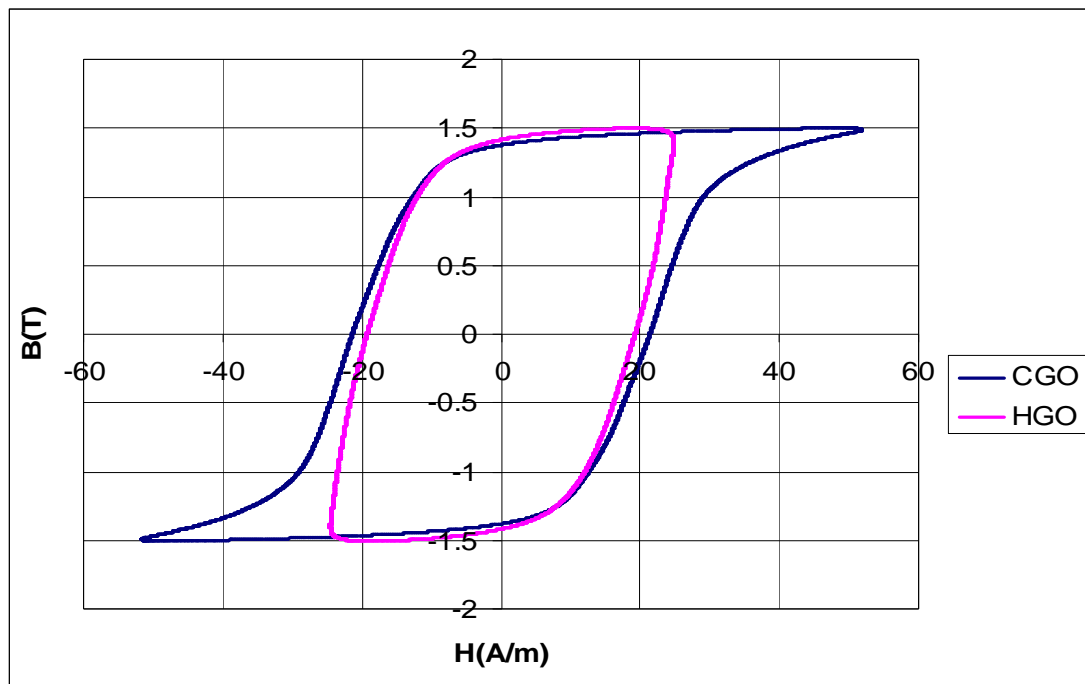
Fig. 6.1: Typical B-H loop of CGO and HGO measured at 1.5 T and 50 Hz.
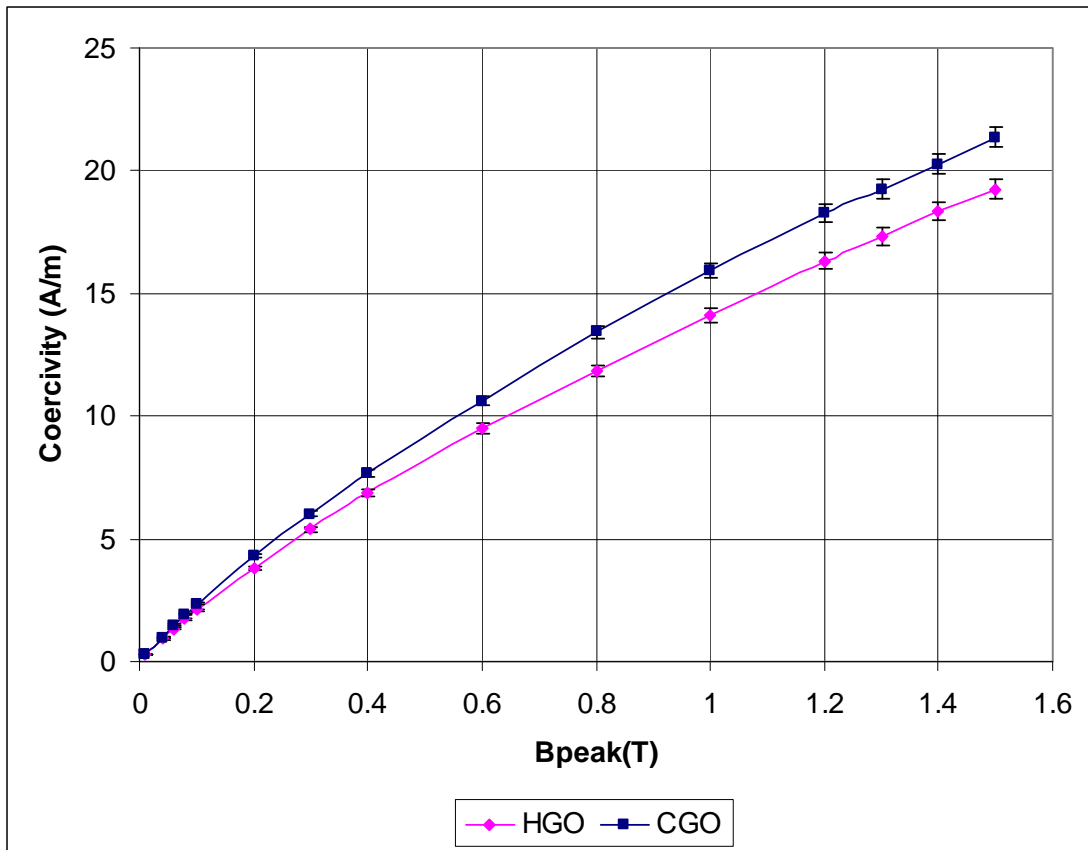
Fig. 6.2: Variation of average coercivities of HGO and CGO with peak flux density.
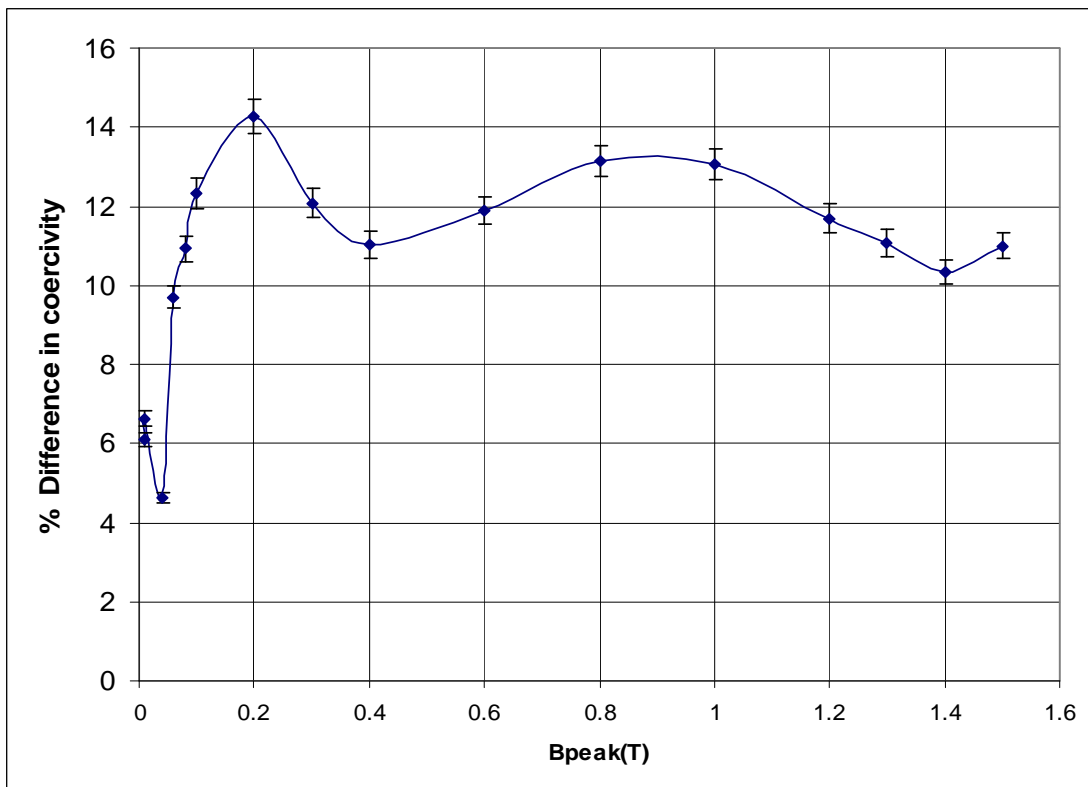
Fig. 6.3: Variation of percentage difference of average coercivity of CGO and HGO with peak flux density.

The coercive field of CGO is higher than that of HGO because the average grain size of HGO is higher than that of CGO. As stated earlier, the average grain size of the tested HGO is 9 mm while that of CGO is 4mm. As the grain size increases, it is expected that coercive field would decrease as larger grains provide fewer pinning sites to impede the movement of the domain walls due to lower volume fraction of grain boundaries as found in decarburised steels at high flux densities (above 0.1 T) [6.1].

In [6.2], coercive field was also found to be higher in conventional 3 % Si-Fe sheets manufactured by Pohang Steel Corporation of Korea having average grain size of 6 mm than in highly grain oriented HiB-8 manufactured by Nippon Steel Corporation of Japan having average grain size of 15 mm. The reason advanced was the increase in the grain boundary area of conventional 3 % Si-Fe acting as obstacle to the domain wall movement. The measurement was carried out at high induction and at magnetising frequencies of 0.05 Hz and 0.1 Hz.

Coercive field is related to how much anisotropy energy is required for magnetic moment rotation away from easy axes to the axis of the applied field and depends to a large extend on the number of pinning sites present in a material.

Figure 6.4 shows the variation of average AC relative permeability of CGO and HGO with peak flux density. It was derived from equation 5.6 in LabVIEW. The measurement uncertainties at low and high flux densities are shown in tables A6 and A7 respectively. The graph of the variation of the percentage difference of average relative permeability of HGO and CGO with peak flux density is shown in figure 6.5. The average AC relative permeability of HGO is higher than that of CGO at both high and low fields. Previous work made at high inductions agrees with this [6.2]. The larger grain size and better grain-grain orientation of HGO are responsible for this. In grain oriented electrical steel, higher grain size implies lower number of grain boundaries and precipitates which usually impede domain wall motion and thus reduces permeability. In the samples under test, the percentage increase in average relative permeability of HGO peaks at 0.04 T and 0.06 T at low flux densities with a value of 39 % and thereafter decreased steadily until 0.6 T and 0.8 T where the value was maintained at 22 %. It thereafter increased steadily peaking at 1.5 T with a value of 110 %. As inferred earlier, the higher level of grain boundaries acting as pinning sites in CGO caused a reduction in grain size thereby reducing the relative

permeability. Magnetic characterisation of grain oriented electrical steel is normally measured at high inductions (1.5 T/ 1.7 T) [6.3] which is suitable for its typical application in power transformers. For a given magnetic material, the permeability is not usually specified over the low flux density range applicable in current transformer cores and other applications where electrical steel is used at low flux densities. Recent work at below 1mT [6.4] shows the permeability of CGO is higher than that of HGO at this regime and confirms that performance at low magnetisation level cannot be predicted from measurements made at high inductions especially when comparing the performance of CGO and HGO.
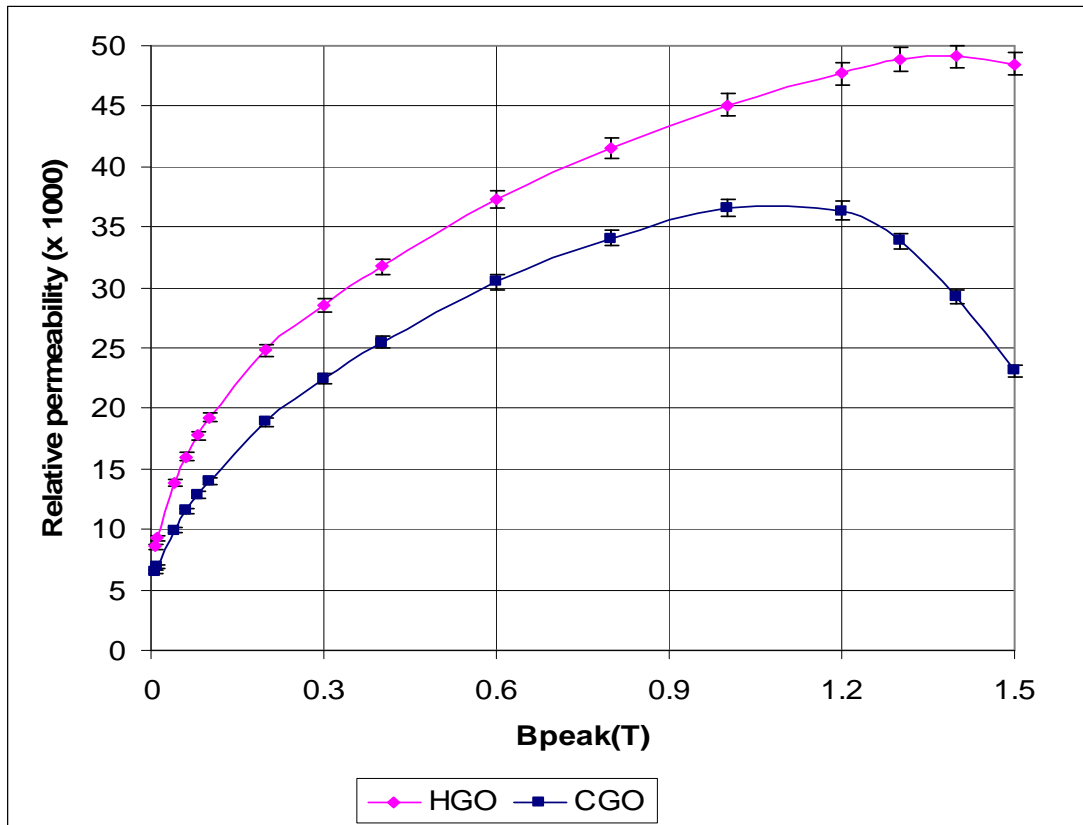
Fig. 6.4: Variation of average AC relative permeability of HGO and CGO with peak flux density.
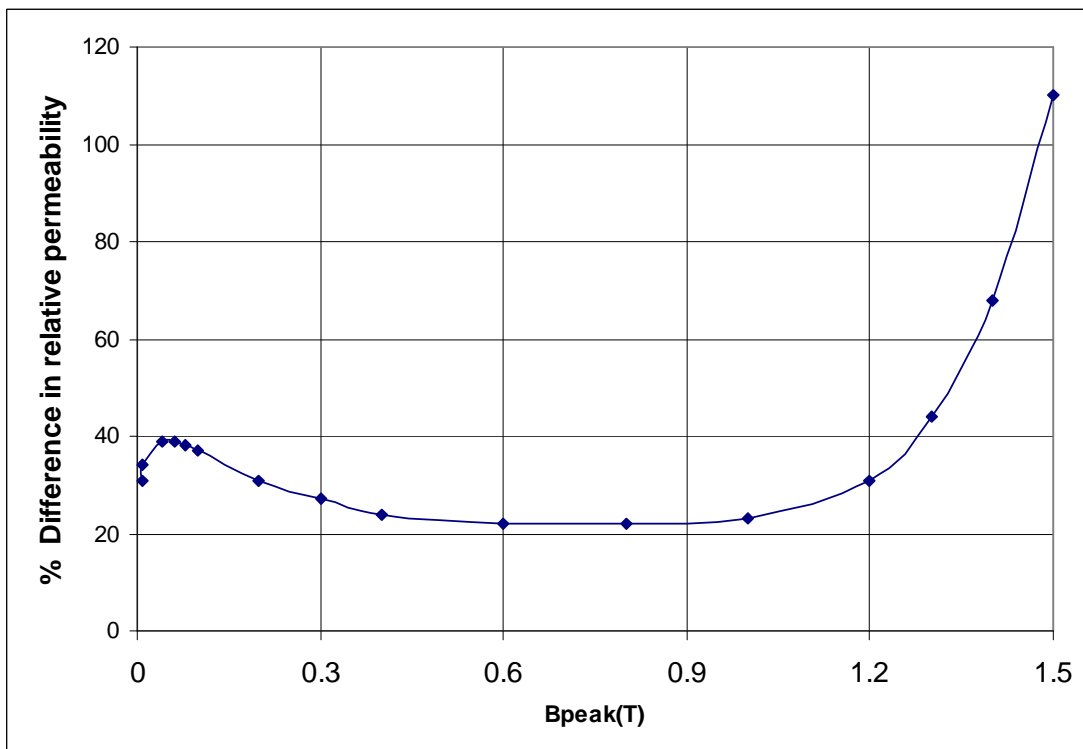
Fig. 6.5: Variation of percentage difference of average relative permeability of HGO and CGO with peak flux density.

Figure 6.6 shows the variation of the power loss (W/kg) of CGO and HGO with peak flux density and the variation of percentage difference of average specific power loss of CGO and HGO with peak flux density shown in figure 6.7. The uncertainty of measurement at low and high flux density regimes are shown in tables A8 and A9. As expected the average specific power loss of CGO samples is higher than the average specific power loss of HGO samples at all flux densities. The percentage difference was erratic below 0.2 T with a peak of 25 % at 0.1 T. It reduced to 11 % at 0.4 T and thereafter increased steadily to 25 % at 1.5 T. As coercivity, power loss depends largely on the number of pinning sites present in a material. These pinning sites reduce the speed of domain wall motion resulting to a decrease in power loss.

Similar reason was given in [6.2] where it was stated the lower power loss of HGO samples is due to a decrease in the grain boundary area and an increase of the 180° domain width of HGO than CGO. As a rule, the grain-grain misorientation in (110)[001] oriented silicon steel increases as the grain size decreases, thus larger grain boundary micro demagnetising fields would be expected in small grained materials [6.5].

 In [6.6], 3 types of uncoated CGO with different amounts of precipitates were compared at field strength of 800 A/m and magnetising frequency of 50 Hz to determine the effects of precipitates on their magnetic properties. It was reported that increased number of precipitates significantly reduced permeability and almost doubled power loss. This drop in magnetic performance was linked to increased number of pinning sites.

This investigation shows that in comparing the magnetic properties of CGO and HGO, the same trend of relationship is found at both low flux densities (8 mT -0.2 T) and high flux densities (above 0.2 T).

 In grain-oriented electrical steel, microstructural features such as grain size, grain boundaries and grain-grain misorientation are the dominant parameters that distinguish CGO and HGO in relation to coercivity, relative permeability, power loss and BN. Hence these parameters influence BN in CGO and HGO.
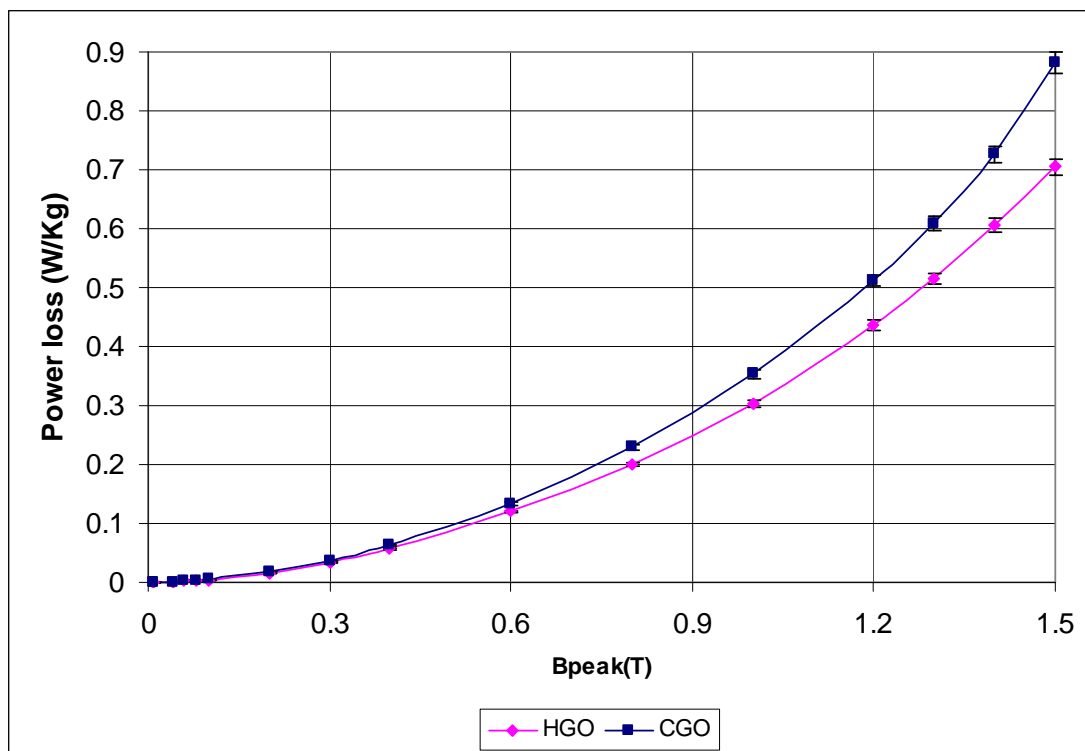
Fig. 6.6: Variation of average specific power loss of CGO and HGO with peak flux density.
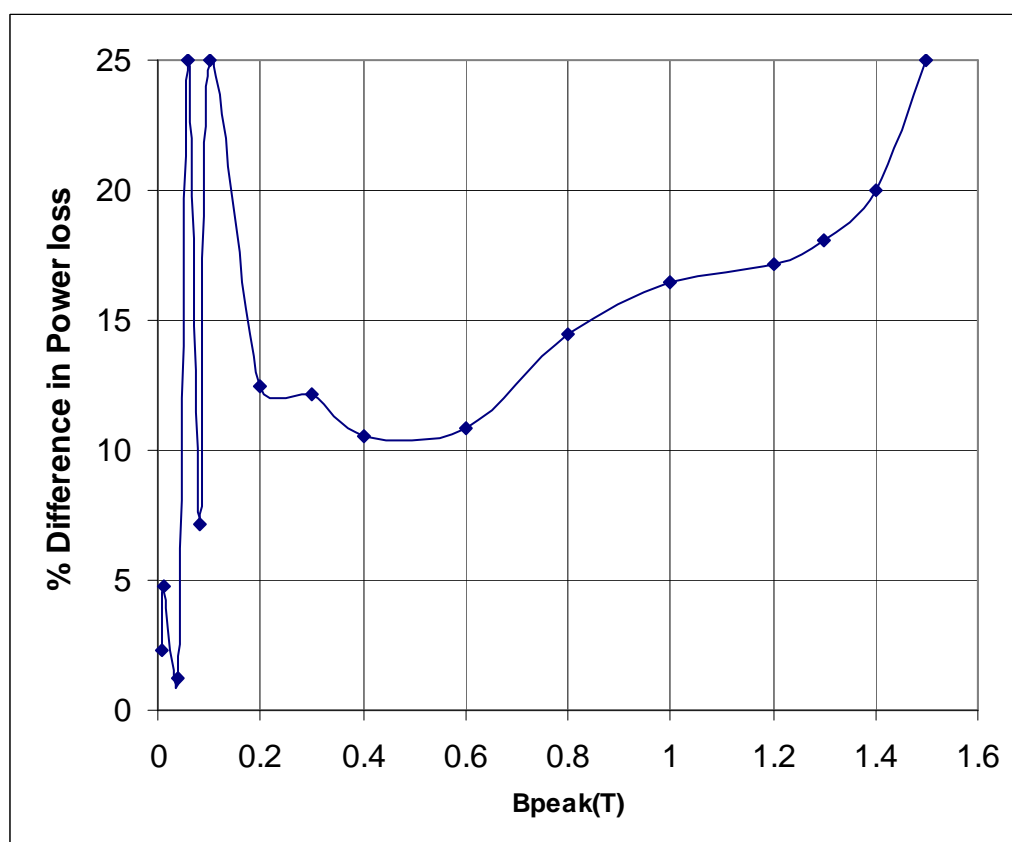
Fig. 6.7: Variation of percentage increase of average specific power loss of HGO over CGO with peak flux density.

6.3   Barkhausen noise measurement of HGO and CGO

This part of the investigation was carried out on samples of CGO and HGO, 305 mm x 30 mm x 0.27 mm from Cogent Power Limited United Kingdom and ThyssenKrupp Electrical Steel, Germany. 40 strips from Cogent Power Company referred to as P1 comprising 20 CGO and 20 HGO strips were tested. Another 40 strips from ThyssenKrupp denoted as P2 comprising 20 CGO and 20 HGO strips were also tested. Each strip was singly magnetised under sinusoidal flux density, Bpeak, from 8.0 mT to 1.5 T at a magnetising frequency of 50 Hz. Each measurement of BN was made three times and then averaged. The uncertainties of measurement at low and high flux densities are shown in tables A10 and A11.

BN studies aimed at non-destructive testing applications are usually carried out under quasi-static or very low frequency magnetisation conditions but 50 Hz has been chosen in this work because it is believed that at this frequency the BN signal is possibly more related to dynamic processes and can give more information about the magnetisation processes which low frequency BN measurements cannot. Such information include eddy current anomalous loss influence on magnetisation.

Figures 6.8 and 6.9 show typical BN spectra obtained from HGO and CGO at 1.2 T and 50 Hz. The sinusoidal curve is the flux density waveform at a 1000 times smaller scale. One cycle of magnetisation is shown. As expected, the BN is highest at points in time corresponding to when the material was experiencing maximum rate of change of magnetisation at the coercive fields [6.7, 6.8]. The coercive fields are the points where the flux density waveforms are zero in the figures. As can be observed from the figures, the BN amplitude is higher in HGO with the maximum peak occurring at 2mV while the maximum peak in CGO occurs at 1.4mV and this shows that the BN induced voltage in HGO is higher than that of CGO especially at high flux densities as subsequent results in this investigation show.
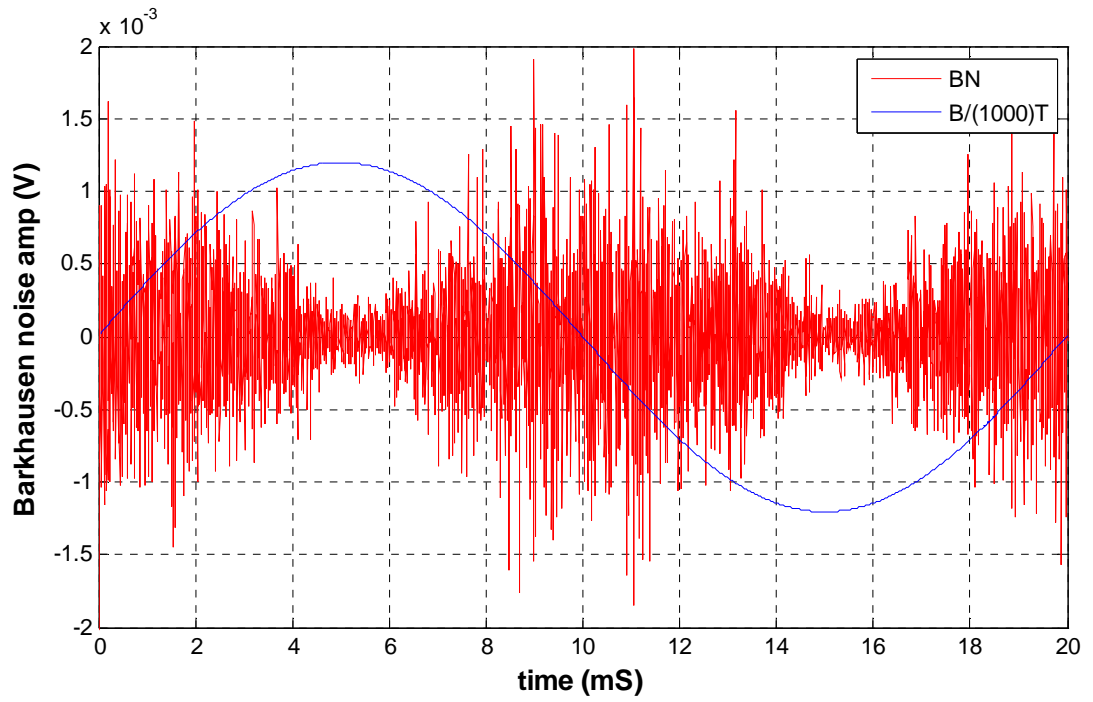
Fig.6.8: BN spectrum of HGO during one cycle of magnetisation at 1.2 T and 50 Hz showing variation of BN amplitude with time.
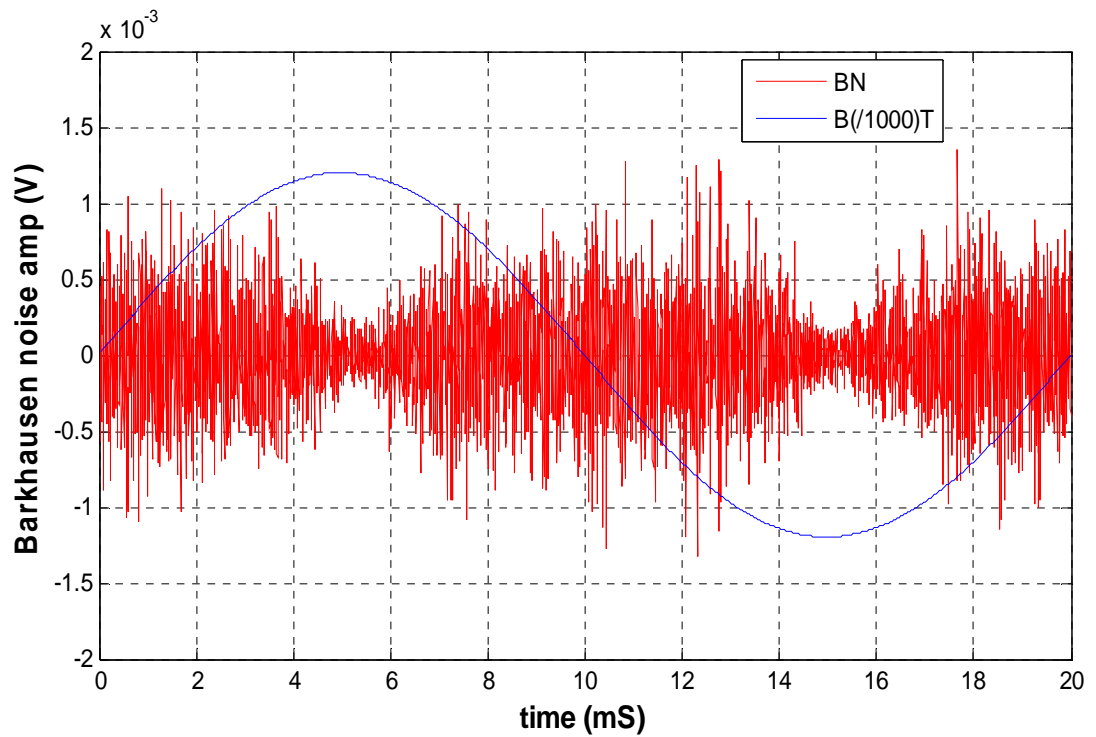
Fig. 6.9: BN spectrum of CGO during one cycle of magnetisation at 1.2 T and 50 Hz showing variation of BN amplitude with time.

Figure 6.10 shows the rms values of the BN spectra shown in figures 6.8 and 6.9 as well as the background noise of the experimental set up at all the peak flux densities measured. Preliminary test determined the background noise level in the experimental set up. The same relationship was obtained when the background noise was plotted against the total sum of amplitudes (TSA) and total number of points (TNP). It can be observed from the figure that the background noise is more than 100 times less that the BN amplitude of the test samples. This was achieved by applying all the background noise reduction techniques discussed in section 5.3. Background noise reduction is particularly challenging at very low inductions and measurements must be made in an environment free from electromagnetic interference.
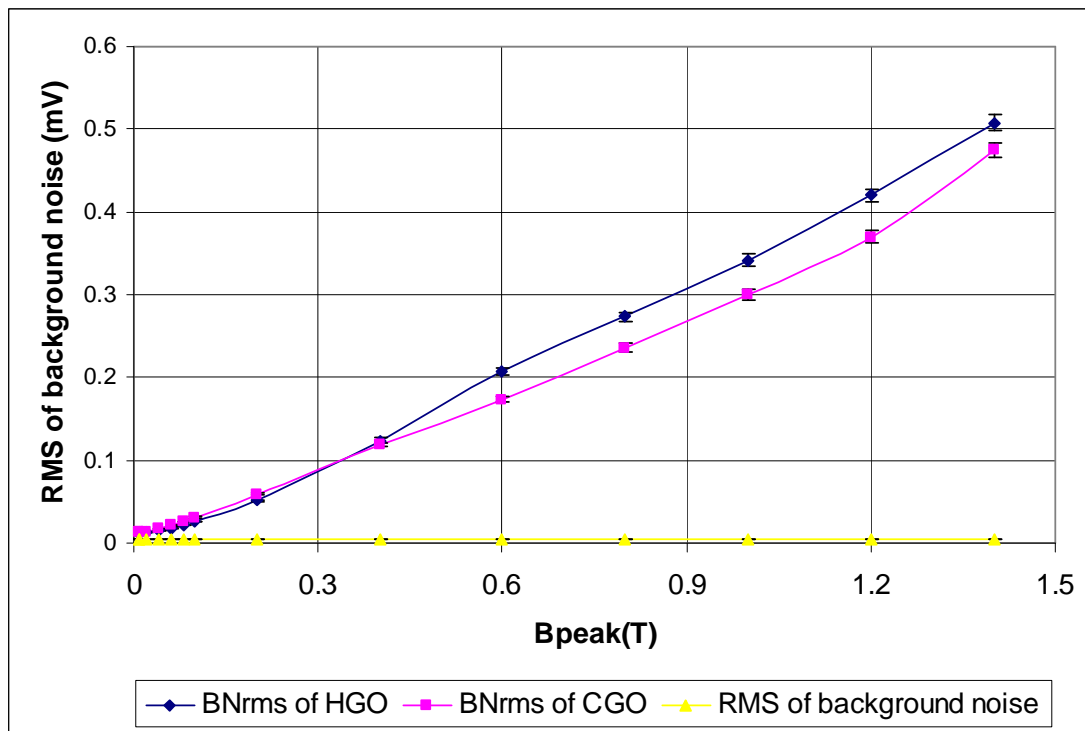
Fig. 6.10: Comparison of average rms BN of CGO and HGO strips at different flux densities at 50 Hz with background noise of Experimental set-up.

Figure 6.11 shows the variation of average rms BN of 20 strips of CGO and 20 strips of HGO from P1 at both high and low flux densities. It can be observed that the average rms BN is higher in HGO than in CGO above 0.2 T but at lower flux densities the trend changes. A similar characteristic was obtained when the same number of test samples from P2 was investigated at both magnetisation regimes. This is shown in figure 6.12. The variation of the percentage difference of the average rms BN of these test samples with peak flux density is shown in figure 6.13.

Figure 6.14 shows the same BN signals expressed in terms of the average TSA of BN peaks of the test samples from P1. As with the rms BN, the TSA of HGO is higher than that of CGO above 0.2 T and the trend changes at lower flux densities. TSA of samples from P2 show the same relationship as with P1 and is plotted in figure 6.15 with the variation in percentage difference at both high and low flux densities shown in figure 6.16.
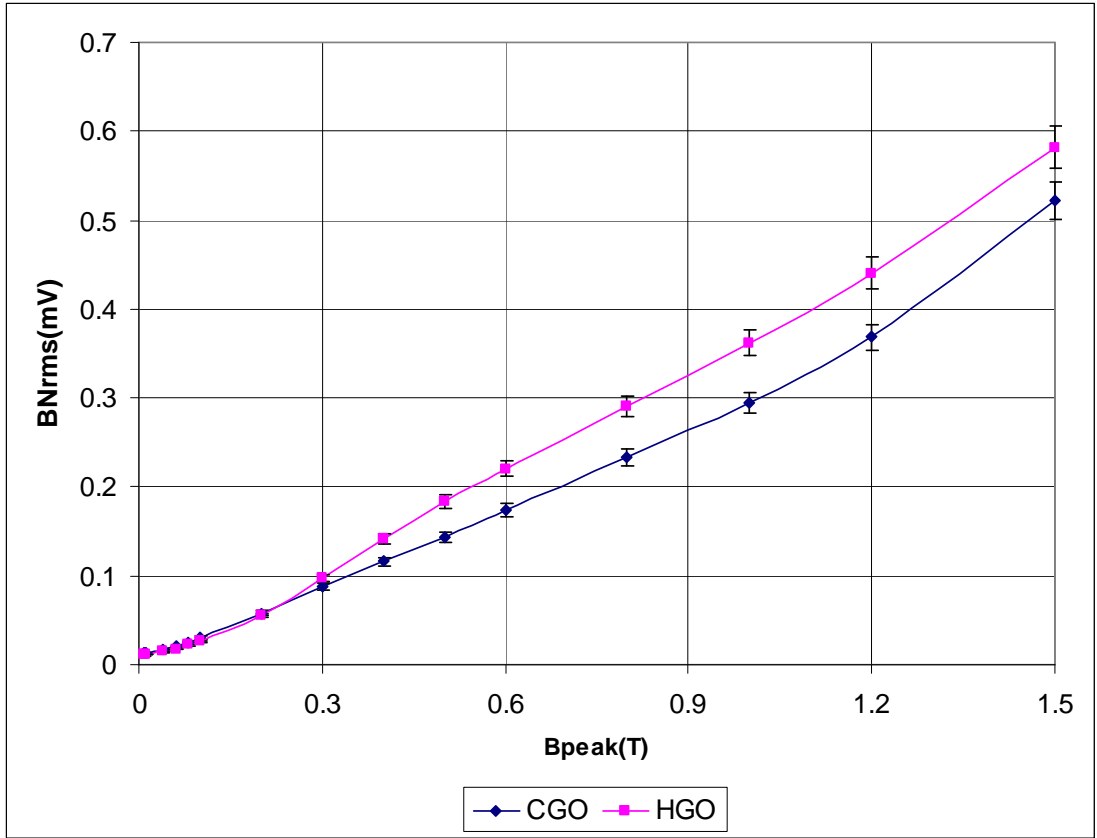
(a)
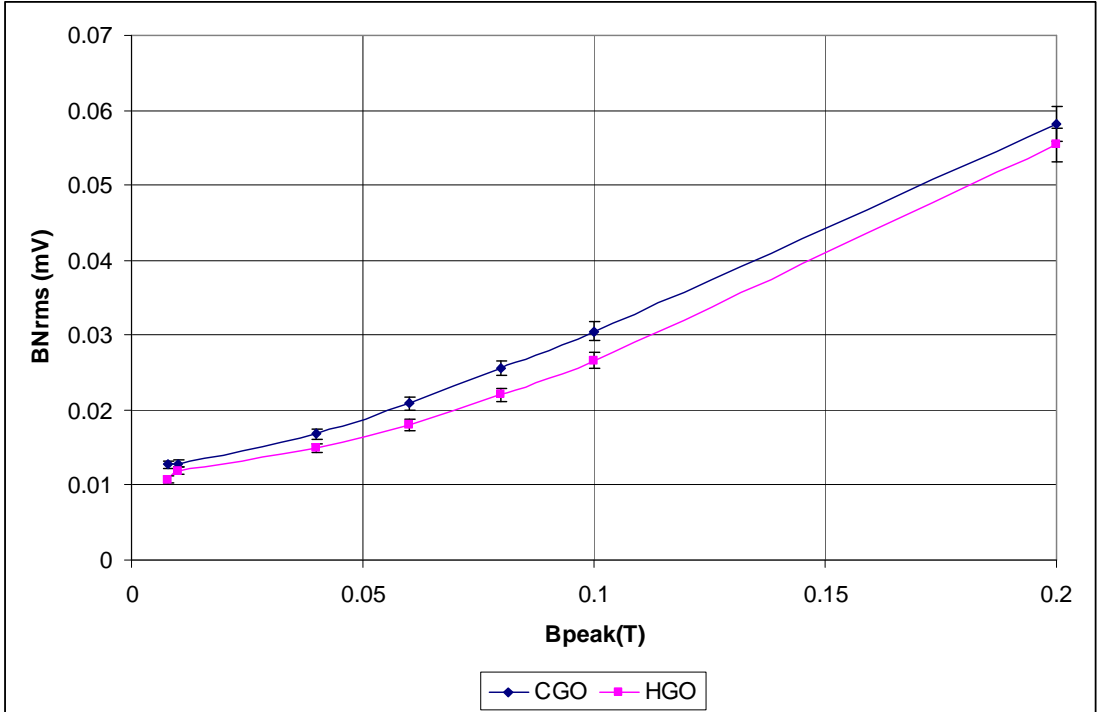
(b)

Fig. 6.11: (a) Variation of average rms BN of 20 strips each of CGO and HGO from P1 with peak flux density (b) the same comparison in the low field regime.
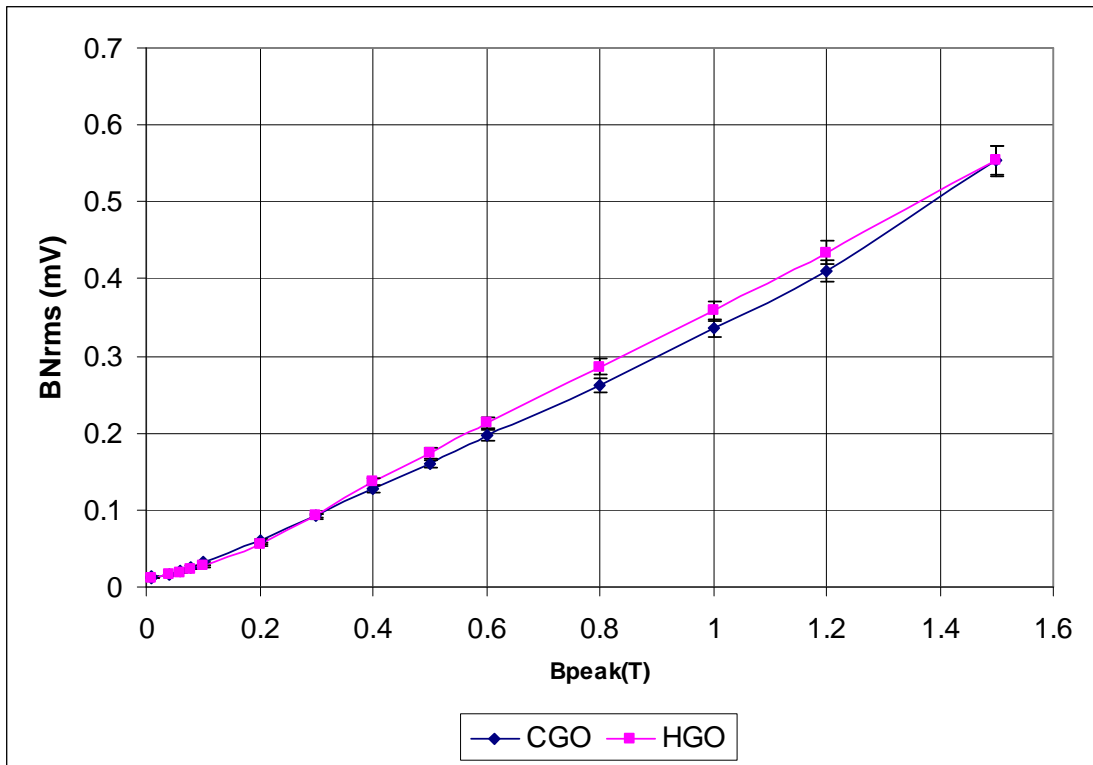
(a)

(b)

Fig. 6.12: (a) Variation of average BNrms of 20 strips each of CGO and HGO from P2 with peak flux density (b) the same comparison in the low field regime.

Fig. 6.13: Variation of percentage difference of average rms BN of HGO and CGO from P1 and P2 with peak flux density.
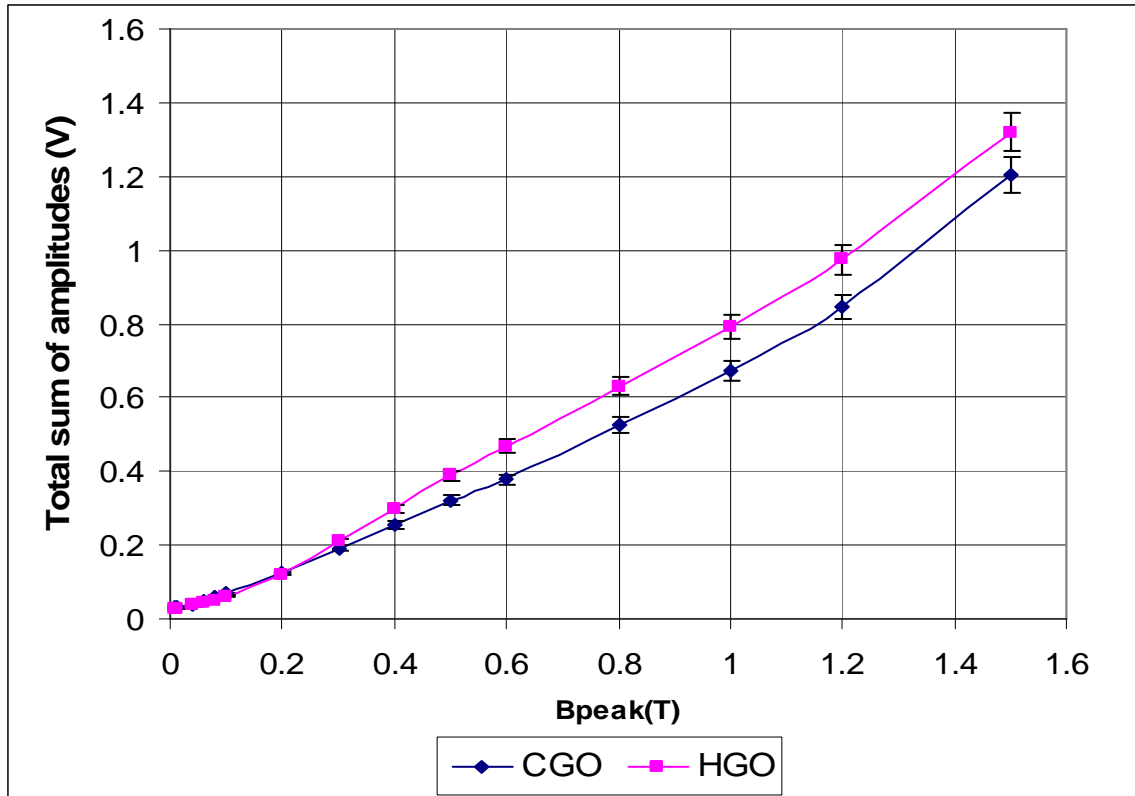
(a)
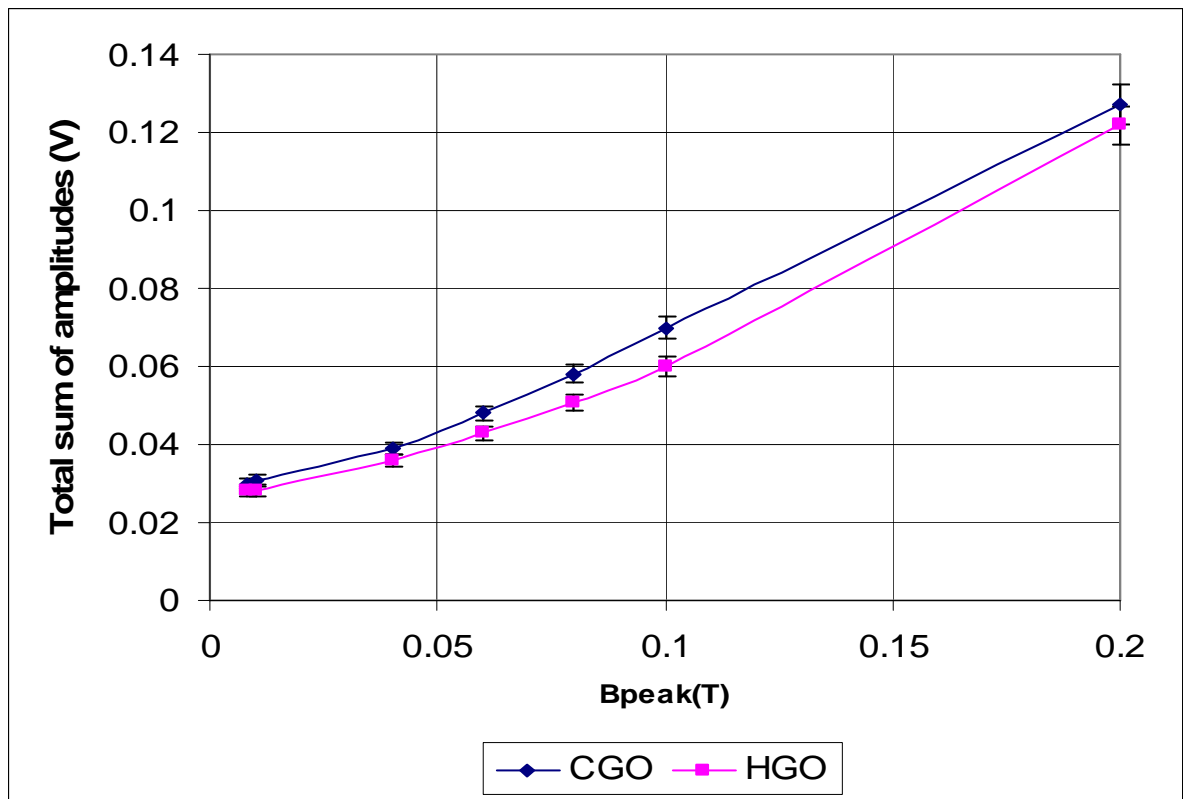
(b)

Fig. 6.14: (a) Variation of average TSA of 20 strips each of CGO and HGO from P1 with peak flux density (b) the same comparison in the low field regime.
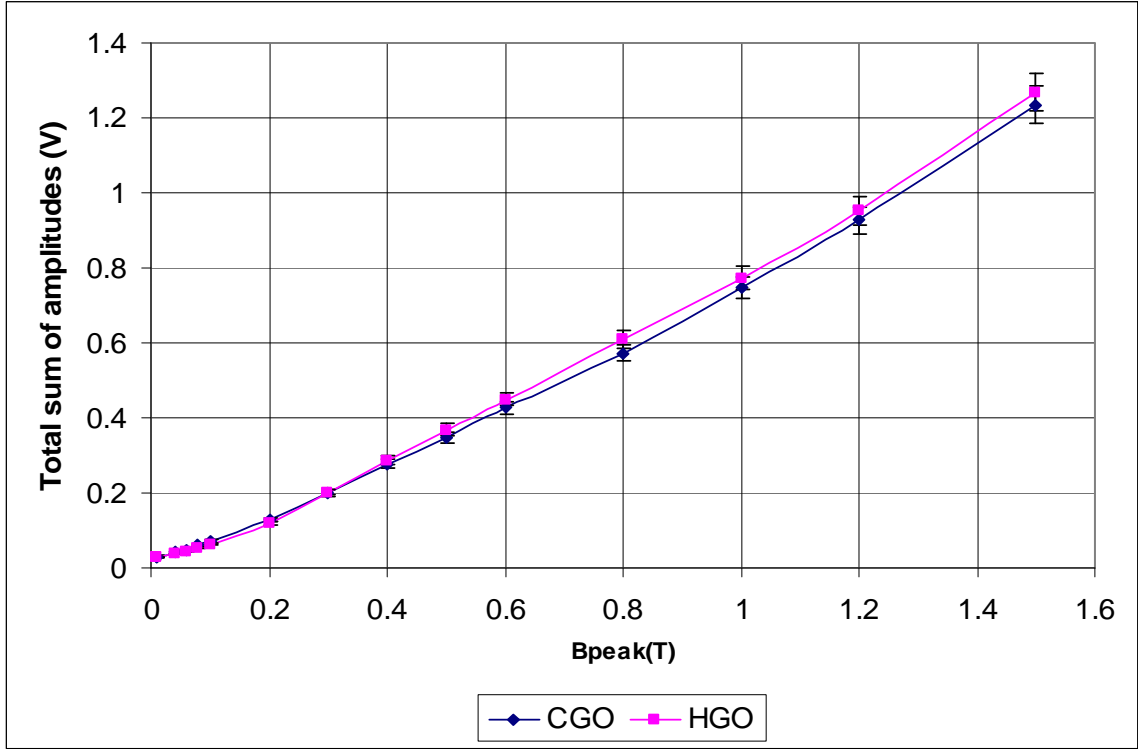
(a)
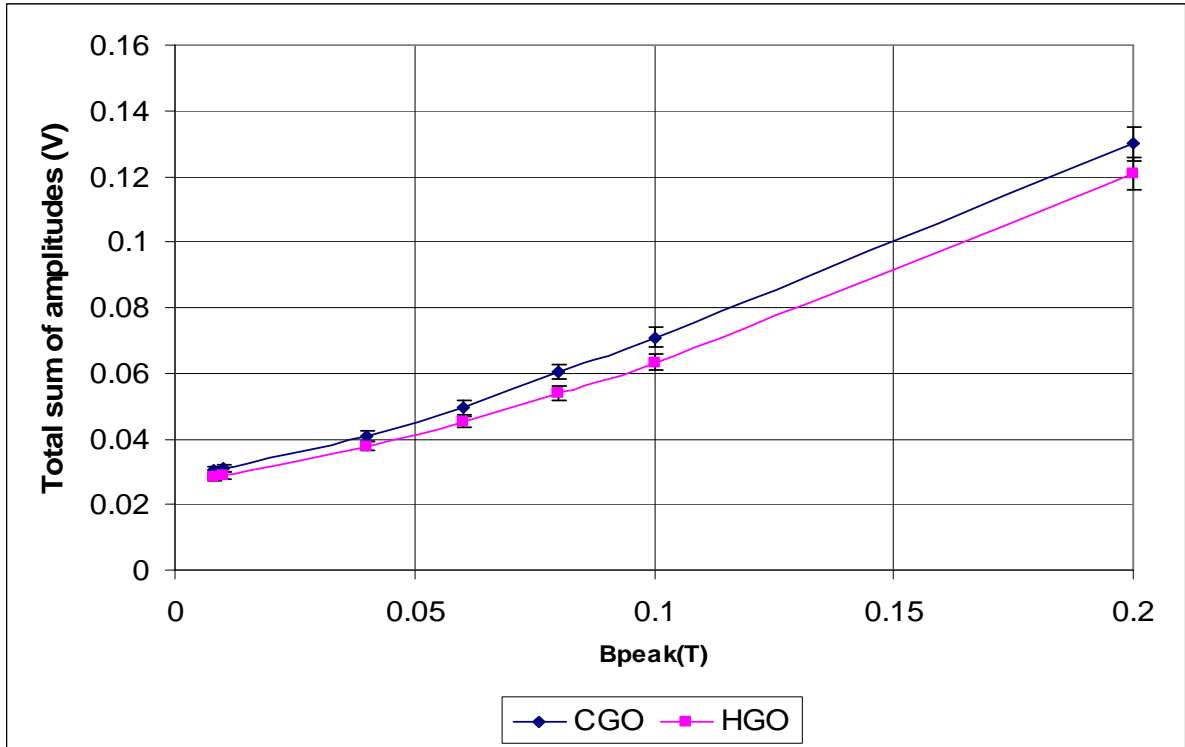
(b)

Fig.6.15: (a) Variation of average TSA of 20 strips each of CGO and HGO from P2 with peak flux density (b) the same comparison in the low field regime.
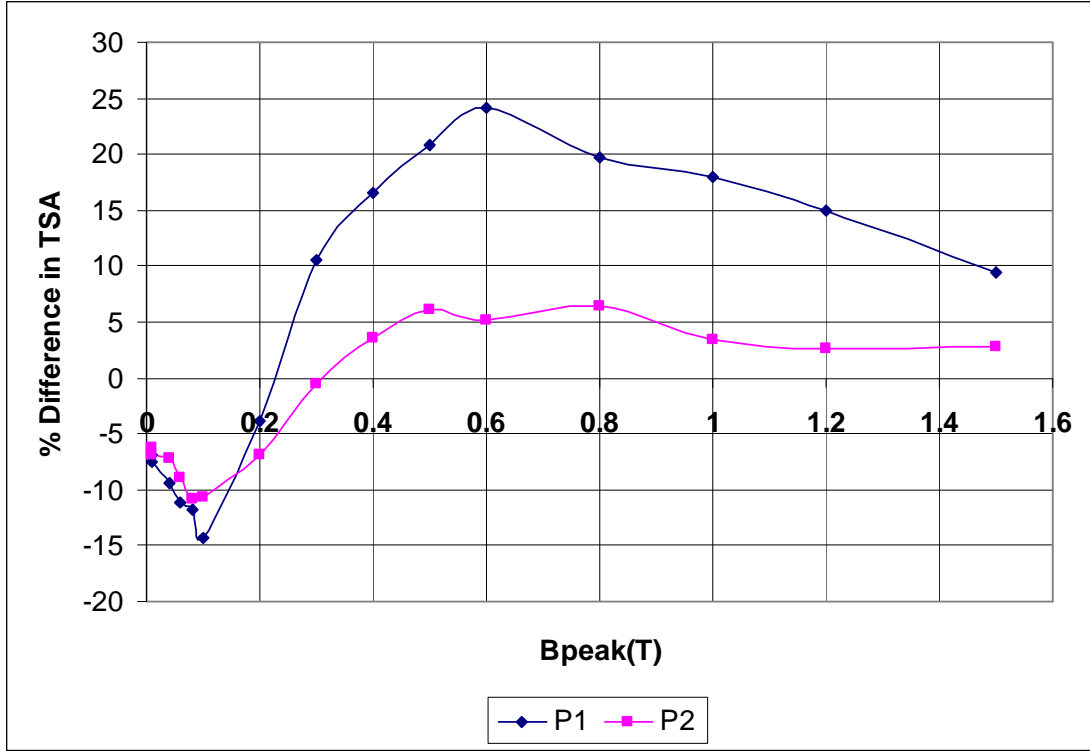
Fig. 6.16: Variation of percentage difference of average TSA of HGO and CGO from P2 with peak flux density.

The BN amplitude of HGO is higher than that of CGO at high flux densities but the trend changes at lower flux densities as shown in all the presented results. As figures 6.13 and 6.16 show, it is interesting that below 0.2 T, the percentage difference in average rms BN of the test samples from P1 and P2 , and that of the average TSA respectively are very similar but at high flux densities, they are far different. This is because domain wall activity is higher at high flux densities so the effects of the difference in microstructure of the samples which account for BN will be more pronounced than at low field regime.

The observed higher BN response in terms of average rms and average TSA of HGO over CGO at higher flux densities in this work is because the grain size of HGO is higher than that of CGO and also grain to grain misorientation in CGO is higher than that of HGO. The domain width in 3% Si-Fe increased with increasing grain size as illustrated in section 8.2. Increased grain size means that domain walls will move further between pinning sites and thereby generate larger changes in magnetization which results in a larger BN signal amplitude.

Secondly, the grain-grain misorientation which is higher in CGO [6.9, 6.10] results in strong depression of the BN level which is caused by a decrease in the instantaneous rate of change of the magnetic flux during Barkhausen jumps, because of increased demagnetizing effects.

Similar results were found at high flux densities in decarburised steel [6.1], carbon steel [6.11], high purity iron [6.12] and grain oriented electrical steel from Nippon Steel Corporation and Pohang Steel Corporation [6.2]. The reason advanced in [6.2] for the lower BN amplitude of CGO compared to HGO is the larger energy loss in CGO due to domain nucleation and annihilation.

However, contradictory result was obtained [6.13] when the BN was measured at 50 Hz and peak flux densities of 0.5 T- 1.4 T in 3 Epstein sized samples comprising of 0.27 mm thick HGO with average grain size of 13 mm, 0.27 mm thick CGO with average grain size of 8 mm, and 0.20 mm thick, 0.1 % silicon NGO with average grain size of 100μm. The investigation showed that the BN amplitude is higher for the material with a smaller grain size.

This apparent contradiction suggests that the BN process is more complex and the results might be associated with materials having different densities of pinning sites, precipitates , grain boundaries, etc possibly higher in smaller grain materials.

BN measurement has not been carried out at low flux densities (below 0.1 T) before. At low fields, domain wall motion has an intermittent, jerky character, with sparse Barkhausen jumps. The implication of this is that smaller grain samples (CGO) which have more grain boundaries acting as pinning sites and hence large fractional volume than HGO will have a greater number of these sparse Barkhausen jumps which will sum up to higher Barkhausen noise amplitude. This explains why at low flux density, the BN amplitude is higher in CGO material. This investigation shows that in comparing CGO and HGO, BN amplitude changes trend at high and low flux densities.

References to chapter 6

[6.1] R. Ranjan, D. C. Jiles and P. K. Rastogi, Magnetic properties of decarburized steels: An investigation of the effects of grain size and carbon content, IEEE Transactions on Magnetics, Vol. 23 , No. 3, pp.1869-1876, 1987.

[6.2] D. G. Hwang, H.C. Kim, C. G. Kim, K.A Lee, Barkhausen noise and magnetic properties of highly grain-oriented HiB-8 and conventional 3% Si-Fe polycrystalline specimens, Journal of Korean Physical Society, Vol. 24, No.6, pp. 493-498, 1991.

[6.3] International Electrotechnical Commission (IEC) Standard 6044-1, 1996.

[6.4] T. Kutrowski, Characterisation of metering transformer cores, PhD thesis, Cardiff University (to be submitted, 2012).

[6.5] J. W. Shilling and G.L.Jr. House, Magnetic properties and domain structure in grain-oriented 3% Si-Fe, IEEE Transactions on Magnetics, Vol. 10, No. 2, 195-222, 1974.

[6.6] S. Turner, A. Moses, J. Hall and K. Jenkins, The effect of precipitate size on magnetic domain behaviour in grain-oriented electrical steels, Journal of Applied Physics, Vol.107, issue 3, pp. 307-309, 2010.

[6.7] H.V. Patel, S. Zurek, T. Meydan, D.C Jiles and L. LI, A new adaptive automated feedback system for Barkhausen signal measurement, Sensors and Actuators A , Vol. 129, pp.112-117, 2006.

[6.8] K. Hartmann, Relationships between Barkhausen noise, power loss and Magnetostriction in Grain-oriented silicon iron, PhD thesis, Cardiff University, March 2003.

[6.9] S. Taguchi, A. Sakakura and H. Takashima, US Patent 3287183, 1966.

[6.10] M. F. Littmann, Structures and magnetic properties of grain oriented 3.2% silicon-iron, Journal of Applied Physics, Vol. 38, issue 3, pp. 1104-1108, 1967.

[6.11] H. Sakamoto, M. Okada and M. Homma, Theoretical analysis of Barkhausen noise in carbon steel, IEEE Transactions on Magnetics, Vol. 23 No.5, pp. 2236-2238, 1987.

[6.12] J. Degaulque, B. Astie, J. L. Porteseil and R Vergne, Predictions of the random potential energy models of domain wall motion, An experimental investigation of high purity iron, Journal of Magnetism and Magnetic Materials, Vol. 128, issue 1-2, pp. 149-153, 1982.

[6.13] K. Hartmann, A.J. Moses and T. Meydan, A system for measurement of AC Barkhausen noise in electrical steels, Journal of Magnetism and Magnetic Materials Vol. 254–255, pp. 318–320, 2003.

Chapter 7   Effect of Domain Refinement on Barkhausen Noise and Magnetic Properties of Grain Oriented Steel

7.1   Introduction

Domain refinement is an effective technique for reducing power loss in highly grain oriented (HGO) electrical steel. It can be accomplished by scribing scratch lines on one surface transverse to the rolling direction of the steel. In this part of the investigation, one surface of each of ten HGO samples from Cogent Power Limited, United Kingdom was mechanically scribed by using a ball pen at 5 mm intervals transverse to the rolling direction. Further domain refinement was carried out on 3 samples of HGO with very large grains of average diameter of 20 mm. Domain scribing was carried out at intervals of 16 mm, 8 mm and 4 mm respectively transverse to the rolling direction. Firstly, BN was measured on the strips without scribing and then subsequently measured after each scribing. The relative permeability, coercivity and power loss of the test samples were also measured. Experimental measurement results at high and low flux densities are also presented and discussed.

An average of 3 measurements made on every strip was used in analysing the result. Between repeatability measurements each sample was removed and then re-inserted into the test system. The percentage difference of the measured properties was quantified using equation 6.1. The actual difference could be positive or negative depending on the values of the measured parameters under consideration.

7.2   Effect of domain scribing on Barkhausen Noise of HGO

 Figure 7.1 shows domain patterns observed on surfaces of an unscribed and scribed strip using magnetic domain viewer. The vertical lines in figure 7.1(b) introduced by scribing acts as additional pinning sites. Figure 7.2 shows the variation of average rms BN of the HGO and domain scribed HGO samples from P1 with peak flux density. It is observed that the BN amplitude is higher in HGO without scribing than in HGO

with scribing at high flux densities but the trend changes at lower flux densities. The variation of the percentage difference in average rms BN of the HGO with and without scribing at different flux densities is shown in figure AC 1 in Appendix C.

Figure 7.3 shows the variation of the average TSA of the tested samples with peak flux density. Similar relationship was found as with the rms BN. The percentage difference in average TSA of the samples with peak flux density is shown in figure AC 2.
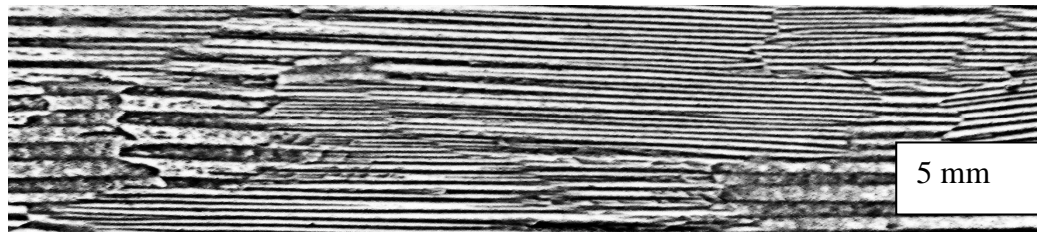
(a)
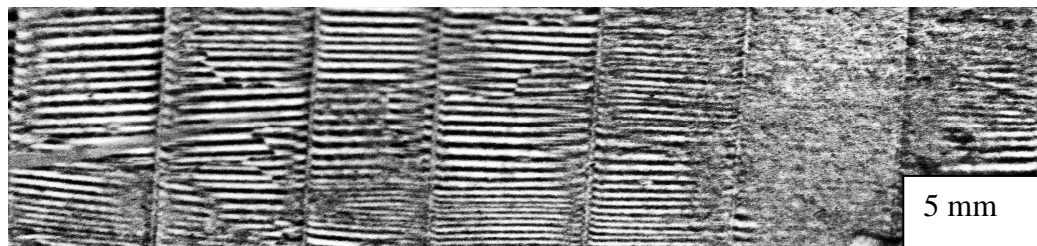
(b)

Fig. 7.1: Static domain patterns observed on surfaces of (a) unscribed (b) scribed strips (5mm scribing interval) of HGO.
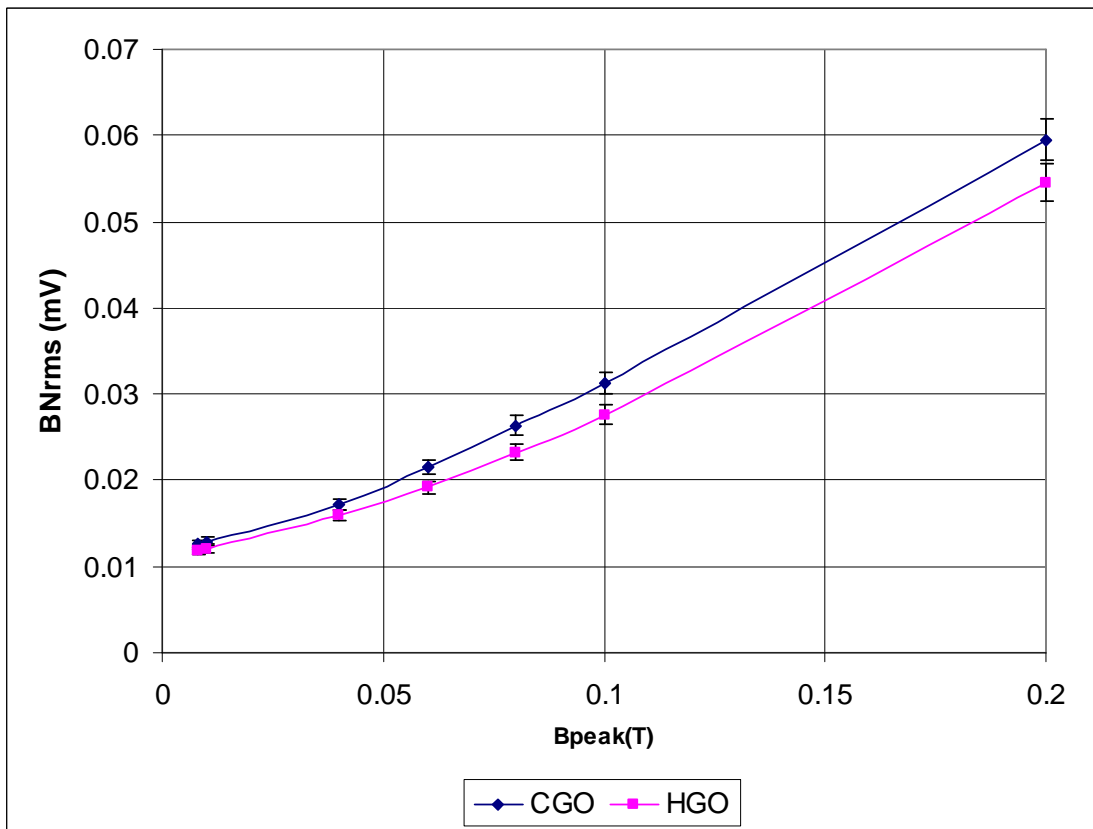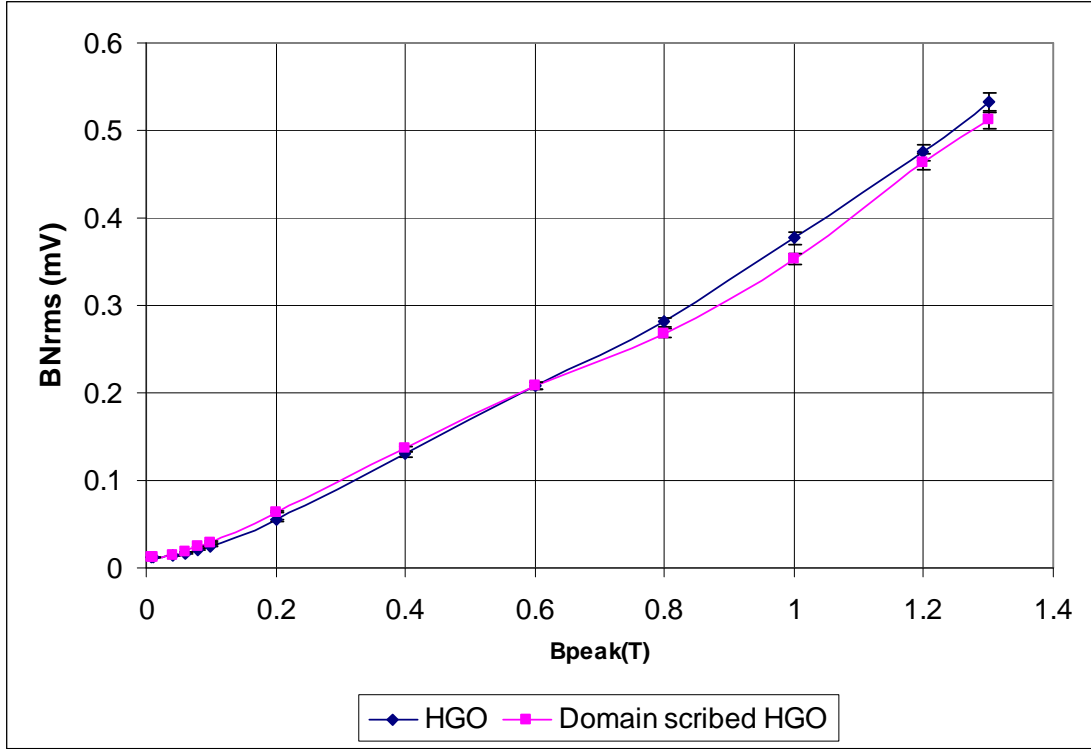
(a)
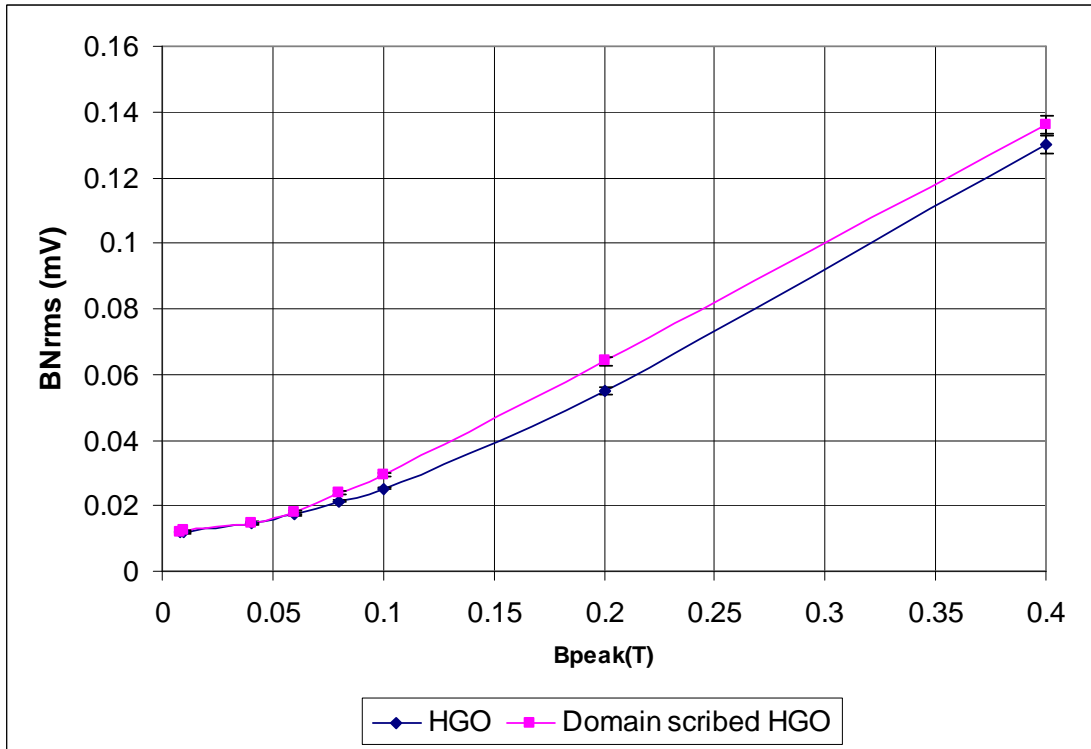
(b)

Fig. 7.2: (a) Variation of average rms BN of 10 strips each of HGO and Domain-scribed HGO from P1 with peak flux density (b) Comparison in the low field regime.
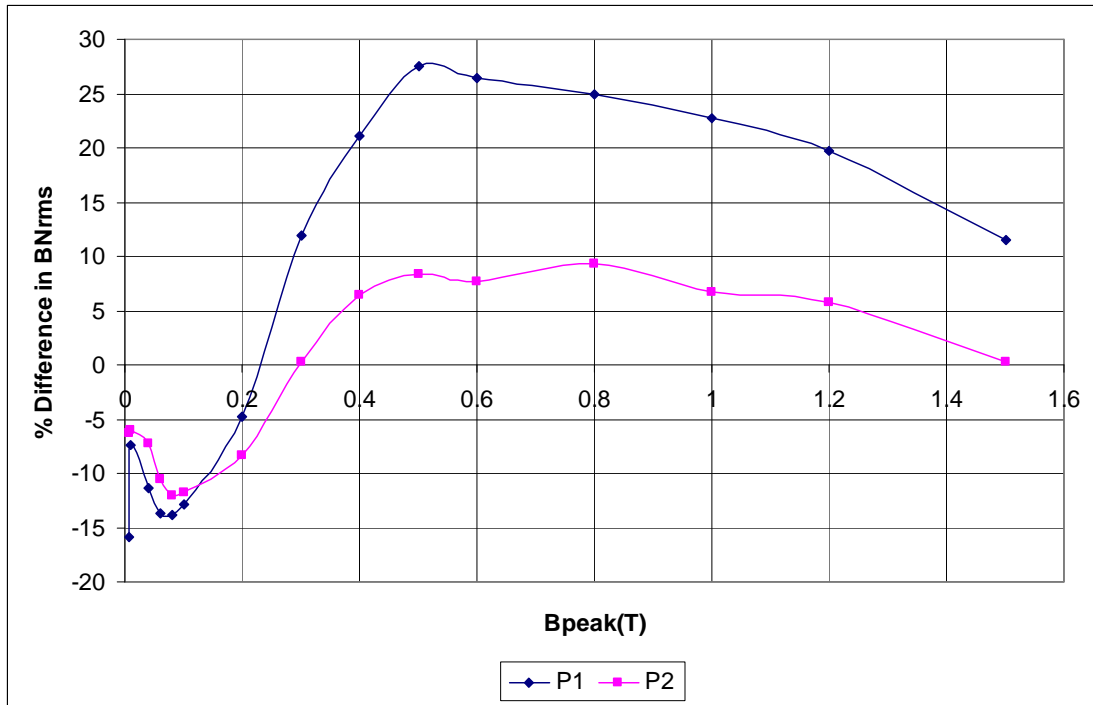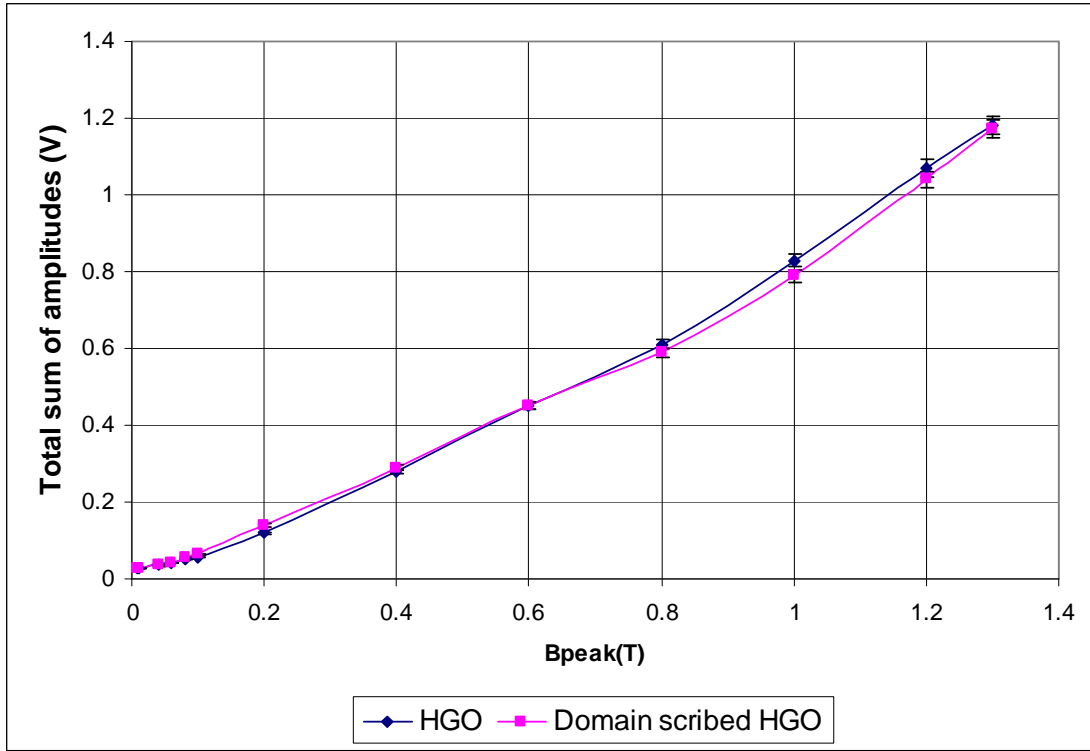
(a)
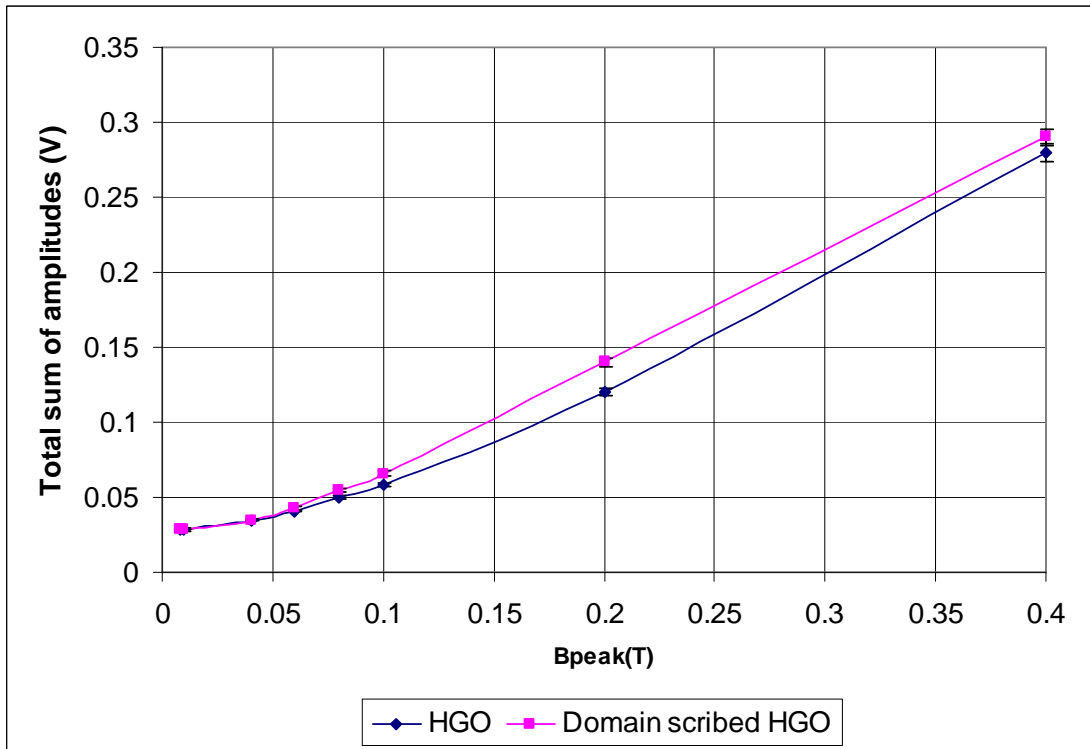
(b)

Fig. 7.3: (a) Variation of average TSA of 10 strips each of HGO and Domain- scribed
HGO with peak flux density from P1 (b) Comparison in the low field regime.

The variation of average rms BN of the HGO with very large grains at different flux densities is shown in figure 7.4. Figure AC 3 shows the variation of percentage difference in average rms BN between HGO without scribing and HGO domain scribed at 16 mm, 8 mm and 4 mm intervals respectively with flux density. The variation of percentage difference in average rms BN between HGO domain scribed at 16 mm and 8 mm; 16 mm and 4 mm; and 8 mm and 4 mm intervals respectively with flux density is shown in figure AC 4.

The average TSA of the same BN signals were also evaluated. Figure 7.5 shows the variation of average TSA of 3 strips each of HGO without scribing and domain-scribed HGO at the different intervals at both high and low field regimes. The percentage difference in average TSA between the test samples is also quantified in figure AC 5. Furthermore, figure AC 6 shows the variation of percentage difference in average TSA between HGO domain scribed at 16 mm and 8 mm; 16 mm and 4 mm; and 8 mm and 4 mm intervals respectively with flux density.
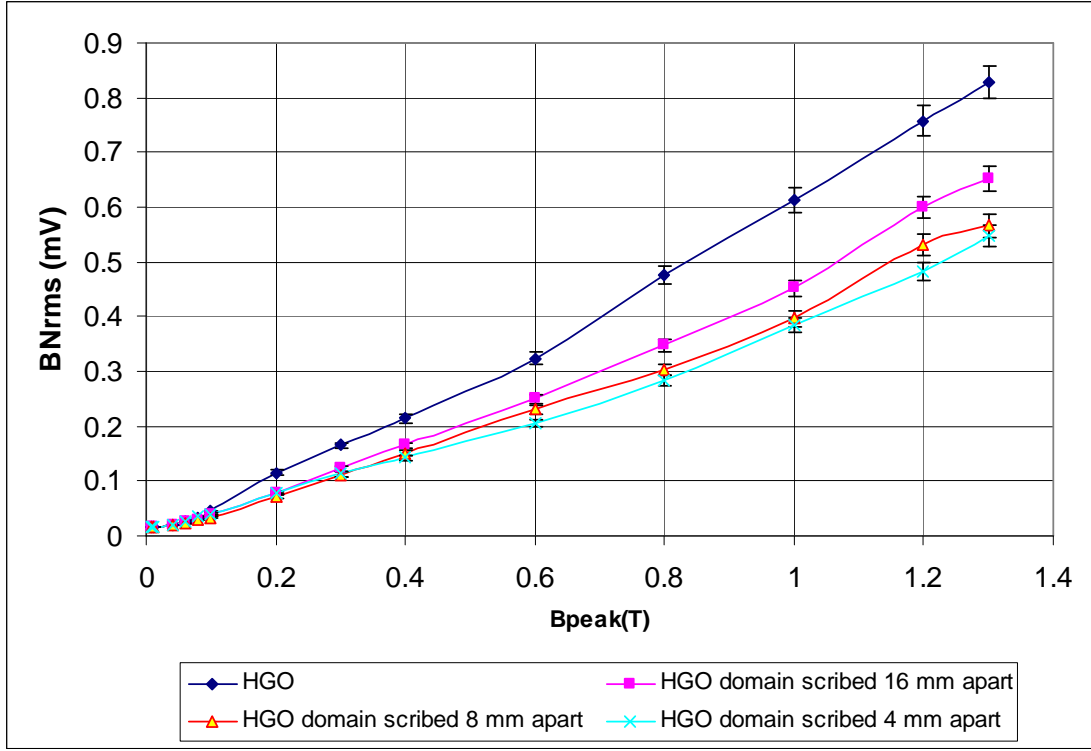
(a)
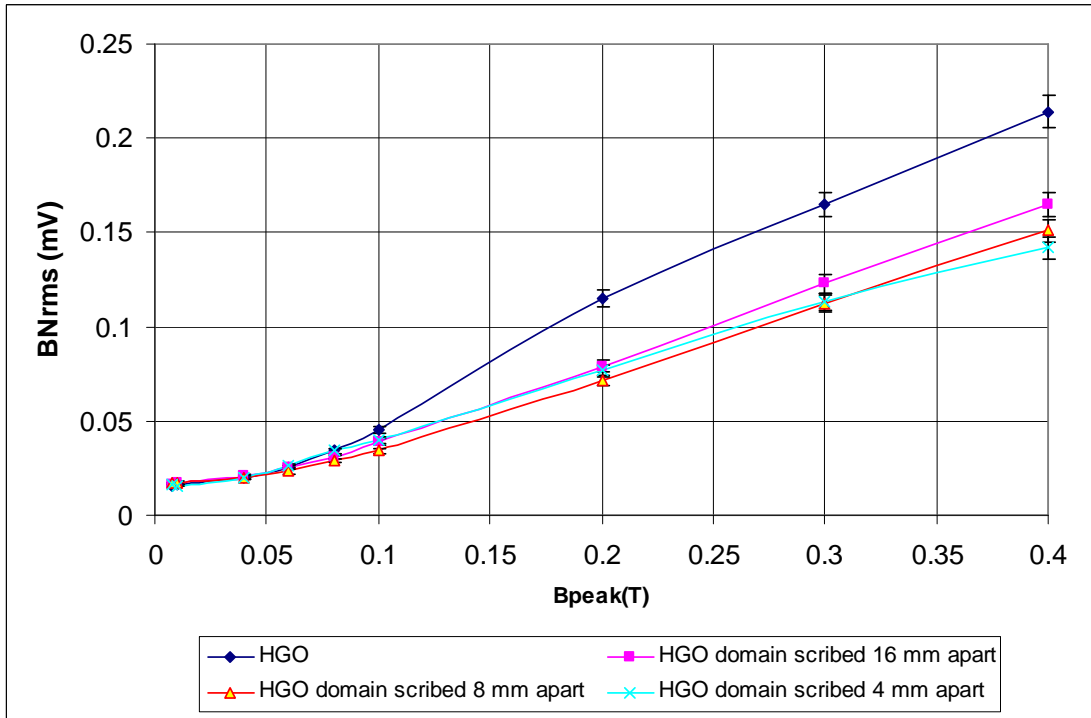
(b)

Fig. 7.4: (a) Variation of average rms BN of 3 strips each of HGO and Domain-scribed HGO with peak flux density (b) Comparison in the lower field regime.
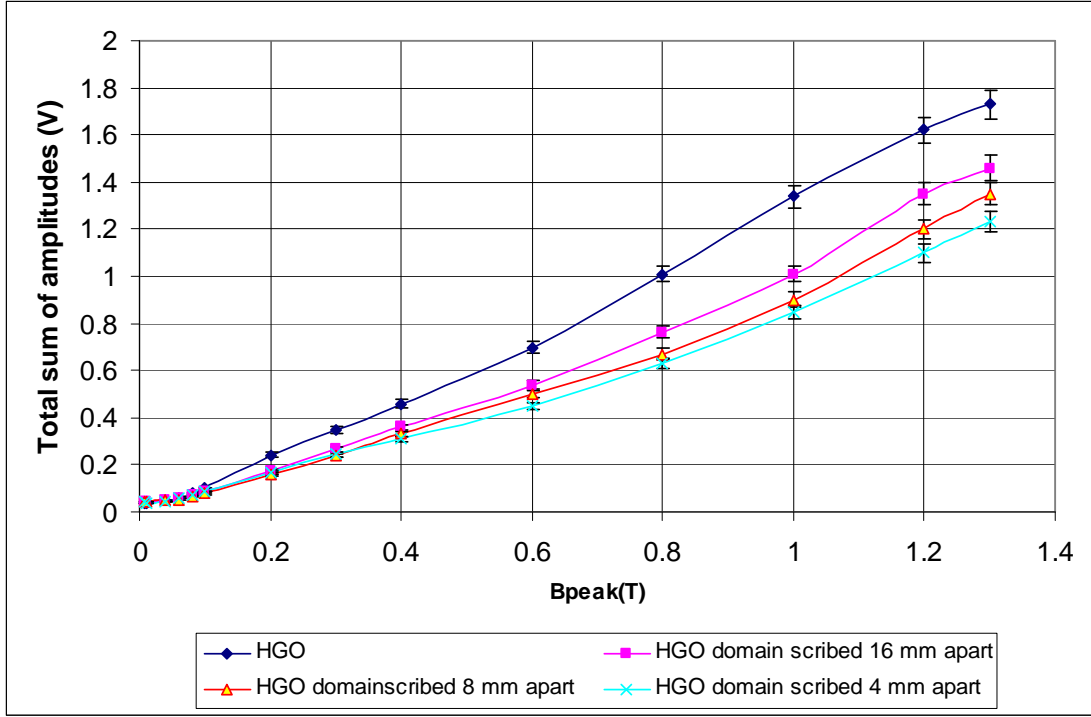
(a)
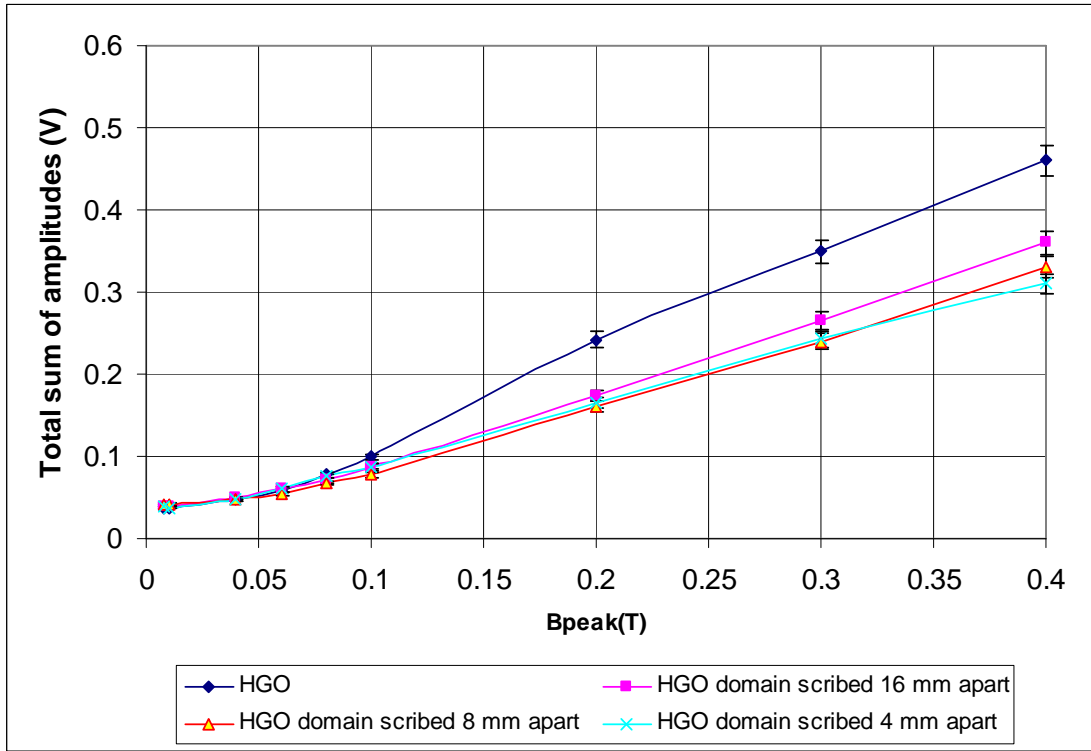
(b)

Fig. 7.5:(a) Variation of average TSA of BN of 3 strips each of unscribed HGO and domain-scribed HGO with peak flux density (b) Comparison in the lower field regime.

The average rms BN and TSA were observed to increase as the grain size and the scribed intervals increases especially at high flux densities. When the 16 mm interval domain scribed samples were compared with the samples without scribing, the average rms BN was found to be higher in the samples without scribing. The percentage difference is highest at 0.2 T being 46 % and having a change in trend at 0.06 T. The average TSA between these two sets of samples have similar trend. The highest percentage difference occurred at 0.2 T with a value of 39 %. However, a change in trend occurs at 0.06 T.

Analysis of the average TSA of BN in the 8 mm intervals samples and the samples without scribing show the highest percentage difference occurring at 0.8 T with a value of 51 % and having a crossover occurring at 0.01 T. The percentage difference in the rms parameter was highest at 0.2 T with a value of 61 % and having a cross over at 0.01 T.

The percentage difference in average TSA of BN between the samples domain scribed at 4 mm and the samples without scribing was highest at 0.8 T with a value of 60 % and lowest at 0.01 T with no percentage difference. Changes in trend occurred at 0.06 T and 0.008 T. Similarly, the percentage difference in average rms BN is highest at 0.8 T with a value of 69 % and lowest at 0.01 T with a value 0f 0.6 % and having cross overs at 0.08 T and 0.008 T.

Between the samples with 8 mm and 16 mm domain scribed intervals, the highest percentage difference in average TSA occurred at 0.1 T with a value of 13 % and having a cross over at 0.01 T. The highest percentage difference in average rms BN occurred at 1.3 T with a value of 15 % and a change in trend similarly occurring at 0.1 T.

For the 4 mm and 16 mm scribed samples, the percentage difference in average TSA of BN was highest at 1.2 T with a value of 23 % and recording no increase at 0.06 T and 0.008 T. For the average rms BN, the highest percentage difference similarly occurred at 1.2 T with a value of 24 % but the crossover occurred at 0.1 T and again at 0.04 T.

Samples with scribed intervals of 4 mm and 8 mm were also analysed. The highest percentage difference in average TSA occurred at 0.6 T with a value of 11 % and crossovers occurred at 0.3 T and 0.04 T. On the other hand, the highest percentage difference in average rms BN is 10 % at 1.2 T. There are crossovers at 0.3 and 0.06 T.

Scribing introduced local strain to the HGO samples resulting in stress by reducing the spike domain population and the 180° domain wall spacing thereby limiting the mean free path of domain walls. Also scribing which leads to domain refinement causes the number of walls which move effectively under alternating field to increase and the velocity of an individual wall in a constant flux density to decrease thereby reducing BN amplitude. Scribing breaks spatial correlation between jumps [7.1]. The multiple changes of trend at low flux densities is probably because of low domain wall activity and the fact that hysteresis processes dominate at low field magnetisation.

This higher BN amplitude as the grain size/scribed interval increases is attributed to the higher mean free path of domain wall movement which leads to higher rate of change of magnetisation. There is no definite trend between BN and grain size/scribed interval below 0.4 T which is thought to be because of reduced domain wall activity and the fact that hysteresis processes dominate at low field regime.

7.3 Effect of domain scribing on the magnetic properties of HGO

The variation of average relative permeability of the HGO with very large grains at different peak flux densities is shown in figure 7.6. Figure AC 7 shows the variation of percentage difference in average relative permeability between HGO without scribing and HGO domain scribed at 16 mm, 8 mm and 4 mm intervals respectively with peak flux density while the variation of percentage difference between HGO domain scribed at 16 mm and 8 mm; 16 mm and 4 mm; and 8 mm and 4 mm intervals respectively with peak flux density is shown in figure AC 8. The relationship between the average coercivity of the test samples at different flux densities is shown in figure 7.7 while the variation of the percentage difference in their average coercivities are shown in figures AC 9 and AC 10. The variation of the average power loss of the same test samples at different peak flux densities is shown in figure 7.8. Figures AC 11 and AC 12 show the variation of their percentage differences.
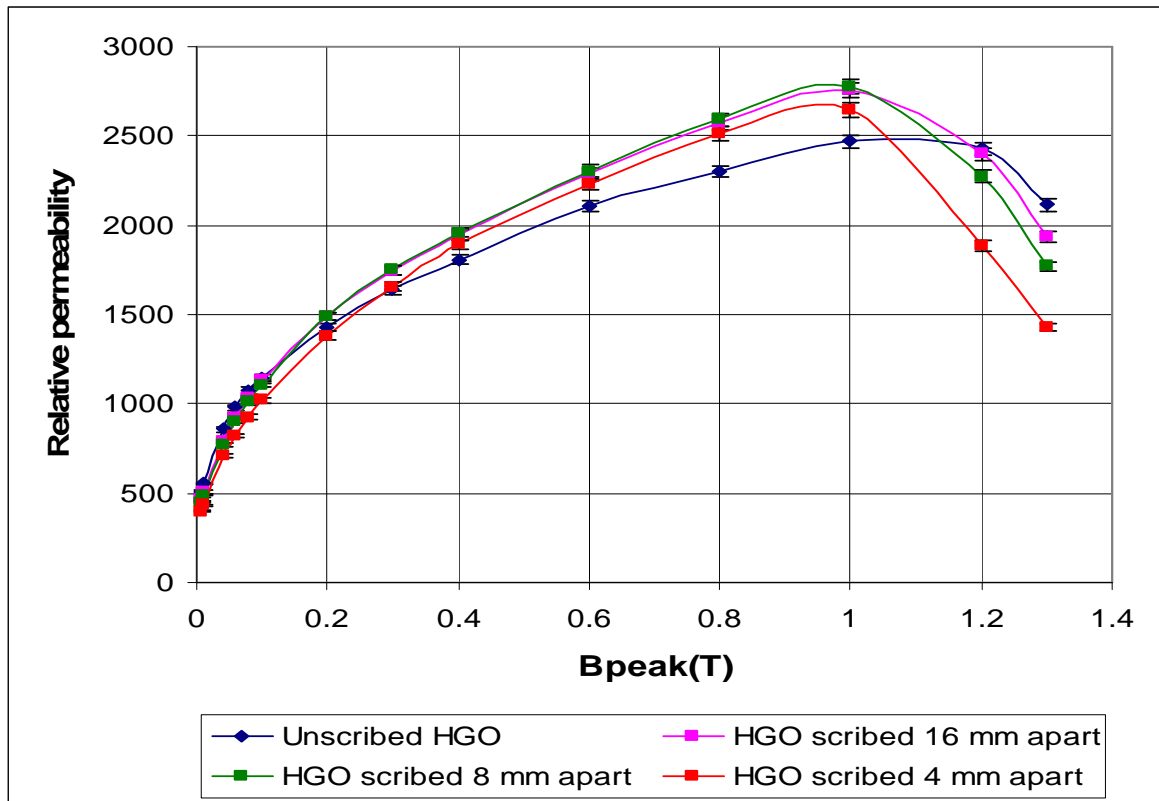
Fig. 7.6: Variation of average relative permeability of 3 strips each of unscribed HGO and domain- scribed HGO with peak flux density.
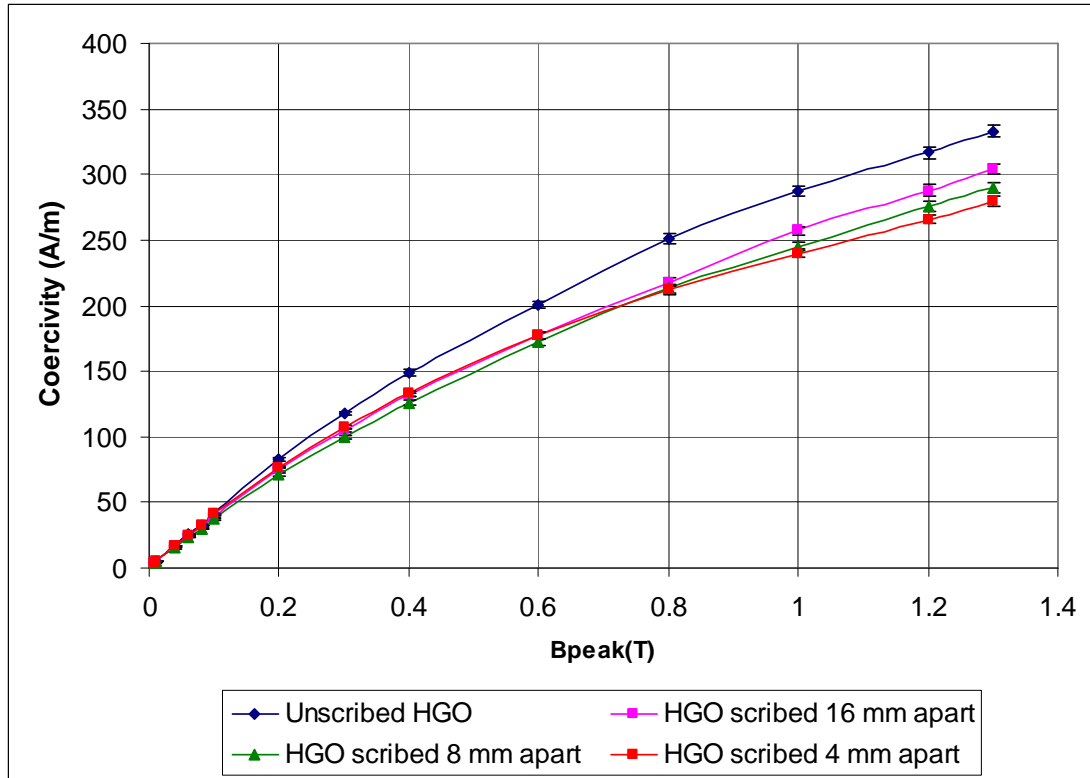
Fig. 7.7: Variation of coercivity of 3 strips each of unscribed HGO and domain-scribed HGO with peak flux density.
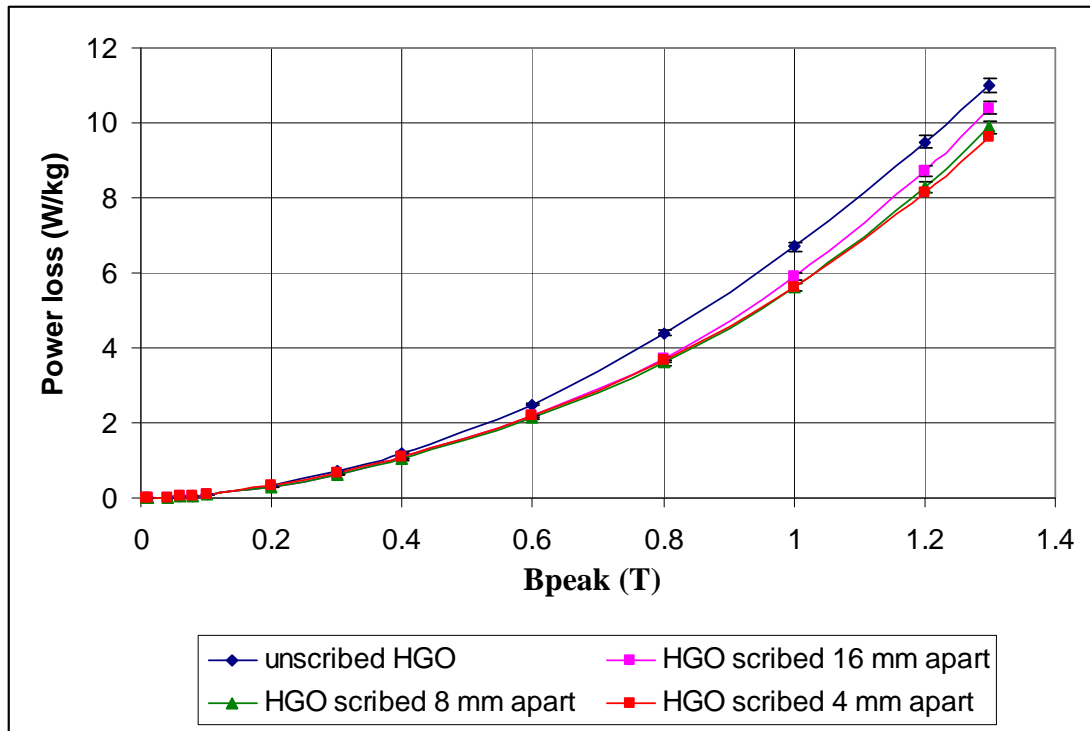
Fig. 7.8: Variation of average power loss of 3 strips each of unscribed HGO and domain- scribed HGO with peak flux density.

The percentage differences between the average relative permeability of test samples at different flux densities are quantified and plotted in figures AC 7 and AC 8. For the unscribed HGO, scribed HGO at 16 mm interval and the scribed HGO at 8 mm interval, the average relative permeability follow almost a particular trend. It increases with increasing grain size/scribe interval above 1.0 T. From 0.3 T -1.0 T, it decreases with increasing grain size/scribe interval but the trend reverses from 0.008 T-0.1 T. At 0.2 T, the average relative permeability is highest in the 16 mm scribed samples and lowest in the unscribed sample hence there is no definite trend here. 0.2 T is the threshold between low and high flux densities. The trend at 0.3 T – 1.0 T is the expected trend over the range of flux densities because very large grain samples (unscribed HGO and the HGO scribed at 16 mm interval) have high power loss because of large 180° domain wall spacing which lead to increase in anomalous loss. It is at this range of flux densities that irreversible domain wall displacement (maximum domain activity) takes place. The trend above 1.0 T and below 0.2 T is probably because domain rotation and reversible domain wall motion take place respectively in these regions with reduced domain activity. The average relative permeability of the 4 mm scribed samples is the least of all flux densities compared to

the other test samples. This is because the 4 mm scribed sample has a small domain width (compared to the 8 mm scribed sample) with the resultant lower domain wall activity.

The variation of the average coercivity and the average power loss of the test samples at different peak flux densities are shown in figures 7.7 and 7.8 respectively and the quantification of their percentage differences shown from figure AC 9 – AC 10 for coercivity and figures AC 11 – AC 12 for power loss. For the unscribed HGO, scribed HGO at 16 mm interval and scribed HGO at 8 mm interval, the coercivity and the average power loss follow a particular trend at all flux densities. These magnetic properties decrease with decreasing grain size/scribed interval. The reason is because more domain refinement occurs as the scribed interval is reduced which decreases the number of closure domains that contributes to increase in power loss and coercivity. There is no particular trend in the coercivity and power loss of the 4 mm scribed HGO sample in relation to the samples. This investigation shows that very large grains and small grains (4 mm scribed interval) do not have good magnetic properties compared to moderately large grains. This is because very large grain or large interval-scribed sample will have very large domain width so domain walls will have freer path to move thus generating more power loss in the process. The small interval-scribed sample will have a lot of stress lines which impedes domain wall motion.

Reference to chapter 7

[7.1] T.W. Krause, L. Clapham, A. Pattantyus and D.L. Atherton, Investigation of the stress dependent magnetic easy axis in steel using magnetic Barkhausen noise , J. Appl. Phys. Vol. 79, No.8, pp. 4242-4252, 1996.

Chapter 8   Effect of Surface Coating and External Stress on Barkhausen Noise of Grain Oriented Electrical Steel

8.1   Introduction

Grain-oriented electrical steel has an insulating surface coating which provides a beneficial stress in the steel. BN is sensitive to changes in the surface condition of steels because magnetic properties of the material are closely linked to stress via magnetoelastic coupling [8.1]. BN measurements have been carried out on strips of HGO and CGO 3% silicon steels from Cogent Power Limited, United Kingdom, at 50 Hz in the peak flux density range 8.0 mT to 1.0 T before and after chemical removal of the coatings. BN was also measured in the decoated samples under external tensile stress. An average of 3 measurements made on every strip was used in analysing the result. Between repeatability measurements each sample was removed and then re-inserted into the test system. The percentage difference of the measured properties was quantified using equation 6.1. The actual difference could be positive or negative depending on the values of the measured parameters under consideration.

The measurement uncertainties at low and high flux densities are shown in tables A12 and A13 respectively.

8.2   Effect of coating stress and external stress on BN of CGO and HGO

Figures 8.1 and 8.2 show typical static domain patterns observed on the surfaces of the coated and decoated CGO and HGO respectively. The coatings were removed by dipping the samples into 36% laboratory grade hydrochloric acid. The centres of the 110 mm x 30 mm, CGO and HGO samples about 30 mm^2 used for the Kerr magneto-optic study were mechanically polished following standard metallurgical preparation technique [8.2]. The final stage was a stress relief anneal under vacuum for 1 h at 810 °C followed by cooling to room temperature at a rate of 15° C per hour. The ends of the samples were screwed to a stressing rig used for domain observation so that tension could be added to the sample as the domains are observed. The tensile stress

was determined using strain gauge attached at the back of the polished samples according to the method described in section 5.3. The average domain width of the samples under investigation increased when decoated and then decreased when the decoated samples were subjected to tensile stress.

The average number of domains in each grain of the coated CGO sample as shown in figure 8.1 (a) is 41 from the dimension given. This computes to 61.5 domains in a 30 mm wide sample giving an average domain width of 0.49 mm. Similarly, in the coated HGO, there are average of 32 domains in each grain of the sample in the given dimension according to figure 8.2 (a). This computes to an average of 48 domains in a 30 mm wide sample resulting in an average domain width 0.63 mm.

For the decoated samples, in CGO, as shown in figure 8.1 (b), there are 8 domains in the 6 mm X 6 mm area observed according to the scale of the Kerr microscope used in the domain observation. This results to an average domain width of about 0.75 mm. For the decoated HGO, as shown in figure 8.2 (b), there are 5 domains in the area observed resulting in the average domain width of 1.2 mm.

For the tensile stressed samples, there are 15 domains in the 6 mm X 6 mm area observed for CGO as shown in figure 8.1 (c) giving an average domain width of 0.4 mm. Tensile stress of 3 MPa was added to the uncoated samples. In the HGO sample as shown in figure 8.2 (c), 10 domains in the same area yields an average domain width of 0.60 mm. All these data are summarised in the bar chart in figure 8.3.
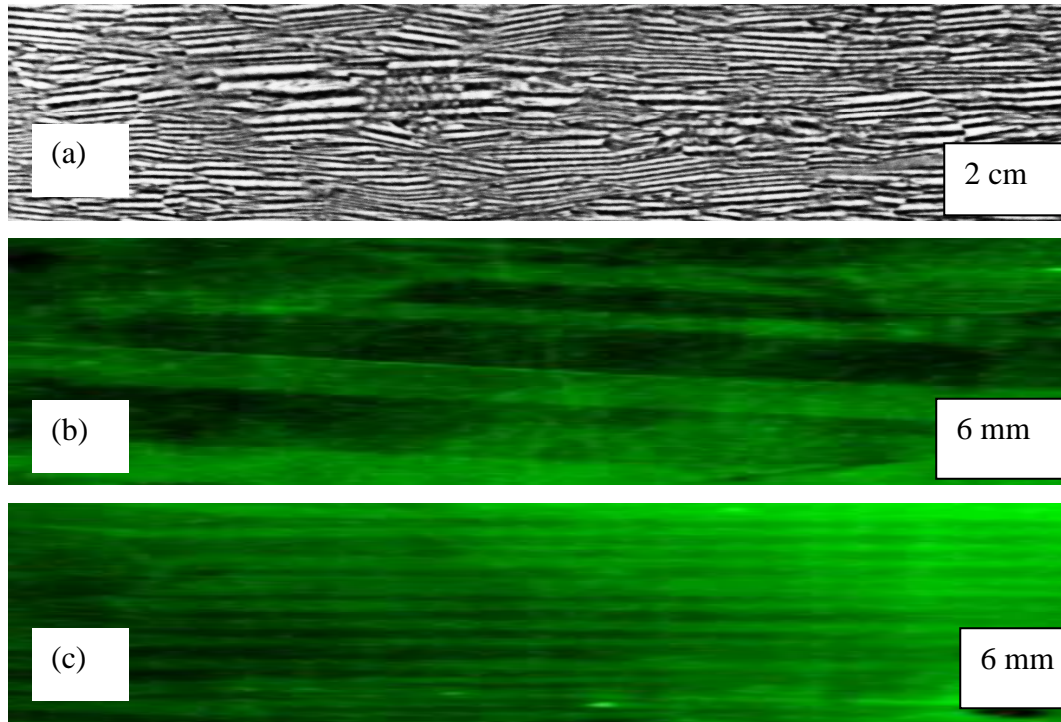
Fig. 8.1: Static domain image of (a) coated CGO using magnetic domain viewer (b) decoated CGO using Kerr Magneto-optic effect showing widening of 180º domains and (c) with tensile stress of 3 MPa applied to the uncoated strip showing narrowing and creation of 180º domains.
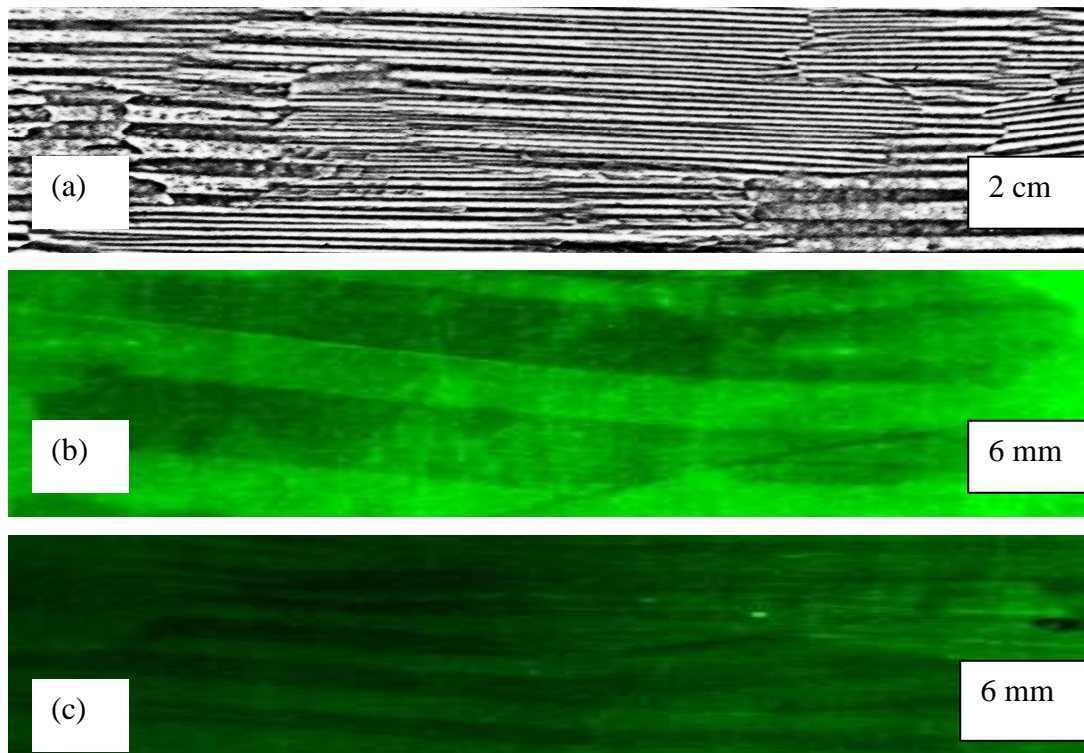
Fig. 8.2: Static domain image of (a) coated HGO using magnetic domain viewer (b) decoated HGO using Kerr Magneto-optic effect showing widening of 180º domains and (c) with tensile stress of 3 MPa applied to the uncoated strip showing narrowing and creation of 180º domains.
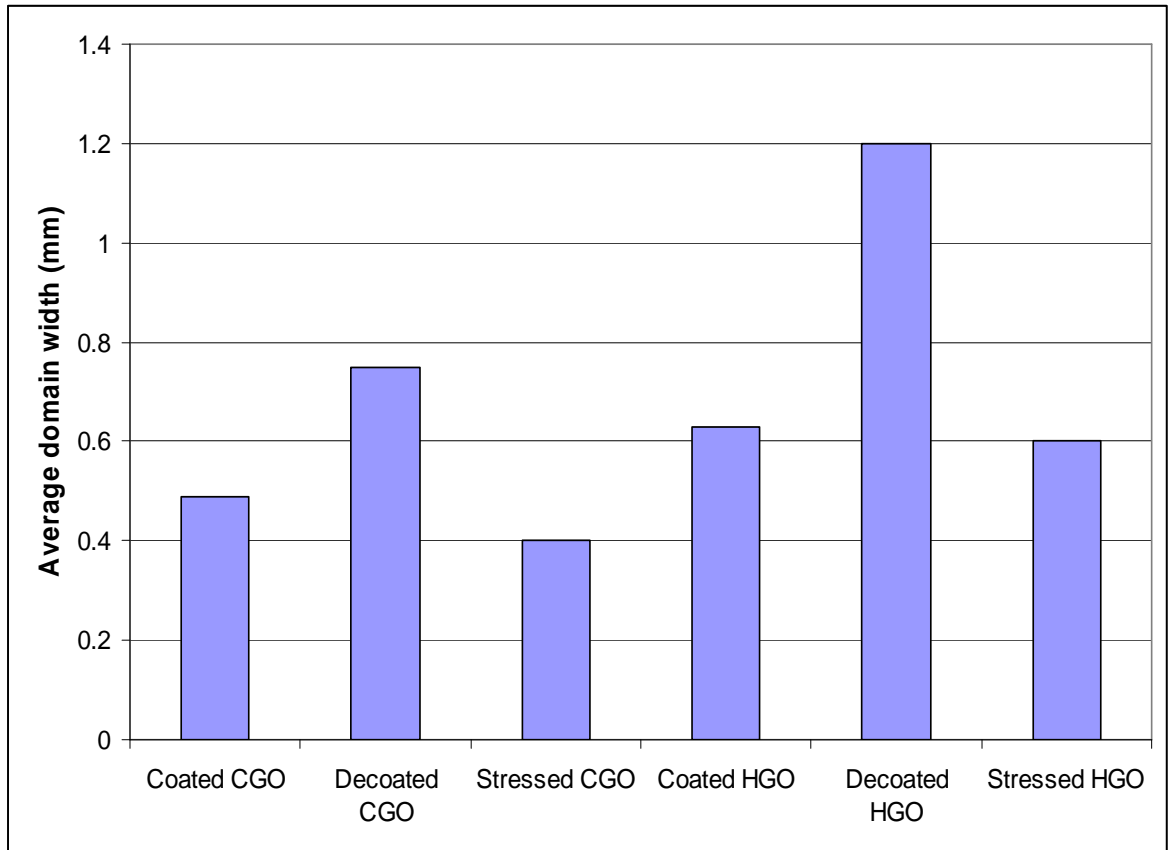
Fig. 8.3: Chart showing average domain width of coated, decoated and stressed-decoated CGO and HGO samples under investigation.

Figures 8.4 and 8.5 show the corresponding variation of average rms BN with peak flux density in the same strips of CGO and HGO respectively before and after coating removal. The samples are the same as the domain viewed samples. The coating removal causes the average rms BN to increase at any flux density in both materials. The percentage increase in average rms BN arising from the coating removal in both CGO and HGO are quantified and plotted in figure 8.6
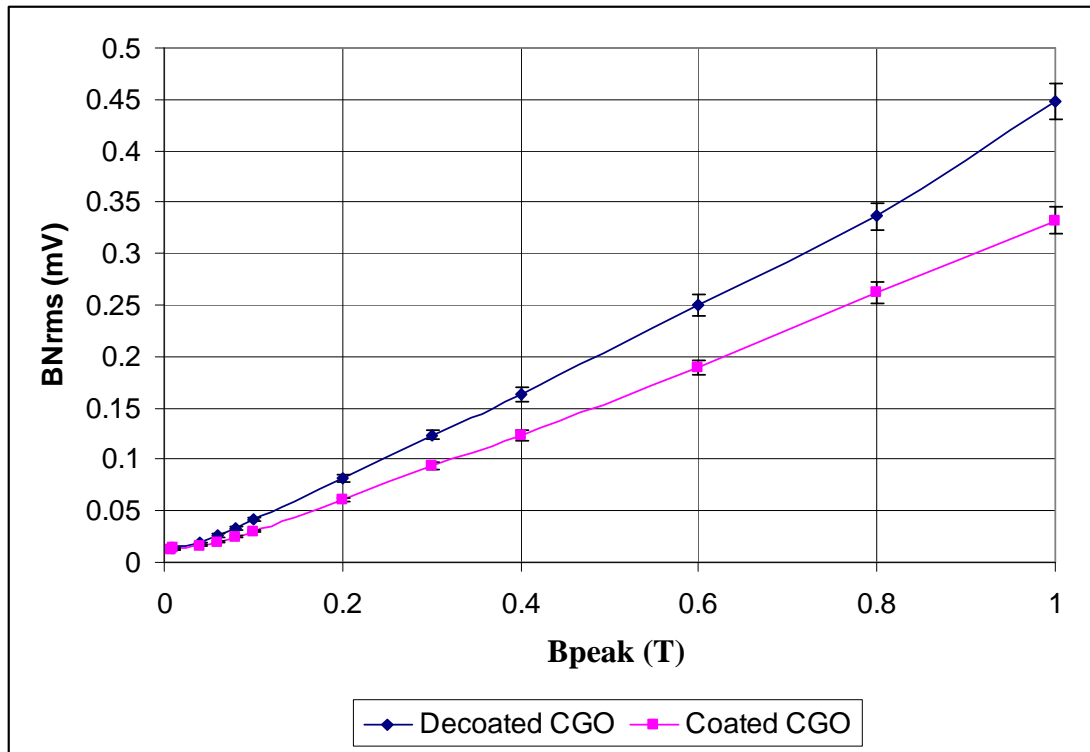
Fig. 8.4: Variation of average rms BN in a strip of CGO before and after decoating with peak flux density.
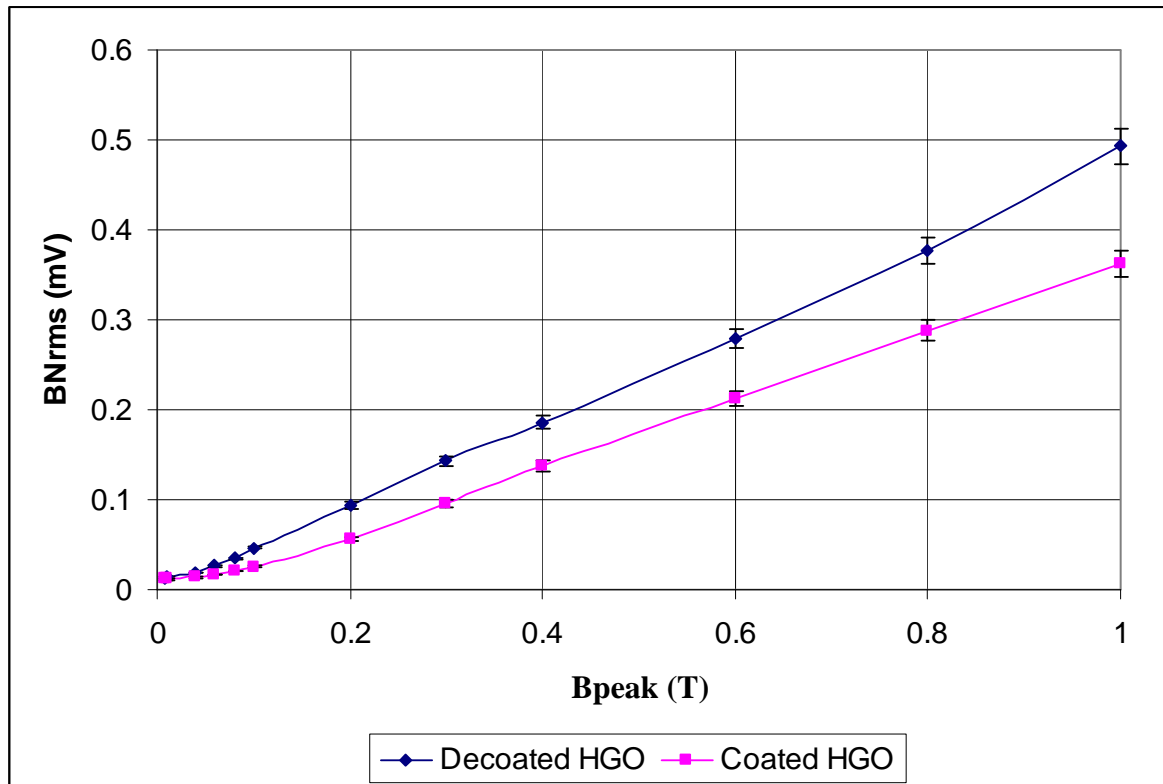
Fig. 8.5: Variation of average rms BN in a strip of CGO before and after decoating with peak flux density.
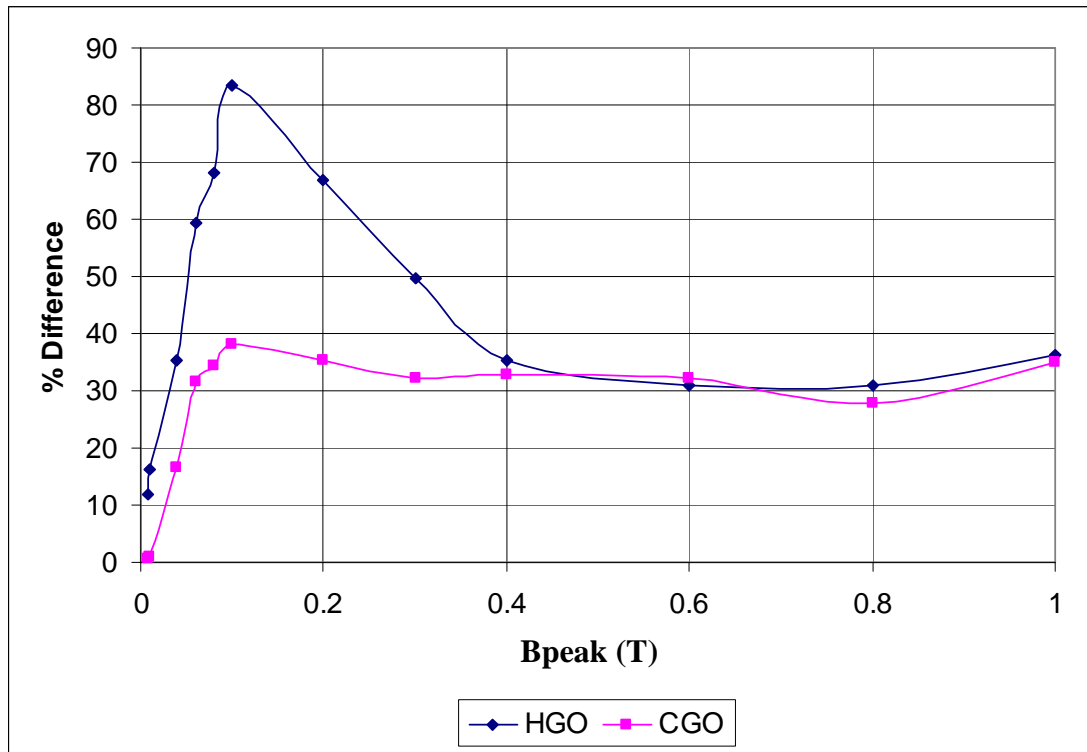
Fig. 8.6: Variation of percentage difference of average rms BN of decoated HGO and coated HGO; and decoated CGO and coated CGO with peak flux density.

Figure 8.7 shows the variation of average rms BN with peak flux densities in coated CGO and coated HGO. It is observed that the average rms BN is higher in HGO than CGO in the coated samples at flux densities above 0.2 T but the trend is opposite at lower flux densities when the rms BN of CGO becomes on average higher than that of HGO. The variation of the percentage difference in average rms BN of both materials with peak flux density is shown in figure 8.8.

Figure 8.9 shows the variation of average rms BN with peak flux density in decoated CGO and decoated HGO. As the graph indicates, the average rms BN of HGO is higher than that of CGO over the full range of peak flux densities. The change in trend observed previously with the coated samples no longer exists fuelling speculation that it is probably caused by the coating stress imparted in the samples during manufacture. The variation of the percentage increase of average rms BN with peak flux density of decoated HGO over decoated CGO is shown in figure 8.10.
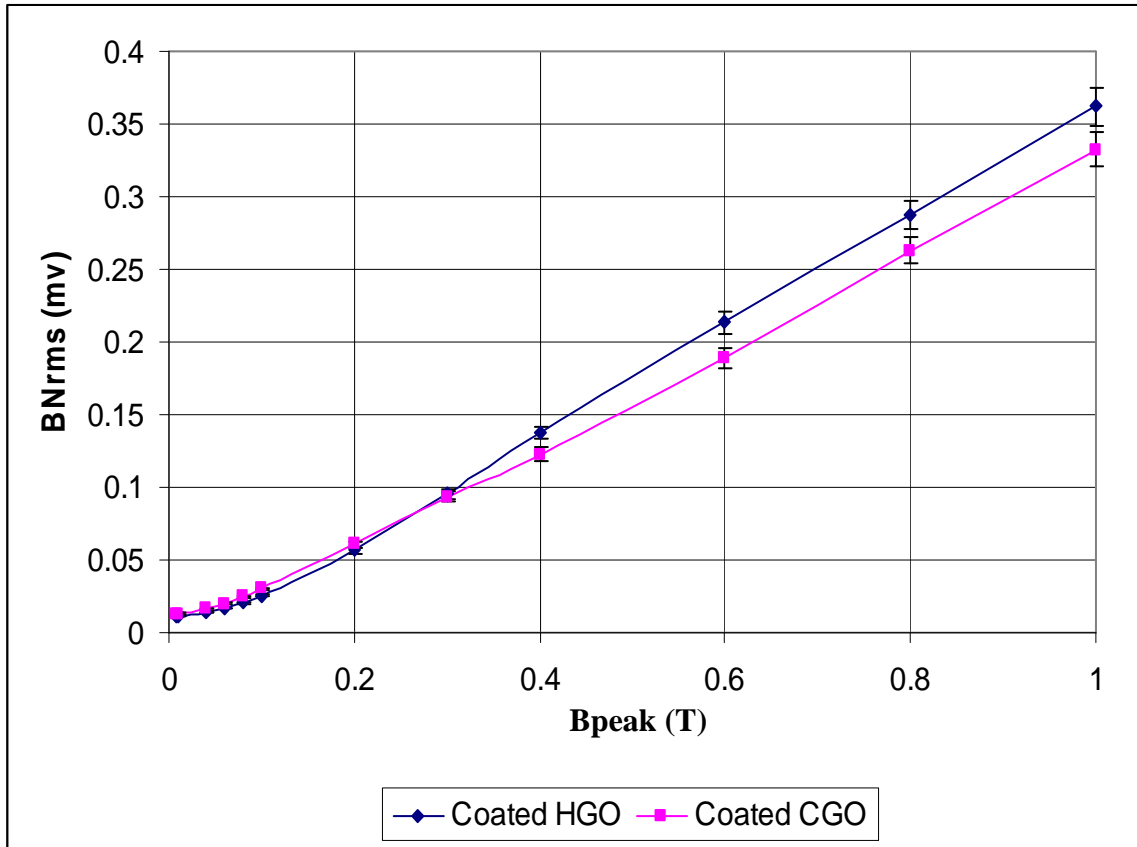
Fig. 8.7: Variation of average rms BN in coated CGO and coated HGO with peak flux density.
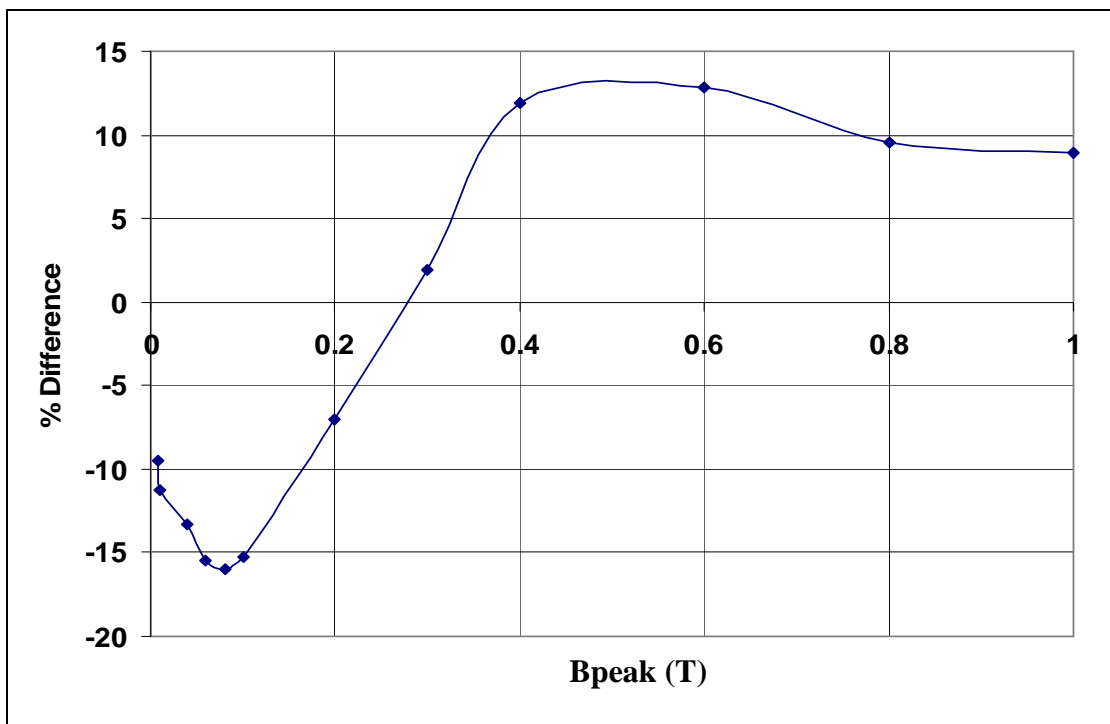
Fig. 8.8: Variation of percentage difference in average rms BN of coated HGO and coated CGO with peak flux density.

112
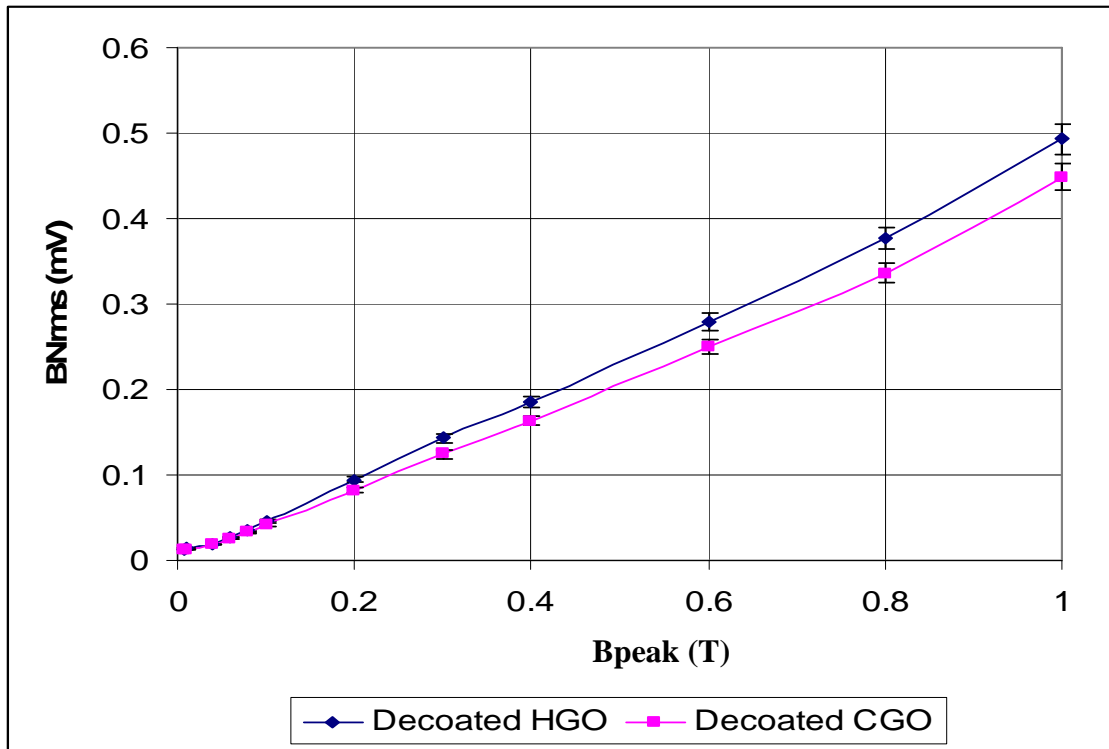
Fig. 8.9: Variation of average rms BN in decoated CGO and decoated HGO with peak flux density.
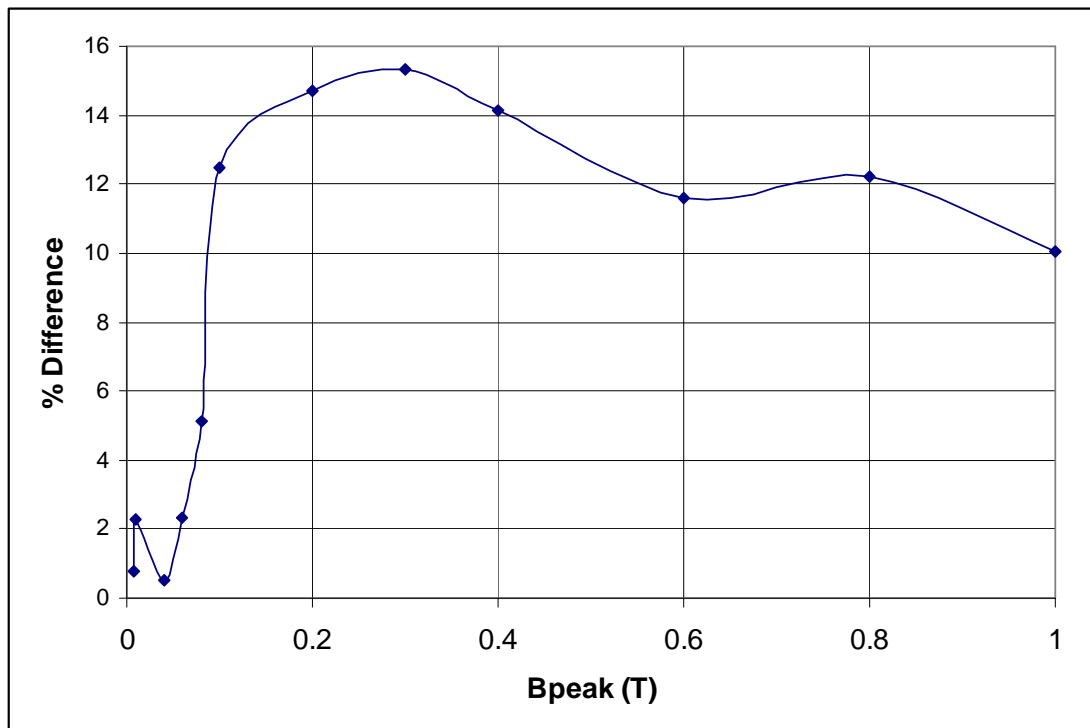
Fig. 8.10: Variation of percentage difference in average rms BN of decoated HGO and decoated CGO with peak flux density.

Between the coated and decoated CGO, according to the data in figure 8.3, the average domain width increased by 53 % while the average rms BN increased by average of 35 % from 0.2 T and above with the highest percentage increase occurring at 0.1 T with 38%.

In HGO, the average domain width increased by 90 % between the coated and the decoated samples while the average rms BN increased by an average of 35 % from 0.4 T and above with the highest percentage increase of 84 % observed at 0.1 T. These results confirm that increased domain width leads to increased BN amplitude. This investigation show that removal of the coating from the surface of grain-oriented electrical steel at power frequency increase the BN due to the widening of the 180° domains as a result of the release of the tensile stress imparted to the material during coating. It was reported in [7.13] that the effective tension of the coating on grain oriented steel is 2-3 MPa.

8.3. Effect of tensile stress on Barkhausen noise

When tensile stress of 3 MPa was applied to the decoated CGO and HGO samples using the method described the section 5.4, the average rms BN decreased in both samples. This is shown in figures 8.11 and 8.12 for HGO and CGO respectively. The graph showing the percentage decrease of rms BN between the decoated HGO and the tensile stressed HGO; and the decoated CGO and the tensile stressed CGO samples at all values of peak flux densities are shown in figure AC 13 and AC 14 in Appendix C respectively.

The average domain width narrowed by 47 % in CGO and 50 % in HGO. The average rms BN decreased in HGO by 31 % at 0.1 T and 25 % at 1.0 T. In CGO, the percentage decrease in average rms BN is 17 % at 0.1 T and 23 % at 1.0 T.

Application of a 3 MPa tensile stress to the decoated CGO and decoated HGO samples caused the rms BN in the decoated CGO up to 0.2 T to be higher than in decoated HGO as shown in figure 8.13 and this is similar to the result obtained in figure 8.7 for the coated CGO and coated HGO demonstrating the close similarity between the effects of coating stress and externally applied stress on BN due to their similar roles in domain refinement. This close similarity is graphically illustrated in figures 8.14 and 8.15 for the CGO and HGO samples respectively.

This investigation shows that changes in static domain width pattern are directly related to the changes in BN in grain oriented electrical steel. As domain widths increase (by decoating the materials), the BN is increased and as the domains become narrower (by applying tensile stress), the BN is reduced.

.
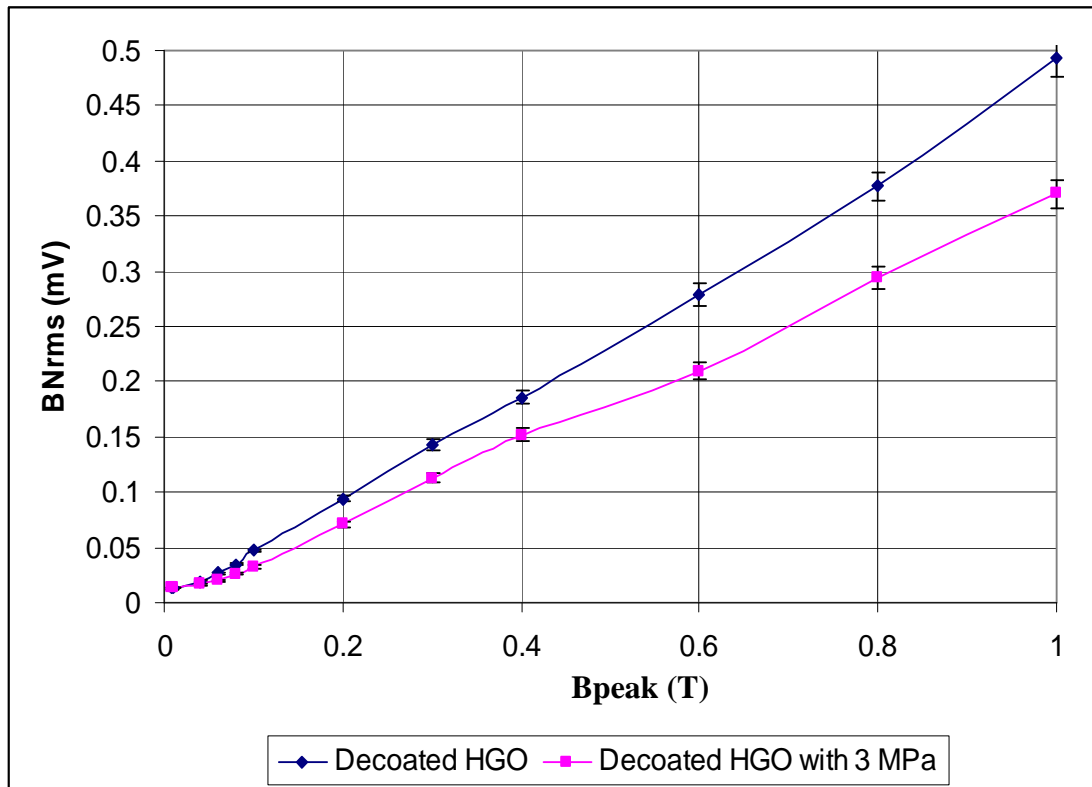
Fig. 8.11: Variation of average rms BN of decoated HGO and decoated HGO with 3 MPa at different values of peak flux density.
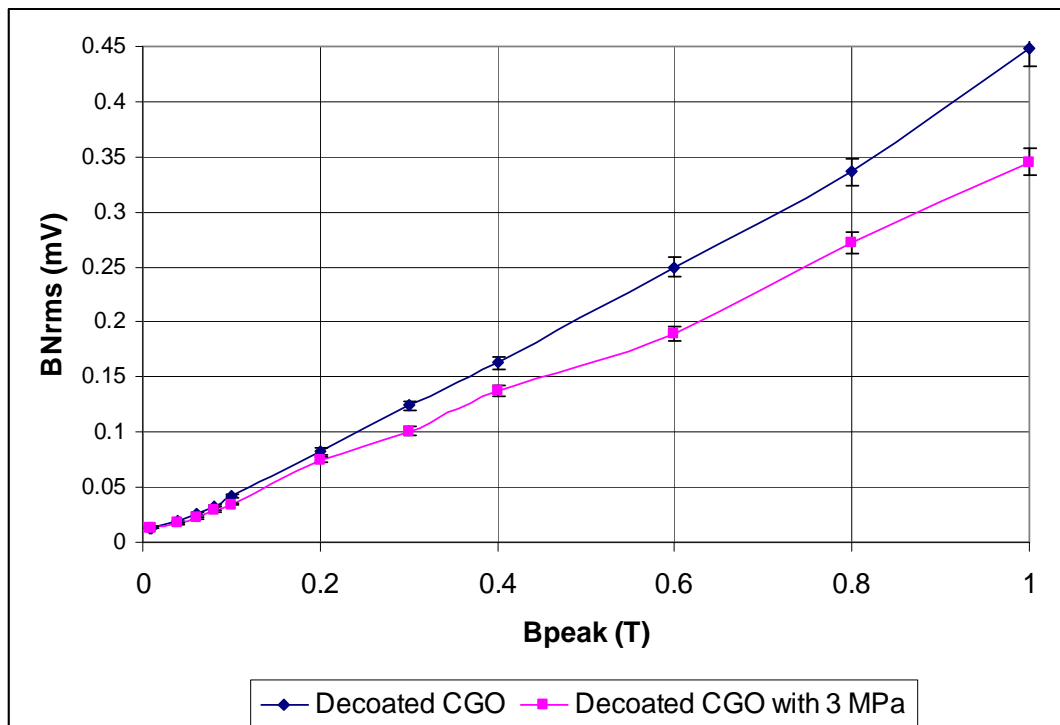
Fig. 8.12: Variation of average rms BN of decoated CGO and decoated CGO with 3 MPa at different values of peak flux density.
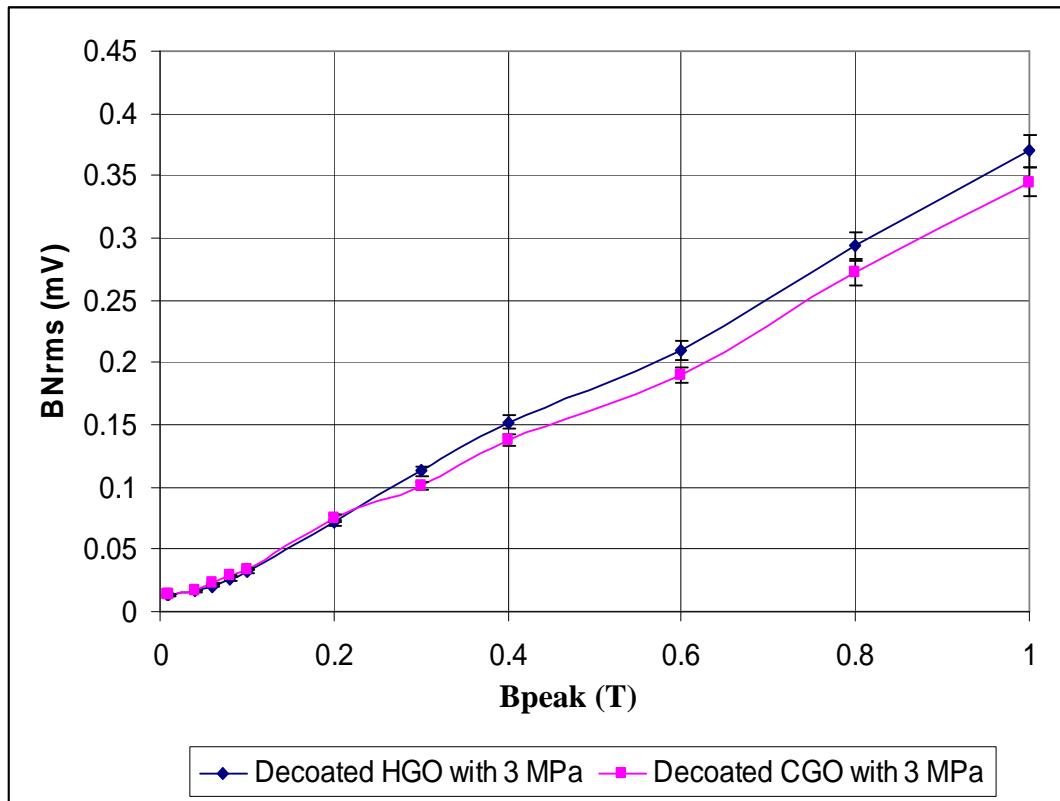
Fig. 8.13: Variation of average rms BN in decoated CGO and HGO with tensile stress of 3 MPa with at the various values of peak flux density.
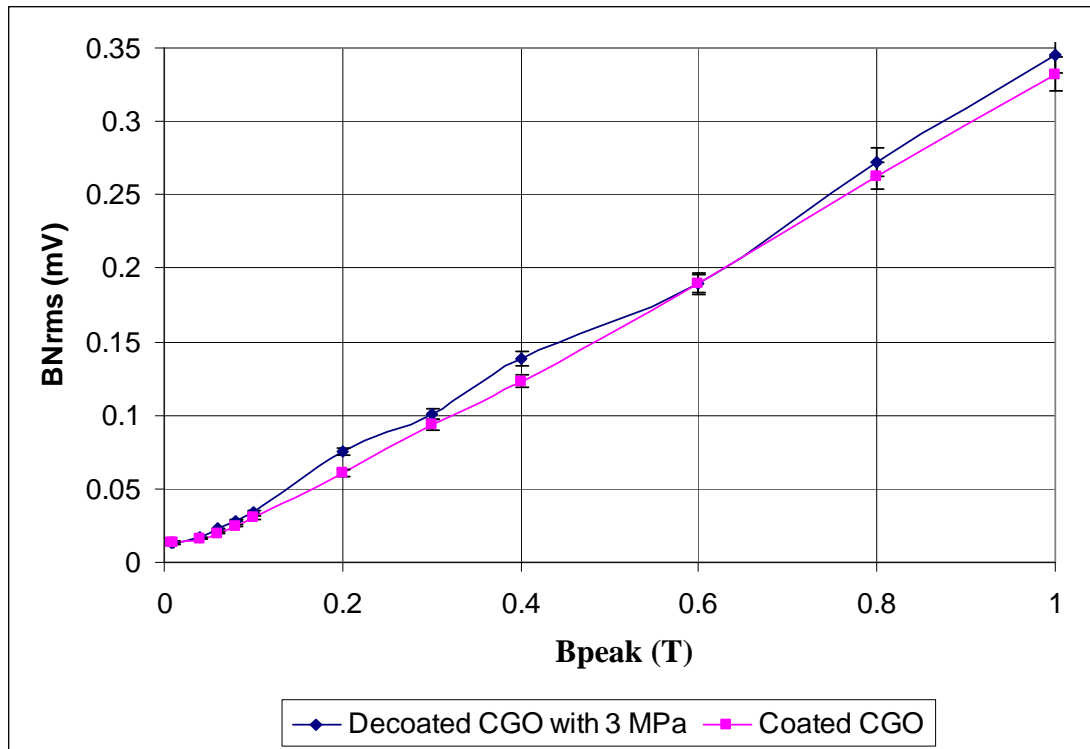
Fig. 8.14: Variation of average rms BN of decoated CGO with 3 MPa and coated CGO with peak flux density.
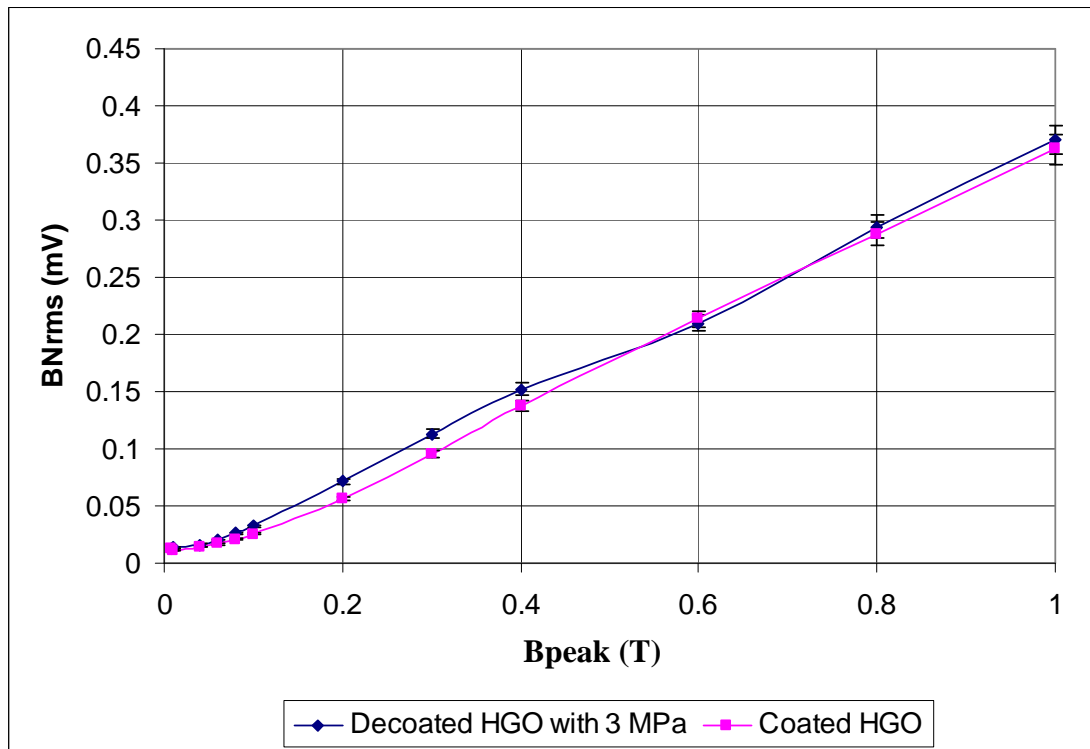
Fig. 8.15: Variation of average rms BN of decoated HGO with 3 MPa and coated HGO with peak flux density.

8.4   Calculation of the distance of domain wall movement in grain oriented steel.

Figure 8.16 is used to simplify the mathematical treatment of calculating the distance of domain wall movement in grain oriented steel which is used to calculate the average velocity of domain wall in the material at various peak flux densities for one period of 50 Hz bulk magnetisation.
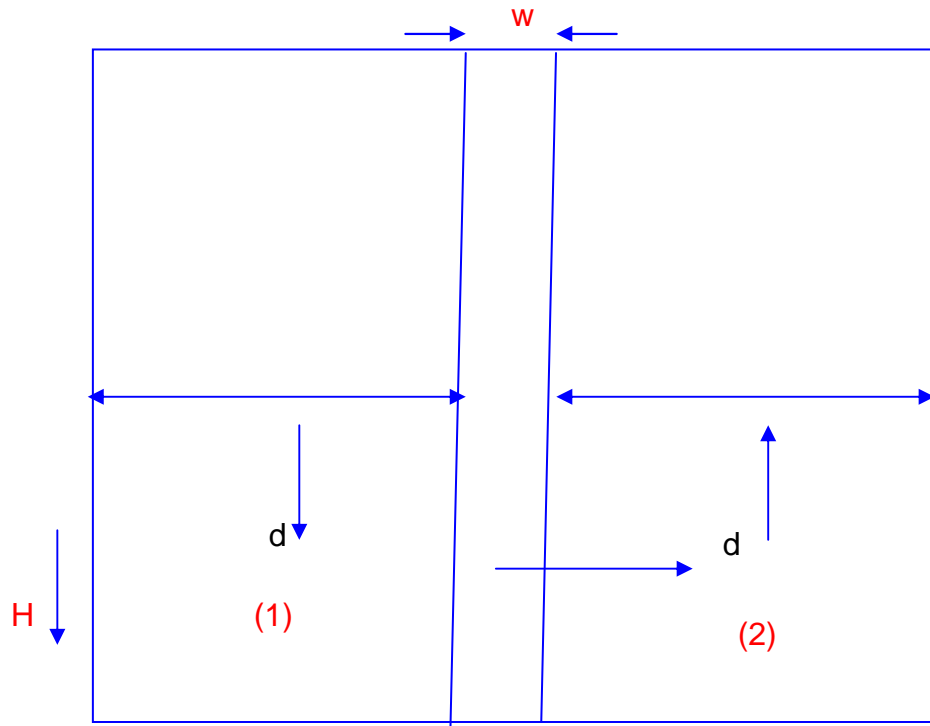
Fig. 8.16: Sketch showing domains of width, d, separated by a domain wall of width, w, in a bulk magnetic material to estimate how far domain wall moves.

When a magnetic field, H, is applied, the domain in region (1) of the figure expands by wall moving right being in the direction of the applied field.

The flux,

$$\phi = BA \qquad\qquad (8.1)$$

where A is the cross sectional area of the material and B is the flux density.

119

In any one domain, $B = B_S$, where B_S is the saturation flux density. Hence for unit length of domains, the flux in the domains in region (1),

$$\phi_1 = B_S d_1 \tag{8.2}$$

If a wall moves distance, x, to the right on application of field, ϕ_1 increases to $B_S(d+x)$ and the flux in the domains in region (2), ϕ_2, decreases to $B_S(d-x)$ hence the

resultant $\phi = B_S * 2x$ and

resultant $B = (B_S * 2x)/2d$

$$= (B_S * x)/d \tag{8.3}$$

In grain oriented steel, $B_S = 2.03T$, so given the domain width, d, and the flux density, B, the distance moved by the wall can be calculated using:

$$x = (B * d)/B_S \tag{8.4}$$
$$= (B * d)/2.03$$

The velocity of domain wall movement for the coated, decoated and the 3 MPa tensile stressed HGO and CGO samples was computed by deriving the average distance of domain wall movement at all the flux densities measured using equation (8.4) and dividing by 0.02 seconds for one period of 50 Hz bulk magnetization. This was plotted against the rms BN at peak flux density. This is shown in figures 8.17 and 8.18 for HGO and CGO bulk samples respectively.
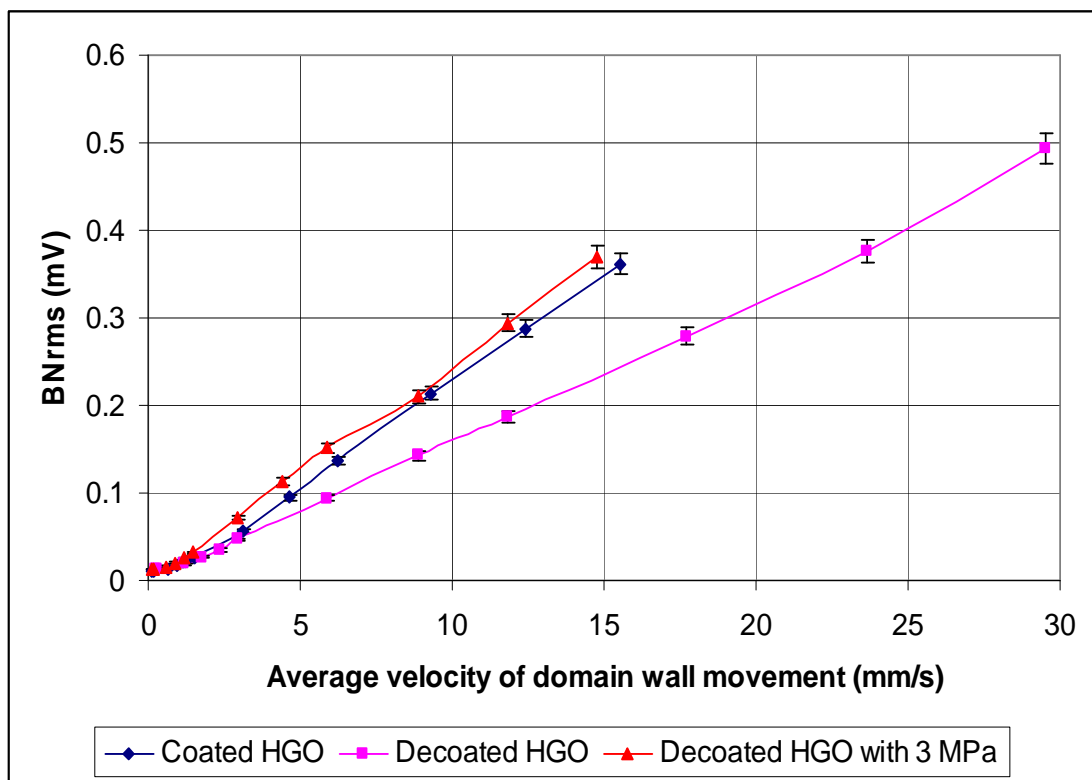
Fig. 8.17: Variation of average rms BN with average domain wall movement in HGO at each value of peak flux density from 8.0 mT to 1.0 T.
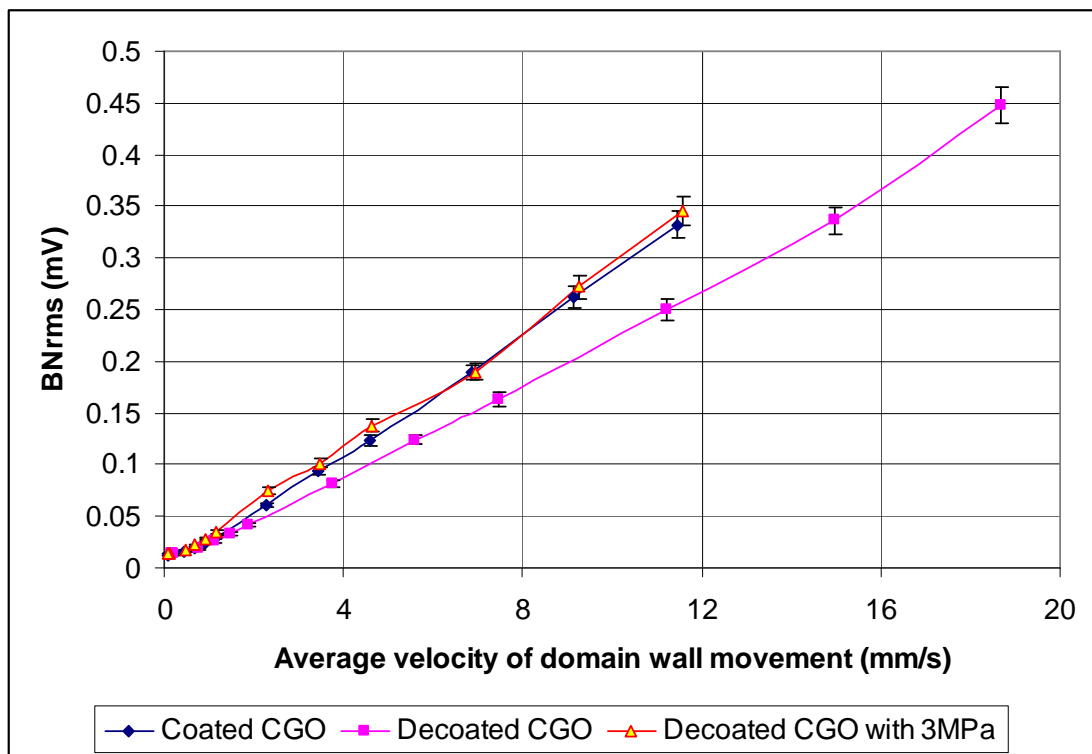
Fig. 8.18: Variation of average rms BN with average domain wall movement in CGO at each value of peak flux density from 8.0 mT to 1.0 T.

The assumption in the above calculation is that domain wall motion does not vary from grain to grain and sample to sample.

A significant correlation was found between the average velocities and changes in BN at all the peak flux densities which demonstrates that the dominant factor responsible for BN emission is the mean free path of domain wall movement and hence the width of the predominant 180° domains in these materials.

Figure 8.19 shows the variation of average rms BN of decoated HGO, decoated HGO with 2.3 MPa and decoated HGO with 3 MPa with peak flux density. It can be observed that the average rms BN of the decoated sample is higher than that of the tensile stressed samples at all the peak flux densities measured. When a tensile stress of 2.3 MPa was applied, the average rms BN of the decoated HGO decreased by 30 % at 0.1 T and 11 % at 1.0 T. When the amplitude of the tensile stress was increased to 3 MPa, the percentage decrease was 31 % at 0.1 T and 25 % at 1.0 T. Figure 8.22 shows the variation of the percentage decrease in average rms BN at all measured flux densities between the decoated HGO and the 2.3 MPa stressed HGO and also between the decoated HGO and the 3 MPa stressed HGO. It can be observed that from 0.1 T and below, the percentage difference between the average rms BN of the decoated HGO and the 2.3 MPa stressed HGO on one hand and the decoated HGO and the 3.0 MPa stressed HGO on the other hand is almost the same. This suggests that in HGO, at low flux densities, increase in tensile stress has very little effect on rms BN unlike at high flux densities where the percentage difference is almost double. It can also be observed that a change in trend occurred below 0.1 T between the tensile stressed samples.

In CGO, as shown in figure 8.21, the average rms BN of the decoated sample is higher than that of the tensile stressed samples at all flux densities except at 0.01 T and 0.008 T where it became lower. When a tensile stress of 2.3 MPa was applied, the average rms BN of the decoated HGO decreased by 18 % at 0.1 T and 12.5 % at 1.0 T. When the tensile stress was increased to 3 MPa, the average rms BN of the decoated CGO decreased by 17 % at 0.1 T and 23 % at 1.0 T. Figure 8.22 shows the variation of the percentage decrease between the average rms BN of the decoated CGO and the tensile stressed CGO at all peak flux densities measured. It can be observed that the amplitude of the average rms BN of the CGO with 2.3 MPa tensile

stress is higher than that of the 3 MPa tensile stress from 0.3 T and above. The trend changes at lower flux densities down to 0.04 T where another change of trend occurred. This observation shows that tensile stress produces different effects at high and low flux densities in the BN of CGO and HGO.

Application of the tensile stress caused the 180° domain structure to be refined with the domains narrowing. The narrowing of the 180° domains reduced the mean free path of domain wall movement leading to lower rate of change of magnetisation hence decreased BN amplitude. The application of a tensile stress parallel to the rolling direction favours an increase in the 180º domains at the expense of the 90º domains because of a shift of the magnetic easy axis towards the direction of applied stress [8.4].
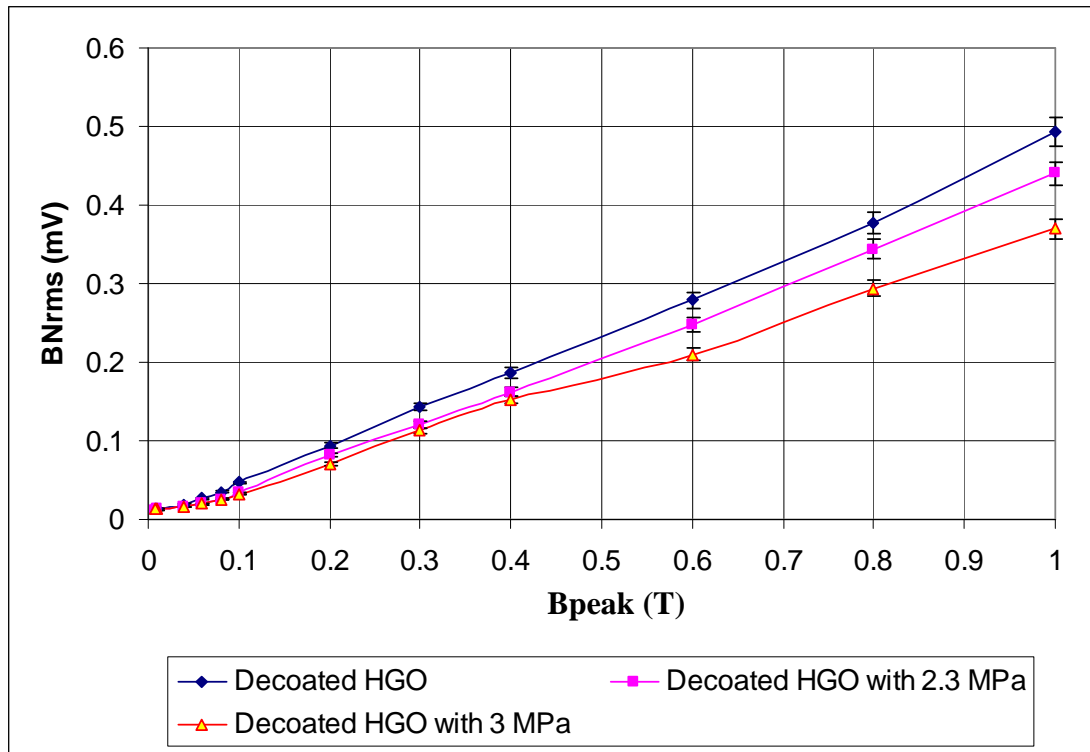
Fig. 8.19: Variation of average rms BN of decoated HGO, decoated HGO with 2.3 MPa and decoated HGO with 3 MPa at various peak flux densities.
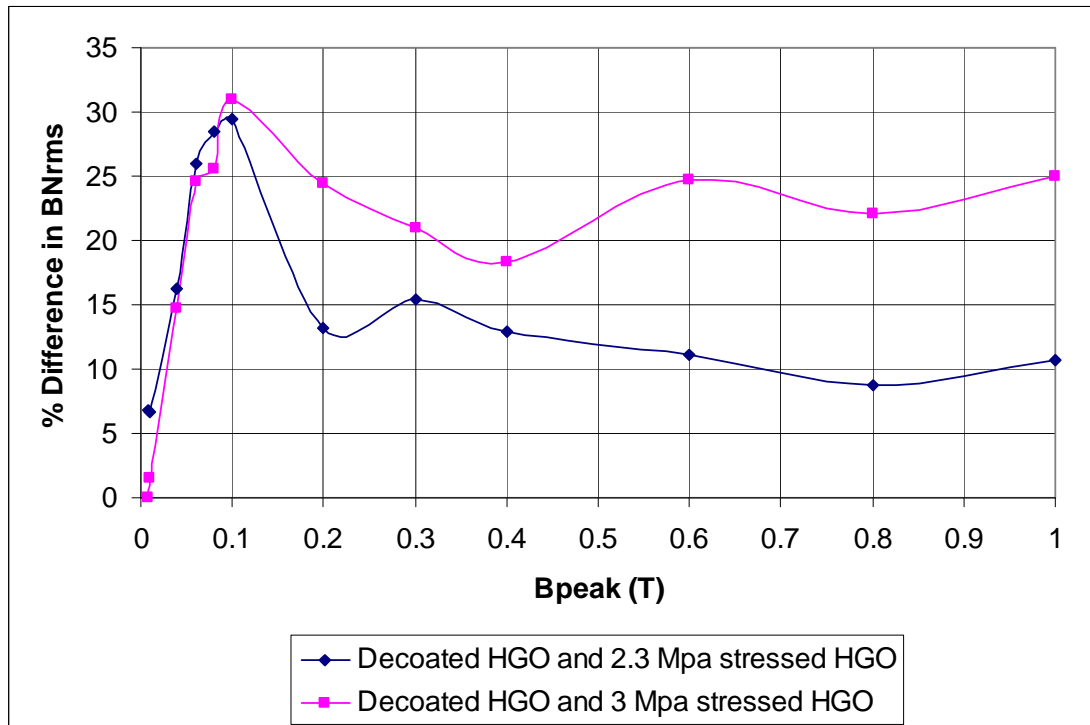
Fig. 8.20: Variation of percentage differences in average rms BN between decoated HGO and decoated HGO with 2.3 MPa and 3 MPa respectively with peak flux density.
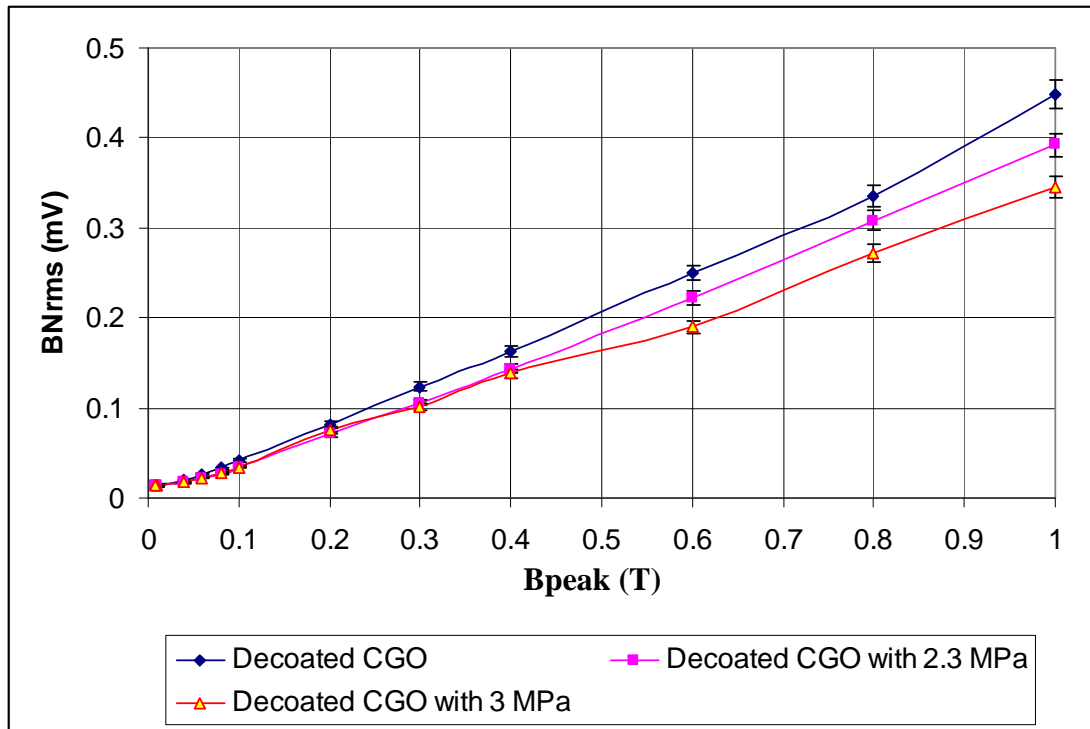
Fig. 8.21: Variation of average rms BN of decoated CGO, decoated CGO with 2.3 MPa and decoated CGO with 3 MPa at various peak flux densities.
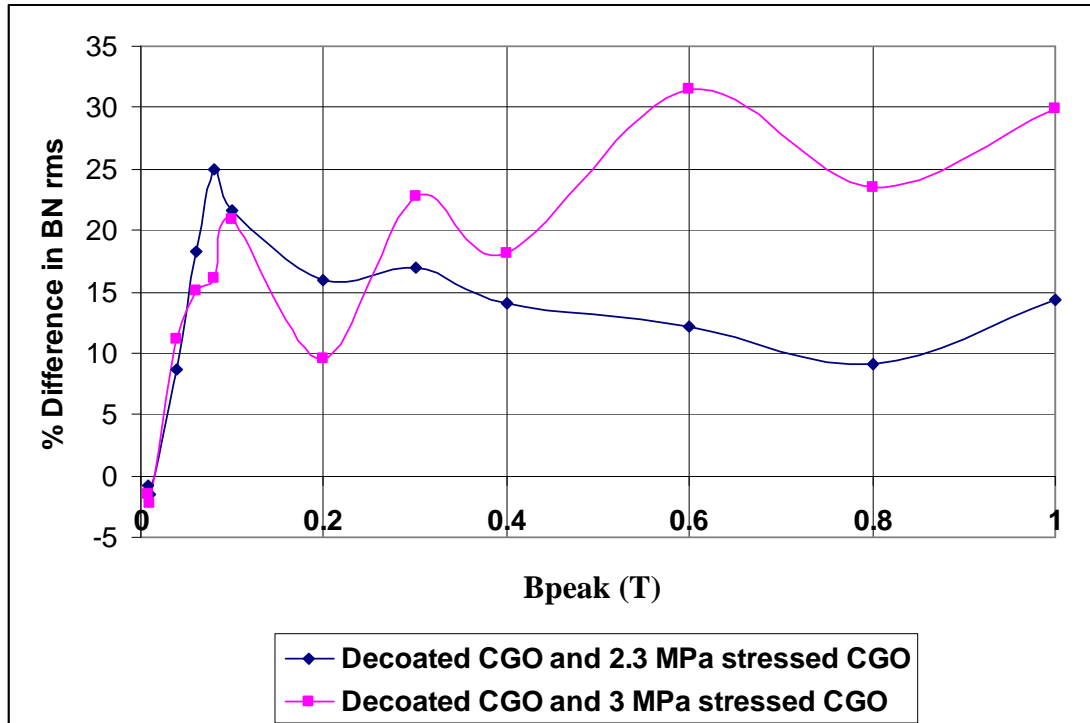
Fig. 8.22: Variation of percentage differences in average rms BN between decoated CGO and decoated CGO with 2.3 MPa and 3 MPa respectively with peak flux density.

References to chapter 8

[8.1] K. Gurruchaga, A. Martinez-de-Guerenu, M. Soto, and F. Arizti, "Magnetic Barkhausen noise for characterization of recovery and recrystallization," IEEE Trans. Magn, vol. 46, no. 2, pp. 513-516, 2010.

[8.2] L. Bjerregaard, K. Geels, B. Ottesen and M. Ruckert, Metalog guide, Struers A/S, Denmark, 1992.

[8.3] B. Fukuda, K. Satoh, T. Ichida, Y. Itoh, and H. Shimanaka, Effect of surface coatings on domain structure in grain oriented 3% Si-Fe, IEEE Transactions on Magnetics, Vol.17, No.6, pp. 2878-2880, 1981.

[8.4] T.W. Krause, L. Clapham, A. Pattantyus and D.L. Atherton, Investigation of the stress dependent magnetic easy axis in steel using magnetic Barkhausen noise , J. Appl. Phys. Vol. 79, No.8, pp. 4242-4252, 1996.

Chapter 9   Effect of Strip Thickness and Silicon Content on Barkhausen Noise of Non Grain Oriented Electrical Steel

9.1   Introduction

Measurements were made on 15 strips of NGO 3% Si-Fe from J. F. E. Steel Corporation, Japan at peak magnetic flux densities from 8 mT to 0.6 T, at 50 Hz magnetising frequency. The 280 mm x 30 mm strips were cut parallel to the rolling direction. Five samples each, 0.65 mm, 0.5mm and 0.35 mm thick were tested.

Another twelve 280 mm x 30 mm x 0.5 mm samples from the same producer, also cut parallel to the rolling direction were tested at peak flux density from 8 mT to 0.3 T. These comprised four strips each with 1.8%, 1.3% and 0.3% silicon content. The investigation was carried out with the measurement system described in section 5.2.

Experimental measurement results at high and low flux densities are also presented and discussed. An average of 3 measurements made on every strip was used in analysing the result. Between repeatability measurements each sample was removed and then re-inserted into the test system. The percentage difference of the measured properties was quantified using equation 6.1. The actual difference could be positive or negative depending on the values of the measured parameters under consideration. The uncertainties of the measurement are as outlined in tables A10 and A11 at high and low flux densities respectively.

9.2   Influence of strips thickness on Barkhausen noise of NGO

The size and distribution of the pinning sites are almost the same for this set of samples as they are from the same batch of materials. The samples also have the same amount of silicon content, therefore the principal reason for differences in Barkhausen emission could mainly be attributed to thickness effects.

Figure 9.1 shows the variation of average rms BN of the groups of strips of NGO 3% Si-Fe of different thicknesses with peak flux density. It is observed that the thinner the

sample, the greater is the rms BN. Figure 9.2 shows the variation of the percentage difference in rms BN of the NGO of different thicknesses with peak flux density. The percentage difference in average rms BN between 0.35 and 0.65 mm thick samples is highest at all peak flux densities. The reason for this is obvious. 0.35 mm is the thinnest of the samples tested which has the highest average rms BN while 0.65 mm is the thickest of the tested samples which has the lowest average rms BN. There is a higher percentage increase in average rms BN amplitude between 0.35 mm and 0.50 mm thick samples than between 0.50 mm and 0.65 mm thick samples although the trend changes from 0.06 T and below. Between the 0.35 mm and the 0.65 mm thick samples, the percentage increase in average rms BN rises from 0.008 T and peaking at 0.2 T with a value of 77 % and thereafter falls to 62 % at 0.6 T. Similarly, between the 0.35 mm and 0.50 mm thick samples, the percentage increase rises from 0.008 T and peaking at 0.2 T with 47 % and then falls to 35 % at 0.6 T. 0.2 T seems to be the threshold flux density between high and low flux densies as different domain activities take place before and after it. The sample sets with thicknesses of 0.5 mm and 0.65 mm however recorded the highest percentage increment at 0.06 T, 0.2 T and 0.6 T with a value of approximately 20 %.

 The variation of the average total sum of BN amplitude (TSA) of the test samples showed similar trend to the rms BN and is shown in figure 9.3. The percentage variation in TSA of the test samples with peak flux density is shown in figure 9.4. Between the samples with thicknesses 0.35 mm and 0.65 mm, the highest percentage increment occurred at 0.2 T with a value of 73 % and falls to 62 % at 0.6 T. The percentage increase rises steadily from 0.008 T and peaks at 0.2 T with a value of 48 % and gradually falls to 36 % at 0.6 T in the sample set with thicknesses of 0.35 mm and 0.50 mm. Also the percentage increase in average TSA of the 0.5 mm and 0.65 mm sample set rises from 0.008 T and peaks at 0.06 T with 22 % and thereafter falls and rises until 0.6 T at a value of 20 %.
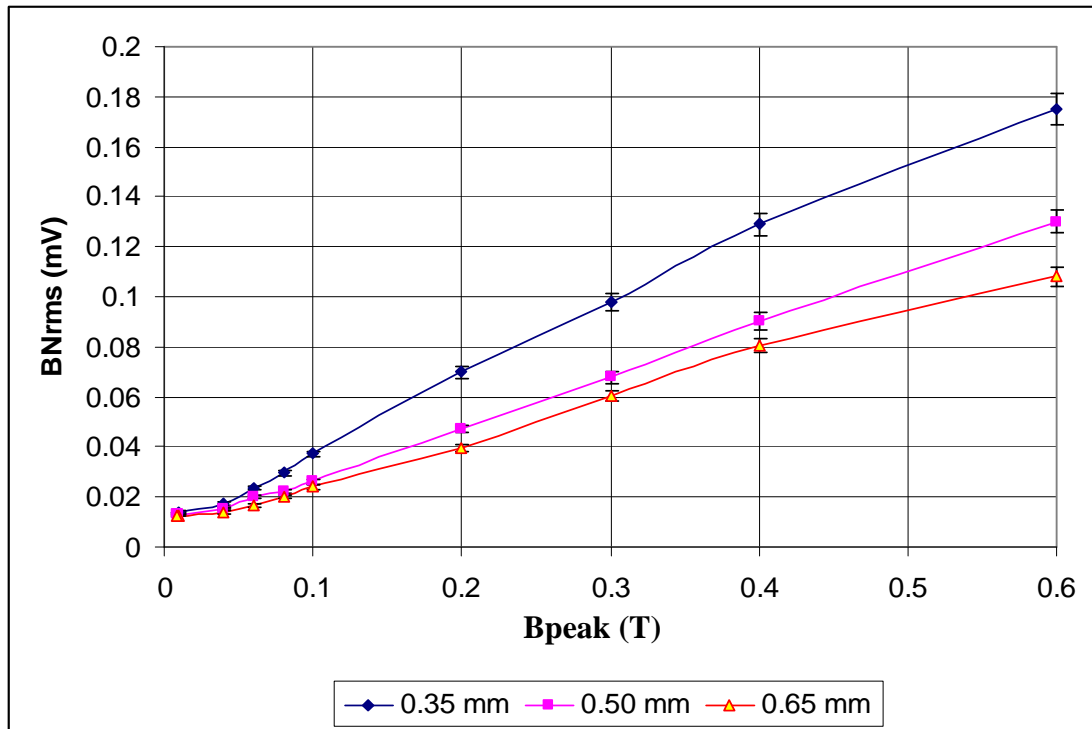
Fig. 9.1: Variation of average rms BN of NGO (3% Si) of different thicknesses with peak flux density.
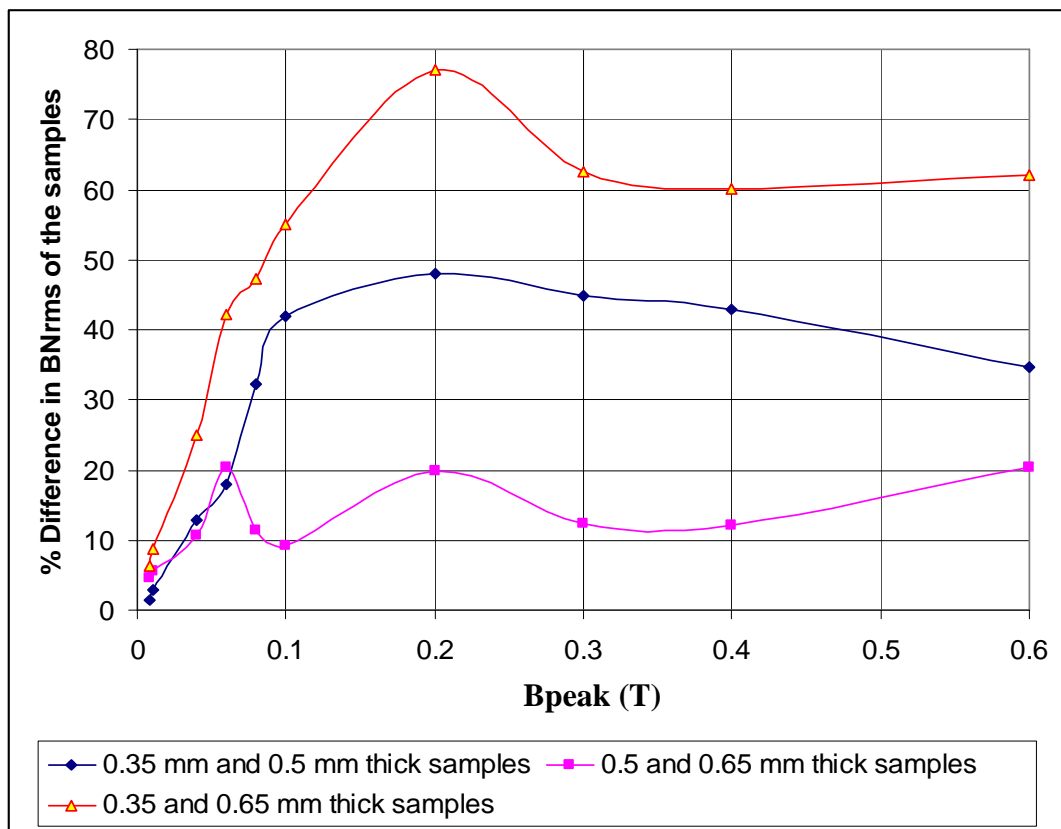
Fig. 9.2: Variation of % difference in average rms BN of NGO of different thicknesses with peak flux density.
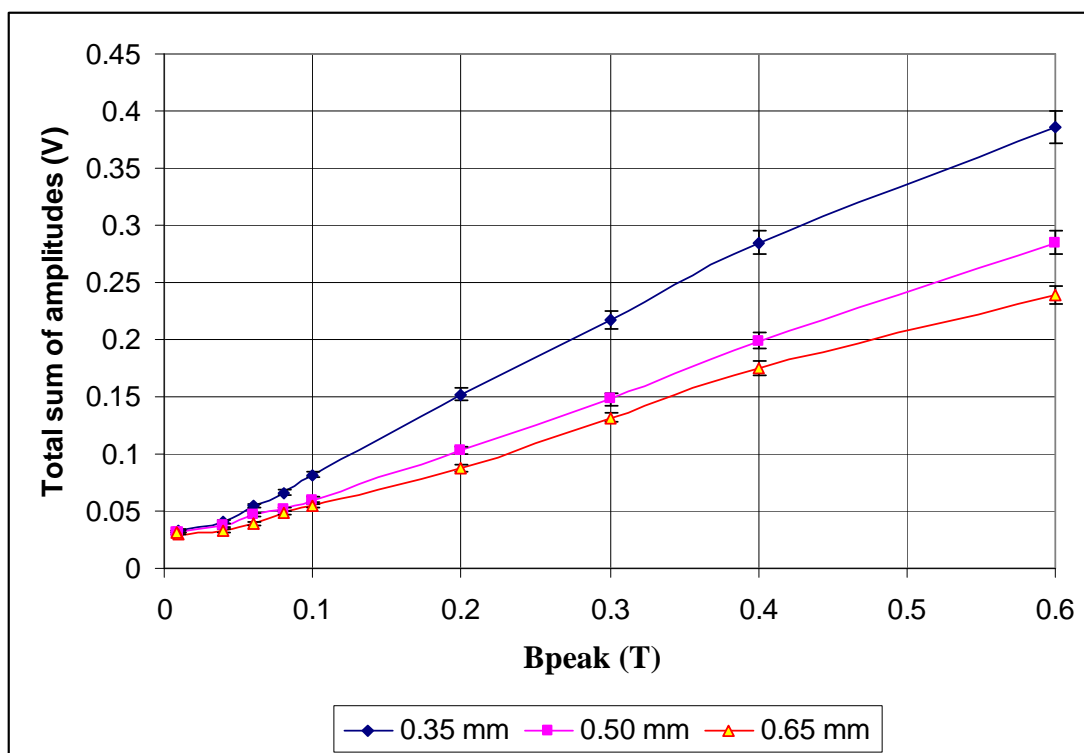
Fig. 9.3: Variation of average TSA of NGO (3% Si) of different thicknesses with peak flux density.
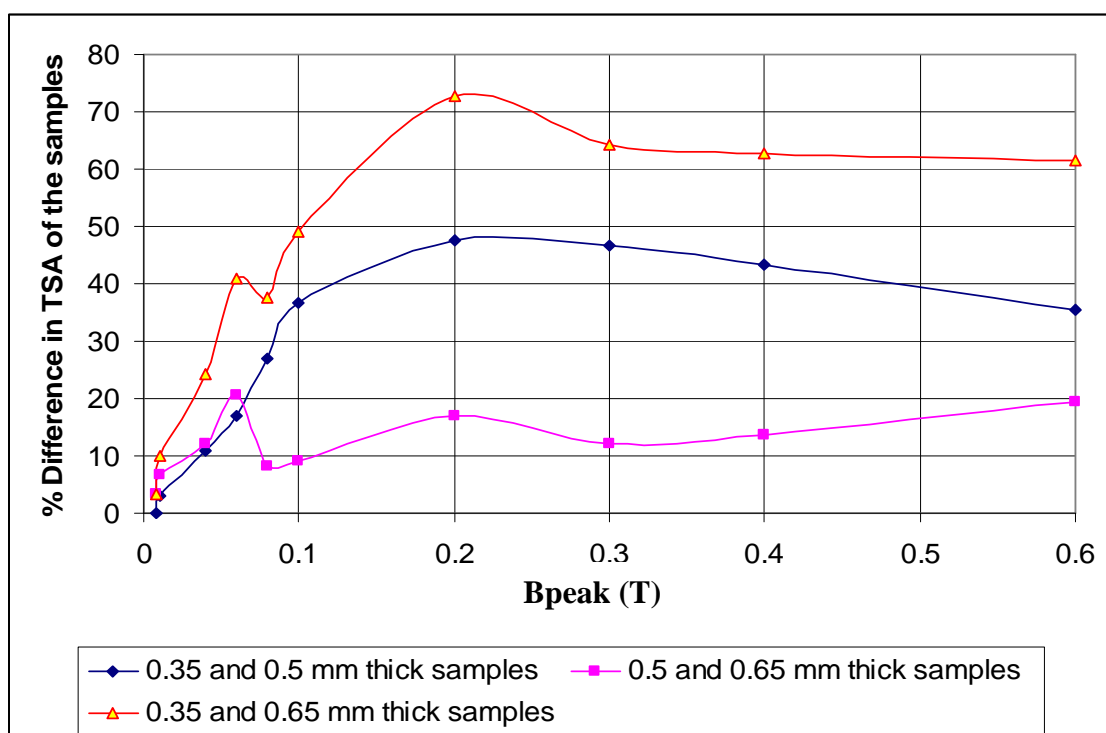
Fig. 9.4: Variation of percentage difference in average TSA of NGO of different thicknesses with peak flux density.

The observed trend is due to eddy current effects which increase with increasing depth (thickness) and thus limits the movement of domain walls as was previously reported in En 36 gear steel [9.1], nine different samples of different thicknesses on unspecified steel materials [9.2] and S235JGR2 steel with a ferrite-pearlite structure [9.3]. A moving domain wall in a conducting sample of ferromagnetic material induces eddy currents which give rise to an effective retarding pressure on the domain wall. In response to the applied magnetic field, the eddy current pressure is proportional to the domain wall velocity, and the resulting motion is damped. The significance of the dynamic effect of eddy current is regulated by the smaller sample dimension hence the thinner the sample, the smaller the effect [9.4].

The total number of BN peaks (TNP) as a function of the peak flux density is shown in figure 9.5. It is observed that the higher the peak flux density, the fewer events are detected and this leads to higher BN amplitude. This agrees with previous work done at flux densities above 0.1 T in non oriented steel [9.5] and a lamination of SiFe from a transformer core [9.6]. So this observation is true in NGO of different thicknesses and at lower flux densities as this work has shown. An increasing number of BN peaks (induced voltages) imply more obstacles (pinning sites) to domain wall movement are present which decreases the mean free path for domain wall movement leading to lower BN amplitude.

Figure 9.6 shows the variation of rms BN with the rate of change of peak flux density (dB/dt). The peak values of the rate of change of peak flux density were calculated in LabVIEW. It is well known that higher rates of change of flux density lead to higher BN amplitude as shown in the figure.
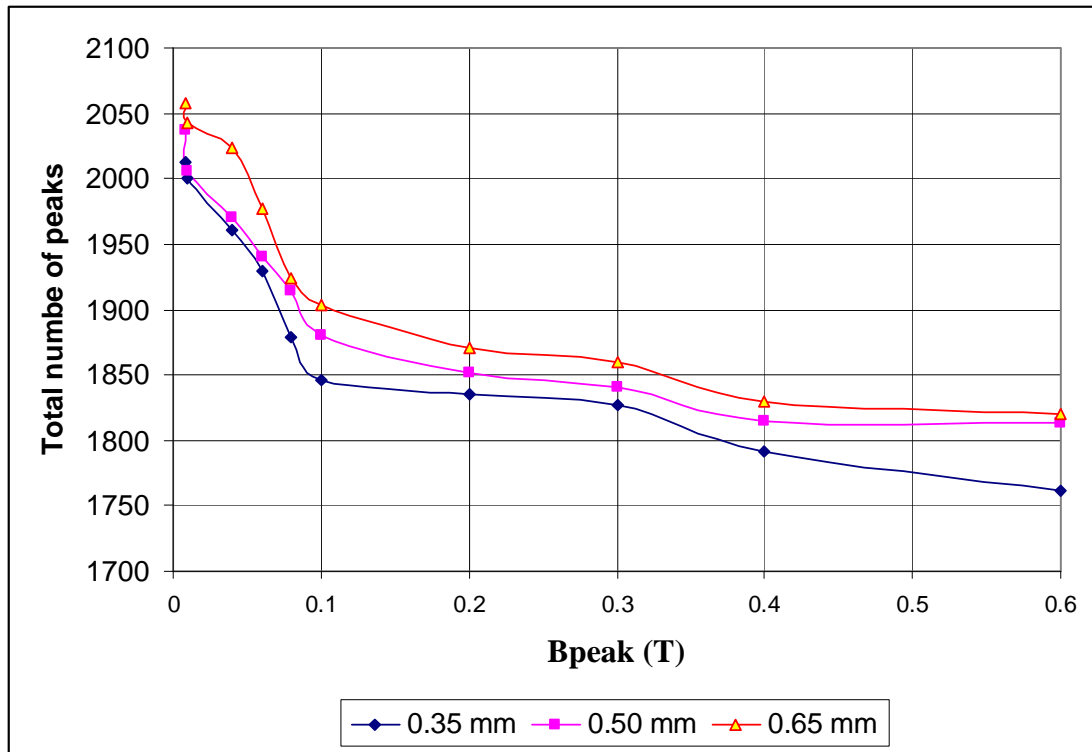
Fig. 9.5: Variation of average TNP with peak flux density in NGO (3% Si) of different thicknesses.
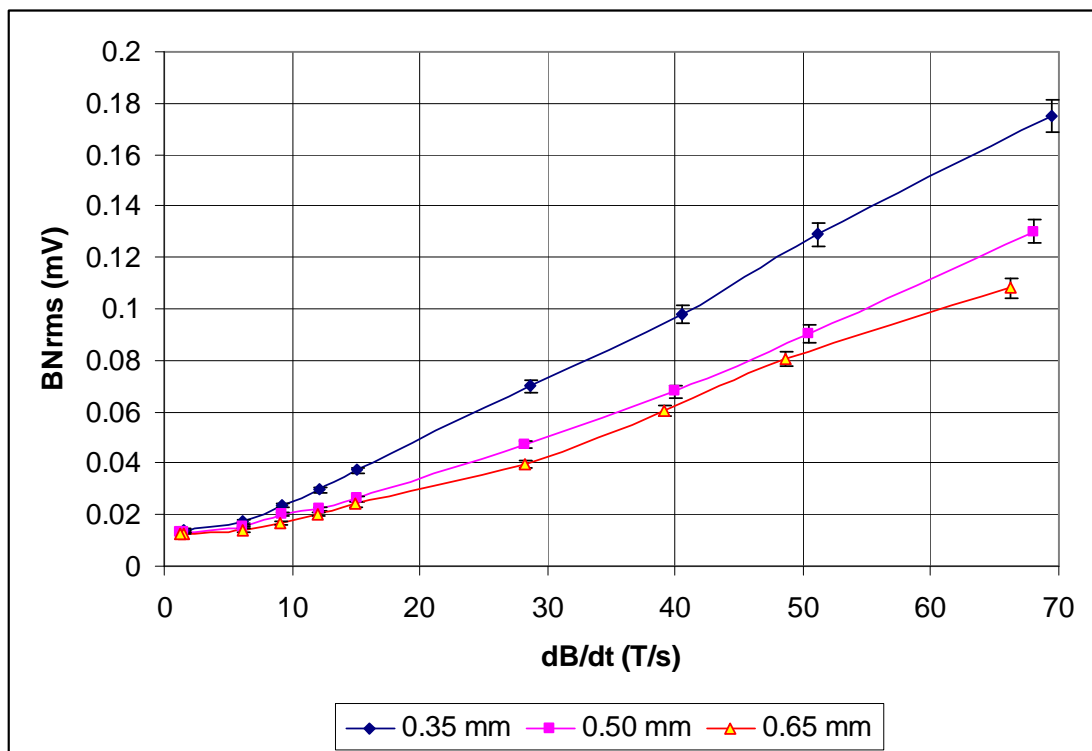
Fig. 9.6: Variation of average rms BN with peak dB/dt in NGO (3% Si) of different thicknesses.

9.3   Influence of silicon content on Barkhausen noise of NGO

Figure 9.7 shows the variation of average rms BN with peak flux density in each of 4 strips of 0.5 mm thick NGO with different silicon contents. It is observed that the rms BN increases as the silicon content increases. The variation of percentage difference of the average rms BN of the test samples with peak flux density is shown in figure 9.8. The rms of BN increased by a much greater percentage between samples with silicon contents of 1.3% and 1.8% than samples with silicon contents of 0.3% and 1.3% although there is a change of trend at 0.08 T and 0.06 T. The highest percentage difference occurs between samples with silicon contents of 1.8% and 0.3% at all the range of peak flux densities measured. The highest percentage increase in average rms BN between the samples with silicon contents of 0.3 % and 1.8 % occurred at 0.3 T with a value of over 155 %. Similarly, between the samples with silicon contents of 1.3 % and 1.8 %, the highest percentage increase occurred at 0.3 T at a value of 112 %. Between the samples with 0.3 % and 1.3 % silicon, the highest percentage increase in average rms BN occurred at 0.08 T with 22 % and then falls and rises to 20 % at 0.3 T.

The average TSA of BN was also found to increase as the silicon content increases as shown in figure 9.9. The percentage increases in TSA between the test samples as shown in figure 9.10 has the same characteristics with the percentage increases in rms BN of the test samples but there is no change of trend at lower flux densities. The percentage increment in average TSA between the samples with silicon contents of 0.3 % and 1.8 % is higher than the percentage increment in all the other set of samples measured. Between these test samples, the percentage difference in average TSA is highest at 0.3 T at a value of 132 %. For the samples with 1.3 % and 1.8 % silicon contents, the percentage difference maintained a steady increase from 0.04 T and peaks at 0.3 T with 105 %. The highest percentage increase occurred 0.1 T with a value of 22 % and fall to 15 % at 0.3 T between the samples with silicon contents of 0.3 % and 1.3 %.

These observations are also due to BN signals being attenuated by eddy current shielding effects. Higher silicon content causes the eddy current shielding effect to be reduced which decreases the retarding eddy current pressure on the domain walls resulting in the higher BN amplitude. Eddy-current losses are inevitable in conducting

133

magnetic materials, and in silicon iron sheets they can be minimised by using thin sheet or increasing silicon content in the steel. By making the sheets thin, the path-resistance for eddy currents is increased, and the magnetic utilisation of the material is improved, since the eddy currents also give rise to a distribution of flux density through the sheet thickness, being greatest at the surface and least at the centre. The use of thin sheets ensures that the penetration depth of the flux is as high as possible.

The second way of reducing eddy currents is to increase the electrical resistivity of the steel. Further increases in resistivity are possible; using greater proportions of silicon, but over addition hardens the grain structure and embrittles the steel which can adversely affect the workability and applicability of the material. BN is primarily a surface test method due to the attenuation of its signal by eddy current shielding effects. This is because the domain wall velocity is limited by microscopic eddy currents [9.4]. The relationship of BN detection frequency and the penetration depth is discussed in section 4.6.
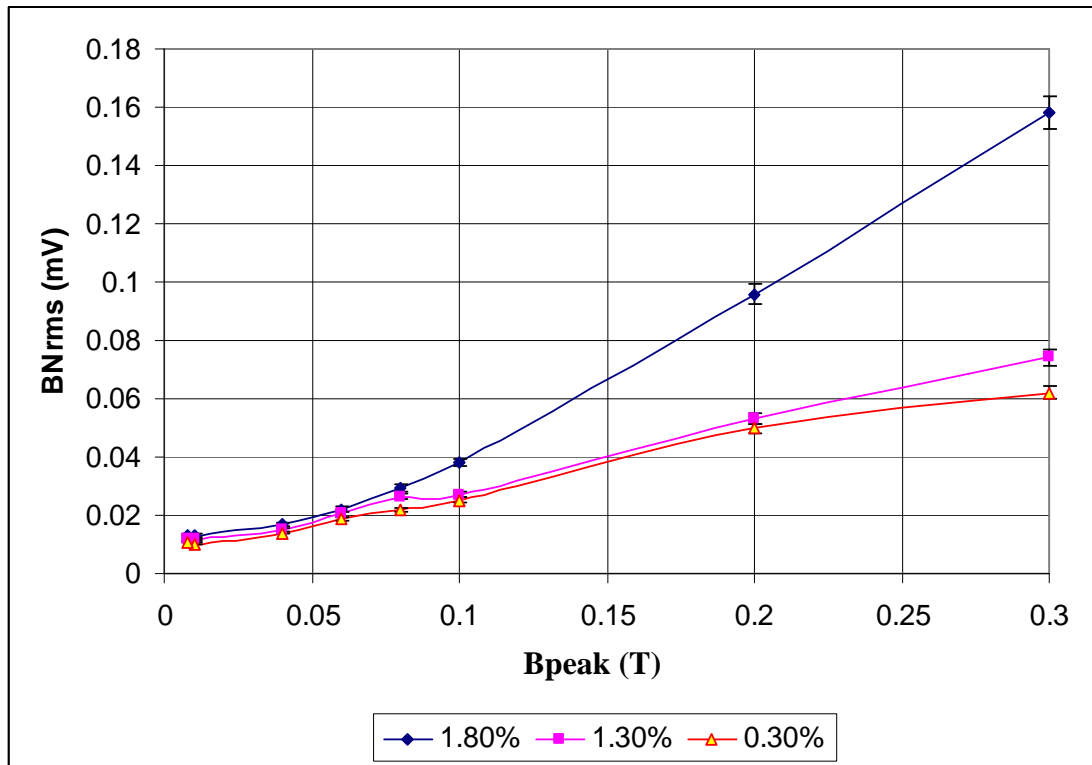
Fig. 9.7: Variation of average rms BN of NGO (0.5 mm thick) of different silicon contents with peak flux density.
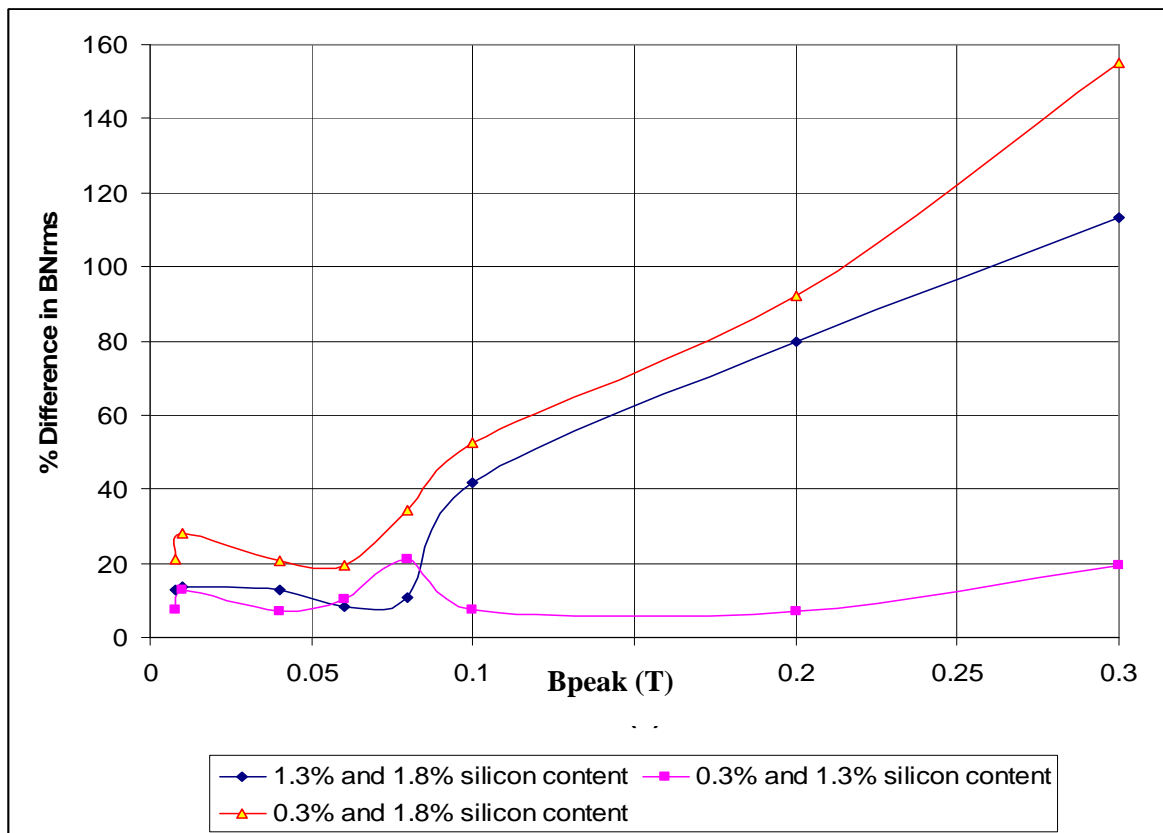
Fig. 9.8: Variation of percentage difference in rms BN of NGO of different silicon contents with peak flux density.
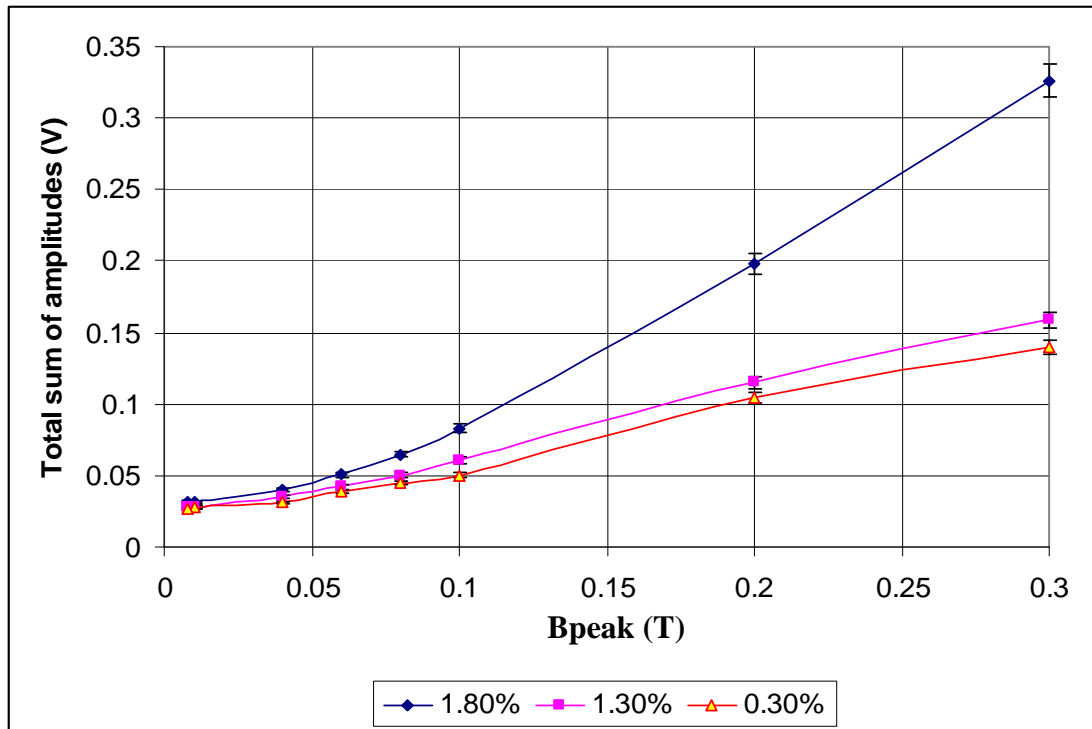
 Fig. 9.9: Variation of average TSA of NGO (0.5 mm thick) of different silicon contents with peak flux density.
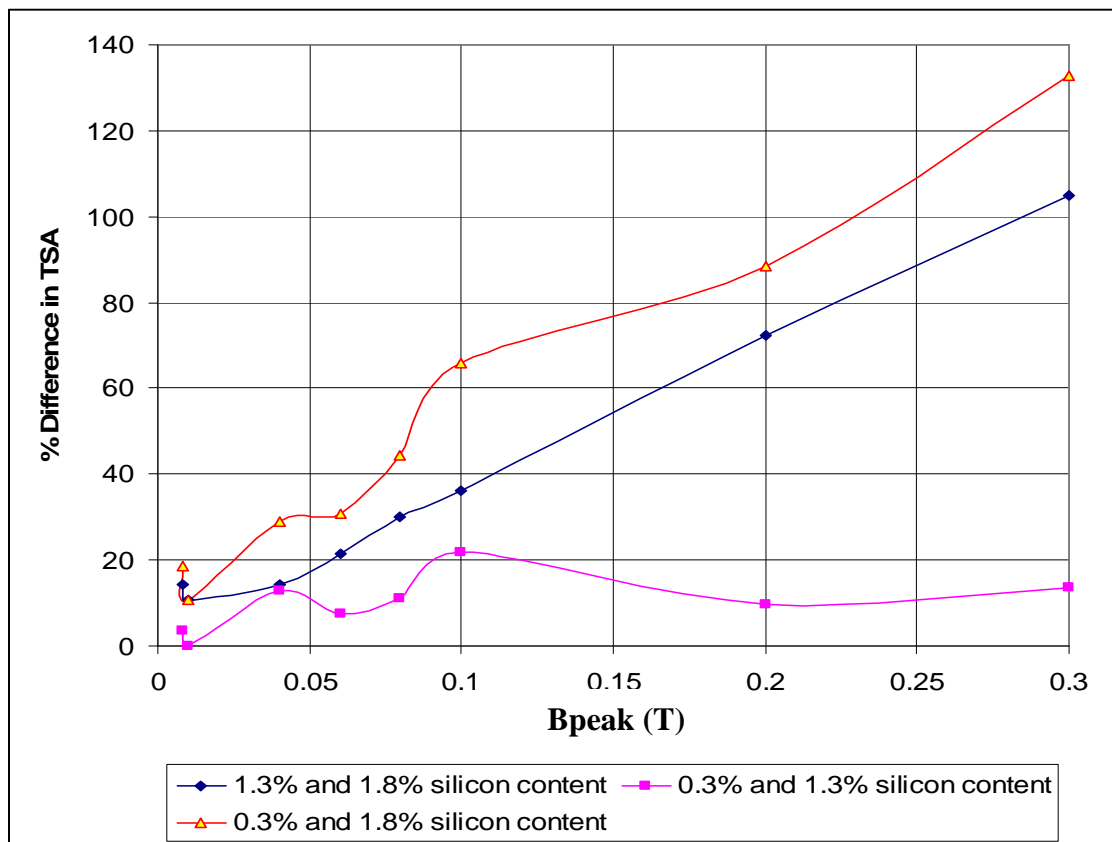
Fig. 9.10: Variation of percentage difference in TSA of NGO of different silicon contents with peak flux density.

Figure 9.11 shows the variation of average rms of BN of 0.50 mm thick NGO of different silicon contents with the rate of change of flux density (dB/dt). As observed in the test samples with different thicknesses, higher rate of change of flux density leads to higher BN amplitude because of increased domain wall movement.

The variation of rms BN with TNP in NGO (0.50 mm thick) of different silicon contents are shown in figure 9.12. It is interesting to observe that BN increases with the total number of peaks as the silicon content increases at increasing peak flux densities. This trend is different to that shown in figure 9.5 where the average rms BN increases as the TNP decreases in the case of NGO (3% Silicon) of different thicknesses. This change in trend is thought to be due to the increasing silicon content reducing the eddy current shielding effect more than the effect of reducing the thickness of the strips. It is reported in [9.7] that addition of only 3.5% silicon increases the resistivity four fold. This accounts for the reason why the BN amplitude increases with the TNP as the silicon contents increases.
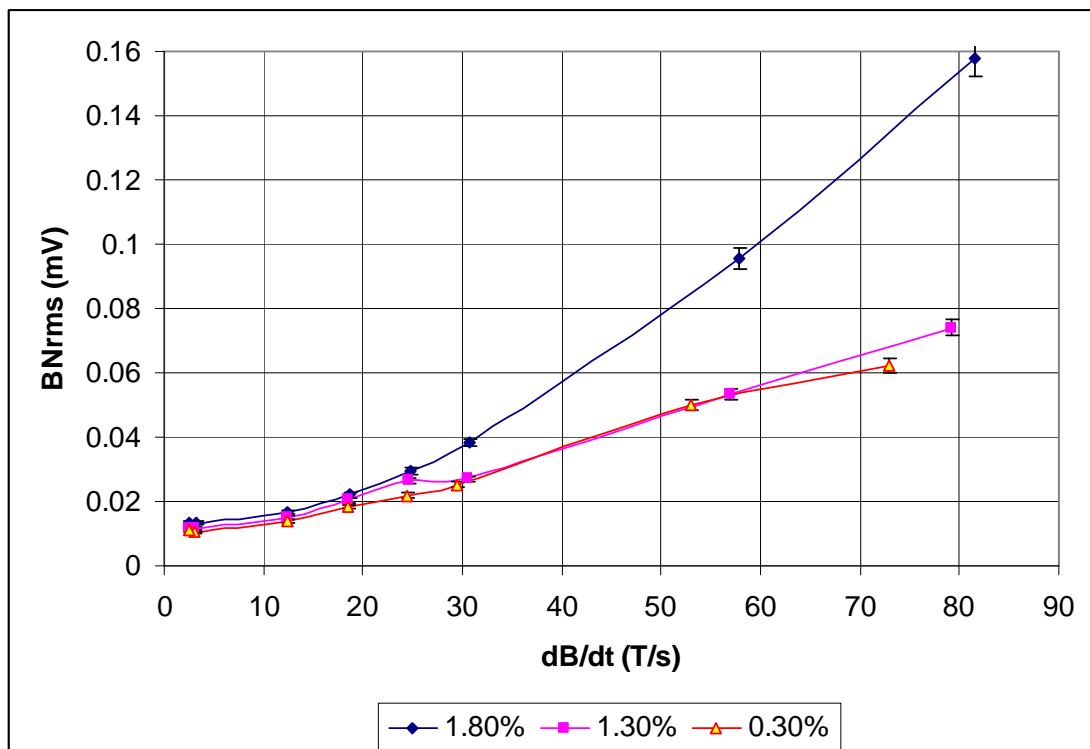
Fig. 9.11: Variation of average rms BN of NGO (0.5 mm thick) of different silicon contents with peak dB/dt at different peak flux densities.
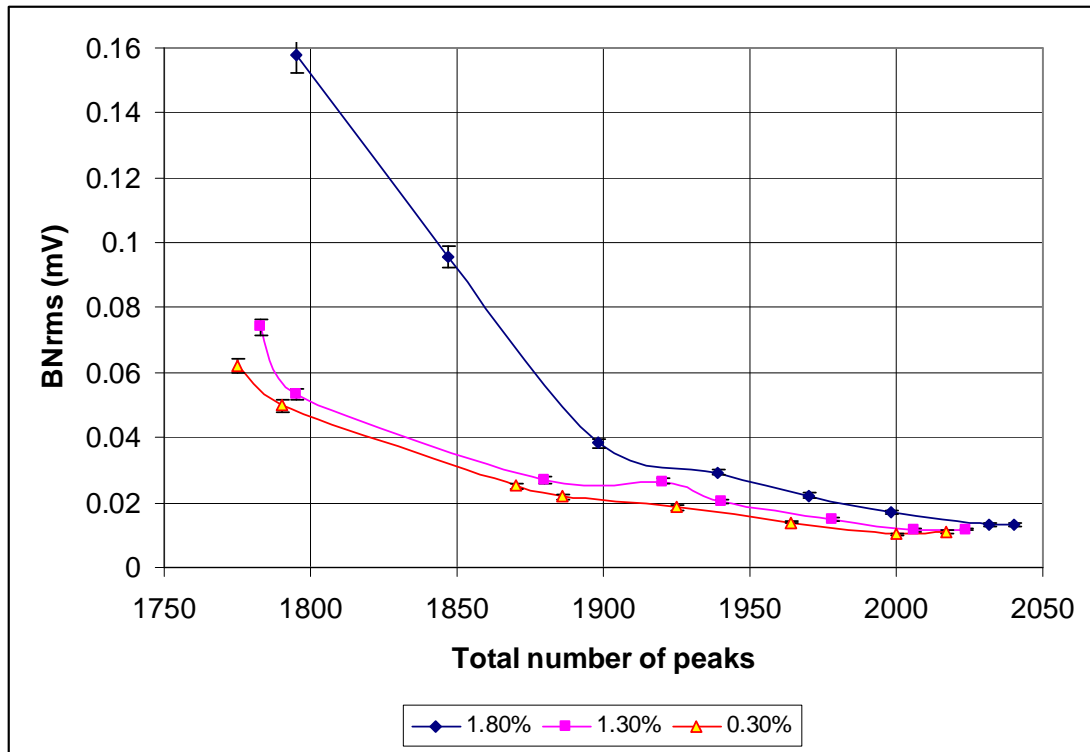
Fig. 9.12: Variation of average rms BN with TNP in NGO (0.50 mm thick) of different silicon contents at different flux densities.

The investigation in this chapter show definite correlations between BN of non-oriented electrical steel with thickness and silicon content. BN was found to increase with decreasing strip thickness and increase with increasing silicon contents owing to eddy current shielding effects. The rms values of the BN and the total sum of amplitudes was found to increase with the rate of change of flux density at all the peak flux densities measured. The findings show that the influence of sample thickness and silicon content is significant and must be taken into consideration when measuring and interpreting BN in non-oriented electrical steel.

References to chapter 9

[9.1] J W. Wilson, G. Y. Tian, V. Moorthy and B. A. Shaw, Magneto-acoustic emission and magnetic Barkhausen emission for case depth measurement in En36 gear steel, IEEE Transactions on Magnetics, Vol. 45, No.1, pp. 177-183, 2009.

[9.2] D. Strand, Parameters and depth of penetration of Barkhausen noise analysis, United States Army Research Laboratory, ARL-TR-5159, pp. 1-11, 2010.

[9.3] T. Garstka, The influence of product thickness on the measurements by Barkhausen noise method, Journal of Achievements in Materials and Manufacturing Engineering, Vol. 27, issue 1, pp. 47-50, 2008.

[9.4] F. Colaiori, G. Durin, and S. Zapperil, Eddy current damping of a moving domain wall: Beyond the quasistatic approximation, Physical Review B 76, 224416, pp. 1-7, 2007.

[9.5] M. Komatsubara, J. L. Porteseil, Influence of grain size and strain on Barkhausen noise power on non-oriented silicon steel, IEEE Transactions on Magnetics, Vol. 23, issue 5, pp. 3506-3508, 1987.

 [9.6] S. White, T. Krause, and L. Clapham, Quantitative analysis of surface Barkhausen noise measurements, Review of Quantitative Non-destructive Evaluation, Vol. 27, pp. 445-452, 2008.

[9.7] F Brailsford, Physical principles of Magnetism, Van Nostrand, London, 1966.

Chapter 10   Effect   of   Strip   Thickness   on Barkhausen Noise of Grain Oriented Electrical Steel

10.1   Introduction

In this part of the investigation, BN measurements were made on 3 Epstein strips each of CGO of thicknesses 0.23 mm, 0.27 mm, 0.30 mm, 0.35 mm and 0.50 mm and HGO 0.27 mm and 0.30 mm from Cogent Power Limited in the peak flux density range of 8 mT to 1.2 T. The investigation was carried out with the measurement system described in section 5.2. The relative permeability, coercivity and power loss of the test samples were also measured. Experimental measurement results at high and low flux densities are also presented and discussed. An average of 3 measurements made on every strip was used in analysing the result. Between repeatability measurements each sample was removed and then re-inserted into the test system. The percentage difference of the measured properties was quantified using equation 6.1. The actual difference could be positive or negative depending on the values of the measured parameters under consideration. The uncertainties of the measurement are outlined in tables A10 and A11 at high and low fields respectively.

10.2   Effects of strips thickness on the Barkhausen noise of CGO

The size and the distribution of the precipitates are assumed to be the same for the respective CGO and HGO samples since they are from the same batch of materials. Therefore the primary reason for the differences in BN could be attributed to grain size and thickness effects. In grain oriented electrical steel, pinning sites are preferentially located at grain boundaries which act as obstacles to the movement of domain walls [10.1] hence it is reasonable to expect some relationship between grain size and BN [10.2].

Figure 10.1 shows the variation of average rms BN of the 3 strips each of CGO of the different thicknesses with peak flux density at 50 Hz excitation frequency. It is observed that average rms BN increases with peak flux density in the entire test samples. In all tested materials, it is interesting to observe that the average rms BN increases with thickness for samples with thicknesses less than 0.35 mm. The eddy

current damping which increases with increasing strips thickness and retards the movement of domain wall thereby reducing the BN amplitude seem to have no effect here. This is because in silicon iron sheet of standard thickness, typically 0.33 mm and below, at 50 Hz magnetisation, the 'skin effect' is negligible [10.3], that is the flux may be taken as being uniformly distributed through the sheet thickness.

The percentage variation of the rms BN of the CGO samples of thicknesses from 0.30 mm and below and the graph showing the variation of the percentage difference in rms BN of the 0.35 mm and 0.50 mm thick CGO samples with peak flux density are shown in figures AC 15 and AC 16 of Appendix C. The percentage increase between samples of thicknesses 0.23 mm and 0.30 mm is higher than the percentage increase between samples of thicknesses 0.23 mm and 0.27 mm and also samples with thicknesses 0.27 mm and 0.30 mm especially from 0.1 T and above. At lower flux densities, there is no particular trend in the percentage difference of rms BN in all the tested samples.
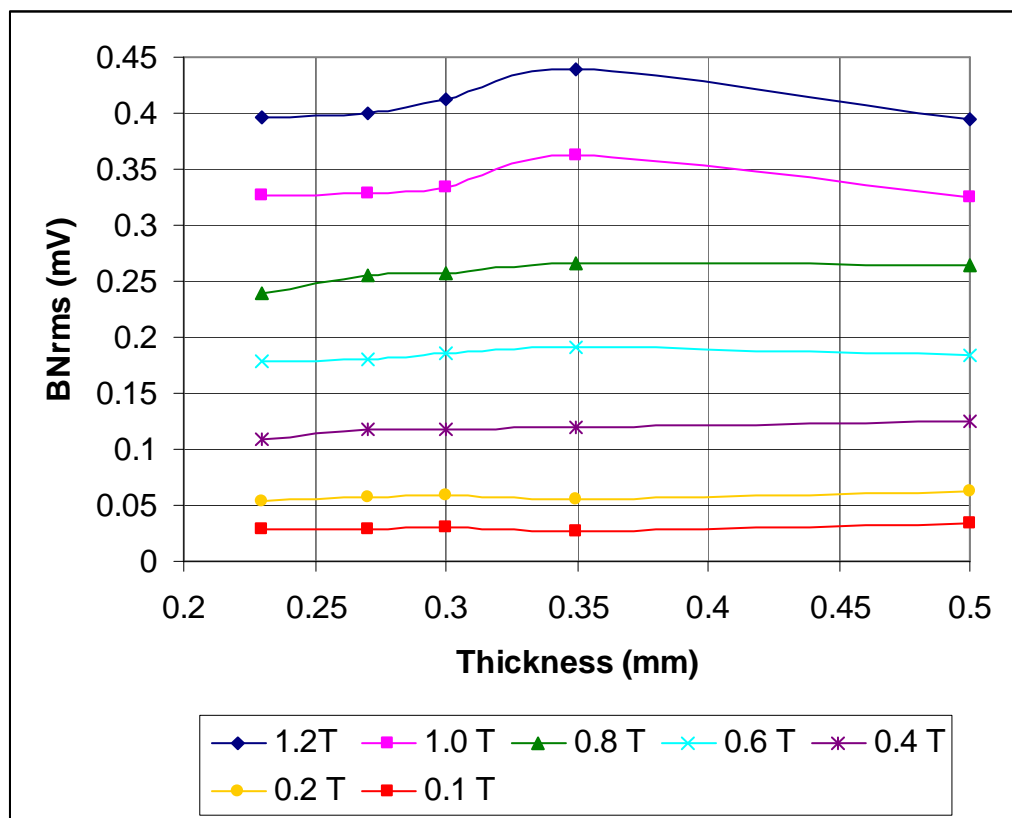
Fig. 10.1: Variation of average rms BN in CGO of different thicknesses at various peak flux density.

As was shown in figure AC 17, the average rms BN of the samples with thickness of 0.35 mm is higher than that of the 0.50 mm thick samples from 0.5 T and above. The trend changes at lower flux densities. This shows that both the domain width and the sample thickness influenced the BN. This is because of eddy current damping which increases with thickness and is always higher at high flux densities. This accounts for the decreased rms BN of the 0.5 mm thick samples in this regime. The influence of domain width hence grain size predominates below 0.5 T which accounts for the higher rms BN of the 0.5 mm thick samples over the 0.35 mm thick samples in this regime.

10.3   Influence of thickness on Barkhausen noise of HGO steels

Figure 10.2 shows the variation of average rms BN of the 3 strips each of HGO of thicknesses of 0.27 mm and 0.30 mm with peak flux density. HGO strips are normally manufactured with thicknesses of 0.27 mm and 0.30 mm. It is observed as in CGO that average rms BN increases with peak flux density in the entire test samples being higher in the 0.3 mm thick samples than in the 0.27 mm specimens. The variation of the percentage increase of rms BN of the 0.30 mm thick samples over the 0.27 mm thick samples with peak flux density is shown in figure AC 18. A change of trend occurred at 0.01 T. It is interesting to also observe that the average rms BN increases with thickness in HGO samples with thicknesses less than 0.35 mm indicating that the so called eddy current effect that increases with thickness of strips and retards domain wall motion wall has no influence as observed.

BN in grain-oriented electrical steel is affected by both average domain width and thickness for strips 0.35 mm thick and above. It increases with increasing domain width and decreases with increasing sample thickness owing to eddy current damping effects as stated previously. Domain width, hence grain size is the only influence on BN for strip thicknesses below 0.35 mm, given the same microstructure.
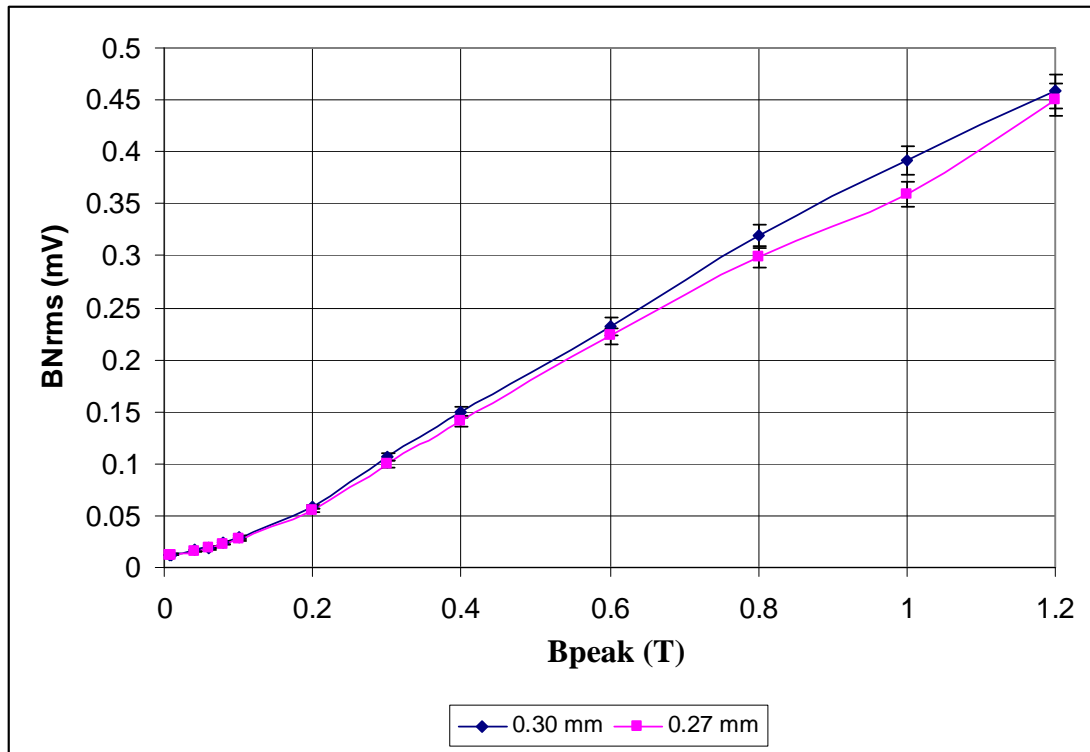
Fig. 10.2: Variation of average rms BN with B in HGO of different thicknesses with peak flux density.

10.4   Influence of thickness on the magnetic properties of CGO and HGO steels

Figure 10.3 shows the variation of average AC relative permeability of the 3 strips each of CGO of the different thicknesses with peak flux density. It is observed that the average AC relative permeability increases with peak flux density in the entire test samples. In all tested materials, it is interesting to observe that the average AC relative permeability is inversely proportional to the thickness of the samples at all the flux densities. The percentage variation of the average AC relative permeability of the CGO samples of thicknesses from 0.30 mm and below and the graph showing the variation of the percentage difference of the 0.35 mm and 0.50 mm thick CGO samples with peak flux density are shown in figures AC 18 and AC 19 of Appendix C.

The variation of the average coercivity of the CGO test samples at different flux densities is shown in figure 10.4. As can be observed, the average coercivity increases

143

as the thickness of the strips increases at all flux densities. The percentage variation of the average coercivity of the test samples is quantified and plotted in figures AC 20 and AC 21 of Appendix C.

The average power loss varies directly with sample thickness at all the flux densities as shown in figure 10.5. The variation of the percentage difference in average power loss of the test samples is shown in figures AC 22 and AC 23 in Appendix C.
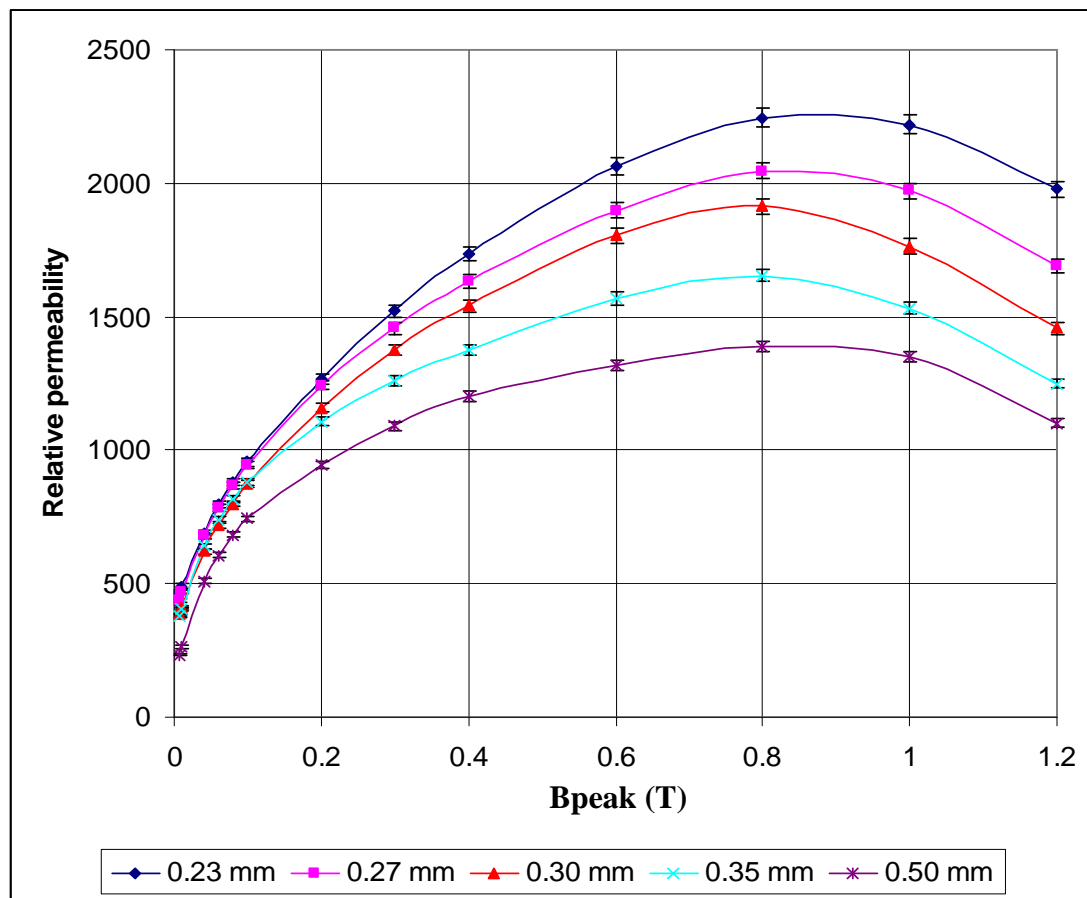
Fig. 10.3: Variation of average relative permeability of CGO of different thicknesses with flux density.
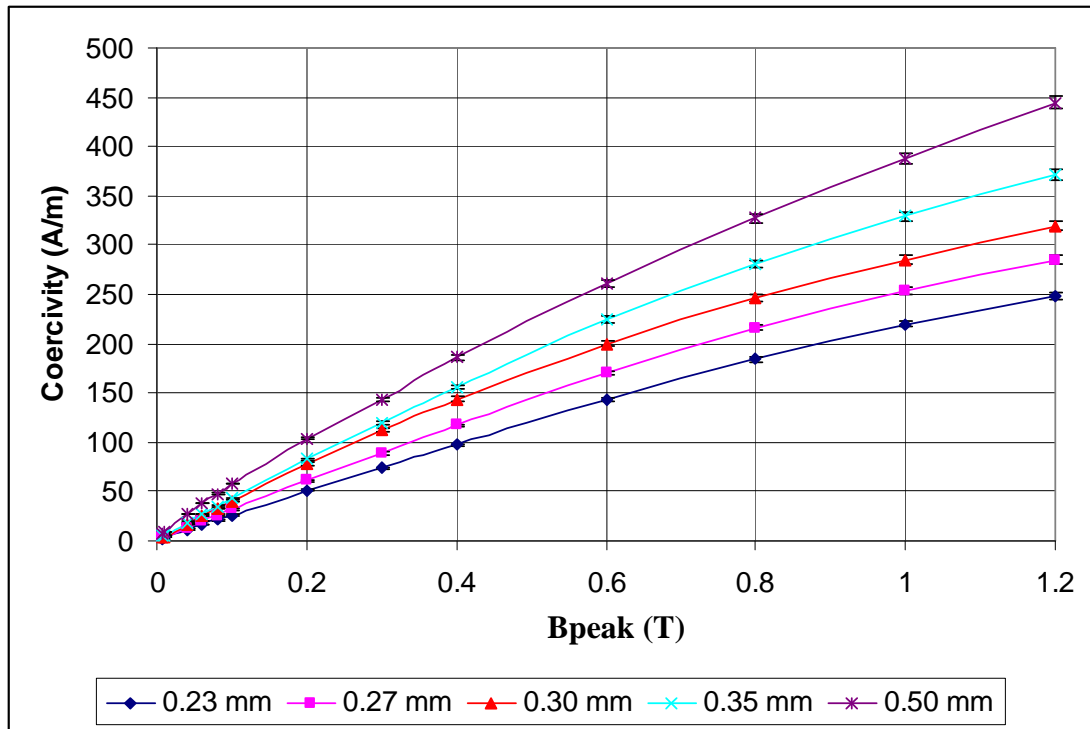
Fig. 10.4: Variation of average coercivity of CGO of different thicknesses with flux density.
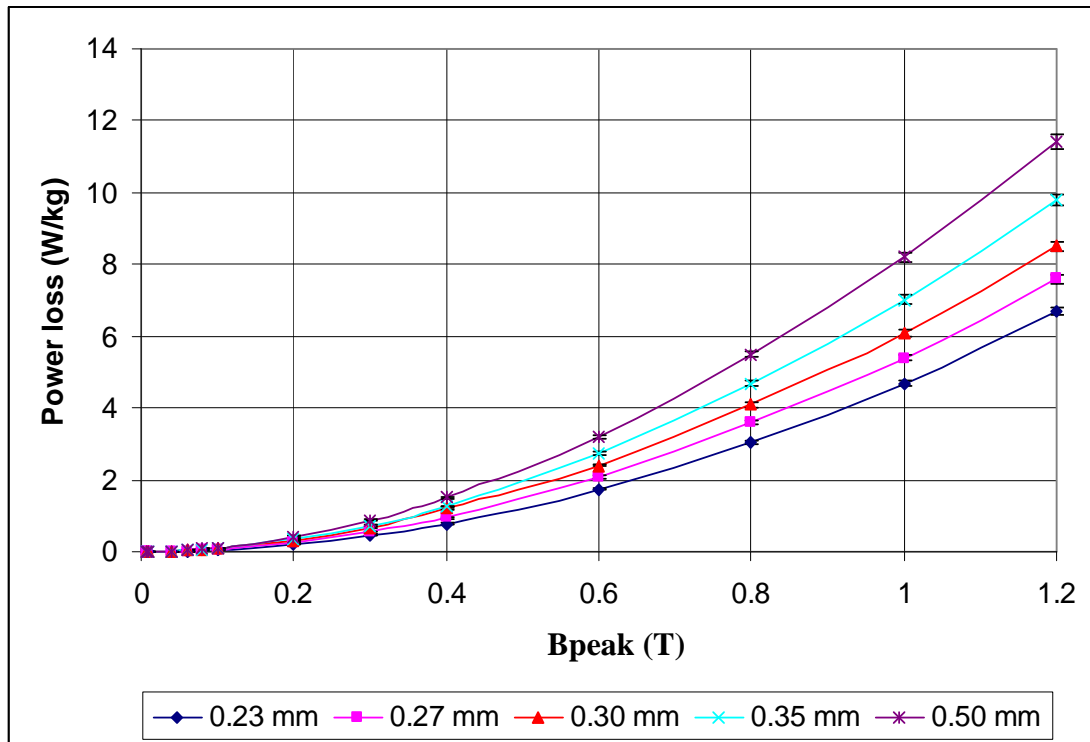
Fig. 10.5: Variation of average power loss of CGO of different thicknesses with peak flux density.

In HGO, the average relative permeability decreases as the sample thickness increases at all flux densities as in CGO. This is shown in figure 10.6 and the quantification of the variation of the percentage differences between the test samples shown in figure AC 24.

Figure 10.7 shows the variation of average coercivity of the 3 strips each of the HGO of thicknesses of 0.27 mm and 0.30 mm with peak flux density. It is observed as in CGO that the average coercivity increases with peak flux density in the entire test samples being higher in the 0.3 mm thick samples. The variation of the percentage difference in average coercivity of the test samples is shown in figure AC 25.

The average power loss show similar trend as coercivity at all flux densities. This is shown in figure 10.8. The variation of the percentage difference in average power loss of the test samples is shown in figure AC 26.

The reason for the observed trends in this part of the investigation is that reducing thickness restrains eddy current loss at power frequency. This accounts for the reduction of power loss and coercivity, and the increase in relative permeability as the thickness decreases in the tested materials.
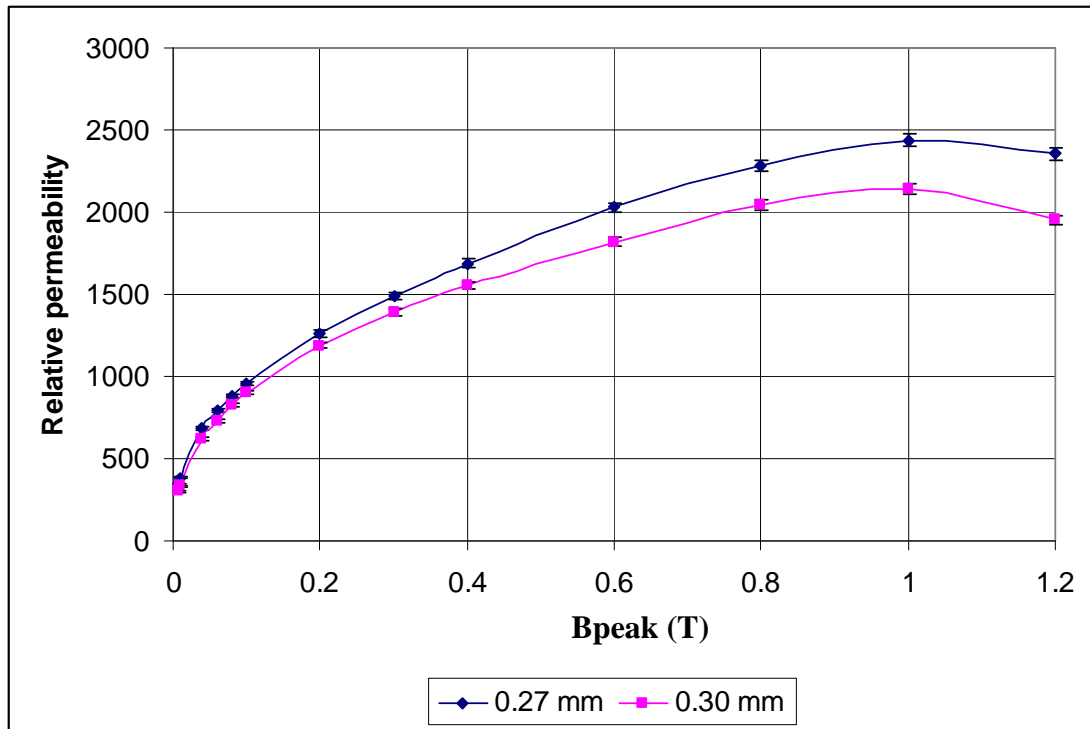
Fig. 10.6: Variation of average relative permeability of HGO of different thicknesses with peak flux density.
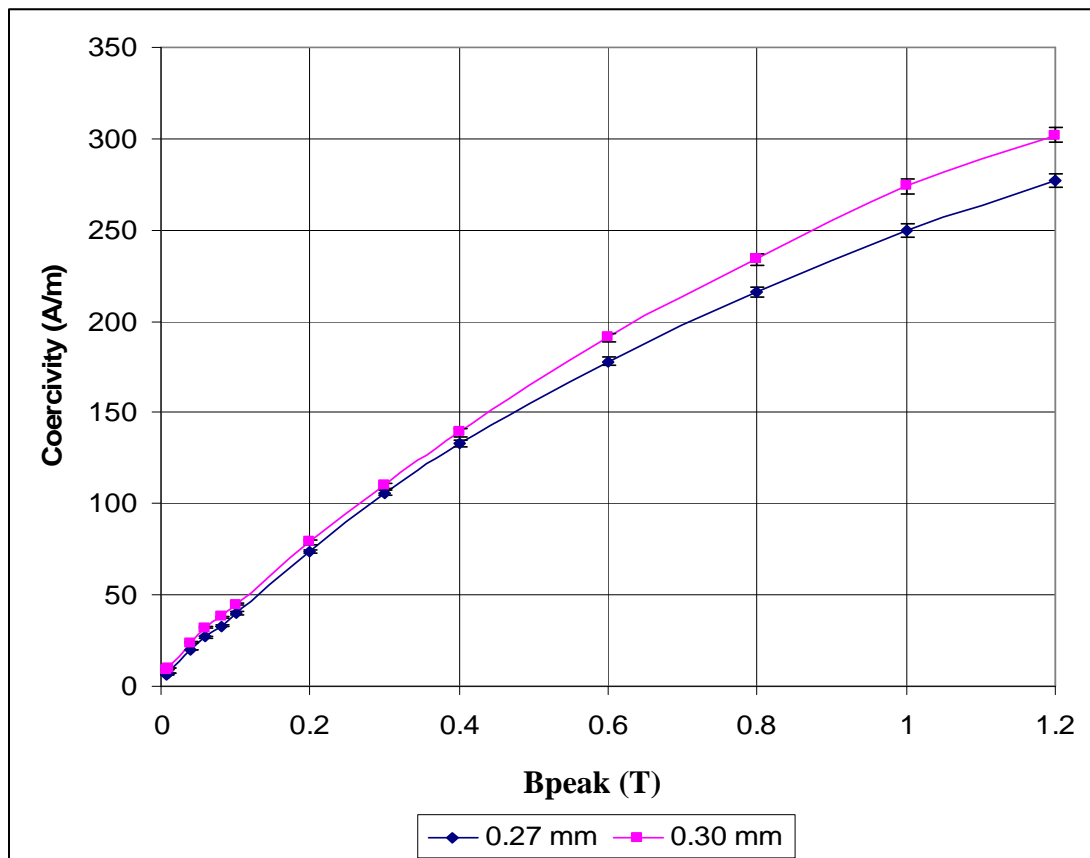
Fig. 10.7: Variation of average coercivity of HGO of different thicknesses with peak flux density.
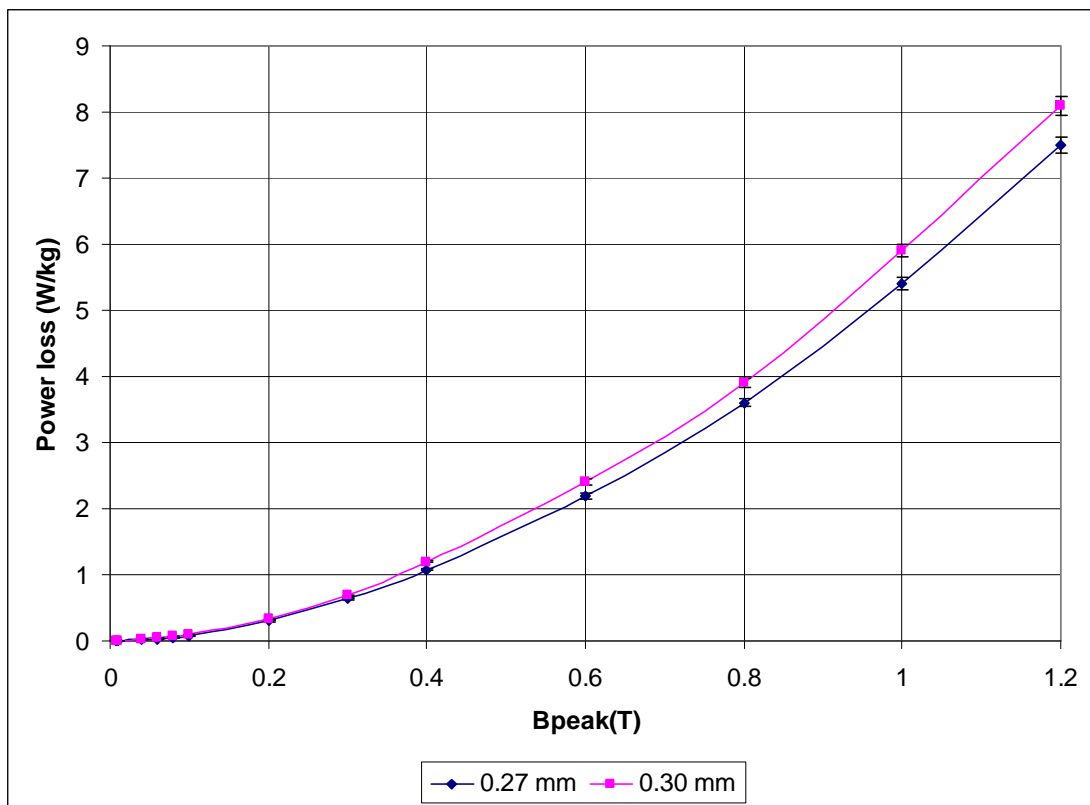
Fig. 10.8: Variation of average power loss of HGO of different thicknesses with peak flux density.

References to chapter 10

[10.1] R. Ranjan, D. C. Jiles and P. K. Rastogi, Magnetic properties of decarburized steels: An investigation of the effects of grain size and carbon content, IEEE Transactions on Magnetics, Vol. 23 , No. 3, pp.1869-1876, 1987.

[10.2] D. G. Hwang, H.C Kim, C.G. Kim, K.A Lee, Barkhausen noise and magnetic properties of highly grain-oriented HiB-8 and conventional 3% Si-Fe polycrystalline specimens, Journal of Korean Physical Society, Vol. 24, No.6, pp. 493-498, 1991.

[10.3] F Brailsford, Physical principles of Magnetism, Van Nostrand, London, 1966.

Chapter 11   Conclusions and future work

11.1   Conclusions

BN in grain-oriented electrical steel at power frequency has different characteristics at high and low flux density.

The larger BN signal of HGO compared to CGO at high flux densities occurs because the grain size of HGO is on average higher than that of CGO. Increased grain size enables domain walls to move further between pinning sites and so generate larger changes in magnetization which results in larger BN signal. In addition, grain to grain misorientation results in a strong suppression of the BN level. At low fields domain walls exhibit a jerky motion consisting of random sequence of Barkhausen jumps whose cumulative effect is higher in amplitude for CGO steels because of increase in the number of grain boundaries and grain boundary area acting as pinning sites since their fractional volume is larger.

Mechanically scribing HGO on one surface transverse to the rolling direction reduced the BN amplitude at high flux densities. This is due to the decrease of domain width by scribing. Then the trend reverses at low flux density. Scribing introduces local strain which decreases domain wall spacing thereby limiting the mean free path of domain walls.

Removal of the coating from the surface of grain-oriented electrical steel at power frequency increase the BN due to the widening of the 180° domains as a result of the release of the tensile stress imparted to the material during coating. The BN characteristics of decoated samples with a 3 MPa tension applied were similar to those observed before decoating demonstrating the close similarity between the effects of coating stress and externally applied stress on BN due to their similar roles in domain refinement. A strong correlation between average velocity of domain wall movement and changes in BN in conventional and high permeability steels was found which demonstrates that the dominant factor responsible for BN emission is the mean free path of domain wall movement and hence the width of the predominant 180° domains in these materials.

BN was also found to be directly proportional to externally applied tensile stress especially at high flux density. As tensile stress is increased, more 180° domain walls are created and this limits the width of domain walls thereby limiting the speed of domain walls movement hence reducing Barkhausen noise amplitude. In this work Barkhausen noise has proved to be a useful technique for detecting the stress sensitivity of grain oriented electrical steel.

BN in grain-oriented electrical steel is affected by both average domain width and thickness for strips 0.35 mm thick and above. It increases with increasing domain width and decreases with increasing sample thickness owing to eddy current damping effects. Domain width, hence grain size is the only influence on BN for strip thicknesses below 0.35 mm, given the same microstructure.

 BN on commercially produced non-oriented steel is influenced by silicon contents and sample thickness. BN was found to increase with decreasing strip thickness and increase with increasing silicon contents owing to eddy current shielding effects. The rms values of the BN and the total sum of amplitudes were found to increase with the rate of change of flux density at all the peak flux densities measured. The findings show that the influence of sample thickness and silicon content is significant and must be taken into consideration when measuring and interpreting BN in non-oriented electrical steel.

11.2   Future work

This investigation has identified the need for further research especially in low field magnetisation and dynamic domain observation in that regime.
There is limited magnetic data at low inductions and no account of the factors which might control the B-H properties. Magnetic characteristics of GOES are measured at high flux densities which are suitable for typical applications in power transformers. The magnetic properties of materials are not usually specified over the low flux density range used in metering current transformer cores and other low flux density applications so performance at this level of magnetisation cannot be predicted with measurements made at high inductions. Little headway is possible unless low flux density characteristics are better assessed and understood.

Dynamic domain observation is required to ascertain the number of domain walls that are active at low and high field magnetization regimes in CGO and HGO steels as BN in electrical steel is principally caused by the movement of domain walls. It may be discovered that dynamic domain observation especially at low fields will reveal new magnetisation features which could be of importance in material development and also to what extent non repeatable domain wall motion occur in that regime.

An extension of the magnetising frequency of the measurement system would be useful as measurements were made at 50 Hz in this work. It will be interesting to observe if similar relationships of BN and magnetic properties seen in this work still exist at higher frequencies.

Further work could also be carried out to understand more the metallurgy of the samples used in this work to have a greater understanding of the results observed in this work.

APPENDIX A

Uncertainty budget of the various parameters measured in the SST under sinusoidal magnetisation at 50 Hz

Table A1: Uncertainty budget of Bpeak in Epstein strips of electrical steel samples measured in the SST under sinusoidal magnetisation.

Sources of uncertainty	Value ± %	Probability distribution	Divisor	c_1	$u(x)$ ± %	v_i or v_{eff}
Accuracy of NI PXI-4461 DAQ	0.347	Normal	2.0000	1	0.1733	∞
Frequency setting	0.002	Normal	2.0000	1	0.0010	∞
Sample mass measurement	0.010	Normal	2.0000	1	0.0050	∞
Sample length measurement	0.100	Rectangular	1.7321	1	0.0946	∞
Control of Bpeak	0.300	Rectangular	1.7321	1	0.1733	∞
Control of form factor	0.300	Rectangular	1.7321	1	0.1733	∞
Sum of squares					0.0989	
Combined uncertainty					0.3146	
Expanded uncertainty					0.6292	
Declared uncertainty in Bpeak					0.6	
at a confidence level of 95 %						

Table A2: Uncertainty budget in Hpeak for Bpeak from 8.0 mT to 0.2 T in Epstein strips of electrical steel samples measured in the SST under sinusoidal magnetisation.

Sources of uncertainty	Value ± %	Probability distribution	Divisor	c_1	$u(x)$ ± %	v_i or v_{eff}
Accuracy of NI PXI-4461 DAQ	0.347	Normal	2.0000	1	0.1735	∞
Frequency setting	0.002	Normal	2.0000	1	0.0010	∞
Shunt resistor	0.009	Normal	2.0000	1	0.0045	∞
Shunt resistor temperature change	0.005	Normal	2.0000	1	0.0025	∞
Magnetic path length	0.100	Rectangular	1.7321	1	0.0577	∞
Dependence on B value	0.629	Rectangular	1.7321	1	0.3631	∞
Repeatability (Type A uncertainty)	0.300	Rectangular	1.7321	1	0.1732	4
Sum of squares					0.1953	
Combined uncertainty					0.4420	
Expanded uncertainty					0.8840	
Declared uncertainty in Bpeak at a confidence level of 95 %					0.9	

Table A3: Uncertainty budget in Hpeak for Bpeak greater than 0.2 T in Epstein strips of electrical steel samples measured in the SST under sinusoidal magnetisation.

Sources of uncertainty	Value ± %	Probability distribution	Divisor	c_1	$u(x)$ ± %	v_i or v_{eff}
Accuracy of NI PXI-4461 DAQ	0.347	Normal	2.0000	1	0.1735	∞
Frequency setting	0.002	Normal	2.0000	1	0.0010	∞
Shunt resistor	0.009	Normal	2.0000	1	0.0045	∞
Shunt resistor temperature change	0.005	Normal	2.0000	1	0.0025	∞
Magnetic path length	0.100	Rectangular	1.7321	1	0.0577	∞
Dependence on B value	0.629	Rectangular	1.7321	1	0.3631	∞
Repeatability (Type A uncertainty)	0.700	Rectangular	1.7321	1	0.4041	4
Sum of squares					0.3286	
Combined uncertainty					0.5733	
Expanded uncertainty					1.146	
Declared uncertainty in Bpeak at a confidence level of 95 %					1	

Table A4: Uncertainty budget in coercivity for Bpeak from 8.0 mT to 0.2 T in Epstein strips of electrical steel samples measured in the SST under sinusoidal magnetisation.

Sources of uncertainty	Value ± %	Probability distribution	Divisor	c_1	$u(x)$ ± %	v_i or v_{eff}
Hpeak uncertainty	0.884	Normal	2.0000	1	0.4420	∞
Repeatability	0.600	Rectangular	1.7321	1	0.3464	4
Sum of squares					0.3154	
Combined uncertainty					0.5616	
Expanded uncertainty					1.123	
Declared uncertainty in Bpeak at a confidence level of 95 %					1.1	

Table A5: Uncertainty budget in coercivity for Bpeak greater than 0.2 T in Epstein strips of electrical steel samples measured in the SST under sinusoidal magnetisation.

Sources of uncertainty	Value ± %	Probability distribution	Divisor	c_1	$u(x)$ ± %	v_i or v_{eff}
Hpeak uncertainty	1.146	Normal	2.0000	1	0.5730	∞
Repeatability	0.700	Rectangular	1.7321	1	0.4041	4
Sum of squares					0.4917	
Combined uncertainty					0.7012	
Expanded uncertainty					1.402	
Declared uncertainty in Bpeak at a confidence level of 95 %					1.4	

Table A6: Uncertainty budget in relative permeability for Bpeak from 8.0 mT to 0.2 T in Epstein strips of electrical steel samples measured in the SST under sinusoidal magnetisation.

Sources of uncertainty	Value ± %	Probability distribution	Divisor	c_1	$u(x)$ ± %	v_i or v_{eff}
Bpeak uncertainty	0.629	Normal	2.0000	1	0.3145	∞
Hpeak uncertainty	0.884	Normal	2.0000	1	0.4420	∞
Repeatability	0.700	Rectangular	1.7321	1	0.4041	4
Sum of squares					0.4576	
Combined uncertainty					0.6765	
Expanded uncertainty					1.3529	
Declared uncertainty in Bpeak at a confidence level of 95 %					1.4	

Table A7: Uncertainty budget in relative permeability for Bpeak greater than 0.2 T in Epstein strips of electrical steel samples measured in the SST under sinusoidal magnetisation.

Sources of uncertainty	Value ± %	Probability distribution	Divisor	c_1	$u(x)$ ± %	v_i or v_{eff}
Bpeak uncertainty	0.629	Normal	2.0000	1	0.3145	∞
Hpeak uncertainty	1.146	Normal	2.0000	1	0.5730	∞
Repeatability	0.400	Rectangular	1.7321	1	0.2309	4
Sum of squares					0.4806	
Combined uncertainty					0.7686	
Expanded uncertainty					1.5373	
Declared uncertainty in Bpeak at a confidence level of 95 %					1.5	

Table A8: Uncertainty budget in specific power loss for Bpeak from 8.0 mT to 0.2 T in Epstein strips of electrical steel samples measured in the SST under sinusoidal magnetisation.

Sources of uncertainty	Value ± %	Probability distribution	Divisor	c_1	$u(x)$ ± %	v_i or v_{eff}
Frequency setting	0.002	Normal	2.0000	1	0.0010	∞
Bpeak uncertainty	0.629	Normal	2.0000	1	0.3145	∞
Hpeak uncertainty	0.884	Normal	2.0000	1	0.4420	∞
Density	0.033	Rectangular	1.7321	1	0.0191	∞
Dependence on B value	0.629	Rectangular	1.7321	1	0.3631	∞
Repeatability (Type A uncertainty)	0.500	Rectangular	1.7321	1	0.2887	4
Sum of squares					0.5098	
Combined uncertainty					0.7140	
Expanded uncertainty					1.4280	
Declared uncertainty in Bpeak at a confidence level of 95 %					1.4	

Table A9: Uncertainty budget in specific power loss for Bpeak greater than 0.2 T in Epstein strips of electrical steel samples measured in the SST under sinusoidal magnetisation.

Sources of uncertainty	Value ± %	Probability distribution	Divisor	c_1	$u(x)$ ± %	v_i or v_{eff}
Frequency setting	0.002	Normal	2.0000	1	0.0010	∞
Bpeak uncertainty	0.629	Normal	2.0000	1	0.3145	∞
Hpeak uncertainty	1.146	Normal	2.0000	1	0.5730	∞
Density	0.033	Rectangular	1.7321	1	0.0191	∞
Dependence on B value	0.629	Rectangular	1.7321	1	0.3631	∞
Repeatability (Type A uncertainty)	0.800	Rectangular	1.7321	1	0.4041	4
Sum of squares					0.7227	
Combined uncertainty					0.8501	
Expanded uncertainty					1.7000	
Declared uncertainty in Bpeak at a confidence level of 95 %					1.7	

Table A10: Uncertainty budget in Barkhausen Noise measurement for Bpeak from 8.0 mT to 0.2 T in Epstein strips electrical steel samples measured in the SST under sinusoidal magnetisation.

Sources of uncertainty	Value ± %	Probability distribution	Divisor	c_1	$u(x)$ ± %	v_i or v_{eff}
Accuracy of NI PXI-4461 DAQ	0.347	Normal	2.0000	1	0.1733	∞
Frequency setting	0.002	Normal	2.0000	1	0.0010	∞
Control of Bpeak	0.300	Rectangular	1.7321	1	0.1733	∞
Control of form factor	0.300	Rectangular	1.7321	1	0.1733	∞
Total harmonic distortion	2.400	Rectangular	1.7321	1	1.3856	∞
Dependence on B value	0.629	Rectangular	1.7321	1	0.3631	∞
Repeatability	2.000	Rectangular	1.7321	1	1.1547	4
Sum of squares					3.4750	
Combined uncertainty					1.8640	
Expanded uncertainty					3.7280	
Declared uncertainty in Bpeak						
at a confidence level of 95 %					4	

Table A11: Uncertainty budget in Barkhausen Noise measurement for Bpeak greater than 0.2 T in Epstein strips of electrical steel samples measured in the SST under sinusoidal magnetisation.

Sources of uncertainty	Value ± %	Probability distribution	Divisor	c_1	$u(x)$ ± %	v_i or v_{eff}
Accuracy of NI PXI-4461 DAQ	0.347	Normal	2.0000	1	0.1733	∞
Frequency setting	0.002	Normal	2.0000	1	0.0010	∞
Control of Bpeak	0.300	Rectangular	1.7321	1	0.1733	∞
Control of form factor	0.300	Rectangular	1.7321	1	0.1733	∞
Total harmonic distortion	2.400	Rectangular	1.7321	1	1.3856	∞
Dependence on B value	0.629	Rectangular	1.7321	1	0.3631	∞
Repeatability	1.200	Rectangular	1.7321	1	0.6928	4
Sum of squares					3.1290	
Combined uncertainty					1.7689	
Expanded uncertainty					3.5378	
Declared uncertainty in Bpeak at a confidence level of 95 %					3.5	

Table A12: Uncertainty budget in measurement of BN of Epstein strips with the application of tension using tension stressing rig for Bpeak from 8 mT to 0.2 T.

Sources of uncertainty	Value ± %	Probability distribution	Divisor	c_1	$u(x)$ ± %	v_i or v_{eff}
Accuracy of NI PXI-4461 DAQ	0.347	Normal	2.0000	1	0.1735	∞
Frequency setting	0.002	Normal	2.0000	1	0.0010	∞
Accuracy of strain amplifier	0.050	Normal	2.0000	1	0.0250	∞
Accuracy of the shunt calibration resistors	0.050	Normal	2.0000	1	0.0250	∞
Thickness of the sample	0.830	Normal	2.0000	1	0.4150	∞
Width of the sample	0.070	Normal	2.0000	1	0.0350	∞
Gauge factor	1.000	Normal	2.0000	1	0.5000	∞
Jaw gripping	2.500	Rectangular	1.7321	1	1.4433	∞
Dependence on B value	0.629	Rectangular	1.7321	1	0.3631	∞
Repeatability	2.000	Rectangular	1.7321	1	1.1546	4
Sum of squares					4.0028	
Combined uncertainty Expanded uncertainty					2.0007 4.0014	
Declared uncertainty in Bpeak at a confidence level of 95 %					4	

Table A13: Uncertainty budget in measurement of BN of Epstein strips with the application of tension using tension stressing rig for Bpeak above 0.2 T.

Sources of uncertainty	Value ± %	Probability distribution	Divisor	c_1	$u(x)$ ± %	v_i or v_{eff}
Accuracy of NI PXI-4461 DAQ	0.347	Normal	2.0000	1	0.1735	∞
Frequency setting	0.002	Normal	2.0000	1	0.0010	∞
Accuracy of strain amplifier	0.050	Normal	2.0000	1	0.0250	∞
Accuracy of the shunt calibration resistors	0.050	Normal	2.0000	1	0.0250	∞
Thickness of the sample	0.830	Normal	2.0000	1	0.4150	∞
Width of the sample	0.070	Normal	2.0000	1	0.0350	∞
Gauge factor	1.000	Normal	2.0000	1	0.5000	∞
Jaw gripping	2.500	Rectangular	1.7321	1	1.4433	∞
Dependence on B value	0.629	Rectangular	1.7321	1	0.3631	∞
Repeatability	1.200	Rectangular	1.7321	1	0.6928	4
Sum of squares					3.1497	
Combined uncertainty Expanded uncertainty Declared uncertainty in Bpeak at a confidence level of 95 %					1.7747 3.5495 3.5	

Appendix B

List of type A uncertainty of measurements

Table B1: Type A uncertainty (U_A) of peak magnetic field (H_{peak}) of test samples measured in the single sheet tester (SST)

B_{peak}(T)	HGO		CGO	
	Average H_{peak}(A/m)	$U_A(H_{peak})$ (%)	Average H_{peak}(A/m)	$U_A(H_{peak})$ (%)
0.008	0.743	0.3	0.98	0.31
0.01	0.859	0.26	1.16	0.28
0.04	2.3	0.29	3.2	0.29
0.06	2.98	0.22	4.14	0.3
0.08	3.59	0.27	4.96	0.3
0.1	4.13	0.2	5.68	0.26
0.2	6.41	0.25	8.43	0.27
0.3	8.37	0.24	10.61	0.35
0.4	10.03	0.36	12.49	0.32
0.6	12.8	0.29	15.67	0.38
0.8	15.31	0.4	18.66	0.45
1.0	17.63	0.5	21.72	0.47
1.2	20.02	0.45	26.25	0.69
1.3	21.18	0.67	30.56	0.65
1.4	22.7	0.6	38.11	0.56
1.5	24.6	0.52	51.62	0.5

Table B2: Type A uncertainty (U_A) of coercivity of test samples measured in the single sheet tester (SST)

B_{peak}(T)	HGO		CGO	
	Average coercivity(A/m)	U_A(coercivity) (%)	Average coercivity(A/m)	U_A(coercivity) (%)
0.008	0.262	0.59	0.278	0.6
0.01	0.302	0.48	0.322	0.55
0.04	0.93	0.55	0.973	0.53
0.06	1.34	0.43	1.47	0.34
0.08	1.74	0.38	1.93	0.43
0.1	2.11	0.45	2.37	0.4
0.2	3.78	0.4	4.32	0.46
0.3	5.38	0.54	6.03	0.38
0.4	6.89	0.6	7.65	0.33
0.6	9.5	0.65	10.63	0.34
0.8	11.86	0.56	13.42	0.61
1	14.1	0.52	15.94	0.42
1.2	16.33	0.38	18.24	0.44
1.3	17.34	0.36	19.26	0.4
1.4	18.36	0.4	20.26	0.35
1.5	19.258	0.35	21.376	0.33

Table B3: Type A uncertainty (U_A) of relative permeability (μ_r) of test samples measured in the single sheet tester (SST)

B_{peak}(T)	HGO		CGO	
	Average μ_r	$U_A(\mu_r)$ (%)	Average μ_r	$U_A(\mu_r)$ (%)
0.008	8567	0.52	23123	0.62
0.01	9253	0.5	29221	0.55
0.04	13843	0.31	33846	0.35
0.06	16031	0.15	36361	0.25
0.08	17754	0.53	36618	0.58
0.1	19257	0.7	34093	0.67
0.2	24828	0.61	30465	0.51
0.3	28534	0.35	25481	0.38
0.4	31717	0.33	22486	0.36
0.6	37304	0.4	18886	0.34
0.8	41570	0.31	14007	0.3
1	45120	0.35	12833	0.25
1.2	47687	0.5	11528	0.36
1.3	48510	0.32	9956	0.22
1.4	48813	0.28	6879	0.38
1.5	49083	0.3	6500	0.32

Table B4: Type A uncertainty (U_A) power loss of test samples measured in the single sheet tester (SST)

B_{peak}(T)	HGO		CGO	
	Average Power loss (W/kg)	U_A(power loss) (%)	Average Power loss(W/kg)	U_A(power loss) (%)
0.008	0.000044	0.5	0.000045	0.48
0.01	0.000063	0.44	0.000066	0.5
0.04	0.00079	0.42	0.0008	0.46
0.06	0.0016	0.38	0.002	0.48
0.08	0.0028	0.45	0.003	0.45
0.1	0.004	0.4	0.005	0.36
0.2	0.016	0.38	0.018	0.39
0.3	0.033	0.36	0.037	0.8
0.4	0.057	0.46	0.063	0.72
0.6	0.12	0.55	0.133	0.7
0.8	0.2	0.58	0.229	0.66
1	0.304	0.65	0.354	0.67
1.2	0.437	0.75	0.512	0.72
1.3	0.515	0.7	0.608	0.68
1.4	0.605	0.71	0.726	0.65
1.5	0.705	0.66	0.881	0.6

Table B5: Type A uncertainty of rms BN of HGO and CGO from Producer 1 measured in the SST

B_{peak}(T)	HGO		CGO	
	Average rms BN (mV)	U_A (rms BN of HGO) (%)	Average rms BN (mV)	U_A(rms BN of CGO)
0.008	0.010744	1.40	0.01277	1.35
0.01	0.01188	1.43	0.01283	1.13
0.04	0.0149	0.71	0.01681	1.30
0.06	0.01805	0.64	0.0209	1.20
0.08	0.02206	0.66	0.02561	0.58
0.1	0.02659	0.89	0.03053	1.11
0.2	0.05541	0.82	0.05822	1.20
0.3	0.09785	0.71	0.08748	0.90
0.4	0.1408	0.82	0.1163	0.81
0.5	0.1835	1.02	0.1439	0.79
0.6	0.2203	1.01	0.1742	0.48
0.8	0.2913	0.77	0.2331	0.39
1.0	0.3618	0.57	0.2949	0.37
1.2	0.4408	0.42	0.3682	0.29
1.5	0.5821	0.12	0.5218	0.30

Table B6: Type A uncertainty of rms BN of HGO and CGO from Producer 2 measured in the SST

B_{peak}(T)	HGO		CGO	
	Average rms BN (mV)	U_A (rms BN of HGO) (%)	Average rms BN (mV)	U_A(rms BN of CGO)
0.008	0.01183	1.31	0.01262	1.26
0.01	0.01209	1.38	0.01286	1.34
0.04	0.016	0.73	0.01724	1.01
0.06	0.01924	0.56	0.02151	1.08
0.08	0.02323	0.56	0.02644	1.01
0.1	0.02763	0.85	0.03134	1.14
0.2	0.05452	0.73	0.05946	1.19
0.3	0.09275	0.76	0.09244	0.87
0.4	0.1359	0.87	0.1276	0.79
0.5	0.1736	0.97	0.1601	0.68
0.6	0.2129	0.89	0.1976	0.41
0.8	0.2859	0.77	0.2616	0.33
1.0	0.359	0.69	0.3364	0.28
1.2	0.4345	0.38	0.4109	0.22
1.5	0.5544	0.19	0.553	0.26

Table B7: Type A uncertainty of TSA of BN of HGO and CGO from Producer 1 measured in the SST

B_{peak}(T)	HGO		CGO	
	Average TSA of BN (V)	U_A (TSA of HGO) (%)	Average TSA of BN (V)	U_A(TSA of CGO)
0.008	0.0282	0.98	0.0303	1.18
0.01	0.0282	0.87	0.0305	0.76
0.04	0.0357	0.53	0.0394	0.62
0.06	0.043	0.48	0.0484	0.53
0.08	0.0511	0.39	0.0579	0.35
0.1	0.0599	0.31	0.0699	0.37
0.2	0.122	0.52	0.127	0.46
0.3	0.211	0.32	0.191	0.37
0.4	0.297	0.35	0.255	0.49
0.5	0.388	0.29	0.321	0.39
0.6	0.468	0.35	0.377	0.31
0.8	0.631	0.31	0.527	0.28
1.0	0.791	0.21	0.671	0.28
1.2	0.974	0.21	0.847	0.17
1.5	1.32	0.15	1.205	0.13

Table B 8: Type A uncertainty of TSA of BN of HGO and CGO from Producer 2 measured in the SST

B_{peak}(T)	HGO		CGO	
	Average TSA of BN (V)	U_A (TSA of HGO) (%)	Average TSA of BN (V)	U_A(TSA of CGO)
0.008	0.0285	1.08	0.0304	1.13
0.01	0.0288	0.88	0.0309	0.86
0.04	0.0378	0.50	0.0407	0.60
0.06	0.0451	0.58	0.0495	0.55
0.08	0.0539	0.49	0.0604	0.36
0.1	0.0634	0.33	0.071	0.31
0.2	0.121	0.56	0.13	0.45
0.3	0.2	0.31	0.201	0.39
0.4	0.288	0.38	0.278	0.42
0.5	0.369	0.31	0.348	0.36
0.6	0.449	0.33	0.427	0.34
0.8	0.61	0.33	0.573	0.29
1.0	0.773	0.22	0.747	0.23
1.2	0.952	0.22	0.927	0.19
1.5	1.269	0.17	1.235	0.14

Table B9: Type A uncertainty of rms of BN of HGO, domain refined HGO and CGO measured in the SST

B_{peak}(T)	HGO		DR HGO		CGO	
	Average rms BN (mV)	U_A (rms BN of HGO (%)	Average rms BN (mV)	U_A (rms BN of DR HGO) (%)	Average rms BN (mV)	U_A (rms BN of CGO) (%)
0.008	0.012	1.32	0.0118	1.06	0.013	1.38
0.01	0.0118	1.40	0.0124	1.37	0.013	1.11
0.04	0.0148	0.71	0.0146	2.01	0.016	0.79
0.06	0.0173	0.56	0.0181	1.88	0.019	0.53
0.08	0.0214	0.56	0.024	1.51	0.024	0.52
0.1	0.0253	0.85	0.0292	1.40	0.028	0.38
0.2	0.0548	0.73	0.064	1.19	0.055	0.50
0.4	0.13	0.76	0.136	0.87	0.113	0.43
0.6	0.209	0.80	0.209	0.79	0.172	0.53
0.8	0.281	0.97	0.268	0.68	0.245	0.61
1	0.377	0.89	0.353	0.41	0.313	0.57
1.2	0.475	0.77	0.464	0.30	0.399	0.31
1.3	0.532	0.49	0.512	0.28	0.448	0.25

Table B10: Type A uncertainty of TSA of BN of HGO, domain refined HGO and CGO measured in the SST

B_{peak}(T)	HGO		DR HGO		CGO	
	Average TSA (V)	U_A (TSA of HGO (%)	Average TSA (V)	U_A (TSA of DR HGO) (%)	Average TSA (V)	U_A (TSA of CGO) (%)
0.008	0.029	1.22	0.028	1.06	0.031	1.30
0.01	0.028	1.10	0.029	1.37	0.032	1.21
0.04	0.035	0.91	0.035	2.01	0.038	0.76
0.06	0.041	0.65	0.043	1.88	0.045	0.56
0.08	0.05	0.58	0.055	1.51	0.055	0.50
0.1	0.058	0.76	0.066	1.40	0.063	0.48
0.2	0.12	0.75	0.14	1.19	0.12	0.59
0.4	0.28	0.79	0.29	0.87	0.25	0.49
0.6	0.45	0.82	0.45	0.79	0.38	0.63
0.8	0.61	0.90	0.59	0.68	0.55	0.71
1	0.83	0.88	0.79	0.41	0.71	0.67
1.2	1.07	0.74	1.04	0.30	0.9	0.41
1.3	1.18	0.46	1.17	0.28	1.01	0.35

Table B11: Type A uncertainty of rms of BN of Coated and Decoated CGO measured in the SST

$B_{peak}(T)$	Coated CGO		Decoated CGO	
	Average rms of BN (mV)	U_A (rms BN of Coated CGO) (%)	Average rms of BN (mV)	U_A(rms BN of Decoated CGO)
0.008	0.013017	0.78	0.0131	0.70
0.01	0.013167	0.85	0.0133	0.65
0.04	0.0162	0.73	0.0189	0.68
0.06	0.019667	0.77	0.0259	0.54
0.08	0.02465	0.48	0.0331	0.43
0.1	0.0301	0.67	0.0416	0.55
0.2	0.060767	0.57	0.0822	0.46
0.3	0.0937	0.49	0.124	0.41
0.4	0.122833	0.78	0.163	0.60
0.6	0.189	0.43	0.25	0.52
0.8	0.262667	0.40	0.336	0.33
1.0	0.332167	0.38	0.448	0.31

Table B12: Type A uncertainty of rms of BN of Coated and Decoated HGO measured in the SST

$B_{peak}(T)$	Coated HGO		Decoated HGO	
	Average rms of BN (mV)	U_A (rms BN of Coated HGO) (%)	Average rms of BN (mV)	U_A(rms BN of Decoated HGO)
0.008	0.011783	0.98	0.0132	1.10
0.01	0.011683	0.89	0.0136	0.96
0.04	0.01405	0.70	0.019	0.62
0.06	0.016633	0.68	0.0265	0.55
0.08	0.0207	0.45	0.0348	0.38
0.1	0.0255	0.37	0.0468	0.51
0.2	0.056467	0.50	0.0943	0.49
0.3	0.095533	0.41	0.143	0.49
0.4	0.1375	0.58	0.186	0.40
0.6	0.213333	0.51	0.279	0.56
0.8	0.287667	0.43	0.377	0.44
1.0	0.361833	0.35	0.493	0.30

Table B13: Type A uncertainty of rms of BN of Decoated HGO and CGO measured in the SST with tension of 3 MPa applied

$B_{peak}(T)$	Decoated HGO with 3 MPa		Decoated CGO with 3 MPa	
	Average rms of BN (mV)	U_A (rms BN of Decoated HGO) (%)	Average rms of BN (mV)	U_A(rms BN of Decoated CGO)
0.008	0.0132	1.21	0.011783	1.40
0.01	0.0136	1.31	0.011683	0.96
0.04	0.019	0.98	0.01405	1.25
0.06	0.0265	1.01	0.016633	1.22
0.08	0.0348	0.75	0.0207	0.88
0.1	0.0468	0.87	0.0255	0.71
0.2	0.0943	0.76	0.056467	0.69
0.3	0.143	0.58	0.095533	0.53
0.4	0.186	0.69	0.1375	0.41
0.6	0.279	0.57	0.213333	0.52
0.8	0.377	0.46	0.287667	0.40
1.0	0.493	0.42	0.361833	0.31

Table B14: Type A uncertainty of rms of BN of NGO (3% Si) of different thicknesses measured in the SST

$B_{peak}(T)$	0.35 mm thick		0.5 mm thick		0.65 mm thick	
	Average rms BN (mV)	U_A (%)	Average rms BN (mV)	U_A (%)	Average rms BN (mV)	U_A (%)
0.008	0.0135	1.55	0.0133	1.46	0.0127	1.32
0.01	0.0138	1.28	0.0134	1.31	0.0127	1.20
0.04	0.0175	1.91	0.0155	1.21	0.014	1.76
0.06	0.0236	1.65	0.02	1.80	0.0166	1.54
0.08	0.0296	0.98	0.0224	1.31	0.0201	0.80
0.1	0.0372	0.96	0.0262	1.00	0.024	0.88
0.2	0.0698	0.70	0.0472	0.80	0.0394	0.49
0.3	0.0982	0.71	0.0678	0.67	0.0604	0.44
0.4	0.129	0.62	0.0903	0.49	0.0806	0.33
0.6	0.175	0.50	0.13	0.48	0.108	0.31

Table B15: Type A uncertainty of TSA of BN of NGO (3% Si) of different thicknesses measured in the SST

B_{peak}(T)	0.35 mm thick		0.5 mm thick		0.65 mm thick	
	Average TSA BN (V)	U_A (%)	Average TSA (V)	U_A (%)	Average TSA BN (V)	U_A (%)
0.008	0.032	1.45	0.032	1.36	0.031	1.39
0.01	0.033	1.21	0.032	1.41	0.03	1.25
0.04	0.041	1.18	0.037	1.20	0.033	1.26
0.06	0.055	1.66	0.047	1.32	0.039	1.14
0.08	0.066	1.08	0.052	1.21	0.048	0.98
0.1	0.082	0.90	0.06	1.02	0.055	0.82
0.2	0.152	0.75	0.103	0.83	0.088	0.53
0.3	0.217	0.77	0.148	0.77	0.132	0.45
0.4	0.285	0.52	0.199	0.45	0.175	0.53
0.6	0.386	0.48	0.285	0.40	0.239	0.41

Table B16: Type A uncertainty of TNP of BN of NGO (3% Si) of different thicknesses measured in the SST

B_{peak}(T)	0.35 mm thick		0.5 mm thick		0.65 mm thick	
	Average TNP	U_A (%)	Average TNP	U_A (%)	Average TNP	U_A (%)
0.008	2013	1.26	2037	1.09	2057	1.18
0.01	2000	1.15	2006	1.21	2043	1.20
0.04	1961	1.10	1970	1.14	2024	1.16
0.06	1930	1.36	1940	1.42	1977	1.23
0.08	1879	1.18	1914	1.02	1924	0.93
0.1	1846	0.91	1880	1.00	1904	0.72
0.2	1835	0.68	1851	0.63	1871	0.59
0.3	1827	0.57	1840	0.70	1860	0.55
0.4	1791	0.60	1815	0.55	1830	0.50
0.6	1762	0.32	1813	0.38	1820	0.44

Table B17: Type A uncertainty of dB/dt of NGO (3% Si) of different thicknesses measured in the SST

B_{peak}(T)	0.35 mm thick		0.5 mm thick		0.65 mm thick	
	Average dB/dt	U_A (%)	Average dB/dt	U_A (%)	Average dB/dt	U_A (%)
0.008	1.265	0.89	1.255	1.12	1.24	1.08
0.01	1.555	1.10	1.555	1.11	1.54	1.14
0.04	6.145	0.96	6.115	1.18	6.115	1.06
0.06	9.225	1.06	9.195	1.02	9.09	0.86
0.08	12.19	0.87	12.175	0.84	12.02	0.73
0.1	15.11	0.90	15.095	0.95	14.885	0.76
0.2	28.605	0.78	28.165	0.68	28.165	0.69
0.3	40.565	0.77	39.96	0.50	39.06	0.58
0.4	51.07	0.69	50.39	0.49	48.675	0.65
0.6	69.465	0.38	68.09	0.41	66.165	0.47

Table B 18: Type A uncertainty of rms of BN of NGO (0.5 mm thick) of different silicon contents measured in the SST

B_{peak}(T)	1.8% Si		1.3% Si		0.3% Si	
	Average rms BN (mV)	U_A (%)	Average rms BN (mV)	U_A (%)	Average rms BN (mV)	U_A (%)
0.008	0.0132	1.05	0.0117	1.16	0.0109	1.22
0.01	0.0132	1.20	0.0116	1.11	0.0103	1.00
0.04	0.0169	1.01	0.015	1.22	0.014	1.16
0.06	0.0221	0.95	0.0204	1.10	0.0185	1.04
0.08	0.0294	0.78	0.0265	0.65	0.0219	0.82
0.1	0.0383	0.92	0.027	0.78	0.0251	0.83
0.2	0.0958	0.67	0.0533	0.80	0.0498	0.41
0.3	0.158	0.61	0.0741	0.67	0.062	0.44

Table B19: Type A uncertainty of dB/dt of NGO (0.5 mm thick) of different silicon contents measured in the SST

B_{peak}(T)	1.8% Si		1.3% Si		0.3% Si	
	Average dB/dt	U_A (%)	Average dB/dt	U_A (%)	Average dB/dt	U_A (%)
0.008	2.54	1.02	2.51	0.85	2.47	1.04
0.01	3.16	1.04	3.12	1.01	3.09	1.02
0.04	12.46	1.11	12.38	1.00	12.36	0.89
0.06	18.71	0.94	18.57	1.02	18.48	0.81
0.08	24.77	1.08	24.61	0.87	24.46	0.98
0.1	30.65	0.87	30.57	1.03	29.5	0.63
0.2	57.77	0.75	56.92	0.54	53	0.47
0.3	81.54	0.65	79.18	0.42	73	0.51

Table B20: Type A uncertainty of dB/dt of NGO (0.5 mm thick) of different silicon contents measured in the SST

B_{peak}(T)	1.8% Si		1.3% Si		0.3% Si	
	Average dB/dt	U_A (%)	Average dB/dt	U_A (%)	Average dB/dt	U_A (%)
0.008	2.54	0.86	2.51	1.10	2.47	1.18
0.01	3.16	1.13	3.12	1.09	3.09	1.01
0.04	12.46	0.92	12.38	1.06	12.36	0.93
0.06	18.71	1.09	18.57	0.97	18.48	0.89
0.08	24.77	0.89	24.61	0.88	24.46	0.75
0.1	30.65	0.92	30.57	0.65	29.5	0.67
0.2	57.77	0.79	56.92	0.61	53	0.58
0.3	81.54	0.70	79.18	0.46	73	0.51

Table B21: Type A uncertainty of TNP of BN of NGO (0.5 mm thick) of different thicknesses measured in the SST

B_{peak}(T)	1.8% Si		1.3% Si		0.3% Si	
	Average TNP	U_A (%)	Average TNP	U_A (%)	Average TNP	U_A (%)
0.008	1795	1.16	1783	1.19	1775	1.17
0.01	1847	1.15	1795	1.11	1790	1.09
0.04	1898	0.91	1880	1.04	1870	1.12
0.06	1939	1.06	1920	1.12	1886	1.13
0.08	1970	1.01	1940	0.85	1925	0.73
0.1	1998	0.78	1978	0.62	1964	0.76
0.2	2032	0.62	2006	0.61	2000	0.54
0.3	2040	0.58	2024	0.40	2017	0.52

Table B22: Type A uncertainty of rms of BN of CGO of different thicknesses measured in the SST

B_{peak}(T)	0.30 mm thick		0.27 mm thick		0.23 mm thick	
	Average rms BN (mV)	U_A (%)	Average rms BN (mV)	U_A (%)	Average rms BN (mV)	U_A (%)
0.008	0.0135	1.02	0.0135	1.08	0.0133	0.96
0.01	0.013	1.00	0.0134	1.17	0.0138	1.01
0.04	0.0161	0.81	0.0161	1.01	0.0167	0.88
0.06	0.0201	0.69	0.0192	1.08	0.0192	0.64
0.08	0.0243	0.59	0.0237	0.69	0.0232	0.57
0.1	0.0296	0.86	0.0291	1.00	0.0287	0.58
0.2	0.059	0.79	0.0563	0.92	0.0541	0.65
0.3	0.0901	0.69	0.0885	0.71	0.0821	0.42
0.4	0.119	0.84	0.118	0.82	0.109	0.61
0.6	0.185	0.78	0.181	0.61	0.178	0.77
0.8	0.258	0.89	0.256	0.53	0.239	0.66
1	0.334	0.64	0.329	0.39	0.327	0.40
1.2	0.412	0.41	0.400	0.36	0.396	0.36

Table B23: Type A uncertainty of rms of BN of CGO of different thicknesses measured in the SST

B_{peak}(T)	0.50 mm thick		0.35 mm thick	
	Average rms BN (mV)	U_A (%)	Average rms BN (mV)	$U_{A\,\%}$
0.008	0.0137	1.18	0.0131	1.12
0.01	0.0137	0.98	0.0133	0.88
0.04	0.0189	1.01	0.0154	0.68
0.06	0.0232	0.89	0.0179	0.95
0.08	0.0284	0.65	0.0215	0.43
0.1	0.0337	0.56	0.0274	0.39
0.2	0.0617	0.58	0.056	0.65
0.3	0.0973	0.71	0.0861	0.43
0.4	0.125	0.49	0.119	0.44
0.6	0.184	0.61	0.191	0.39
0.8	0.264	0.73	0.266	0.36
1	0.325	0.38	0.363	0.49
1.2	0.394	0.39	0.44	0.43

Table B24: Type A uncertainty of rms of BN of HGO of different thicknesses measured in the SST

B_{peak}(T)	0.50 mm thick		0.35 mm thick	
	Average rms BN (mV)	U_A (%)	Average rms BN (mV)	U_A(%)
0.008	0.0122	0.99	0.012367	1.10
0.01	0.0123	0.91	0.0125	0.67
0.04	0.0165	1.03	0.0154	0.78
0.06	0.0197	1.05	0.0183	0.79
0.08	0.0243	0.81	0.022333	0.67
0.1	0.0294	0.54	0.0272	0.43
0.2	0.0589	0.78	0.0556	0.60
0.3	0.107	0.77	0.0996	0.53
0.4	0.15	0.41	0.141	0.64
0.6	0.232	0.64	0.223	0.51
0.8	0.319	0.70	0.299	0.42
1	0.392	0.42	0.359	0.50
1.2	0.458	0.35	0.45	0.41

Table B25: Type A uncertainty of rms of BN of HGO with black marks defects on whole and half sample length measured in the SST

B_{peak}(T)	Black marks on half sample length		Black marks on full sample length	
	Average rms BN (mV)	U_A (%)	Average rms BN (mV)	U_A (%)
0.008	0.0137	1.81	0.013	1.29
0.01	0.0138	1.68	0.0135	1.38
0.04	0.0168	1.73	0.0202	1.31
0.06	0.0213	1.56	0.0256	1.38
0.08	0.025	0.96	0.0293	1.21
0.1	0.0307	0.85	0.0348	1.11
0.2	0.0593	0.93	0.061	1.10
0.3	0.0834	0.79	0.0848	0.97
0.4	0.117	1.17	0.112	0.72
0.6	0.173	1.07	0.162	0.98
0.8	0.22	0.88	0.213	0.91
1.0	0.287	0.79	0.272	1.13
1.2	0.371	0.79	0.334	0.88
1.3	0.398	0.48	0.373	0.52

Table B26: Type A uncertainty of rms of BN of HGO with burst marks, smudge marks and rough surface defects measured in the SST

B_{peak}(T)	Burst mark defects		Smudge mark defects		Rough surface defects	
	Average rms BN (mV)	U_A(%)	Average rms BN (mV)	U_A (%)	Average rms BN (mV)	U_A(%)
0.008	0.0137	1.62	0.0162	1.57	0.0154	1.41
0.01	0.0151	1.60	0.0159	1.43	0.0158	1.88
0.04	0.0209	1.03	0.0242	1.23	0.0255	1.23
0.06	0.0263	1.37	0.0323	1.06	0.0323	1.51
0.08	0.0309	0.90	0.0401	0.92	0.0406	1.06
0.1	0.0385	1.85	0.0491	0.81	0.0458	0.82
0.2	0.0676	0.99	0.0937	0.90	0.0893	1.13
0.3	0.0967	1.01	0.135	0.88	0.135	0.73
0.4	0.128	1.10	0.166	1.18	0.179	1.10
0.6	0.176	1.00	0.243	1.03	0.27	1.07
0.8	0.239	0.84	0.311	0.76	0.35	0.98
1.0	0.317	0.89	0.396	0.71	0.416	0.70
1.2	0.373	0.75	0.482	0.92	0.511	0.99
1.3	0.42	0.46	0.548	0.88	0.569	0.68

APPENDIX C

Graphs of variations of percentage difference of the measured properties at different peak flux densities
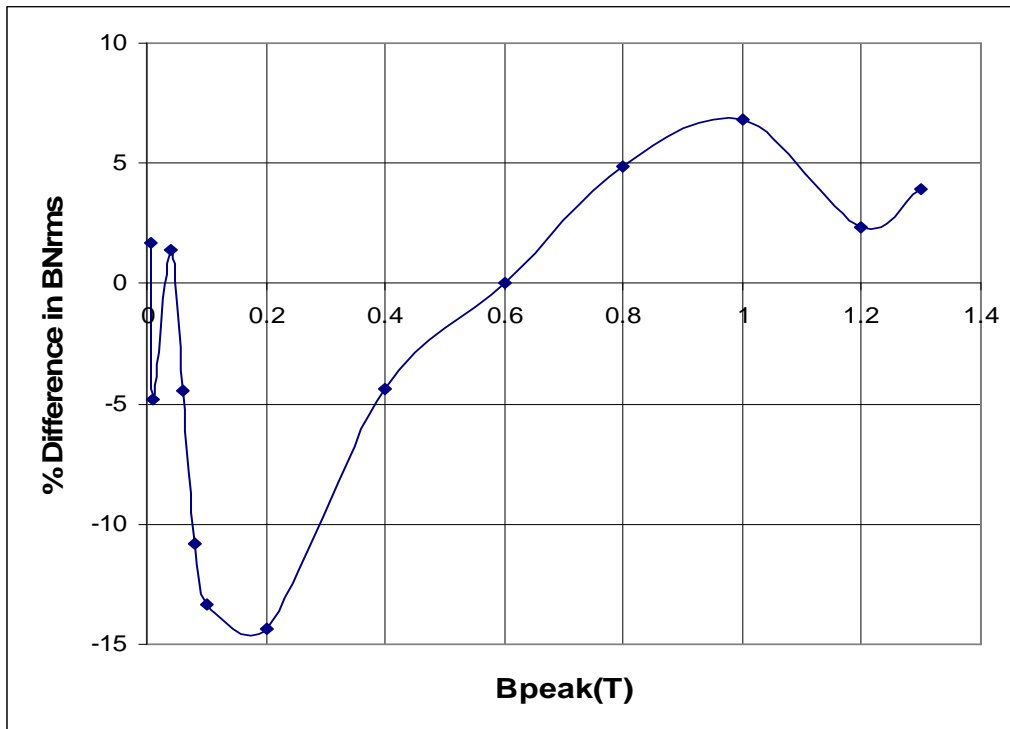
Fig. AC 1: Variation of percentage difference of average rms BN of HGO and domain scribed HGO from P1 with peak flux density.
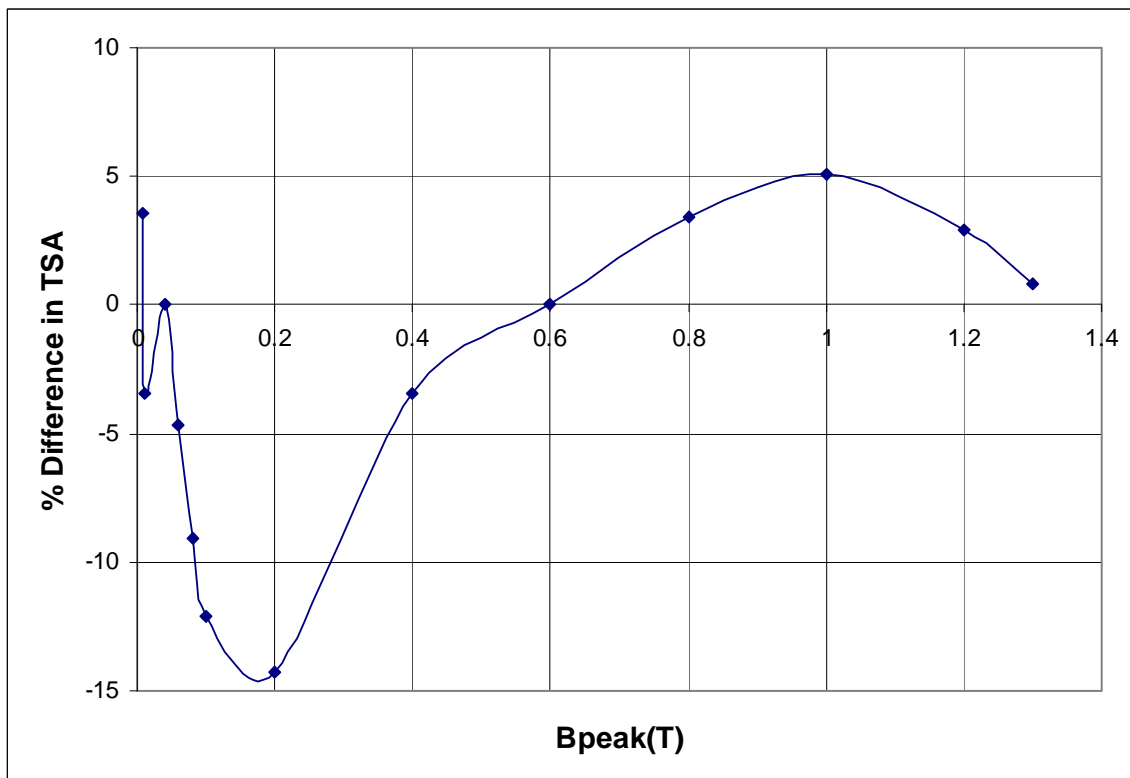
Fig. AC 2: Variation of percentage difference of average TSA of HGO and domain scribed HGO from P1 with peak flux density.
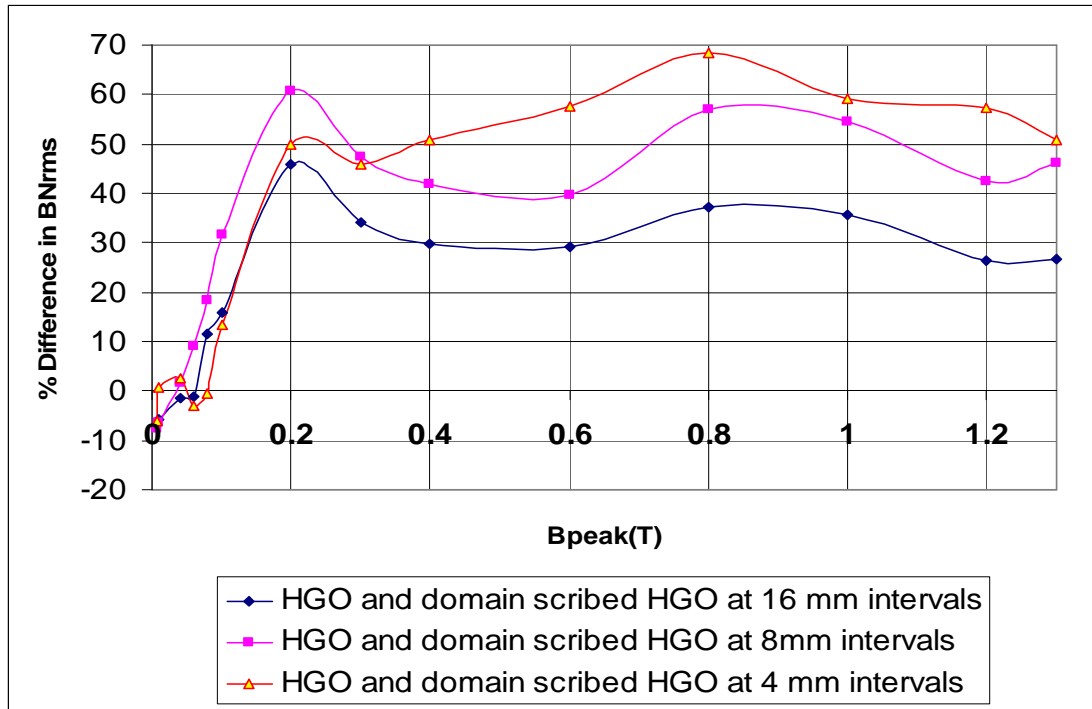
Fig. AC 3: Variation of percentage difference in average rms BN between unscribed HGO and HGO domain scribed at 16 mm, 8 mm and 4 mm intervals respectively with peak flux density.
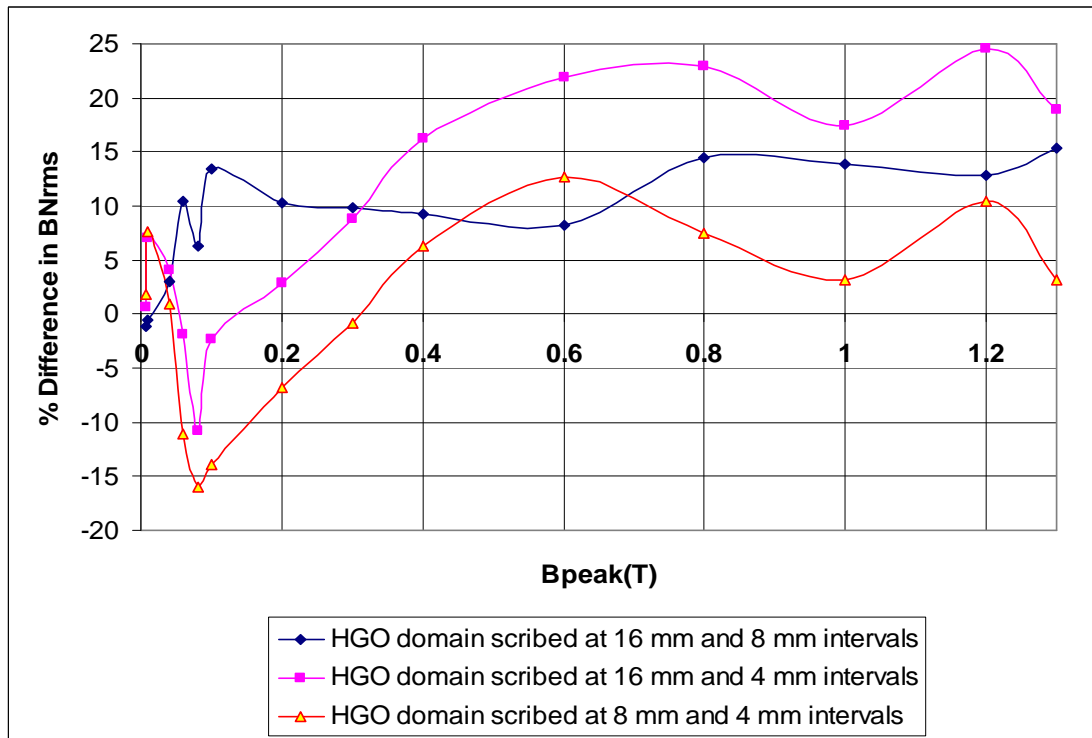
Fig. AC 4: Variation of percentage difference in average rms BN between HGO domain scribed at 16 mm and 8 mm, 16 mm and 4 mm, and 8 mm and 4 mm intervals with peak flux density.
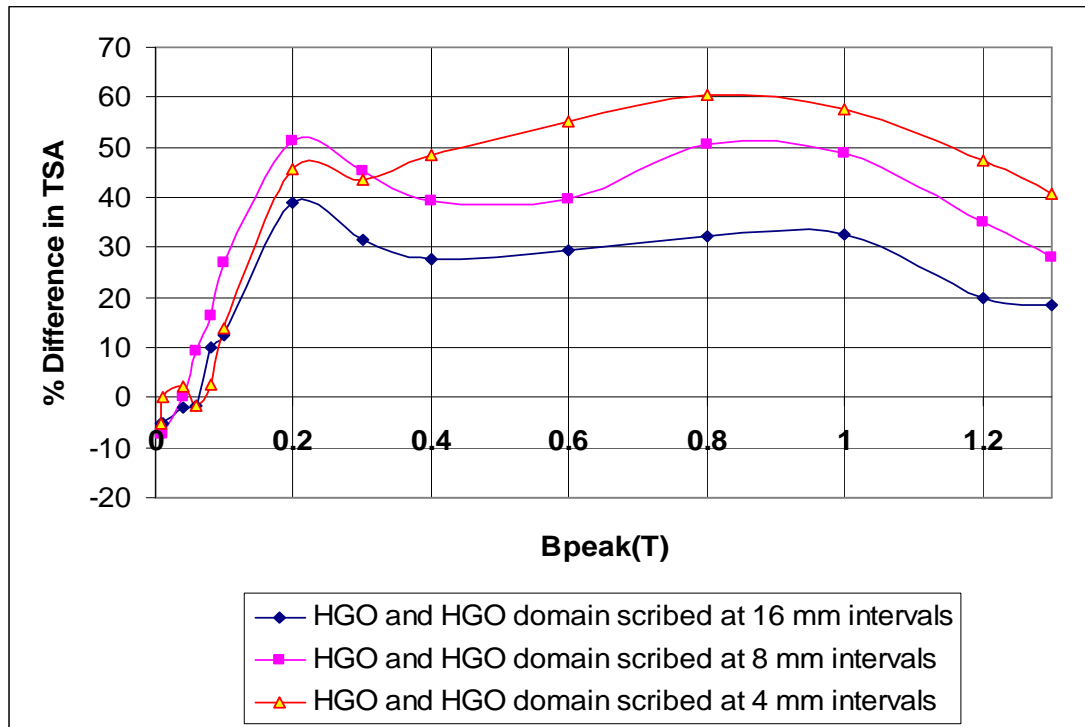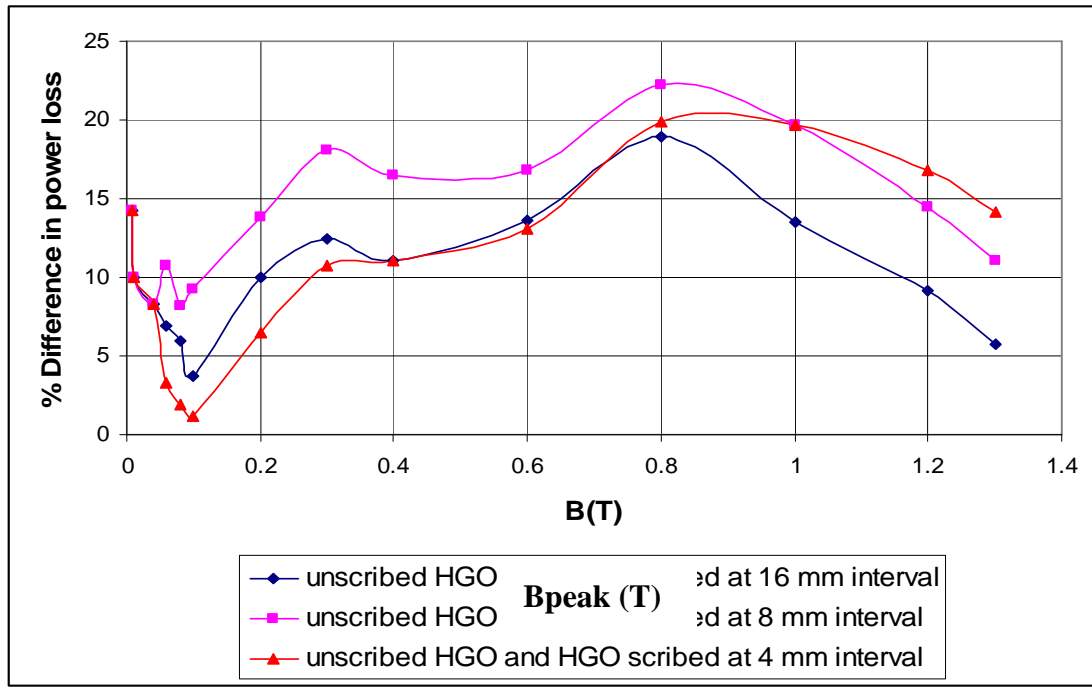
Fig. AC 5: Variation of percentage difference in average TSA of unscribed HGO and HGO domain scribed at 16 mm, 8 mm and 4 mm intervals respectively with flux density.
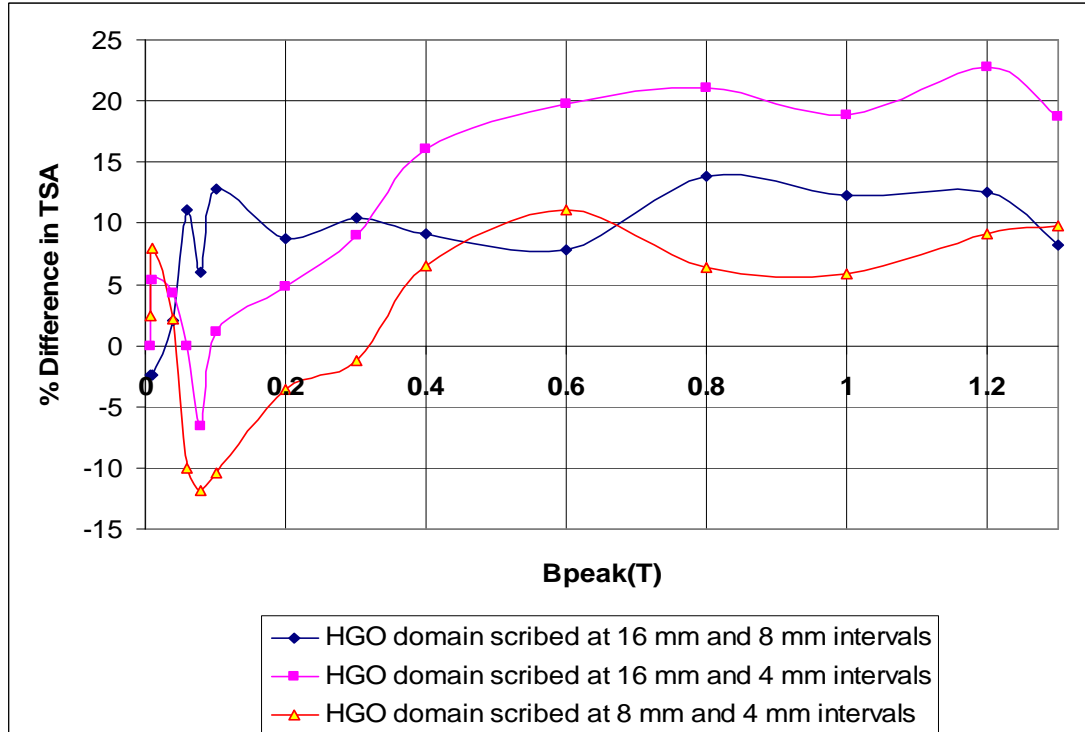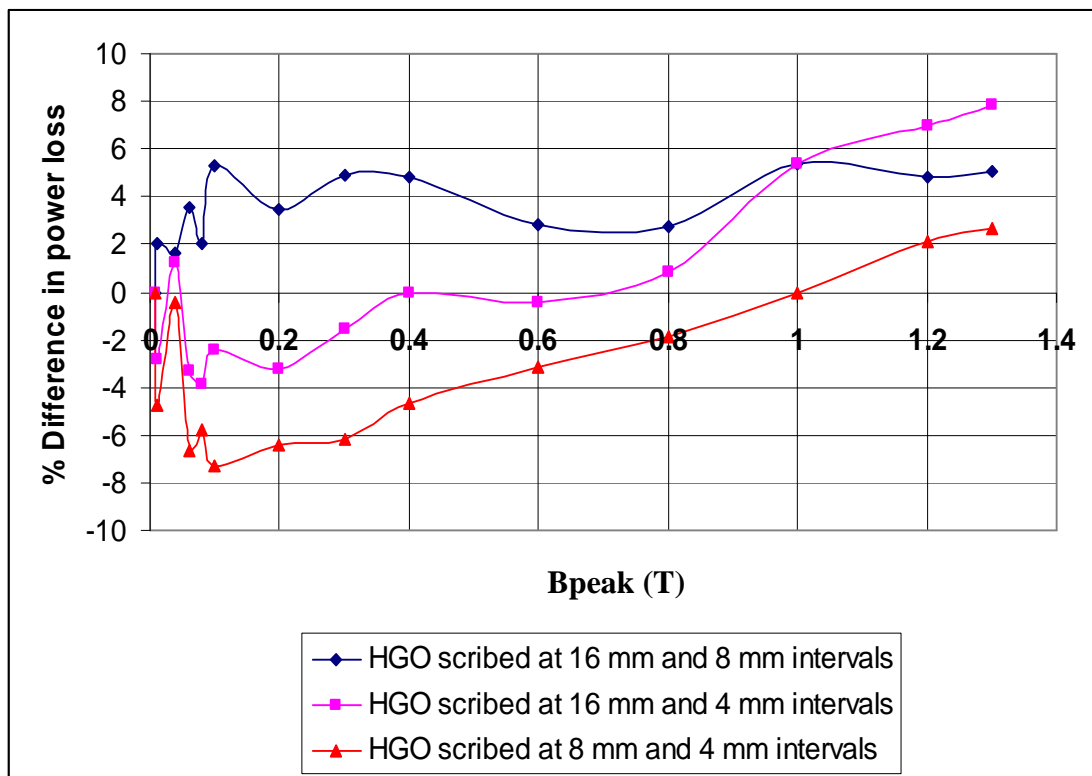

Fig. AC 6: Variation of percentage difference in average TSA between HGO domain scribed at 16 mm and 8 mm, 16 mm and 4 mm, and 8 mm and 4 mm intervals with flux density.
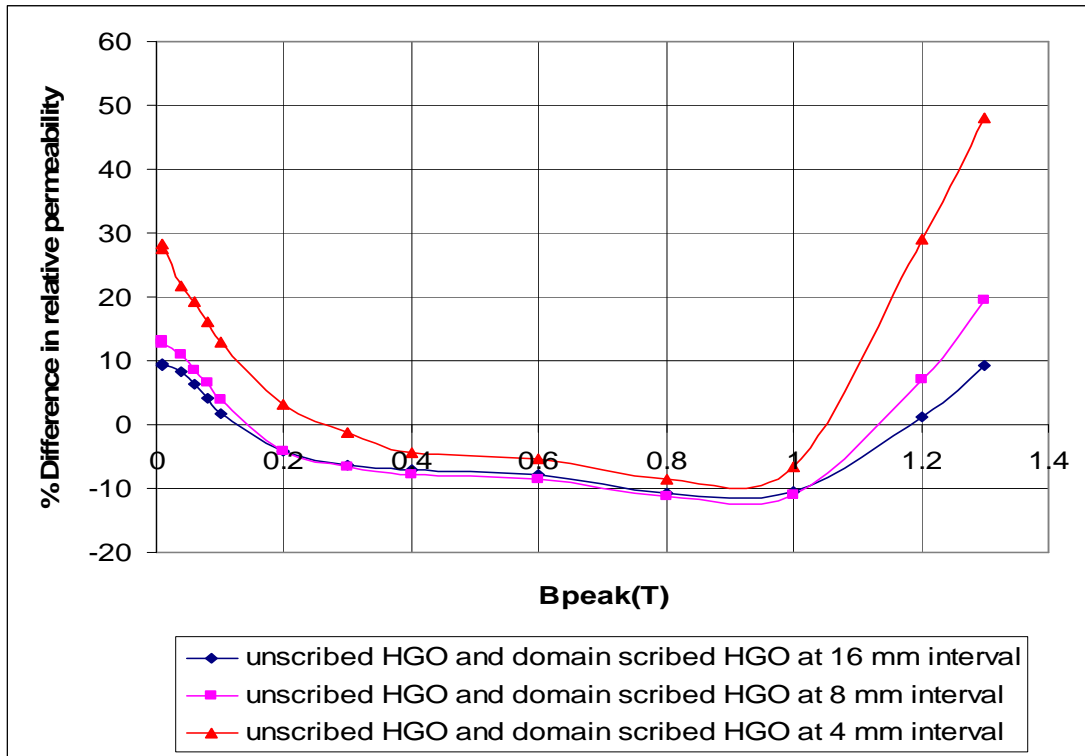
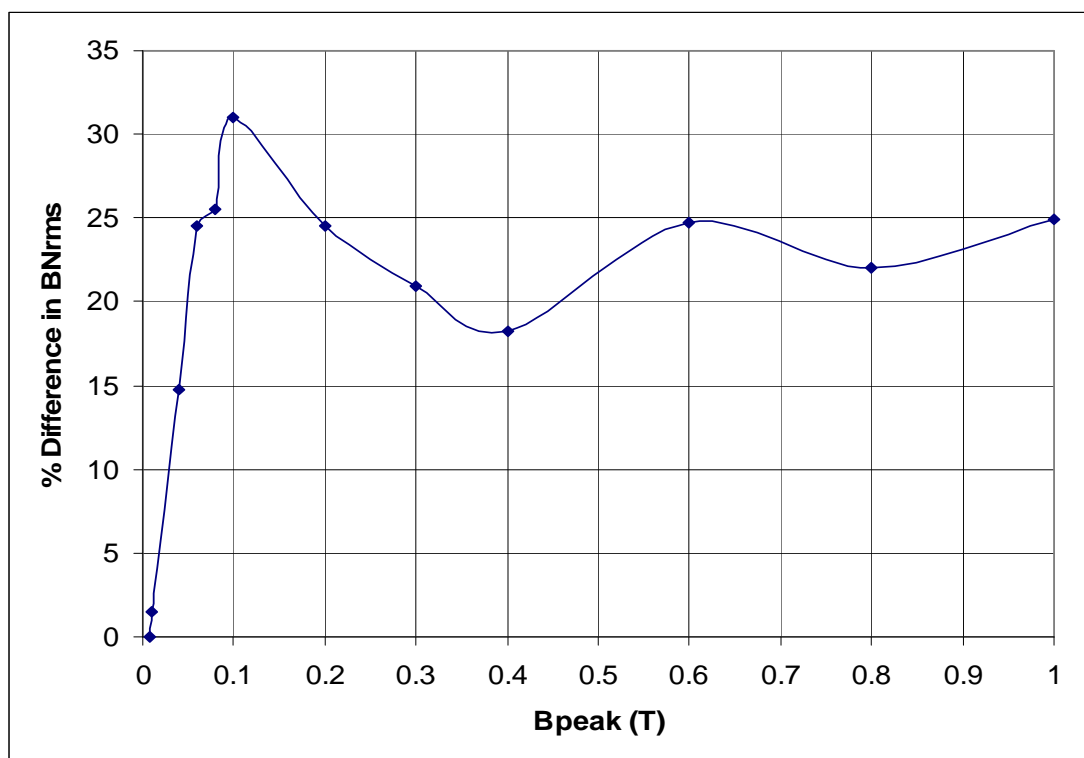Fig. AC 7: Variation of percentage difference in average relative permeability of unscribed HGO and HGO domain scribed at 16 mm, 8 mm and 4 mm intervals respectively with peak flux density.
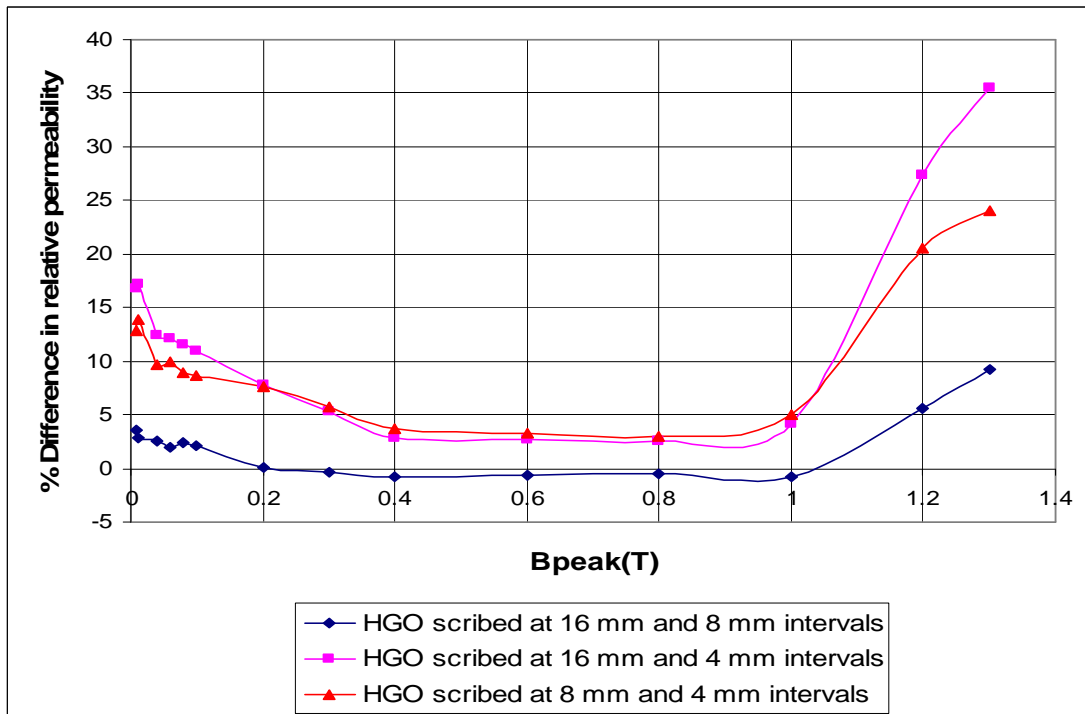
Fig. AC 8: Variation of percentage difference in average relative permeability between HGO domain scribed at 16 mm and 8 mm, 16 mm and 4 mm, and 8 mm and 4 mm intervals with flux density.
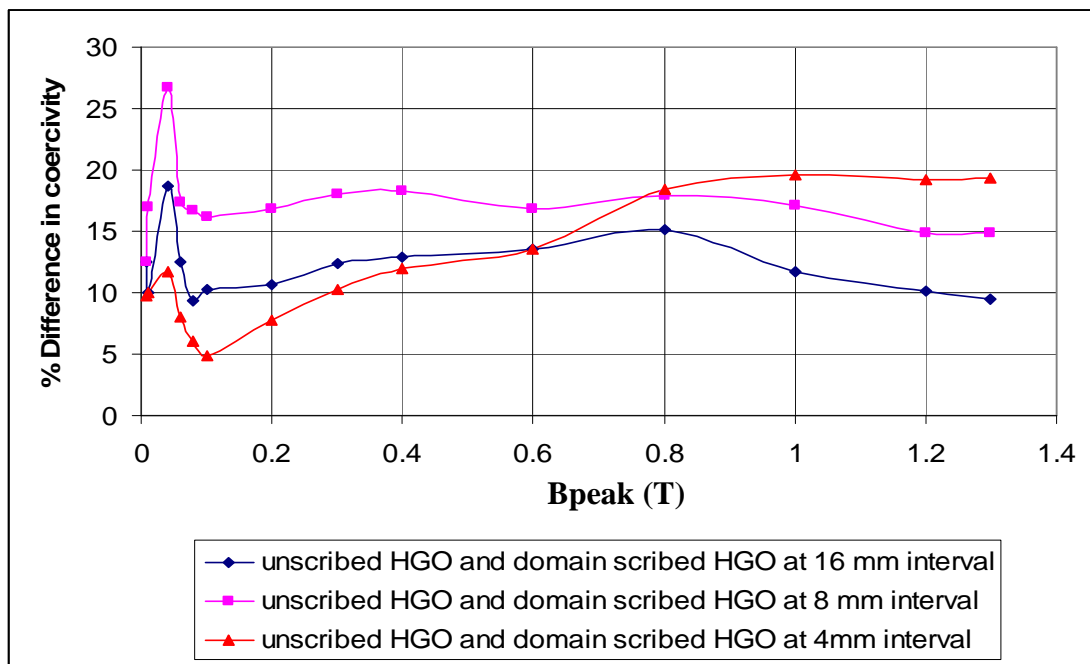
Fig. AC 9: Variation of percentage difference in average coercivity of unscribed HGO and HGO domain scribed at 16 mm, 8 mm and 4 mm intervals respectively with flux density.
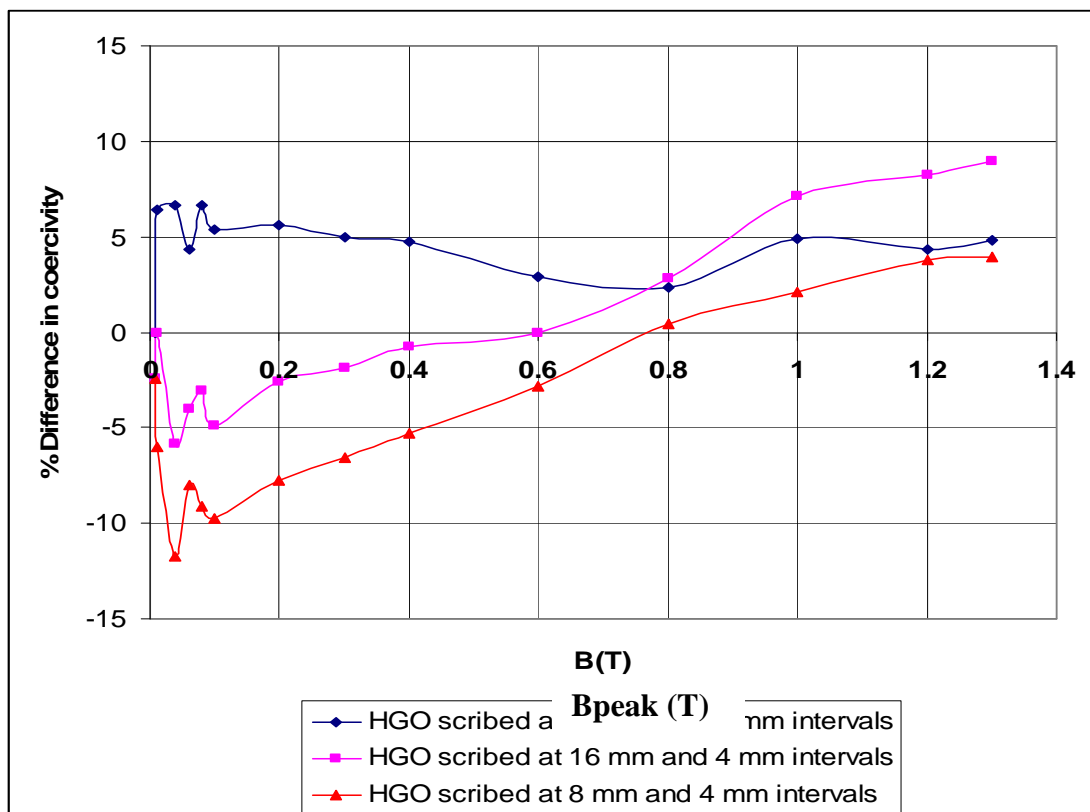
Fig. AC 10: Variation of percentage difference in average coercivity between HGO domain scribed at 16 mm and 8 mm, 16 mm and 4 mm, and 8 mm and 4 mm intervals with flux density.

Fig. AC 11: Variation of percentage difference in average power loss of unscribed HGO and HGO domain scribed at 16 mm, 8 mm and 4 mm intervals respectively with flux density.

Fig. AC 12: Variation of percentage difference in average power loss between HGO domain scribed at 16 mm and 8 mm, 16 mm and 4 mm, and 8 mm and 4 mm intervals with flux density.

184

Fig. AC13: Variation of percentage difference in average rms BN of decoated HGO caused by applying 3 MPa at different values of peak flux density.
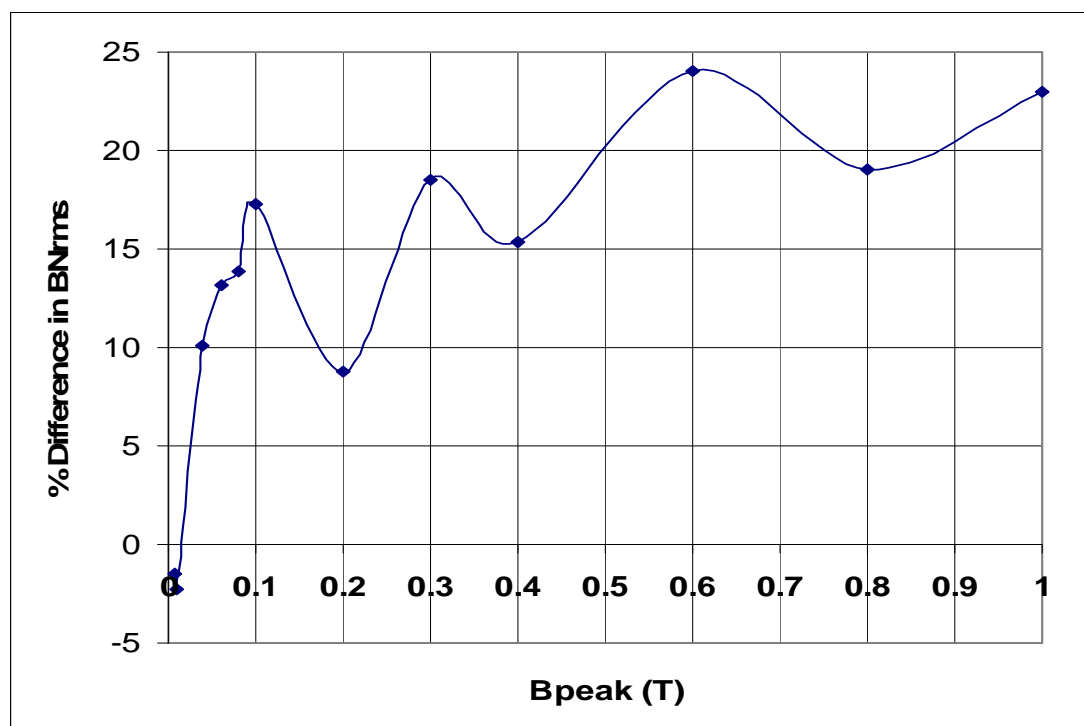
Fig. AC14: Variation of percentage difference in average rms BN of decoated CGO caused by applying 3 MPa at different values of peak flux density.
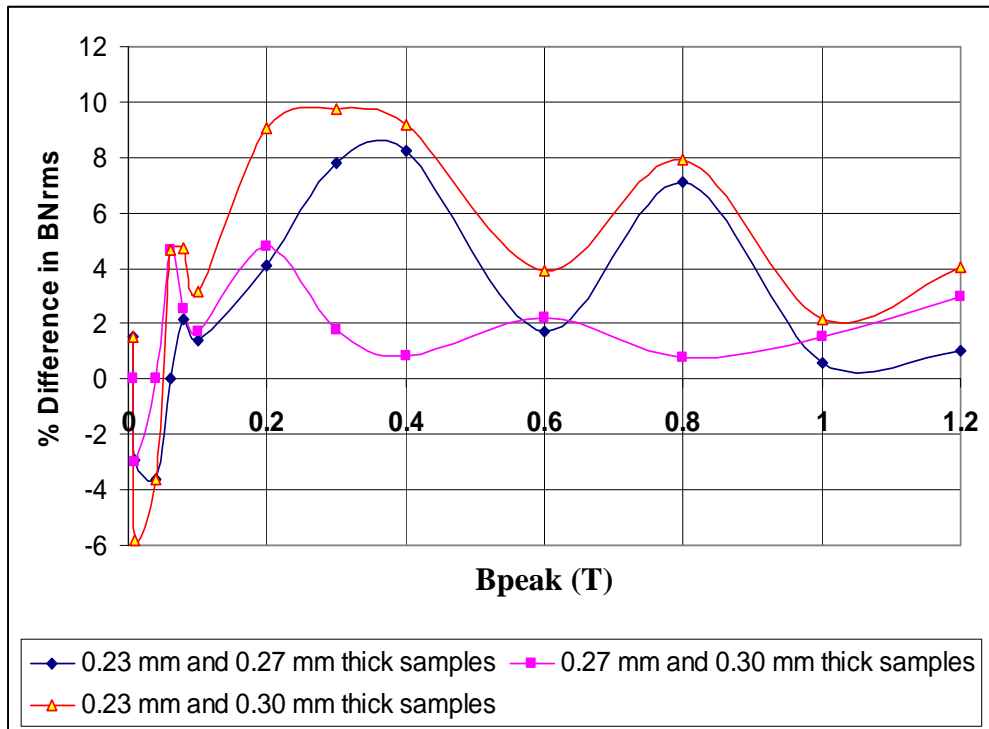
Fig. AC 15: Variation of the percentage difference in rms BN between samples of CGO of named thicknesses with peak flux density.
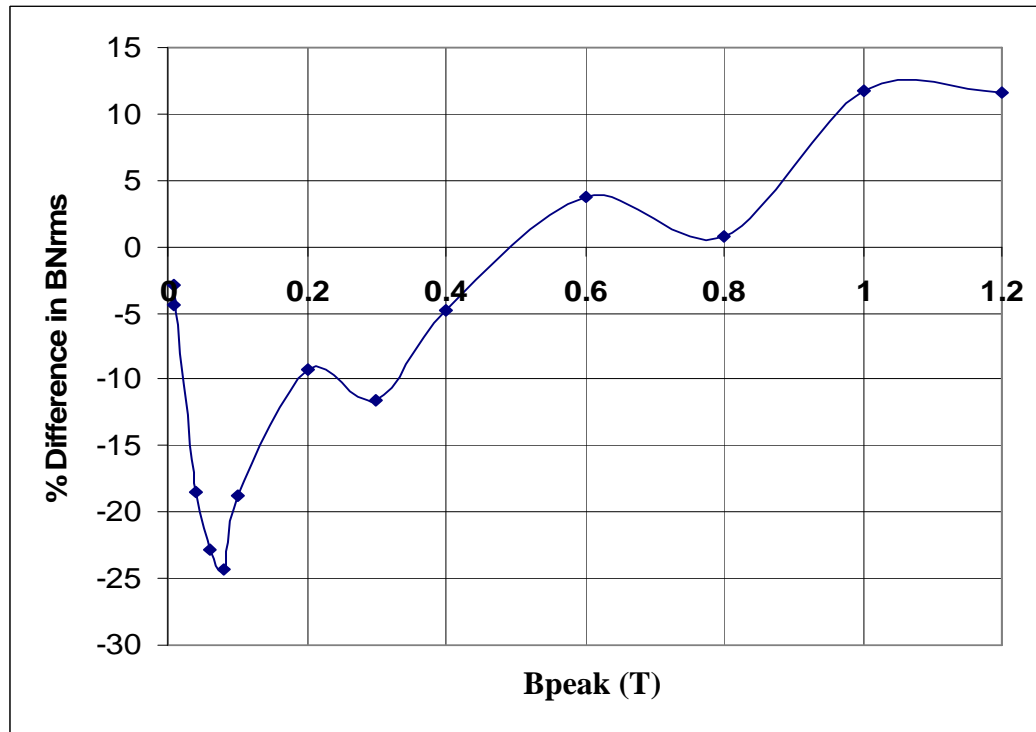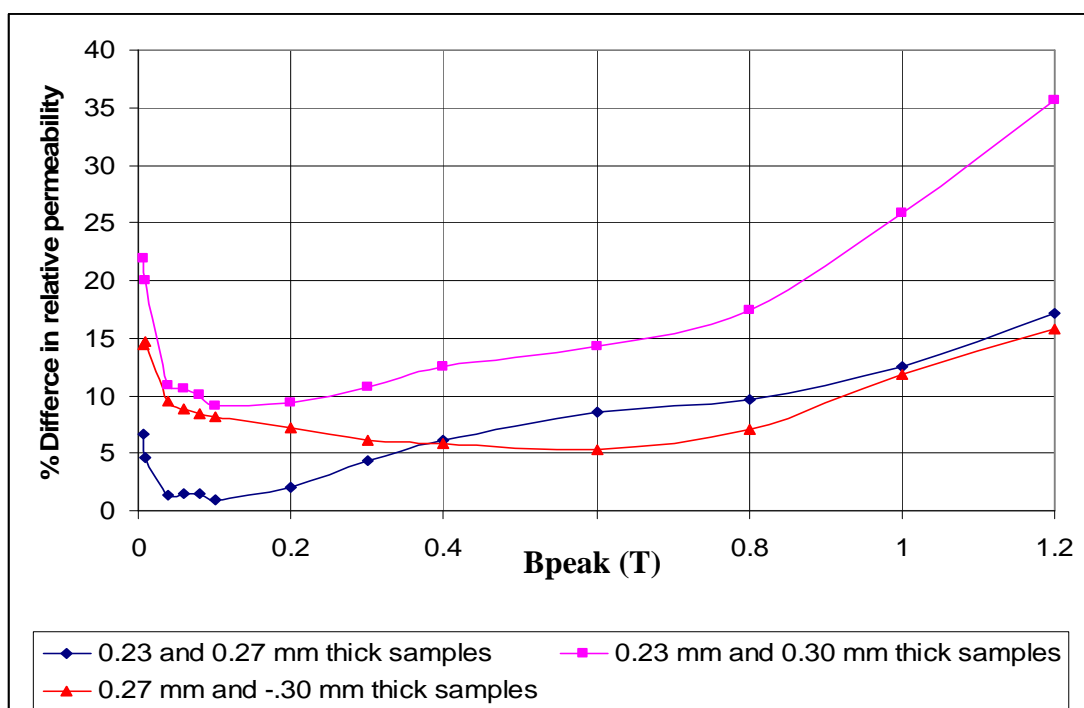

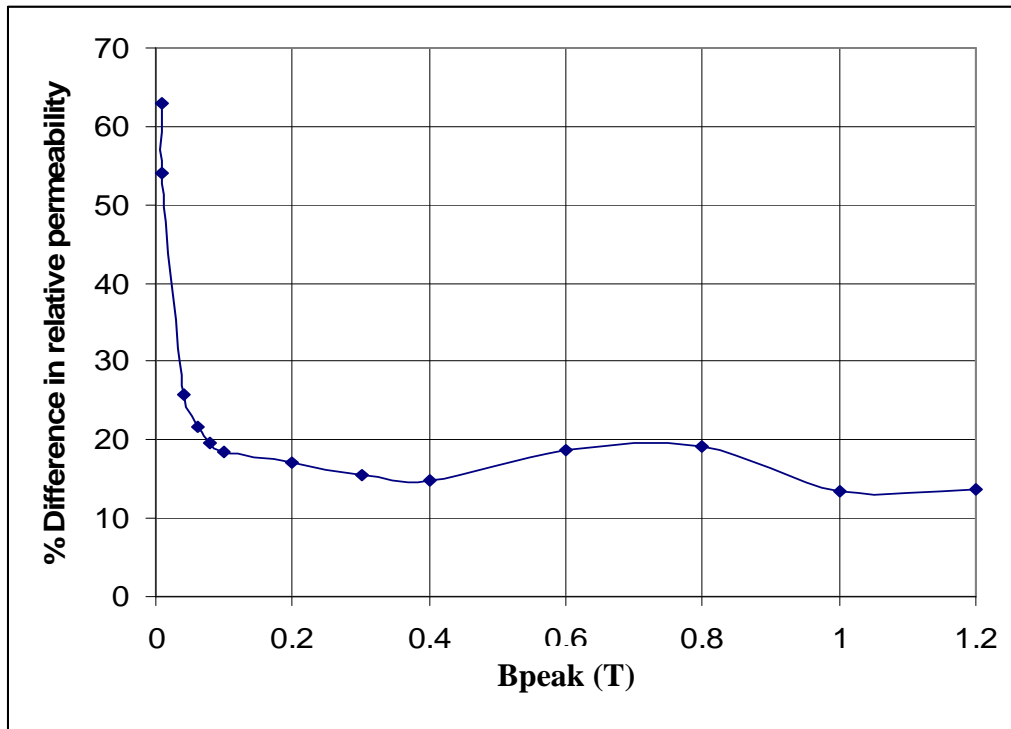Fig. AC 16: Variation of the percentage difference in rms BN of CGO samples of thicknesses 0.35 mm and 0.50 mm with peak flux density.
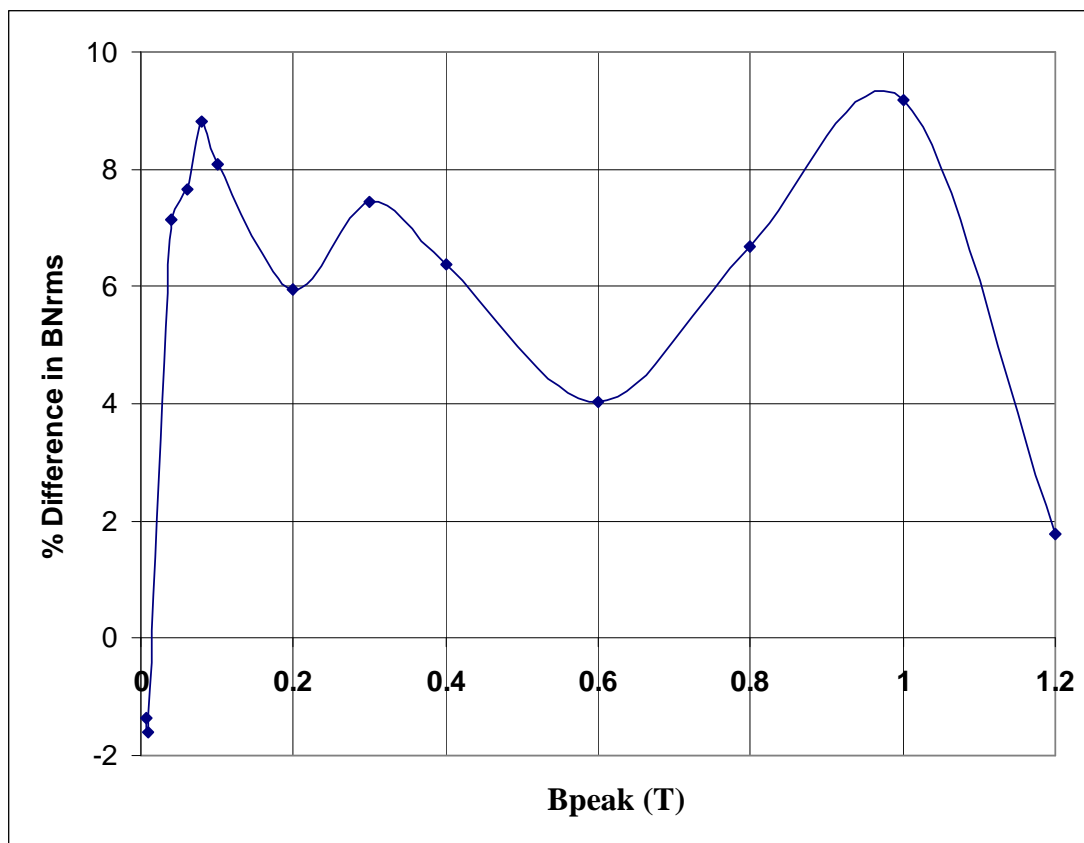
Fig. AC 17: Variation of percentage difference in BNrms of HGO samples of thicknesses 0.27 mm and 0.30 mm with peak flux density.

Fig. AC 18: Variation of the percentage difference in average relative permeability between samples of CGO of named thicknesses with peak flux density.

Fig. AC 19: Variation of percentage difference in average relative permeability of CGO samples of thicknesses 0.35 mm and 0.50 mm with peak flux density.
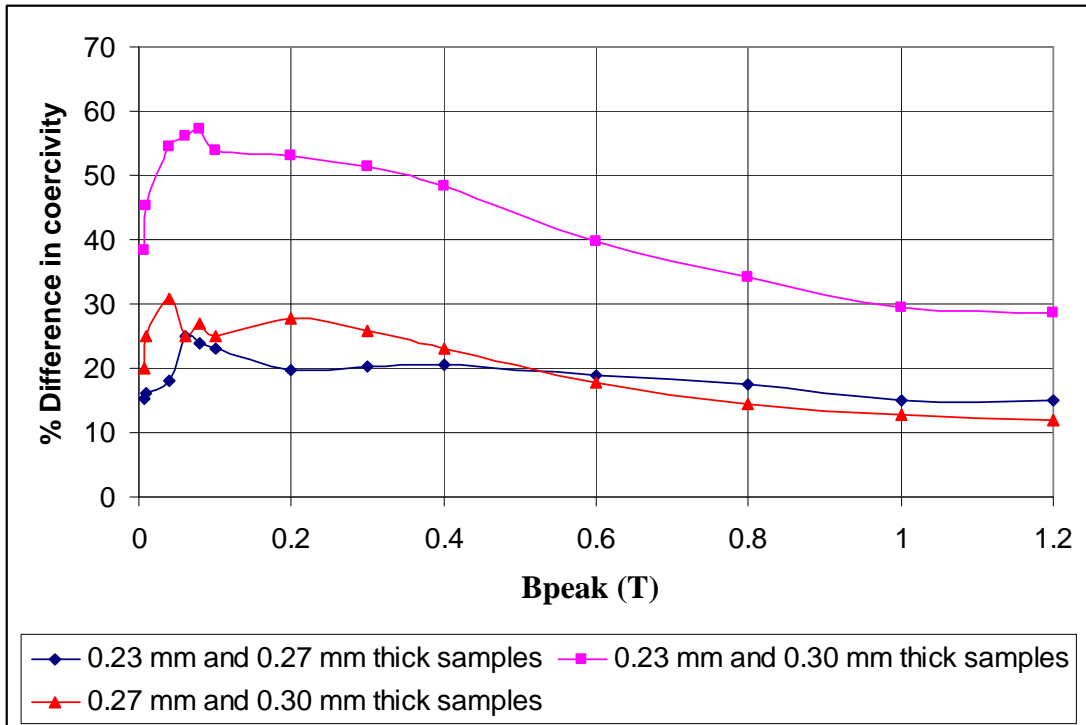

Fig. AC 20: Variation of the percentage difference in average coercivity between samples of CGO of named thicknesses with peak flux density.
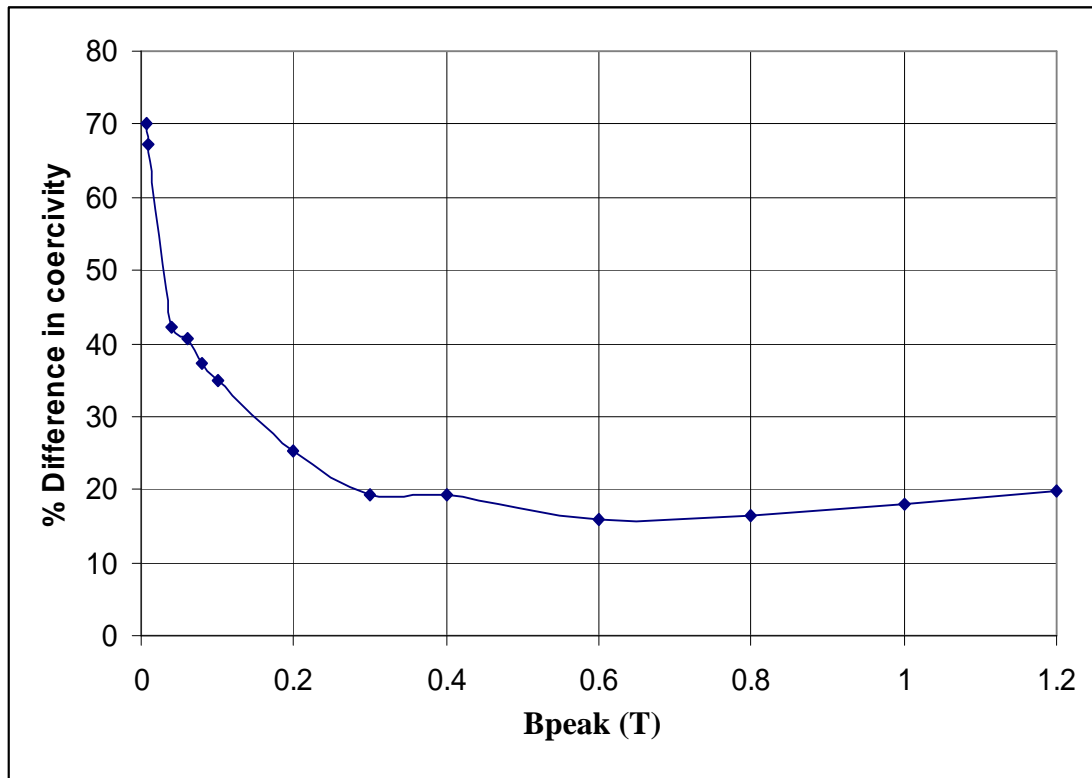
Fig. AC 21: Variation of percentage difference in average coercivity of CGO samples of thicknesses 0.35 mm and 0.50 mm with peak flux density.
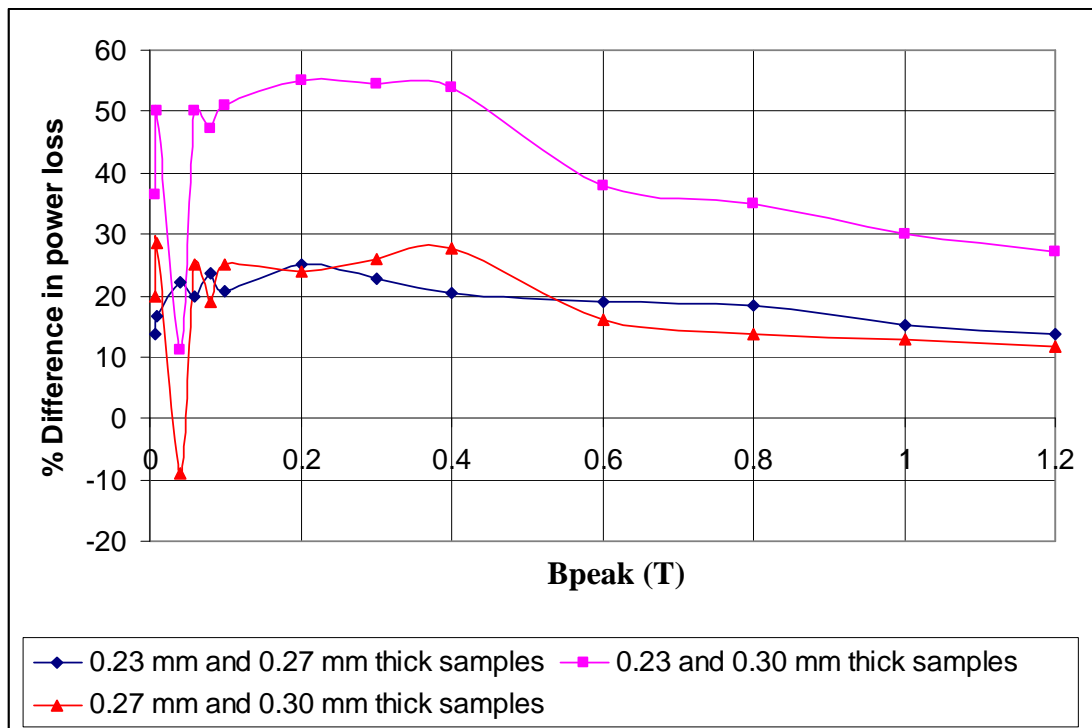

Fig. AC 22: Variation of the percentage difference in average power loss between samples of CGO of named thicknesses with peak flux density.
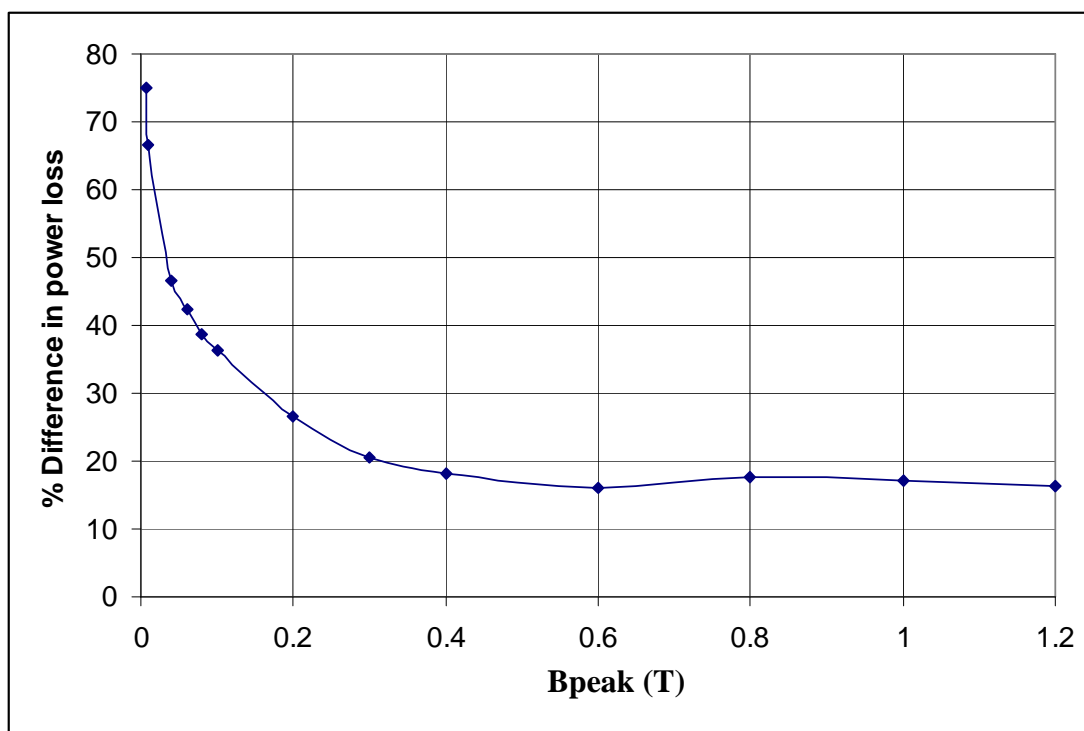
Fig. AC 23: Variation of percentage difference in average power loss of CGO samples of thicknesses 0.35 mm and 0.50 mm with peak flux density.
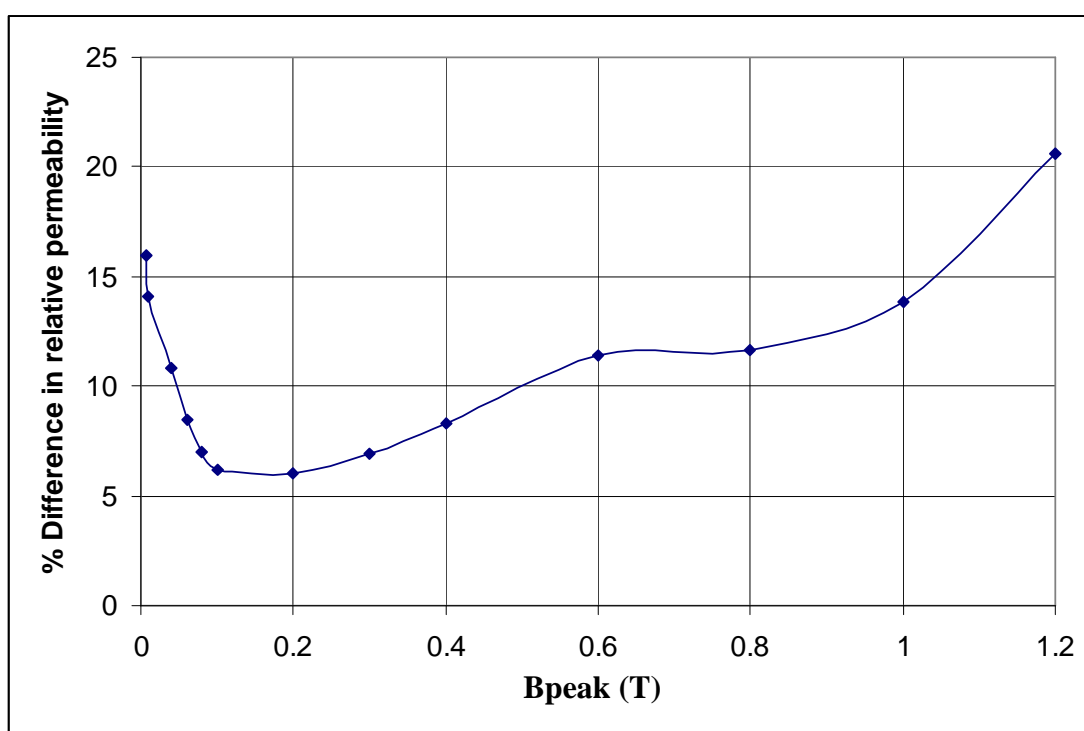

Fig. AC 24: Variation of percentage difference in average relative permeability of HGO samples of thicknesses 0.27 mm and 0.30 mm with peak flux density.
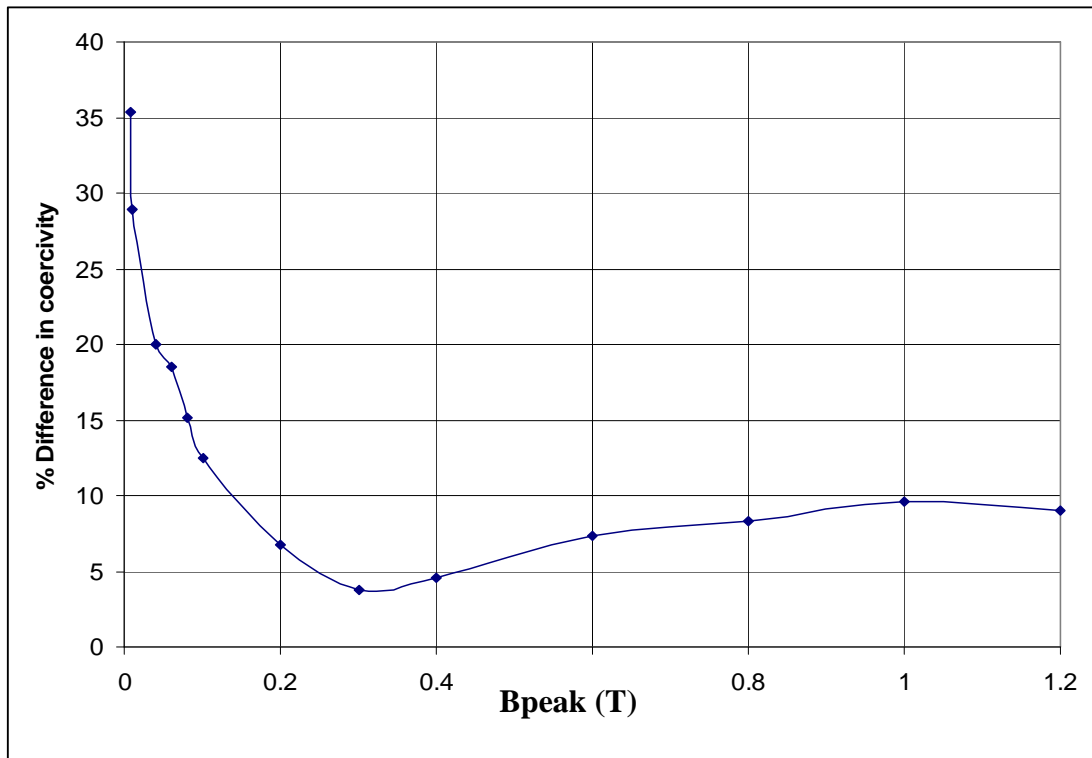
Fig. AC 25: Variation of percentage difference in average coercivity of HGO samples of thicknesses 0.27 mm and 0.30 mm with peak flux density.
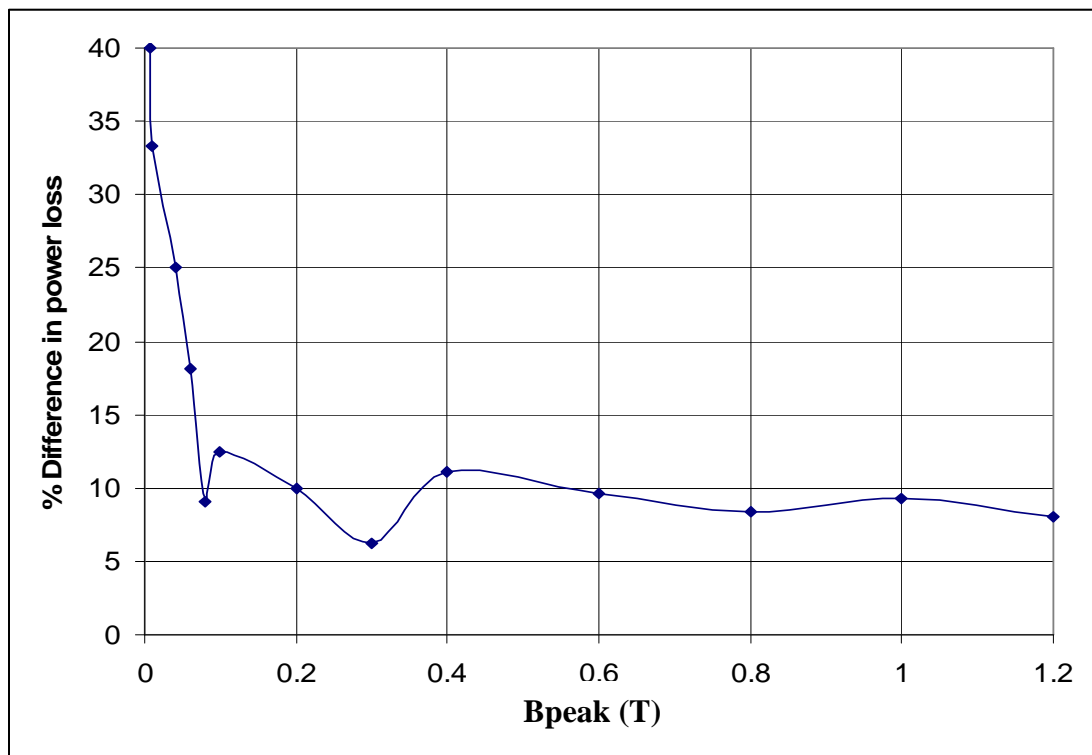

Fig. AC 26: Variation of percentage difference in average power loss of HGO samples of thicknesses 0.27 mm and 0.30 mm with peak flux density.

APPENDIX D

LIST OF PUBLICATIONS

Publications

1. **Nkwachukwu Chukwuchekwa**, Anthony Moses and Phil Anderson, Barkhausen noise in 3% Si-Fe at 50 Hz, Journal of Electrical Engineering, Vol 61. No 7/s, 69-72, 2010, ISBN/ISSN: 1335-3632.

2. Moses A. J., Anderson P. I., **Chukwuchekwa N.,** Hall J P, Williams P I, Xu X T, Analysis of magnetic fields on the surface of grain oriented electrical steel, Measurements 2011, Proceedings of the 8th International Conference, pp. 106-110 Smolenice, Slovakia,

3. **Nkwachukwu Chukwuchekwa**, Anthony J. Moses and Phil Anderson, Study of the effects of surface coating on magnetic Barkhausen noise in grain-oriented electrical steel, IEEE Transactions on Magnetics, Vol. 48, No. 4, April 2012.

4. **Nkwachukwu Chukwuchekwa**, Anthony J. Moses and Phil Anderson, Investigation of the effects of strips thickness and grain size on AC magnetic Barkhausen noise of grain-oriented electrical steel, Przeglad Elektrotechniczny (Electrical Review). **ACCEPTED FOR PUBLICATION**.

5. **Nkwachukwu Chukwuchekwa**, Anthony J. Moses and Phil Anderson, Effects of Strip Thickness and Silicon Content on Magnetic Barkhausen Noise of Non-oriented Electrical Steel at 50 Hz, International Journal of Applied Electromagnetics and Mechanics, **ACCEPTED FOR PUBLICATION**.

Conference Presentations

1. **Nkwachukwu Chukwuchekwa**, Anthony Moses and Phil Anderson, Barkhausen noise in grain-oriented 3% Si-Fe at 50 Hz, Magnetic Measurement Conference, 12-15 September, 2010, Prague, Czech Republic **ORAL PRESENTATION.**

2. Moses A J, Anderson P I, **Chukwuchekwa N**, Hall J P, Williams P I, Xu X T, Analysis of magnetic fields on the surface of grain oriented electrical steel, Measurement 2011 Conference. 27-30 April, 2011, Smolenice Castle, Slovakia. **ORAL PRESENTATION**.

3. **Nkwachukwu Chukwuchekwa**, Anthony J. Moses and Phil Anderson, Effects of sample thickness and silicon content on Barkhausen noise of Non-oriented electrical steel at 50 Hz, 15th International Symposium on Applied Electromagnetics and Mechanics, 7-9 September 2011,Napoli, Italy. **ORAL PRESENTATION**.

4. **Nkwachukwu Chukwuchekwa**, Anthony Moses, Phil Anderson and Yevgen Melikhov, Barkhausen noise technique for non destructive evaluation of grain and non grain oriented electrical steels, Universal Network of Magnetic Non Destructive Evaluation (UNMNDE), 24 September 2011, Kos Island, Greece. **ORAL PRESENTATION.**

5. **Nkwachukwu Chukwuchekwa**, Anthony J. Moses and Phil Anderson, Study of the effects of surface coating on magnetic Barkhausen noise in grain-oriented electrical steel , 20th Soft Magnetic Materials(SMM) Conference, 18-22 September 2011, Kos Island, Greece. **POSTER PRESENTATION**.

6. **Nkwachukwu Chukwuchekwa**, Anthony J. Moses and Phil Anderson, Investigation of the effects of strips thickness and grain size on AC magnetic Barkhausen noise of grain-oriented electrical steel, X Symposium on Magnetic Measurements, 17-19 October 2011, Warsaw, Poland. **ORAL PRESENTATION**.